Università degli Studi di Bergamo
School of Engineering
Department of Engineering and Applied Sciences
Doctoral Programme in Engineering and Applied Sciences

Time and Frequency Domain output-only system identification from earthquake-induced structural response signals

Doctoral Dissertation of:
Fabio PIOLDI

Advisor:
Prof. Egidio RIZZI

The Chair of the Doctoral Program:
Prof. Valerio RE

A.Y. 2016/2017 – XXIX Cycle (2014-2016)

Acknowledgements

Acknowledgements.

Abstract

OUTPUT-ONLY Time and Frequency Domain system identification techniques are developed in this doctoral dissertation towards the challenging assessment of current structural dynamic properties of buildings from earthquake-induced structural response signals, at simultaneous heavy damping. Three different Operational Modal Analysis (OMA) techniques, namely a *refined Frequency Domain Decomposition (rFDD)* algorithm, an *improved Data-Driven Stochastic Subspace Identification (SSI-DATA)* procedure and a novel *Full Dynamic Compound Inverse Method (FDCIM)* are formulated and implemented within MATLAB, and exploited for the strong ground motion modal dynamic identification of selected buildings. First, the three OMA methods are validated by the adoption of synthetic earthquake-induced structural response signals, generated from numerical integration on benchmark linear shear-type frames. Then, real seismic response signals are effectively processed, by getting even closer to real Earthquake Engineering identification scenarios. In the end, the three OMA methods are systematically applied and compared. The present thesis demonstrates the reliability and effectiveness of such advanced OMA methods, as convenient output-only modal identification tools for Earthquake Engineering and Structural Health Monitoring purposes.

Summary

In the present doctoral dissertation, research focus goes on Time and Frequency Domain output-only system identification methods relying on earthquake-induced structural response signals. The aim of such a wave-front research investigation is that of assessing current structural modal properties of civil engineering buildings, by three original modal dynamic identification implementations within an Earthquake Engineering and Structural Health Monitoring context.

Specifically, the formulated Operational Modal Analysis (OMA) techniques are a Frequency Domain *refined Frequency Domain Decomposition (rFDD)* algorithm, a Time Domain *Data-Driven Stochastic Subspace Identification (SSI-DATA)* procedure and a new Time Domain *Full Dynamic Compound Inverse Method (FDCIM)*. Such investigation scenario appears quite challenging in the dedicated scientific and technical literature. Indeed, by taking earthquake-induced structural responses as input signals for the identification process, typical OMA validity assumptions like that of stationary white noise input no longer hold. Additionally, heavy damping conditions (in terms of identification challenge) are considered all together.

The three original OMA implementations are formulated and developed within MATLAB. Synthetic earthquake-induced structural response signals are generated first from different linear shear-type frames, with variable structural features, which are taken as benchmark structures, for necessary validation purposes. Then, real seismic response signals from a selected building are effectively processed, by getting even closer to real Earthquake Engineering identification scenarios.

The rFDD algorithm, a main subject of the present thesis, may be conceived as an advanced evolution of classical FDD methods, as specifically devised here to deal with earthquake-induced structural response signals and heavy damping conditions. Through novel dedicated algorithmic

and computational strategies, the present rFDD implementation results in a rather robust tool, within such a challenging identification context. The rFDD technique is specifically validated by adopting a complete seismic dataset, namely by considering the twenty-two Far-Field multicomponent (NS, WE) seismic base excitations from the FEMA P695 earthquake database, as applied to three linear shear-type frames (a two-, a three- and a six-storey frame).

Further, the rFDD technique is innovatively expanded to operate also under Soil-Structure Interaction conditions, in order to deal with both flexible- and fixed-base conditions. The developed analyses are performed on earthquake-induced synthetic response signals, which are computed from a benchmark linear five-storey shear-type frame, under several earthquake excitations and at variable foundation properties. Then, rFDD originally operates within an OMAX (Operational Modal Analysis with eXogenous input) environment on the base-excited buildings. This aims at detecting also the underlying fixed-base condition and at quantifying the amount of Soil-Structure Interaction to which the building under analysis may be subjected to.

The SSI-DATA identification algorithm, instead, is developed in an optimized version, which aims at exploring and improving the classical Stochastic Subspace Identification performance in the presence of seismic response signals and heavy damping. In particular, specifically developed stabilization diagrams have been conceived, jointly with the best setting of the processing tool and of its computational parameters, in order to handle the present challenging Earthquake Engineering context.

Finally, the new FDCIM technique is an innovative output-only element-level system identification and input estimation method, which works fine towards the simultaneous identification of modal parameters, input excitation time history and structural features at the element-level, by adopting earthquake-induced structural response signals only. The method operates within a deterministic state-space form, by an original two-stage iterative algorithm, and arrives at consistent identification results in the Earthquake Engineering range.

The doctoral thesis thoroughly analyses and compares the outcomes from such three implemented OMA techniques, by demonstrating their reliability and effectiveness, as convenient output-only modal identification tools towards innovative Earthquake Engineering and Structural Health Monitoring purposes.

Contents

1 Introduction **1**

2 Operational Modal Analysis under strong ground motion structural response signals **5**

2.1 Time Domain and Frequency Domain output-only modal identification under earthquake-induced structural response signals 6

2.2 Time Domain and Frequency Domain OMA with seismic excitation under Soil-Structure Interaction conditions 10

2.3 Output-only element-level system identification and input estimation under earthquake base excitation 14

3 Refined Frequency Domain Decomposition: theoretical background **21**

3.1 Fundamentals of the refined Frequency Domain Decomposition technique 21

3.1.1 Main theoretical background of the rFDD algorithm . 22

3.1.2 Refined FDD technique for earthquake-induced structural response signals and heavy damping 24

3.1.3 Main novelties of the present rFDD algorithm 28

3.2 Refined FDD modal dynamic identification of natural frequencies and mode shapes 30

3.2.1 Time-Frequency signal analysis and suitably-developed filtering for the rFDD technique 30

3.2.2 Auto- and cross-correlation matrix processing 31

3.2.3 Integrated approach for PSD matrix computation . . 32

3.2.4 Strategies for natural frequency and mode shape modal dynamic identification 35

3.3 Modal damping ratio estimates by refined FDD 36

3.3.1 Classical Enhanced FDD algorithm 37

3.3.2 Damping estimates by refined FDD: iterative loop and optimization algorithm 38
3.3.3 Enhancement of modal parameter estimates via coupled Chebyshev Type II bandpass filters 42
3.4 Further rFDD computational procedures at seismic input and heavy damping 46
3.4.1 Reconstruction of the original SDoF spectral bells . . 46
3.4.2 Frequency resolution enhancement 48
3.4.3 Modal detection and validation via MAC indexes and complexity analysis 49

4 Refined Frequency Domain Decomposition: main results 51
4.1 Adopted earthquake dataset and numerical models 52
4.2 Results from synthetic output-only modal dynamic identification 54
4.2.1 Analyses and results with a reference three-storey frame 54
4.2.2 Further synthetic identification analyses with a realistic ten-storey frame 57
4.3 Extensive validation with the FEMA P695 earthquake database 60
4.3.1 Adopted FEMA P695 seismic database 60
4.3.2 Numerical rFDD identification results 62
4.3.3 Further rFDD identification analyses at heavy damping 73

5 Further rFDD results with Soil-Structure Interaction under earthquake-induced structural response signals 77
5.1 Soil-Structure Interaction and structural response modeling 77
5.1.1 Idealization of a shear-type frame with Soil-Structure Interaction effects 78
5.1.2 Adopted numerical models 80
5.2 Results from synthetic output-only modal dynamic identification under Soil-Structure Interaction 84
5.3 OMAX evaluation of Soil-Structure Interaction effects . . . 92
5.3.1 Identification of Soil-Structure Interaction conditions . 92
5.3.2 Empirical method for the estimation of Soil-Structure Interaction effects 94
5.4 Remarks and conclusions for the rFDD algorithm in the presence of Soil-Structure Interaction 96

6 Data-Driven Stochastic Subspace Identification: theory and results 99
6.1 Fundamentals of the Data-Driven Stochastic Subspace Identification technique 99
6.1.1 Main theoretical background of the SSI-DATA algorithm 100
6.1.2 Implemented SSI-DATA algorithm: computational steps 104
6.1.3 Novelties of the present SSI-DATA algorithm 106
6.1.3.1 Definition of the weighting matrices 107
6.1.3.2 Specifically-developed stabilization diagrams . 107
6.1.3.3 System order selection and modal dynamic identification 109
6.2 Results from synthetic output-only modal dynamic identification 110
6.2.1 Analyses and results with a reference three-storey frame 111
6.2.2 Further synthetic identification analyses with a realistic ten-storey frame 114

7 Full Dynamic Compound Inverse Method: theory and results 117
7.1 Fundamentals of the Full Dynamic Compound Inverse Method 117
7.1.1 Basic mathematical model of the FDCIM algorithm . 118
7.1.2 Two-stage identification algorithm 124
7.1.3 Element-level identification procedure 129
7.2 Full Dynamic Compound Inverse Method with General and Rayleigh damping 130
7.2.1 FDCIM mathematical model with General and Rayleigh damping 130
7.2.2 FDCIM two-stage identification algorithm with General and Rayleigh damping 134
7.2.3 Estimation of Rayleigh damping coefficients 135
7.3 Results from synthetic output-only modal dynamic identification 136
7.3.1 Analyses and results with a reference three-storey frame 137
7.3.1.1 Element-level identification estimates for a three-storey frame 140
7.3.2 Further synthetic identification analyses with a realistic ten-storey frame 143

7.3.2.1 Element-level identification estimates for a ten-storey frame 145

8 Analysis and comparison between the three investigated OMA techniques 149

8.1 rFDD, SSI-DATA and FDCIM analyses with real earthquake-induced structural response signals 149

8.1.1 Real case study description 149

8.1.2 Performed analyses and results 151

8.1.2.1 Element-level identification and input estimation via FDCIM 156

8.2 Main conclusions on the performed OMA analyses 157

9 Conclusions 161

List of Figures 169

List of Tables 175

Bibliography 177

Chapter 1

Introduction

The determination of current modal dynamic properties from earthquake-induced structural response signals displays a key importance in the contexts of Earthquake Engineering and Structural Health Monitoring, with the aim of investigating the assessment of structural dynamic properties of civil engineering buildings in the seismic engineering range. Through prompt modal parameter estimates, also structural changes at pre-, current and post-earthquake stages may be potentially detected by specifically-developed identification techniques, either in the linear or in the nonlinear range. Also, heavy damping conditions may characterize the structural behaviour along the development of earthquake events.

During the past years, the adoption of seismic structural responses, as connected to the identification of modal dynamic properties of civil buildings, has been the subject of several researches [6, 7, 33, 50]. Various fields of application may adopt the outcomes of these specific identification tools, as for example Structural Health Monitoring, condition assessment, design process, development or validation of predictive models, evaluation of retrofitting procedures, damage detection, finite element model updating and insertion of possible active, semi-active and passive control devices [2, 3, 28, 35, 75, 78, 111, 112, 133].

The adopted modal identification techniques generally pertain to two different classes, i.e. to Experimental Modal Analysis (EMA) or to Operational Modal Analysis (OMA). EMA techniques rely on the knowledge of both input excitation and output structural response, and are the most diffused identification techniques since from the sixties [36, 41, 75]. OMA (or output-only) procedures, instead, are based on the adoption of structural responses signals only, which in general are induced by unknown ambient excitations, such as by operating loads, wind and traffic [13, 104].

Then, the use of seismic response signals towards modal identification has been attempted in several works, especially within Experimental

Modal Analysis [6, 7, 21, 46, 56], where the seismic input is assumed to be known and measured. Instead, within Operational Modal Analysis, where the seismic input is actually unknown, fewer works attempted successfully such a difficult task [51, 68, 74, 77, 78].

This is the main subject of the present doctoral dissertation. In particular, the research focus goes here on Time and Frequency Domain output-only system identification methods, by relying on earthquake-induced structural response signals. Most OMA techniques are specifically conceived to work with free or ambient vibration recordings, where (small-amplitude) vibrations may be well approximated by stationary Gaussian white noise [17,121]. Rather, the aim of the present investigation is that of assessing current structural modal properties of civil engineering buildings, by three original modal dynamic identification methods within an Earthquake Engineering and Structural Health Monitoring context (Chapter 2).

Specifically, the formulated Operational Modal Analysis (OMA) techniques are a Frequency Domain refined Frequency Domain Decomposition (rFDD) algorithm, a Time Domain Data-Driven Stochastic Subspace Identification (SSI-DATA) procedure and a new Time Domain Full Dynamic Compound Inverse Method (FDCIM). Such investigation scenario appears quite challenging in the dedicated scientific and technical literature. Indeed, by taking earthquake-induced structural responses as input signals for the identification process, typical OMA validity assumptions, like that of stationary white noise input, no longer hold. Additionally, heavy damping conditions (in terms of identification challenge) are considered all together, towards getting even closer to real earthquake scenarios and applications.

The three original OMA implementations are all formulated and developed autonomously within MATLAB (Chapters 3, 6 and 7). Synthetic earthquake-induced structural response signals are generated first from two different linear shear-type frames (a three- and a ten-storey frame) with variable features, which are then taken as benchmark structures for necessary validation purposes. The response signals are generated via direct Newmark's integration from a set of ten selected earthquake records, taken as instances of base excitation (Chapter 4). Subsequently, real seismic response signals are effectively processed (Chapter 8), by getting even closer to real Earthquake Engineering identification scenarios.

The rFDD algorithm [91, 92], a main subject of the present thesis, may be conceived as a considerable evolution of classical FDD methods [16, 17, 125], as specifically devised here to deal with earthquake-induced structural response signals and heavy damping conditions. FDD methods are based on the calculation of the Power Spectral Density (PSD) matrix of the structural response signals, and on its Singular Value De-

composition (SVD), towards modal parameters estimation. Through novel dedicated algorithmic and computational strategies, the present rFDD implementation results in a rather robust identification tool in such a challenging identification context (Chapter 3).

After the preliminary analysis with the three- and ten-storey frames, the rFDD technique is specifically validated by adopting a complete seismic dataset, namely by considering the twenty-two Far-Field multicomponent (NS, WE) seismic base excitations from the FEMA P695 earthquake database [97]. These earthquake instances are applied as base excitation to three linear shear-type frames (a two-, a three- and a six-storey frame), with different structural features (Chapter 4).

Further, the rFDD technique is innovatively expanded here to operate also under Soil-Structure Interaction conditions, in order to deal with both flexible- and fixed-base conditions [101, 102]. The developed analyses are performed on earthquake-induced synthetic response signals, which are computed from a benchmark linear five-storey shear-type frame with an underlying Sway-Rocking Soil-Structure Interaction model. Structural responses are calculated by adopting the earlier set of ten selected earthquake excitations, with five different types of soils, i.e. of foundation properties, from the rigid to the very soft soil cases. Then, rFDD originally operates within an OMAX (Operational Modal Analysis with eXogenous input) environment on the base-excited buildings. This aims at detecting also the underlying fixed-base conditions and to quantify the amount of Soil-Structure Interaction to which the building under analysis may be subjected to (Chapter 5).

The SSI-DATA identification algorithm, instead, starting from seminal works [83, 84, 121], is developed in an optimized version, which aims at explaining and improving the classical Stochastic Subspace Identification performance with seismic response signals and heavy damping [94, 98]. The best setting of the SSI-DATA processing tool and computational parameters, namely signal processing and filtering, Block Hankel matrix features, SVD truncation order and weightings and calculation of the State Space matrices aim at handling such a peculiar and challenging application field. Also, specifically developed stabilization diagrams have been conceived, designed as a "fusion" of rFDD and SSI-DATA information. All these refinements are developed in order to handle the present demanding Earthquake Engineering context, and are demonstrated in their efficacy with the three- and ten-storey benchmark structures (Chapter 6).

Then, the new FDCIM technique is an innovative output-only element-level system identification and input estimation method [96, 99], which takes its roots from earlier seminal works [23, 67, 124]. This method works fine towards the simultaneous identification of modal parameters, input

excitation time history and structural features at the so-called "element-level", by adopting earthquake-induced structural response signals only. The method operates within a deterministic state-space form, by an original two-stage iterative algorithm, and arrives at consistent identification results in the Earthquake Engineering range. Specifically developed procedures, such as a Statistical Average technique, a modification process, a parameter projection strategy and a Rayleigh damping parameter estimation method concur to this FDCIM challenging OMA identification. The remarkable effectiveness of the FDCIM algorithm is demonstrated with the application on a three- and a ten-storey benchmark frame (Chapter 7).

Finally, the three methods are compared all together, after the analysis performed with synthetic seismic response signals, in the further challenging scenario of adopting real earthquake-induced structural response signals. The adopted real signals come from a six-storey office building in San Bruno, California, and are taken from the Center for Engineering Strong Motion Data (CESMD) [22]. Then, the real case-study comparison of the outcomes from such three advanced OMA techniques aims at demonstrating once again their reliability and effectiveness as convenient output-only modal identification tools towards innovative Earthquake Engineering and Structural Health Monitoring purposes (Chapter 8).

Main global conclusions of the present doctoral dissertation are finally reported in closing Chapter 9.

Chapter 2

Operational Modal Analysis under strong ground motion structural response signals

In the field of Operational Modal analysis (OMA), where identification techniques are based on structural response signals only, just a few works attempted successfully to deal with the modal estimation under earthquake-induced response data. That since most of OMA techniques are specifically conceived to work with free or ambient vibration recordings, where (small-amplitude) vibrations may be well approximated by stationary Gaussian white noise [17, 121]. Furthermore, most of the times adequately long acquisitions are required, in order to possibly reduce noise and errors during the estimation procedures. Thus, seismic response signals are very much different than classically-adopted output-only ambient vibration signals.

Despite that, the knowledge of modal dynamic properties not only at the pre- and post-earthquake stages, but also during the sequences of main seismic events, delineates a very challenging and fundamental field of study within structural dynamics and seismic engineering. For example, tasks like Structural Health Monitoring, conditions assessment, predictive response modelling, damage detection and evaluation of retrofitting procedures may take significant advantages from the knowledge of current strong ground motion modal parameters.

After the preamble of the Introduction, the present section aims at setting a state of the art in the field. In first Section 2.1, main contributions, explanations and details concerning the theoretical background and positioning of the rFDD and SSI-DATA identification techniques treated in the thesis will be one main subject of discussion. In Section 2.2, a brief overview on the adoption of Soil-Structure Interaction conditions within output-only modal identification will be reported. Then, in subsequent Section 2.3, the focus will move on the main contributions and

the theoretical background concerning element-level and input estimation techniques, to which the present original FDCIM algorithm developed in the thesis belongs to.

2.1 Time Domain and Frequency Domain output-only modal identification under earthquake-induced structural response signals

Nowadays, several identification methods just rely on output-only conditions, by knowing structural response signals only [104, 106]. By employing these OMA procedures, only a few attempts with earthquake-induced structural response signals (adopted as input channels for the identification algorithms) have been performed in the literature. On that, a brief and likely non-exhaustive literature overview on recent contributions, either in the Time Domain or in the Frequency Domain, is reported in the following.

Most of the current state-of-the-art OMA techniques adopting seismic structural response input refer to Time-Domain methods. In 2003, Smyth et al. [114] developed a combination of linear (Least-Squares based) and non-linear (non-parametric) system identification techniques, in order to obtain a complete reduced-order, Multi-Input Multi-Output (MIMO) dynamic model of the Vincent Thomas Bridge, based on the dynamic response of the structure to two main earthquakes under study.

In 2004, Pridham and Wilson [103] proposed a combination of standard Stochastic Subspace Identification (SSI) with a Maximum-Likelihood (Expectation Maximization - EM) algorithm, in order to refine SSI estimates. Five ensembles of synthetic response signals, generated from shear-type frames under seismic base excitation, were employed in Monte Carlo simulations, to illustrate the applicability of the method. For certain system characteristics, more accurate system pole estimates can be identified by adopting the combined SSI-EM formulation, but problems still remain on the damping ratio estimations.

In 2005, Lin et al. [68] developed a modified Random Decrement method coupled with an Ibrahim Time Domain technique, by relying only on a few floor acceleration earthquake-response records. The aim was that of identifying modal parameters on asymmetric buildings, modelled as general torsionally coupled structures. By analytically deriving the general relationship between the reduced Random Decrement signature and the true free vibration response, they were able to identify the structural dominant modal parameters, even with coupled modes and the addition of noise.

In 2009, Kun et al. [61] proposed an identification method where the

support excitation acting on a structure was modelled by orthogonal polynomial approximations, with the derivation of the sensitivities of structural dynamic response with respect to its physical parameters and orthogonal coefficients. The identification equation was based on a Taylor's first-order approximation, and was solved by a damped iterative Least-Squares procedure. Their method could also detect local damage and identify the unknown support excitation from the structural responses of the structure.

In 2013, Ghahari et al. [43] presented an OMA method based on two steps. First, the Time-Frequency distributions of the response signals were used for blind identification of classical mode shapes and modal coordinate signals. Second, the cross-relations among the modal coordinates were employed to determine the natural frequencies and the damping ratios of the system under analysis. All that in the premise of linear behaviour for the structural system. They adopted both simulated and real seismic response data to validate their method.

Still in 2013, Gouache et al. [47] developed an output-only procedure that was able to deal with harmonic and transient input forces, instead of classically adopted white noise. The feature was that transient and harmonic inputs were no longer considered as parasitic input, as for most of the OMA techniques (which are designed to be robust to such harmonic contributions), but as the main force applied to the structure under analysis. That was possible by using a phase analysis, adapted to a transient context, to conduct OMA under harmonic transient input. They exposed the related theoretical developments and algorithmic implementations in order to apply the method to a laboratory SDoF test setup and to validate the procedure.

Finally, in 2014, Lei et al. [63] developed a Time Domain Extended Kalman Filter (EKF) estimator approach for the identification of multi-storey shear-type buildings under an unknown earthquake-induced ground motion, by using partial measurements of the structural absolute acceleration responses. This method also allowed for estimating the ground motion base-excitation, by adopting LS estimation coupled with EKF.

Then, by adopting OMA techniques with earthquake-induced structural response input in the Frequency Domain, dedicated algorithms seem to have been less investigated than those in the Time Domain. Few notable exceptions may be listed in the following. In 2005, Ventura et al. [122] studied the dynamical behaviour of the Painter Street Overpass (Rio Dell, California) through a series of ambient vibration tests and more than ten significant recorded strong motion data. The aim was that of comparing the dynamic characteristics of the bridge at low levels of vibration with those measured during strong motion events. The adopted OMA algo-

rithms belongs to a commercial software version of Frequency Domain Decomposition [17] (Time Domain Stochastic Subspace Identification [84] was adopted, too).

In 2007, Mahmoudabadi et al. [74], starting from a method for parametric system identification of classically damped linear systems in the Frequency Domain, proposed an extension based on iterative LS that was able to deal with non-classically damped linear systems subjected to up to six components of earthquake ground motions. The results of the identification on synthetic and real buildings showed that the adoption of non-classical damping and the inclusion of the multi-components effect of the earthquake ground motions can improve the Least-Squares match between the Finite Fourier Transforms of the recorded and calculated acceleration responses.

Finally, in 2010 Michel et al. [78] examined the seismic response of the Grenoble City Hall building (Grenoble, France), based on ambient vibrations and weak earthquakes, and performed OMA through a classical Frequency Domain Decomposition algorithm. They compared the frequencies from the ambient vibrations to those from weak earthquakes recorded by the instrumentation that was installed to monitor the building.

By making reference to main OMA techniques, earthquake-induced structural responses are adopted in the body of this work as input channels for a *refined Frequency Domain Decomposition (rFDD)* algorithm [17] and an *improved Data-Driven Stochastic Subspace Identification (SSI-DATA)* technique [84]. Both were implemented autonomously within MATLAB, for rFDD in [90–92, 97] and for SSI-DATA in [82, 94, 98]. The traditional versions of these algorithms rely on the typical assumption of (stationary) white noise input, which no longer holds true with (non-stationary) seismic response input. On the contrary, the present methods have been specifically developed to deal with earthquake-induced structural responses and at simultaneous heavy damping (in terms of identification challenge, i.e. with modal damping ratios larger than only a few percents, and up to 10% or even higher).

As concerning rFDD (Chapters 3, 4 and 5 of the thesis), the ancestor works came from FDD developments and inspections of Brincker and co-workers [15,17]. The classical FDD technique allows for estimating natural frequencies and mode shapes of the structural system; in its Enhanced EFDD formulation, also of modal damping ratios and undamped natural frequencies [14, 130]. A third generation of FDD, i.e. Frequency Spatial Domain Decomposition (FSDD), was recently developed to eliminate some disadvantages of EFDD algorithms [15, 125, 131]. However, the present rFDD algorithm refines and redefines classical FDD algorithms, through

specific computational strategies, allowing for the structural identification at seismic input and concomitant heavy damping.

Starting from those earlier FDD methods, the theoretical background and efficacy of the present rFDD technique have been first outlined and demonstrated in [92], where preliminary attempts with single and multiple input earthquakes have been considered. Then, in [92] a further investigation on the theoretical aspects has been performed, where original strategies for the correlation and Power Spectral Density (PSD) matrices were developed. There, an extended set of structures and earthquakes was adopted, jointly with noise addition.

As a necessary validation condition, synthetic response signals in the linear range have been adopted in both [91, 92] works. In order to further demonstrate the rFDD validity, the achieved estimates have been compared to those coming from classical FDD, implemented by a commercial software. Furthermore, several trials with real earthquake-induced structural response signals have been effectively performed in [93], by addressing specific computational issues related to real acquisitions. Damage scenarios in the nonlinear range, retrofit stages and Soil-Structure Interaction effects have been considered as well. Soil-Structure Interaction effects have been also investigated in [101, 102], in order to estimate fixed- and flexible-base modal parameters under earthquake-induced structural response signals.

Then, in [97] the original rFDD technique was improved with a coupled Chebyshev Type II bandpass filters procedure, in order to obtain even much effective estimations of natural frequencies, mode shapes and modal damping ratios, when tough seismic input and heavy damping conditions apply. Also, the proper procedure tuning was achieved by a time-frequency Gabor Wavelet Transform (GWT) analysis [11]. A systematic and comprehensive validation of the rFDD method was provided through the adoption of the complete "Far-Field" seismic record set (22 NS and 22 WE earthquake acquisitions) coming from the FEMA P695 earthquake database [37]. This earthquake dataset was also preliminary adopted in [95], with previous rFDD instances [91, 92], while in [100] further analyses with the most demanding earthquakes and structural conditions (including heavy damping until $\zeta = 13\%$) have been attempted, based on work [97].

As concerning SSI-DATA (Chapter 6), the ancestor works came from first SSI developments by Van Overschee and De Moor [121], where the SSI-DATA theoretical background was examined in detail, by taking a general overview on the identification problem. The further work of Peeters and co-workers [83–85], instead, introduced the use of SSI-DATA within the civil engineering field, by taking into account all the related issues, as

for example the adoption of reference channels, and so on. Starting from the models outlined from these works, classical SSI-DATA has been enhanced here and improved to be able to deal also with earthquake-induced structural response signals and heavy damping.

A preliminary study on SSI-DATA efficacy within the present challenging field was performed in [82], where the algorithm was first implemented and validated with white noise signals and then analysed with seismic response signals. Then, in [94] a further study on the SSI-DATA algorithm application with seismic input was performed, by adopting a three-DoFs reference frame. There, a first comparison of SSI-DATA outcomes with rFDD ones was attempted.

Then, in [98] the SSI-DATA was definitively rearranged and improved to deal with earthquake response signals and heavy damping. Specifically, the best setting of the SSI-DATA processing tool and computational parameters, namely signal processing and filtering, Block Hankel matrix features, SVD truncation order and weightings and calculation of the State Space matrices aim at this peculiar application field. Also, specifically developed stabilization diagrams have been conceived, designed as a "fusion" of rFDD and SSI-DATA information. In that work, SSI-DATA and rFDD estimates were compared in detail, by adopting an increased number of frames and seismic excitations at the base. First, the autonomously implemented rFDD and SSI-DATA techniques were separately adopted to identify the modal properties of two linear heavy-damped shear-type frames under several strong ground motions. Then, real earthquake response signals were considered, in order to extract general and specific considerations on the efficiency and consistency of both OMA algorithms and to investigate and compare their effectiveness in identifying all current strong ground motion modal parameters.

2.2 Time Domain and Frequency Domain OMA with seismic excitation under Soil-Structure Interaction conditions

As connected to the dynamic characterization of real engineering structures, the determination of modal parameters via OMA takes a significant role within Earthquake Engineering, especially as connected to the adoption of earthquake-induced structural response signals. In this framework, seismic Soil-Structure Interaction [59,60,127] may play a considerable role.

The dynamic response of a structure laying on a soft soil may substantially differ, in amplitude and frequency content, from that of an identical structure based on a stiff ground [127]. A building subjected to Soil-Structure Interaction displays a coupling between the foundation and the superstructure motions. The recorded dominant frequency is al-

ways smaller than that of the corresponding fixed-base building, and of the foundation itself, when no building is present [108].

If local Soil-Structure Interaction effects are small, the recorded responses at the foundation level are not influenced by the motions of the upper stories, and the building may be assumed as laying on a "fixed base" [5, 28]. The motion at the foundation level may be taken as a base excitation for the adopted structural model. Otherwise, if the interaction becomes significant, this assumption is no longer valid, since the foundation input motion and the output response of the structure turn out to be coupled to each other [60]. Then, the response of the building is characterized by a "flexible-base" Soil-Structure Interaction condition.

By knowing the building structural recordings, the identification of Soil-Structure Interaction effects may be possible if acquisitions would be available also from the foundations, or from free-field or nearby downhole locations. During the last decades, several studies on Soil-Structure Interaction identification and quantification have been thoroughly attempted, see e.g. [26, 72, 107, 108, 115, 117, 119]. By using Operational Modal Analysis (OMA), a few attempts have been performed, specifically in the Frequency Domain context, by aiming at the detection of flexible-base conditions and by accounting for Soil-Structure Interaction effects on the buildings, as e.g. in [43, 44]. Thus, a brief overview on recent contributions on Soil-Structure Interaction identification and quantification, by focusing especially on main contributions that inspired the rFDD inspection in this field (Chapter 5), is reported in the following.

First attempts on Soil-Structure Interaction modelling for buildings likely came in 1974 from the work of Chopra and Gutierrez [28]. They developed a method, based on the Ritz concept, for the dynamic analysis of the response of multi-storey buildings including foundation interaction under earthquake ground motion. The considered system was a shear building on a rigid circular disc footing, attached to the surface of a linear elastic halfspace.

In 1988, Luco et al. [72] described an EMA series of forced vibration tests designed to isolate the effects of Soil-Structure Interaction for a nine-storey reinforced concrete building. They experimentally determined the fixed-base natural frequencies and modal damping ratios of the superstructure, which significantly differed from the resonant frequencies and damping ratios of the complete structure-foundation-soil system.

Still in 1988, Pais and Kausel [81] proposed several approximate formulas to describe the variation with frequency of the dynamic stiffnesses of rigid embedded foundations. These formulas were obtained by fitting mathematical expressions to accurate numerical solutions for cylindrical and rectangular embedded foundations, computed by assuming a one-

dimensional wave propagation theory.

In 1995, Safak [108] studied the causality of the building's impulse response, towards the detection of the presence of Soil-Structure Interaction effects. That since for causal systems, the amplitudes of the impulse response function at negative times are zero, whereas for noncausal systems they are comparable to those at positive times. Then, he studied also the identification of Soil-Structure Interaction, in terms of extracting the natural frequencies of the fixed-base building from the recordings of the foundation and of the upper stories. He proved that the ratio of the Fourier amplitude spectrum of the top-story accelerations to that of the foundation accelerations allows for the identification of the natural frequency of the fixed-base building.

In 1996, Celebi [20] presented a comprehensive assessment of damping values and other dynamic characteristics of five buildings, using strong-motion and low-amplitude (ambient vibration) data. For each building, he found that the modal damping ratios and the corresponding fundamental periods determined from low-amplitude data are appreciably lower than those determined from strong-motion recordings. After a thorough inspection, he attributed these differences to Soil-Structure Interaction and other non-linear behaviour affecting the structures during strong shaking.

In 1997, Wolf [128] studied the behaviour of a simple spring-dashpot-mass model with frequency-independent coefficients for the modelling of foundations on deformable soils. He scheduled the foundation coefficients for a homogeneous half-space and the homogeneous layer fixed at its base, for varying parameters as the ratios of foundation dimensions and Poisson's ratio.

In 1998, Stewart and Fenves [115] developed an EMA parametric system identification method to evaluate seismic Soil-Structure Interaction effects on buildings, i.e. for the detection of both flexible- and fixed-base modal parameters. They adopted the recordings of lateral free-field, foundation, roof motion and foundation rocking for the evaluations of the modal parameters for both cases of base fixity.

In 1999, Heredia-Zavoni et al. [52] analysed the optimal instrumentation of structures on soft soils, by adopting a criterion based on the stochastic response of a linear MDoF Soil-Structure Interaction system on a flexible-base. The structures were shear buildings, with uncertain lateral stiffness, subjected to random earthquake ground motions. They discussed the optimal location of the accelerometers, the reduction of prior uncertainty on the lateral stiffness, the effects of the base flexibility, the relative influence of translation and rocking of the base, and the influence of the recording noise.

In 2004, Choi et al. [26] developed an EMA identification technique that

was able to identify input and Soil-Structure Interaction system parameters, by adopting earthquake response data. Identification was carried out on a real test structure, i.e. a 1/4-scale reinforced concrete containment building of a nuclear power plant. Identified quantities were the input ground acceleration, the shear wave velocities (and then the shear moduli) of the near-field soil regions and the Young's moduli of the shell sections of the structure. The Soil-Structure Interaction system was modelled by Finite Elements combined with an Infinite Element formulation for the unbounded layered soil medium.

In 2013, Renzi et al. [107] performed a parametric analysis of seismic Soil-Structure Interaction effects of a large number of idealised ordinary shear-type buildings. They modelled the structures as generalised SDoF systems via the principle of virtual displacements, by assuming shallow squared foundations resting on different soil types. The outcomes of the numerical analyses were used as a statistical base in order to obtain simple analytical and non-dimensional relationships for estimating seismic Soil-Structure Interaction effects in terms of modified period and damping.

Still in 2013, Ghahari et al., in two different works [43,44], developed an OMA procedure that was able to deal with Soil-Structure Interaction conditions. In [43] (presented in previous Section 2.1) they applied a two-step parametric Time Domain method also in case of Soil-Structure Interaction, both with synthetic and real earthquake-induced structural response signals. In [44], instead, they studied an OMA procedure that was able to deal with non-classically damped Soil-Structure Interaction systems. That since in most cases the soil provides additional damping due to material hysteresis and radiation, which cannot be represented in classical form, rendering complex-valued mode shapes. In this way, the response of the soil-foundation system can be represented through frequency-dependent real and imaginary impedance functions, representing the stiffness and damping of the system, respectively. Thus, they developed a second-order blind identification method that was able to extract complex-valued mode shapes from free or ambient vibration recordings, and also the frequency-dependent soil-foundation impedance functions.

Within an OMA field, the analyses presented later in Chapter 5 vastly investigate the novel application of the rFDD algorithm under seismic Soil-Structure Interaction conditions, in order to identify flexible-base modal parameters of linear frame structures with earthquake base excitation. This inspection is rooted on preliminary trials sketched in works [101, 102]. Within this seismic and Soil-Structure Interaction research mainstream, this study is connected to that on papers [109, 110], where a complementary study investigated the effectiveness of passive Tuned Mass Dampers (TMDs) as possible vibration reduction devices under seismic

Soil-Structure Interaction conditions.

Innovatively, the rFDD algorithm is expanded to operate also in an OMAX (OMA with eXogenous input) environment [48]. This concept takes benefit from the advantages of both OMA and EMA techniques: operational (unknown) forces (causing the earthquake response of the superstructure) as well as artificial (known) forces (foundation and/or free-field recordings in this case) are processed simultaneously by the rFDD-OMAX algorithm, towards achieving a correct detection of potential Soil-Structure Interaction effects and an effective estimation of fixed-base modal parameters too. Foundation and/or free-field recordings are adopted as (exogenous) input for the algorithm, which develops in a self-contained framework some tools for Soil-Structure Interaction detection and quantification, taken and re-elaborated from previous contributions [107, 108].

2.3 Output-only element-level system identification and input estimation under earthquake base excitation

The field of Earthquake Engineering is considered here as a main target of interest of structural dynamics identification, specifically as connected to potential Structural Health Monitoring approaches, which are devoted to the assessment of current structural properties and to the evaluation of potential damages that may occur in civil structures, due to the action of strong ground motion excitations.

Most of the works here inspected the identification of structural dynamics properties at seismic input, either within EMA [6, 7, 21, 33, 46, 56], where the excitation input is known and/or controlled, or within OMA [43, 51, 68, 77, 103, 113], where the input action is unknown (output-only techniques). In these works, specifically-developed strategies have been developed to identify the modal parameters from earthquake-induced structural response signals.

Indeed, even though modal parameters shall be considered as representative of the global dynamic properties of a given structure, referring to its mass, damping and stiffness characteristics, their usefulness may be insufficient in practical cases, in order to quantify the amount of damage that may have occurred within individual structural elements [49]. In fact, structural degradations will be reflected in modifications of the global structural behaviour. As a consequence, these damages are dependent on changes that may be detected in individual structural elements, i.e. at the so-called "*element-level*", specifically in terms of time variations of stiffness and damping structural characteristics (assuming time-invariant systems in terms of mass). Also, nearly all of the available techniques for modal

dynamic identification and damage detection at seismic input pertain to EMA methods, i.e. they need the knowledge (or the acquisition) of the input ground motion (i.e. the knowledge of the external action), too.

At this stage, current OMA (output-only) methods may be viewed on different levels of sophistication. The first level appears to be the lower one: it leads to the estimation of structural modal properties only, i.e. of natural frequencies, mode shapes and modal damping ratios (and, in case of parametric algorithms, also of "*realizations*", in terms of a set of State-Space structural matrices referred to a given input-output behaviour [34]). The second level of detail pertains to the further refinement of mass, damping and stiffness matrix estimation. The aim is to target each of their characteristic parameters, i.e. to achieve the so-called "*identification at the element-level*". The third level of focus, finally, refers to the estimation of the "*input excitation*" acting on the system, specifically here of the shaking ground motion, which induces the structural response recorded from the available instrumentation.

Thus, the simultaneous identification of modal parameters, structural features at the element-level and excitation input still appears to be rather challenging in the present dedicated OMA literature [30, 67, 124], and specifically in the Earthquake Engineering context, a main target of the present doctoral dissertation.

By using output-only acquisitions of the structural response, during the past years several identification techniques have been proposed to jointly estimate the structural parameters and the unknown seismic input at the base. On that, a literature overview on fundamental contributions is reported in the following, as an underlying framework for the innovative steps and approaches presented by the new *Full Dynamic Compound Inverse Method (FDCIM)*, later outlined in Chapter 7.

In 1989, Toki et al. [118] proposed that the "coda" of the response time history (i.e. the tail, namely the last seconds of the acquisition following the end of the earthquake excitation) may be representative of the free vibration response of the structural system. Their assumption was that the coda is not affected by the input ground motion, and then the ratio between mass and stiffness or damping coefficients shall be constant from this part of the record on. So, modal parameters may be identified by Extended Kalman Filtering (EKF) [53]. Also, they improved the method to estimate the input ground motion by the Kalman Filter estimation error [80].

In 1994, Benedetti and Gentile [10] suggested a Frequency Domain algorithm, which worked in two stages, to identify the properties of structures subjected to input ground motion. With this method, the responses at two different locations of the structure were assumed to be available,

while the requirements for the input excitation were avoided, by using the ratio between the Fourier amplitude transforms of the two acquired response signals. However, the input time history could not be determined by that identification procedure.

Still in 1994, Wang and Haldar [124] proposed an iterative Finite Element-based procedure in the Time Domain to evaluate both stiffness and damping matrices at the element-level, jointly with the input force excitation (which could be a generic force or seismic loading). Only a small number of observation time points was required for the development of the algorithm, where the solicitations were assumed to be initially zero for the starting of the iterative Least-Squares procedure, and then were updated step by step, until convergence was reached. Finally, the complete input time history could be evaluated by using the estimated stiffness and damping parameters and the full-length measured structural responses.

In 1995, Hoshiya and Sutoh [54] suggested a method to identify both the input and the stiffness and damping matrix coefficients for shear-type frames. A combination of a smoothing algorithm on the input ground excitation and of an Extended Kalman Filtering was formulated, by adopting the coda of the system responses. They used a Weighted Global Iteration (WGI) procedure to obtain a fast convergence to the optimum solution and to achieve stability, as previously outlined in [53]. A problem related to these methods concerned how to choose the coda of the response time history, i.e. the exact start of the free response part of the acquisition, without a prior knowledge of the input ground motion excitation.

Afterwards, in 1997, Haldar et al. [49] expanded their previous work to cases with limited response measurements (or limited observations), i.e. when the structure was monitored only at a few dynamic degrees of freedom. They combined their former iterative Least-Squares algorithm with a Weighted Global Iteration procedure applied to an Extended Kalman Filter technique.

In 2000, Li and Chen [66] proposed an iterative Time Domain method for solving hybrid inverse problems. Structural parameters and inverse time history of input excitation were simultaneously estimated, by relying on structural response signals only. In that work, additional conditions were set on the input force, by relying on its mechanical characteristics. Then, a Statistical Average algorithm (SA) was developed, in terms of a properly-defined transfer coefficient. The computational steps of the algorithm relied on their previous work, Li and Chen [65].

Still in 2000, Cho and Paik [25] refined the algorithm by Wang and Haldar [124], by proposing an improved Least-Squares method based on a Multiple models QR Decomposition (MQRD). This method enhanced the Least-Squares convergence and allowed for a more accurate identification

of structural element properties and potential damages.

In 2002, Chen et al. [24] took the element-level Time Domain method developed by Wang and Haldar [124] and implemented a refinement, which looked at identifying both the earthquake excitation and the structural parameters (at the element-level), by using a combination of an iterative Least-Squares technique and of a specifically-developed Statistical Average method. They named the algorithm as *Dynamic Compound Inverse Method (DCIM)*, label which has been kept here as a base for the subsequent developments put forward by the present FDCIM algorithm.

Along the same line, in 2003, Li and Chen [67] published an improved version of their previous work [66], by improving the Statistical Average algorithm for the DCIM solution. The adopted solicitations spread from ambient recordings to seismic ground motions, acting on different structures.

In 2004, Chen and Li [23] proposed a further implementation, which took into account the use of Rayleigh damping $\mathbf{C} = \alpha\mathbf{M} + \beta\mathbf{K}$, instead of general viscous damping used until then. Unknown Rayleigh damping coefficients α and β and the stiffness parameters of matrix $\mathbf{K}$ were coupled to each other, leading the classical MDoF equations of motion to a set of non-linear identification equations in terms of the unknown structural parameters. Then, by relying on their previous algorithm, they developed a two-stage iterative method to avoid such a non-linear identification problem. An inner modification process was applied between each iterative step, to convert the spatial information of the external excitation into mathematical conditions for the iterative algorithm. In that work, the focus was on possible forced vibration surveys of the system, i.e. on cases where the structure was excited by actuators installed at several locations of the building. No ground motions or ambient vibrations were considered at that stage. The present FDCIM procedure relies much on the two contributions above, and attempts to provide a more general and robust analysis, towards achieving a full identification approach.

Still in 2004, Ling and Haldar [69] developed a further approach to take into account the possible use of Rayleigh proportionally damped systems. They proposed a modified Iterative Least-Squares method with Unknown Input (ILS-UI), to identify such types of systems at the element-level. They used Taylor series approximations to transform the non-linear set of identification equations (arising from the equations of motion with Rayleigh damping) into a set of linear equations. Again, no ground motions or ambient vibrations were considered.

In 2006, Zhao et al. [132] demonstrated that the structural parameters and the earthquake ground motion could not be uniquely identified when absolute structural response signals were used, instead of relative ones.

Then, they proposed a hybrid identification method to tackle the problem. First, that algorithm identified the structural parameters above the first-floor of a multi-storey shear-type building, by using Least-Squares. Later, the minimum modal information was introduced to find out the first floor parameters and to avoid the shortcoming of non-uniqueness. After that, all structural parameters were identified. The unknown earthquake ground motion was estimated by solving a first-order differential equation.

In 2008, Perry and Koh [86] proposed an element-level parameter and input estimation technique with a non-classical approach based on a Genetic Algorithm (GA). They made use of a modified GA-based method, to adopt the strategy of the Search Space Reduction Method [87]. They revised this method through a modification of the numerical integration scheme, in order to be used also for output-only identification. Still in 2008, Wang and Cui [124] suggested a two-step method, which generalized the work of Chen et al. [24], apt to identify both element-level structural parameters and input time history.

Concerning the intelligent monitoring of multi-storey buildings by a wireless sensor network, in 2012, Lei et al. [63] suggested an element-level and input ground motion identification algorithm based on a two-stage Kalman Filter estimator. That method worked with absolute coordinates through the use of sub-structuring methods. Still in 2012, Lourens et al. [71] proposed an extension of an existing joint input-state estimation Kalman Filter, which was derived by using a linear minimum-variance unbiased estimation. The novelty consisted in the use of an optimal estimate in place of the true value of the input for the Kalman Filter steps.

Then, in 2014, Ding et al. [32] developed a method which could be used to identify structural parameters and input time history, either for linear or non-linear hysteretic frames, with limited observations. With this method, they decomposed the structural excitation by orthogonal approximation and then applied an Extended Kalman Filter for the identification process. Only forces acting on the floors of the frames were considered at that stage.

Recently, Bayesian methods also started to be applied for OMA input and element-level identification. Relevant examples may be found in Behmanesh et al. [8] (2015), where a probabilistic Finite Element (FE) model updating technique based on Hierarchical Bayesian modelling was proposed for the identification of civil structural systems under changing ambient/environmental conditions. Further, the works of Au and Zhang [4] and Zhang and Au [129] (2016), suggested the adoption of a modified two-stage Bayesian identification approach, towards the estimation of modal properties and structural parameters.

Still in 2015, Concha et al. [30] suggested an adaptive observer which simultaneously estimated the damping/mass and the stiffness/mass ra-

tios, as well as the state of seismically-excited shear buildings. Their work started from the research of Jiménez and Icaza [57], where the parametrization of a shear-type frame equipped with a Magneto-Rheological Damper (MRD) had been considered; the assumptions were the knowledge of the structural parameters (at a first approximation, accounting for some uncertainties) and of the seismic ground acceleration, the accelerations of each floor and the MRD damper force (direct measurement). Similar assumptions were assumed in Concha et al. [30], where the identification scheme relied on the knowledge (i.e. on the measurement) of ground and floor accelerations and of first floor mass m_1. This method achieved the estimation of a reduced-order model, if some floors only may be equipped with available instrumentation. Computationally, the algorithm relied on Least-Squares and on a Luenberger state estimator for the estimation process.

A crucial common denominator between all the aforementioned works is the fact that they take the full mass matrix to be given for granted, both in its matrix structure and in the values of its mass parameters. Then, despite the output-only feature of the algorithms, the knowledge of structural responses only (either in terms of accelerations, velocities or displacements) is not sufficient for their functioning. A slight exception comes from the work of Concha et al. [30], where first floor mass m_1 and the seismic ground acceleration had been considered to be known, to return the element-level identifications for all the stiffness, damping and mass matrices.

In this framework, the present *Full Dynamic Compound Inverse Method (FDCIM)* is an innovative, complete element-level system identification and input estimation technique that takes and detaches from the previous contributions above. It is specifically developed to operate with earthquake-induced structural response signals, collected from seismically-excited MDoF shear-type frames. The FDCIM method releases strong assumptions implied by the earlier techniques, especially the required knowledge of the full mass matrix (or at least of its specific elements), to provide an effective identification of the modal parameters of the system, i.e. natural frequencies, mode shapes and modal damping ratios, of the excitation input and of a realization of the state matrices.

In fact, the present FDCIM algorithm requires the knowledge of structural response signals only, while mass, damping and stiffness matrices, and obviously the exciting earthquake input, may be completely unknown. Accurate estimations of the input ground motion time history and of the states at the element-level are provided through a two-stage iterative algorithm. This method works jointly with a Statistical Average technique, a modification process and a parameter projection strategy, which are

adopted at each iteration to provide correct and stronger constraints for the estimates, allowing for faster and much reliable convergence.

Initial hypotheses affect only the supposed behaviour of the structural matrices, i.e. diagonal mass matrix and tridiagonal symmetric damping and stiffness matrices, where the structural coefficients are coupled to each other. Damping behaviour is treated through two different ways, i.e. as lumped (see [96]) or General damping, which contains as a special case also the Rayleigh damping behaviour (see [99]). In the present case, lumped damping means that the damping parameters are considered as lumped between two consecutive floors, in terms of n damping coefficients c_i, where n is the number of floors, as it is for stiffness coefficients k_i.

General damping, instead, considers an implementation that further widens and generalizes the FDCIM algorithm, by adopting a more general damping behaviour. In this way, each single damping parameter c_{ij} is uncoupled from the remaining ones, by allowing for the analysis and identification of structures characterized by unknown "General damping". Further, as a particular case, it becomes possible to effectively identify "Rayleigh damping" ($\mathbf{C} = \alpha\mathbf{M} + \beta\mathbf{K}$), as it was also considered by the earlier DCIM attempts quoted above. This actually constitutes a much challenging case, since it apparently leads to non-linear identification equations in terms of the unknown structural parameters (see [23, 69] and Section 7.2).

The use of General and Rayleigh damping becomes possible by introducing several dedicated modifications and improvements into the original FDCIM formulation for lumped damping, in terms of different iteration matrices and dimensions, modified vectors of unknown variables, innovative parameter projection technique, novel procedure for Rayleigh damping coefficients estimation, and so on (Section 7.2).

Moreover, the proposed FDCIM method (as opposed to other methods operating within the stochastic framework) appears to be completely deterministic and it is fully developed in *State-Space form*. It does not require transformations from continuous-time to discrete-time and it does not depend on the adopted initial conditions or on the state estimation, in order to identify the modal parameters and the input ground motion. Further, all the structural features as element-level mass, damping and stiffness matrices, may be accurately identified merely by knowing any single component of one of these matrices, or even by relying on an estimate of a global structural parameter, like for instance the total mass of the building. Then, the adopted formulation is suitable for integration or support to other common output-only methods working within State-Space parametric Time Domain frameworks.

Chapter 3

Refined Frequency Domain Decomposition: theoretical background

3.1 Fundamentals of the refined Frequency Domain Decomposition technique

Classical Frequency Domain approaches are based on the processing of a time-correlated signal through a Discrete Fourier Transform (DFT) procedure, with the purpose of evaluating the Power Spectral Density (PSD) functions of the structural system responses [13, 17]. Then, Frequency Domain Decomposition methods operate a Singular Value Decomposition (SVD) at each line of the frequency spectrum. This procedure separates noisy data from disturbances of various source [104] and appears able to pick-up close modes with better accuracy, while resulting not excessively sensitive to ambient noise. The PSD matrix is thus decomposed into a set of auto-spectral density functions. Each of these correspond to that of a SDoF system, from which natural frequencies and mode shapes can be estimated [16]. Typical underlying hypotheses of Frequency Domain Decomposition (FDD) methods are: white noise input, very low structural modal damping ratios (below 1%) and geometrically-orthogonal mode shapes of close modes [125].

The present refined FDD (rFDD) technique attempts to clear these latter limitations, in the context of earthquake response input. In the present section, all crucial steps of the theoretical framework of the rFDD algorithm are exposed, by relying on theoretical works [15,16,91,92] (Section 3.1.1). Then, the main workflow and novelties of the present rFDD algorithm are introduced in Sections 3.1.2 and 3.1.3. Furthermore, in Sections 3.2-3.4 these innovations are explained in detail.

3.1.1 Main theoretical background of the rFDD algorithm

The classical FDD theory is based on the typical input/output relationship of a general stationary random process for a n-DoF system [9, 15, 125]:

$$\mathbf{G}_{yy}(\omega) = \overline{\mathbf{H}}(\omega)\mathbf{G}_{xx}(\omega)\mathbf{H}^{\mathrm{T}}(\omega) \tag{3.1}$$

where $\mathbf{G}_{xx}(\omega) \in \mathcal{R}^{r\times r}$ is the PSD matrix of the input, r being the number of input channels (references), $\mathbf{G}_{yy}(\omega) \in \mathcal{R}^{m\times m}$ is the PSD matrix of the output, m being the number of output signals (responses or measurements), $\mathbf{H}(\omega) \in \mathcal{R}^{m\times r}$ is the Frequency Response Function (FRF) matrix; overbar denotes complex conjugate and apex symbol T transpose. Both $\mathbf{G}_{xx}(\omega)$ and $\mathbf{G}_{yy}(\omega)$ matrices derive from Finite Fourier Transforms for the PSD evaluation (see [9] for the details). Also, the FRF $\mathbf{H}(\omega)$ may be written in pole/residue form [75]:

$$\mathbf{H}(\omega) = \sum_{k=1}^{n} \frac{\mathbf{R}_k}{\mathrm{i}\,\omega - \lambda_k} + \frac{\overline{\mathbf{R}}_k}{\mathrm{i}\,\omega - \overline{\lambda}_k} \tag{3.2}$$

where n is the number of vibration modes, $\lambda_k = -\zeta_k\omega_k + \mathrm{i}\omega_{dk}$ and $\overline{\lambda}_k$ are the kth poles (in complex conjugate pairs) of the FRF function [75], being ζ_k the modal damping ratio and ω_k and $\omega_{dk} = \omega_k\sqrt{1-\zeta_k^2}$ the kth natural and damped frequency, respectively. Then, $\mathbf{R}_k = \boldsymbol{\phi}_k\boldsymbol{\Gamma}_k^{\mathrm{T}} \in \mathcal{R}^{m\times r}$ is the residue matrix [15, 104], which is obtained by the product between mode shape vector $\boldsymbol{\phi}_k \in \mathcal{R}^{m\times 1}$ and modal participation factor vector $\boldsymbol{\Gamma}_k^{\mathrm{T}} \in \mathcal{R}^{r\times 1}$. When all output measurements are taken as input references (i.e. when $m = r$), $\mathbf{H}(\omega)$ becomes a square matrix. So, Eq. (3.1), through Eq. (3.2), can be rewritten as [16]:

$$\mathbf{G}_{yy}(\omega) = \sum_{k=1}^{n}\sum_{s=1}^{n}\left(\frac{\overline{\mathbf{R}}_k \mathrm{G}_{xx}}{-\mathrm{i}\,\omega - \overline{\lambda}_k} + \frac{\mathbf{R}_k \mathrm{G}_{xx}}{-\mathrm{i}\,\omega - \lambda_k}\right)\left(\frac{\mathbf{R}_s^{\mathrm{T}}}{\mathrm{i}\,\omega - \lambda_s} + \frac{\mathbf{R}_s^{\mathrm{H}}}{\mathrm{i}\,\omega - \overline{\lambda}_s}\right) \tag{3.3}$$

where Hermitian apex symbol H denotes complex conjugate and transpose. This formulation is possible since PSD matrix $\mathbf{G}_{xx}(\omega)$ *is a single scalar constant* G_{xx} *for stationary zero mean white noise input* [9]; due to this fact and remembering the formulations of the PSD matrices by Short Time Fourier Transforms [9], the PSD matrix $\mathbf{G}_{xx}(\omega)$ becomes real-valued and non-negative. Thus, by recalling the properties of $\mathbf{G}_{xx}(\omega)$ and by applying the Heaviside partial fraction expansion theorem to Eq. (3.3), one obtains the final reduced pole/residue form for the output PSD matrix as follows [16, 125]:

$$\mathbf{G}_{yy}(\omega) \simeq \sum_{k=1}^{n} \frac{\mathbf{A}_k}{\mathrm{i}\,\omega - \lambda_k} + \frac{\mathbf{A}_k^{\mathrm{H}}}{-\mathrm{i}\,\omega - \overline{\lambda}_k} + \frac{\overline{\mathbf{A}}_k}{\mathrm{i}\,\omega - \overline{\lambda}_k} + \frac{\mathbf{A}_k^{\mathrm{T}}}{-\mathrm{i}\,\omega - \lambda_k} \tag{3.4}$$

where $\mathbf{A}_k \in \mathcal{R}^{m\times m}$ is the residue matrix of the PSD output corresponding to k^{th} pole λ_k. As for the PSD output itself, the residue matrix is an Hermitian matrix and is given by [16]:

$$\mathbf{A}_k = \sum_{s=1}^{n}\left(\frac{\mathbf{R}_s}{-\lambda_k-\lambda_s}+\frac{\overline{\mathbf{R}}_s}{-\lambda_k-\overline{\lambda}_s}\right)\mathrm{G}_{xx}\mathbf{R}_k^{\mathrm{T}} \tag{3.5}$$

When the structural system is lightly damped (small modal damping ratios $\zeta_k \ll 1$), the pole can be expressed in approximate form as $\lambda_k = -\zeta_k\omega_k + \mathrm{i}\omega_{dk} \simeq -\zeta_k\omega_k + \mathrm{i}\omega_k$; then, in the vicinity of the kth modal frequency, only the $\overline{\mathbf{R}}_k$ term survives, so that the residue matrix can be derived approximately from Eq. (3.5) as [15]:

$$\begin{aligned}\mathbf{A}_k &= \left[\frac{\mathbf{R}_k}{2(\zeta_k\omega_k-\mathrm{i}\omega_k)}+\frac{\overline{\mathbf{R}}_k}{2\zeta_k\omega_k}\right]\mathrm{G}_{xx}\mathbf{R}_k^{\mathrm{T}} \simeq \frac{\overline{\mathbf{R}}_k\mathrm{G}_{xx}\mathbf{R}_k^{\mathrm{T}}}{2\zeta_k\omega_k} = \\ &= \frac{\overline{\boldsymbol{\phi}}_k\boldsymbol{\Gamma}_k^{\mathrm{H}}\mathrm{G}_{xx}\boldsymbol{\Gamma}_k\boldsymbol{\phi}_k^{\mathrm{T}}}{2\zeta_k\omega_k} = \mathrm{d}_k\overline{\boldsymbol{\phi}}_k\boldsymbol{\phi}_k^{\mathrm{T}}\end{aligned} \tag{3.6}$$

where only the $\overline{\mathbf{R}}_k$ term survives, since the $2\zeta_k\omega_k$ denominator is dominant with respect to the $2(\zeta_k\omega_k - \mathrm{i}\omega_k)$ one, while $\mathrm{d}_k = \boldsymbol{\Gamma}_k^{\mathrm{H}}\mathrm{G}_{xx}\boldsymbol{\Gamma}_k/(2\zeta_k\omega_k)$ is a real scalar. Then, index k spans the modes of vibration, $k = 1,\ldots,n$. So, by substituting Eq. (3.6) into Eq. (3.3) one gets:

$$\mathbf{G}_{yy}(\omega) = \sum_{k=1}^{n}\frac{\mathrm{d}_k\overline{\boldsymbol{\phi}}_k\boldsymbol{\phi}_k^{\mathrm{T}}}{\mathrm{i}\,\omega-\lambda_k}+\frac{\mathrm{d}_k\overline{\boldsymbol{\phi}}_k\boldsymbol{\phi}_k^{\mathrm{T}}}{-\mathrm{i}\,\omega-\overline{\lambda}_k}+\frac{\mathrm{d}_k\boldsymbol{\phi}_k\boldsymbol{\phi}_k^{\mathrm{H}}}{\mathrm{i}\,\omega-\overline{\lambda}_k}+\frac{\mathrm{d}_k\boldsymbol{\phi}_k\boldsymbol{\phi}_k^{\mathrm{H}}}{-\mathrm{i}\,\omega-\lambda_k} \tag{3.7}$$

In the narrow band with spectrum lines in the vicinity of a modal frequency, the last two terms in Eq. (3.7) can be ignored, since their denominator terms $\mathrm{i}\,\omega - \overline{\lambda}_k = \overline{-\mathrm{i}\,\omega - \lambda_k} \simeq \zeta_k\omega_k + 2\mathrm{i}\,\omega_k$ are bigger with respect to the first two, $-\mathrm{i}\,\omega - \overline{\lambda}_k = \overline{\mathrm{i}\,\omega - \lambda_k} \simeq \zeta_k\omega_k$. Taking this into account, the previous equation can be simplified as [15]:

$$\mathbf{G}_{yy}(\omega) \simeq \sum_{k=1}^{n}\frac{\mathrm{d}_k\overline{\boldsymbol{\phi}}_k\boldsymbol{\phi}_k^{\mathrm{T}}}{\mathrm{i}\,\omega-\lambda_k}+\frac{\mathrm{d}_k\overline{\boldsymbol{\phi}}_k\boldsymbol{\phi}_k^{\mathrm{T}}}{-\mathrm{i}\,\omega-\overline{\lambda}_k} = \overline{\boldsymbol{\Phi}}\left\{\mathrm{diag}\left[\Re\mathrm{e}\left(\frac{2\mathrm{d}_k}{\mathrm{i}\,\omega-\lambda_k}\right)\right]\right\}\boldsymbol{\Phi}^{\mathrm{T}} \tag{3.8}$$

where $\boldsymbol{\Phi}$ is the eigenvector matrix, gathering all n eigenvectors $\boldsymbol{\phi}_i$ as columns. Previous Eq. (3.8) represents a modal decomposition of the output PSD matrix. The contribution to the spectral density matrix from a single mode k can be expressed as:

$$\mathbf{G}_{yy}(\omega_k) \simeq \overline{\boldsymbol{\phi}}_k\left\{\mathrm{diag}\left[\Re\mathrm{e}\left(\frac{2\mathrm{d}_k}{\mathrm{i}\,\omega-\lambda_k}\right)\right]\right\}\boldsymbol{\phi}_k^{\mathrm{T}} \tag{3.9}$$

The final form of the $\mathbf{G}_{yy}(\omega_k)$ matrix in Eq. (3.9) is then decomposed, using a SVD technique, into a set of singular values and corresponding singular vectors. From the former, natural frequencies are extracted; from the latter, approximate mode shapes are obtained.

3.1.2 Refined FDD technique for earthquake-induced structural response signals and heavy damping

The response of the structure $\mathbf{y}(t)$ can be expressed in terms of modal coordinates:

$$\mathbf{y}(t) = \sum_{k=1}^{n} \boldsymbol{\phi}_k \mathrm{p}_k(t) = \boldsymbol{\Phi}\mathbf{p}(t) \tag{3.10}$$

where $\mathbf{p}(t)$ is the vector of principal coordinates $\mathrm{p}_k(t)$. The response signals (input signals for the algorithm, as the accelerations considered here) shall be correlated in time to obtain the matrix of the auto- and cross-correlations in the time domain, $\mathbf{R}_{yy}(\tau)$, a starting point for the developed rFDD algorithm:

$$\mathbf{R}_{yy}(\tau) = \mathrm{E}\left[\overline{\mathbf{y}}(t+\tau)\mathbf{y}^{\mathrm{T}}(t)\right] = \mathrm{E}\left[\overline{\boldsymbol{\Phi}}\mathrm{p}(t+\tau)\mathbf{p}^{\mathrm{T}}(t)\boldsymbol{\Phi}^{\mathrm{T}}\right] = \overline{\boldsymbol{\Phi}}\mathbf{R}_{pp}(\tau)\boldsymbol{\Phi}^{\mathrm{T}} \tag{3.11}$$

where $\mathbf{R}_{pp}(\tau) = \mathrm{E}\left[\overline{\mathbf{p}}(t+\tau)\mathbf{p}^{\mathrm{T}}(t)\right]$ is the auto- and cross-correlation response matrix (in principal coordinates), E denotes the expected value and instant τ spans the interval from 0 to t, i.e. $0 \leq \tau < t$. In the present algorithm the $m \times m \times N$ auto- and cross-correlation matrix (given m the number of measurement channels, $N = t$ the total number of considered time lags) is calculated numerically, for a finite signal length, with the following biased estimator [9]:

$$\mathbf{R}_{yy}(t,\tau) \approx \mathbf{R}_{yy}(\tau) \simeq \frac{1}{t}\sum_{t=1}^{t-\tau} \overline{\mathbf{y}}(t+\tau)\mathbf{y}^{\mathrm{T}}(t) \tag{3.12}$$

In general, for a non-stationary input the correlation matrix shall be stated as a function of time t and of lag τ, i.e. $\mathbf{R}_{yy} = f(t,\tau)$. The approximation in Eq. (3.12), ignoring the time dependence on behalf of that on lag only, can be explained as follows.

For some selected non-stationary input, as for the adopted earthquake responses, it is possible, within a good approximation, to ignore the frequency dependence of the input PSD matrix for a specific frequency interval, corresponding to a subset of the frequency lines of the original input spectrum.

Unlike for the PSD of a white noise input (that runs-out approximately constant at every frequency instance of the spectrum), the PSD of an

earthquake excitation shall change with time and frequency, due to the non-stationarity nature of the signal [105]. Otherwise, in most cases it may change slowly over a frequency range, especially for an interval that appears adequately wide to include all the structural modal frequencies. Then, in a specific frequency region $\omega_{Sub} = \mathrm{Sub}(\omega) \in \omega$ some seismic signals may be considered as "*weakly stationary*" [105], i.e. the first two statistical moments (mean and autocorrelation) of the signals do not significantly vary in time. In simple terms, in these weakly stationary cases the spectrum may be considered sufficiently flat to approximate the trend of a white noise excitation with reasonable accuracy. Then, it is possible to ignore the frequency dependence of the input PSD matrix for this specific frequency interval, corresponding to a subset of the frequency lines of the original input spectrum, $f_{\mathrm{Sub}} = \mathrm{Sub}(f) \in f \Rightarrow \omega_{\mathrm{Sub}} = 2\pi f_{\mathrm{Sub}} = 2\pi \mathrm{Sub}(f) = \mathrm{Sub}(\omega) \in \omega$, as the following:

$$f_{\mathrm{Sub}} = \mathrm{Sub}(f) = \left[0,\ \frac{f_{\mathrm{Nyq}}}{2m} = \frac{f_s}{4m}\right] \in f = [0,\ f_s = 2f_{\mathrm{Nyq}}] \tag{3.13}$$

where $f_{\mathrm{Nyq}} = f_s/2$ is the Nyquist frequency, f_s is the adopted sampling frequency and m is a positive integer which delineates the subinterval of frequencies.

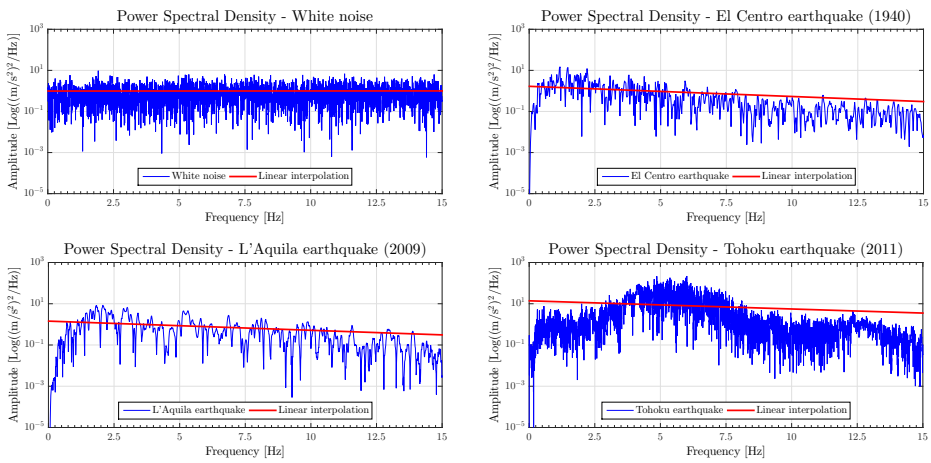

Figure 3.1: *Auto-Power Spectral Density of some of the adopted structural input excitations with related linear interpolation in the frequency range between 0 and 15 Hz.*

This assertion may be illustrated in Fig. 3.1, where, over the frequency range between 0 Hz and 15 Hz, a sample interval which may contain the examined structural modal frequencies, a linear interpolation is represented, proving through its slight angular coefficient the fairness of the present weakly-stationary assumption.

So, the developed rFDD algorithm considers, among other strategies, the feature of defining $\mathbf{G}_{xx}(\omega) \Rightarrow \mathrm{G}_{xx} = \overline{\mathrm{G}}_{xx}$ for a frequency interval $\omega_{\mathrm{Sub}} \in \omega$. Therefore, remembering Eq. (3.3), it is possible to obtain:

$$\mathbf{G}_{yy}(\omega_{\mathrm{Sub}}) = \sum_{k=1}^{n}\sum_{s=1}^{n}\left(\frac{\overline{\mathbf{R}}_k \mathrm{G}_{xx}}{-\mathrm{i}\,\omega - \overline{\lambda}_k} + \frac{\mathbf{R}_k \mathrm{G}_{xx}}{-\mathrm{i}\,\omega - \lambda_k}\right)\left(\frac{\mathbf{R}_s^{\mathrm{T}}}{\mathrm{i}\,\omega - \lambda_s} + \frac{\mathbf{R}_s^{\mathrm{H}}}{\mathrm{i}\,\omega - \overline{\lambda}_s}\right)\Bigg|_{\omega=\omega_{Sub}} \tag{3.14}$$

Thus, all equations from Eq. (3.4) to Eq. (3.9) are still valid, recalling the approximation due to the use of the Sub(ω) interval. Accordingly, over this frequency range, the PSD can be approximately represented as to be merely frequency-dependent, allowing to follow classical PSD computations [105].

As a direct consequence of that treatment, the correlation matrix of Eq. (3.12) can be approximately expressed as a function of lag only, without the need of expressing it as a function of time, too.

Further examples of the previous statements can be seen in Figs. 3.2 and 3.3. In Fig. 3.2, a representation of the accelerogram, the Auto-PSD and the Gabor Wavelet Transform related to the WE component of the Tabas (TA) ground motion is depicted. Then, Fig. 3.3 represents the instantaneous Auto-Correlation Function (ACF) of this earthquake excitation, which proves again that a locally-stationary (weakly stationary) amplitude domain of the spectra may be detected and thus used for the analysis.

These slight time-frequency changes may be gradual enough to not significantly affect any individual modal peak of the structure, by aiming at using the strong ground motion responses instead of the white noise input generally adopted for the OMA procedures. Additionally, in the literature some works justify the use of stationary models for the representation of the seismic signals [55, 120], based on the fact that accelerograms simulated as series of pulses, white noise and filtered white noise give rise to response spectra with damping, which are similar to those obtained from real earthquakes of great magnitude in a limited frequency range. The need to model seismic motion by means of non-stationary stochastic processes arises when the ground and/or the structure behaviour is clearly non-linear because, in this case, the system might undergo a deterioration with a strength loss during the major motion phase of the earthquake, and this would result in a reduction of its natural frequencies.

Finally, concerning the possibility of extracting reliable estimates also at concomitant heavy damping, although theoretical derivations belong to the assumption of light damping, the following remarks may be expressed. The hypothesis of lightly-damped structures has been made in Eq. (3.6),

where the pole can be anyway expressed as $\lambda_k = -\zeta_k\omega_k + \mathrm{i}\,\omega_{dk} \simeq -\zeta_k\omega_k + \mathrm{i}\,\omega_k$ even with heavy damping. In fact, by assuming a modal damping ratio $\zeta_k = 10\%$, the former equation leads to an error of about $5 \cdot 10^{-3}$ rad/s on the ω_{dk} computation (with respect to $5 \cdot 10^{-5}$ rad/s arising from $\zeta_k = 1\%$), an acceptable value in engineering terms.

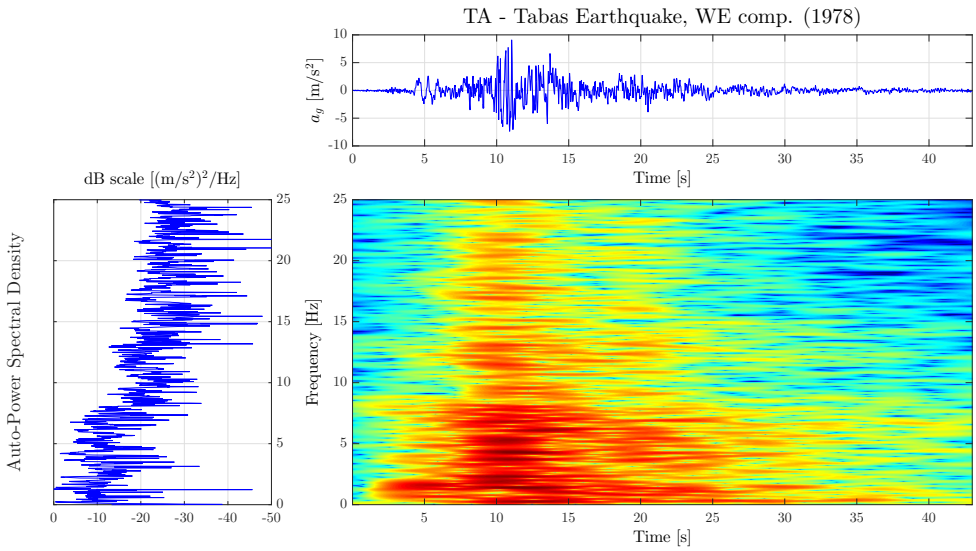

Figure 3.2: *Accelerogram, Auto-PSD and Gabor Wavelet Transform of Tabas earthquake signal, WE component.*

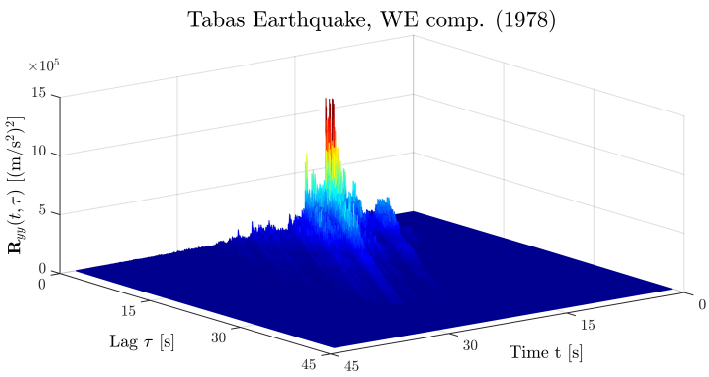

Figure 3.3: *Instantaneous Auto Correlation Function (ACF) of Tabas earthquake signal, WE component.*

Accordingly, relations from Eq. (3.6) to Eq. (3.9) work properly, proving the theoretical effectiveness of the algorithm at heavy damping. With respect to the subsequent procedures for heavy damping estimates, theoretical derivations are still fully valid. Flattening of the peaks and ex-

tremely noisy SVs lead to critical conditions for classical FDD procedures. The developed algorithm, with its procedures and strategies, returns well-defined peaks and SVs, leading to effective modal parameter estimates, as it can be appreciated from the illustrative results reported in Chapter 4.

3.1.3 Main novelties of the present rFDD algorithm

Main assumptions of classical FDD methods consist of (stationary) white noise input, light damping (modal damping ratios in the order of 1%) and geometrically-orthogonal mode shapes of close modes [17].

The present rFDD method, whose original theoretical background has been reported in [91, 92], conceptually derives from classical FDD methods [17], but has been specifically developed to deal with earthquake-induced structural response signals and concurrent heavy damping conditions (in terms of FDD identification challenge, i.e. for realistic modal damping ratios up to 10%).

Pioldi et al. [90–92] have discussed the theoretical validity and efficacy of the present rFDD technique, through the use of synthetic seismic response signals in the linear range. Trials with real earthquake responses and damage scenarios in the non-linear range have been effectively performed as well in [93]. In [95, 97], further rFDD computational strategies have been introduced, by adopting excitation data from the complete FEMA P695 earthquake database, towards achieving an extensive validation in the Earthquake Engineering range. In [101, 102], the rFDD technique has been also applied to frames under Soil-Structure Interaction (SSI) effects, towards obtaining the identification of flexible- and fixed-base modal parameters from earthquake-induced structural response signals (see also Chapter 5).

For the sake of completeness, the following computational steps (and references quoted therein) summarize the main workflow of the present rFDD algorithm:

- Suitably-developed filtering applied to the structural response input signals (earthquake-induced structural responses) before starting the modal identification process [92].

- Coupling of the rFDD algorithm to a time-frequency Gabor Wavelet Transform (GWT), towards achieving a correct evaluation of the time-frequency features of the signals and a best setup for rFDD identification [97].

- Processing of the auto- and cross-correlation matrix entries, by aiming at obtaining clearer and well-defined SVs out of seismic response signals [91].

- Integrated PSD matrix computation, implementing simultaneously both Wiener-Khinchin's approach and Welch's modified periodogram method [91, 92]. Wiener-Khinchin's procedure works especially well with short signals, allowing for a clearer peak detection, not only on the first SV curve, but also on the subsequent ones. Welch's method, instead, implements averaging and windowing before the frequency-domain convolution, allowing to achieve better mode shapes, despite for the not so good separation of the signals in the modal space. Then, the integrated PSD matrix computation aims at extracting better modal estimates, by taking simultaneous advantage of both PSD evaluation methods.

- Iterative loop and optimization algorithm towards achieving effective modal damping ratio estimates, especially under heavy-damping identification conditions [92].

- Coupled Chebyshev Type II bandpass filters computational procedure, aiming at enhancing the SDoF spectral bells towards estimation improvement, when challenging seismic input and heavy-damping conditions apply [97].

- Estimation of modal parameters by operating on different SVs and on their composition, to detect each SV contribution and to reconstruct the original SDoF spectral bells [92].

- Inner procedure for frequency resolution enhancement, without the need of higher frequency sampling, as first outlined in [92].

- Combined use of different MAC indexes towards modal validation purposes [92, 93]. After a preliminary "peak-picking" [92], the use of Modal Assurance Criterion (MAC) and Modal Phase Collinearity (MPC) indexes [91] becomes necessary to discern "spurious peaks" from true (physical) modal ones. In particular, these indexes have been used to discard spurious peaks that exhibit a complex-number character (i.e. displaying modal deflection phases that significantly deviate from 0 or π).

3.2 Refined FDD modal dynamic identification of natural frequencies and mode shapes

3.2.1 Time-Frequency signal analysis and suitably-developed filtering for the rFDD technique

As explained earlier in Section 3.1.2, for some selected non-white noise input, as for several earthquake response signals, over the frequency interval ω_{Sub}, which is chosen to include the structural modal frequencies under target (or at least some of them), the spectrum may change rather slowly. The selected frequency interval ω_{Sub} may be defined according to the specific study being undertaken. If the target would be that of predicting the seismic response by modal properties, as it is performed here, the focus would be placed on the lower-frequency global response parameters; if the intent would be that of identifying potential structural damage, a focus on the higher-frequency local response parameters would be considered.

The previous "weakly-stationary" assumption may be better appreciated by looking at Fig. 3.4, where El Centro earthquake (later adopted in Chapter 4) has been taken as an example. Over the specified range between 0 Hz and 10 Hz, a linear interpolation of the spectrum has been represented. The slightness of its angular coefficient and the flat distribution of the regression residuals suggests that the spectrum may be approximated with reasonable accuracy as being "weakly stationary" (or at least similar to a pink noise, i.e. a signal that falls off at 3 dB per frequency octave in terms of power at a constant bandwidth [105]). The Gabor Wavelet Transform (GWT) [11] of the adopted earthquake record, despite its global non-stationarity, confirms the assumption of a weakly stationary signal for narrow frequency intervals, too.

The present time-frequency distribution and spectrum flatness analysis is a necessary step when dealing with earthquake-induced structural response signals (not only with synthetic signals, but also with real data), in order to be confident on the choice of the correct frequency interval (if a such kind of frequency interval exists) for a reasonable validity of the flat spectrum assumption. This time-frequency analysis is a mandatory pre-processing step that integrates the rFDD algorithm. Basically, a frequency interval must necessarily be found where the spectrum is approximately flat, which contains as much natural frequencies as possible, pertaining to the monitored structure. This procedure, which shall be extended also to the output spectrum, enables for the selection of the correct frequency range, to be adopted in the following computational steps. Otherwise, it would not possible to ensure the reliability of the achieved estimates. After the selection of the ω_{Sub} interval, the remaining part of

the frequency spectrum shall be discarded through an appropriate (low-, band- or high-pass) filtering.

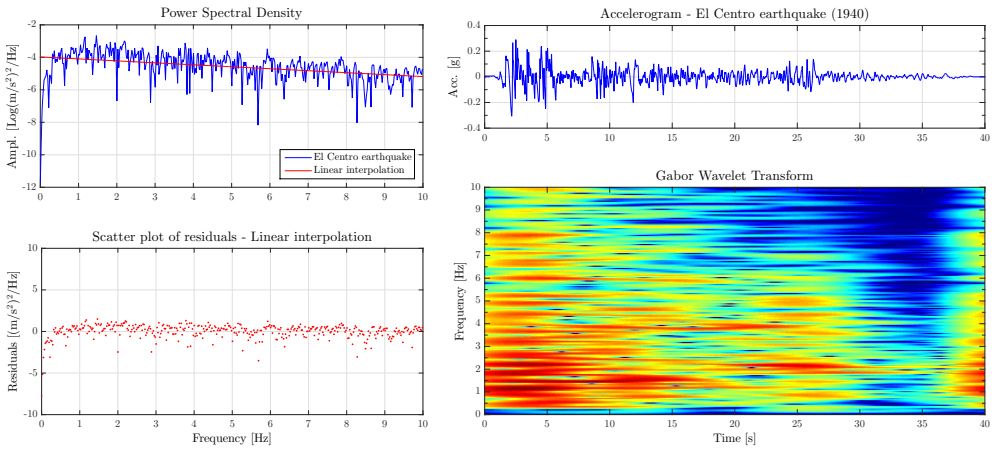

Figure 3.4: *Accelerogram, Auto-PSD with linear regression, residuals and Gabor Wavelet Transform (GWT) of El Centro earthquake (1940).*

Also, a further data filtering may be necessary before modal identification, with respect to the use of a random excitation, since additional undesired frequency contents, that for civil structures correspond to the high frequency components of the spectra, shall be left-out. This portion of the spectra may be significant with earthquakes, and must be removed (or, at least, reduced) by an adequate low-pass filtering of the acquisitions. Estimates take quite a significant advantage from this feature.

3.2.2 Auto- and cross-correlation matrix processing

In the presence of noisy or weakly-stationary data (or non-stationary data, as earthquakes), the $\mathbf{R}_{yy}(\tau)$ matrix can be further processed to obtain an untrended well-defined version, as outlined in the subsequent steps (see also [91] for more details). Practically, each of the m^2 combinations of channels resulting from the $\mathbf{R}_{yy}(\tau)$ matrix may be fitted by the following linear estimator:

$$\hat{\mathbf{R}}_{yy}(\tau) = \mathbf{A} + \mathbf{X}_{\mathrm{R},\tau}\mathbf{B} \tag{3.15}$$

where $\mathbf{X}_{\mathrm{R},\tau}$ is the matrix of the time instants τ, described for every column of $\mathbf{R}_{yy}(\tau)$, and $\mathbf{A}$, $\mathbf{B}$ are the vectors of the parameters to be fitted, with a_k and b_k components, $k = 1, \ldots, m^2$. These parameters can be calculated

by the minimization of function R below as follows:

$$\mathrm{R}^2(\mathrm{a}_k, \mathrm{b}_k) = \sum_{\tau=1}^{t} \Big[\mathbf{R}_{yy,\tau} - \big(\mathrm{a}_k + \mathbf{X}_{\mathrm{R},\tau} \mathrm{b}_k \big) \Big]^2 \Rightarrow \begin{cases} \mathrm{J}_{\mathrm{a},k} = \dfrac{\partial\,(\mathrm{R}^2)}{\partial\,\mathrm{a}_k} = 0 \\ \mathrm{J}_{\mathrm{b},k} = \dfrac{\partial\,(\mathrm{R}^2)}{\partial\,\mathrm{b}_k} = 0 \end{cases} \tag{3.16}$$

where $\mathrm{J}_{\mathrm{a},k}$ and $\mathrm{J}_{\mathrm{b},k}$ are the kth terms of the Jacobian matrix $\mathbf{J}$. Solving for a_k and b_k, it is possible to obtain the estimates of the linear trends $\hat{\mathbf{R}}_{yy}(\tau)$ in Eq. (3.15). Finally, the de-trended correlation matrix can be formulated as:

$$\mathbf{R}_{yy}^{\mathrm{detr}}(\tau) = \mathbf{R}_{yy}(\tau) - \hat{\mathbf{R}}_{yy}(\tau) \tag{3.17}$$

where the de-trended correlation matrix $\mathbf{R}_{yy}^{\mathrm{detr}}(\tau)$ shows the important property of a zero mean. This processing of the correlation matrix helps in removing possible troubles related to non-stationary or weakly non-stationary data, leading to a refinement of the achievable estimates, specifically in the seismic response input scenario. In Fig. 3.5 a comparison between the SVD obtained from the application (Fig. 3.5b) or not (Fig. 3.5a) of the de-trended correlation matrix $\mathbf{R}_{yy}^{\mathrm{detr}}(\tau)$ is presented. It can be noticed that the application of this procedure may return clearer and well-defined SVs, a fact which positively reflects in the achievable modal estimates.

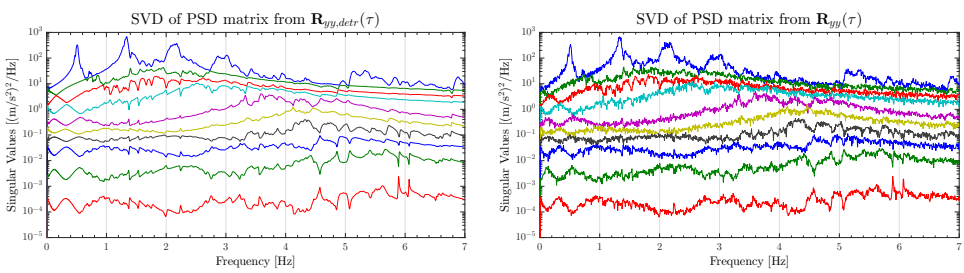

Figure 3.5: *SVD obtained by the rFDD algorithm (a) without ($\mathbf{R}_{yy}(\tau)$) and (b) with ($\mathbf{R}_{yy}^{\mathrm{detr}}(\tau)$) processing of the correlation matrix, ten-storey frame, L'Aquila earthquake, NS component.*

3.2.3 Integrated approach for PSD matrix computation

Output PSD matrix $\mathbf{G}_{yy}(\omega_{Sub})$, selected for the frequency interval ω_{Sub}, shall be computed through numerical methods. The integrated approach for the PSD matrix computation presented in this work simultaneously implements the Wiener-Khinchin [9] and the Welch's modified periodogram [126] methods in a sequential way.

The Wiener-Khinchin algorithm is based on the direct Fourier Transform (FT) of the correlation matrix $\mathbf{R}_{yy}^{\mathrm{detr}}(\tau)$ (see Eqs. (3.11) and (3.12)), in order to obtain the PSD matrix of the responses $\mathbf{G}_{yy}^{\mathrm{detr}}(\omega_{Sub})$:

$$\mathbf{G}_{yy}^{\mathrm{detr}}(\omega_{Sub}) = \mathscr{F}\left[\mathbf{R}_{yy}^{\mathrm{detr}}(\tau)\right] = \mathscr{F}\left[\overline{\mathbf{\Phi}}\,\mathbf{R}_{pp}^{\mathrm{detr}}(\tau)\mathbf{\Phi}^{\mathrm{T}}\right] = \overline{\mathbf{\Phi}}\,\mathbf{G}_{pp}^{\mathrm{detr}}(\omega_{Sub})\mathbf{\Phi}^{\mathrm{T}} \tag{3.18}$$

where $\mathbf{G}_{pp}^{\mathrm{detr}}(\omega_{Sub}) = \mathscr{F}\left[\mathbf{R}_{pp}^{\mathrm{detr}}(\tau)\right]$ is the PSD matrix of responses (in terms of principal coordinates p_i), obtained as FT of the untrended correlation matrix $\mathbf{R}_{pp}^{\mathrm{detr}}(\tau)$ (see [91] for more details), expressed again in principal coordinates. This makes the close relationship between the modal decomposition of Eq. (3.8) and Eq. (3.18) clearly visible. Steps from Eq. (3.15) to Eq. (3.18) define the method that shall be called *Correlation Approach (Corr)*.

After the use of the Corr approach, the second method adopted by the rFDD algorithm for the estimation of the $\mathbf{G}_{yy}(\omega_{Sub})$ matrix derives from the Welch's modified periodogram, starting from [126]:

$$\mathbf{G}_{yy}(\omega_{Sub}) \simeq \frac{1-r}{K}\sum_{k=1}^{K/(1-r)} \frac{\left[\sum_{t=0}^{L-1}\overline{\mathbf{y}}_k(t)\mathrm{W}(t)e^{-\mathrm{i}\omega\frac{t}{L}}\right]\left[\sum_{t=0}^{L-1}\mathbf{y}_k^{\mathrm{T}}(t)\mathrm{W}(t)e^{-\mathrm{i}\omega\frac{t}{L}}\right]}{\left[\sum_{t=0}^{L-1}\mathrm{W}(t)^2\right]} \tag{3.19}$$

where K is the number of segments of length L and overlapping r ($r = 2/3$ in the present work) in which the initial signal $\mathbf{y}(t)$ has been divided, $\mathbf{y}_k(t)$ is the kth segment of the original signal and $\mathrm{W}(t)$ is the considered windowing function, i.e. an Hanning window as in this case [9]. The method resumed in Eq. (3.19) shall be called *Welch Approach (Welch)*. This method implements averaging and windowing, formerly than frequency domain convolution; this leads to slightly better estimates, especially with long recordings, despite for the appearance of noisier singular values.

The present rFDD algorithm displays the innovative and powerful feature of the simultaneous implementation of both Corr and Welch methods, into an integrated process, in order to take advantage of the peculiarities of both approaches. First, a run with the Corr approach is performed, by applying the peak-picking procedure on the sharper and better defined SVs (and then, clearer and well-defined peaks) provided by this method. The peak-picking technique is supported by the use of MAC, Auto-MAC, MPC and Auto-MPC indexes (later introduced in Section 3.4.3), through comparison of the mode shapes of each potential peak with those of the others in its proximity. In this way the correct peaks (i.e. the correct

frequency lines related to the modes of vibration) may be detected. This method works well especially with short signals, as for those coming from earthquake records, though it may produce slightly less accurate mode shapes. Peaks may be detected not only on the first SV curve, but also on the remaining ones.

Then, the PSD matrix is recomputed through the Welch's approach, which is applied sequentially to the Corr method. This aims at extracting the final modal estimates, read in correspondence of the formerly-detected frequency lines $\omega = \omega_k$ arising from the Corr method. This method implements averaging and windowing, previous to the frequency-domain convolution, leading to slightly better estimates, especially with long recordings, despite for the appearance of noisier singular values. With this method, only the peaks on the first SV are adopted, in order to avoid leakage on the achievable estimates.

In short, the contribution of the Corr approach detects the correct resonance peaks, allowing to process noisy SVs that may arise from the Welch's procedure more effectively, which otherwise would return merged and doubtful peaks. According to the characteristics of the recorded structural responses, this may effectively help in the final modal estimates.

This original integrated procedure leads to a substantial improvement of the seismic modal estimates, not only in case of synthetic response signals, but also – and specifically – in case of real earthquake response input. This potential feature can be appreciated in Fig. 3.6, where the two methods for the computation of the PSD matrix are displayed, focusing on the results (i.e. on the detected frequency lines) provided by the subsequent SVD computation.

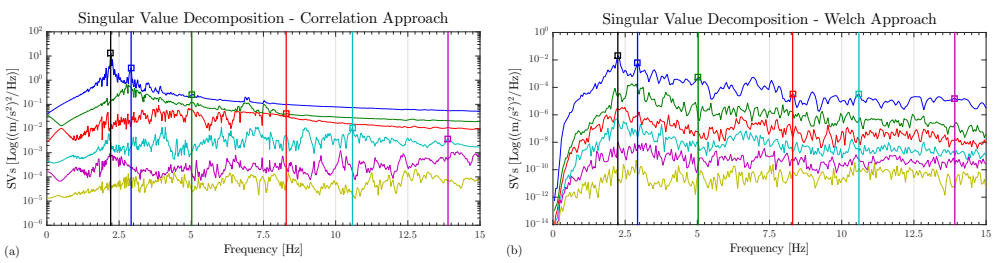

Figure 3.6: *Singular Value Decomposition obtained from integrated computation of the PSD matrix: (a) Corr Approach; (b) Welch Approach; response to Encino earthquake (2014), NS component. The peak frequency lines detectable by the Corr Approach (a) are transferred to the Welch Approach (b), where the modal peaks are hardly visible for direct peak-picking.*

3.2.4 Strategies for natural frequency and mode shape modal dynamic identification

Now, as it is common in stochastic dynamics, it is possible to assume that the modal coordinates are uncorrelated; whenever this assumption is valid, or whenever the input is flat [17,75], the PSD matrix can be decomposed as seen in previous Eqs. (3.8) and (3.9). For classical FDD, the hypothesis of light damping [17] becomes necessary for this step. Anyway, for the rFDD algorithm this last assumption shall be overcome, by leaving room also for highly damped cases, with still a reliable approximation.

Accordingly, the input cross-correlation functions vanish, so that matrices $\mathbf{R}_{pp}(\tau)$ and $\mathbf{G}_{pp}(\omega)$ are assumed diagonal. Then, if the mode shapes (the columns of matrix $\mathbf{\Phi}$) are orthogonal to each other, Eq. (3.18) represents a spectral decomposition. The $\mathbf{G}_{yy}(\omega)$ matrix can be represented as the summation of n $\mathbf{G}_k(\omega)\overline{\boldsymbol{\phi}}_k\boldsymbol{\phi}_k^{\mathrm{T}}$ terms, where $\mathbf{G}_k(\omega)$ is the auto-spectral density function of the kth modal coordinate. Although the SVD forces the singular vectors to be orthogonal, notice that in general experimental mode shapes are not orthogonal [13]. This will introduce a bias error in the mode shape estimation, towards the orthogonality between adjacent eigenvectors, which directly depends on the distance between adjacent singular values (the larger the difference, the smaller the error) [13]. Then, this hypothesis (or at least mode shapes orthogonality for close modes) is a requirement, inter alia (the others are white noise input and light damping), to achieve an accurate SVD of the spectral matrix. If these assumptions are not satisfied (as in this seismic heavy-damped case), the decomposition becomes approximate, but may still be accurate [9], justifying then the adoption of the current rFDD technique.

Then, remembering Eqs. (3.8) and (3.18), it is possible to consider a SVD of the transpose of the response PSD matrix:

$$\mathbf{G}_{yy}^{\mathrm{T}}(\omega) \simeq \mathbf{\Phi}\left\{\mathrm{diag}\left[\Re\mathrm{e}\left(\frac{2\mathrm{d}_k}{\mathrm{i}\,\omega-\lambda_k}\right)\right]\right\}\mathbf{\Phi}^{\mathrm{H}} = \mathbf{U}\mathbf{S}\mathbf{U}^{\mathrm{H}} \tag{3.20}$$

where $\mathbf{U}$ is a unitary complex matrix (i.e. $\mathbf{U}\mathbf{U}^{\mathrm{H}} = \mathbf{U}^{\mathrm{H}}\mathbf{U} = \mathbf{I}$) holding the singular vectors (i.e. the eigenvectors) and $\mathbf{S}$ is a real diagonal matrix holding the singular values (i.e. the eigenvalues). In general, the SVD of an arbitrary matrix $\mathbf{A}$ is given by $\mathbf{A} = \mathbf{U}\mathbf{S}\mathbf{V}^{\mathrm{H}}$ (see e.g. [36,75]), where $\mathbf{U}$ and $\mathbf{V}$ are unitary matrices holding the left and right singular vectors and $\mathbf{S}$ is a rectangular matrix holding the non-zero singular values. Remembering that $\mathbf{G}_{yy}(\omega)$ is Hermitian and positive definite [9] (since all PSD matrices embed energy content), this brings $\mathbf{U} = \mathbf{V}$; thus, the SVD of a PSD matrix can always be expressed by Eq. (3.20), factorization also known as spectral theorem [9, 15].

The above-mentioned SVD technique is performed at each frequency line $\omega = \omega_i$. Starting from the SVD of Eq. (3.20), modal identification can be made around a modal peak in the frequency domain, that can be located by a peak-picking procedure on the singular values representation. The previous peak-picking can be applied also to the SV product plot, supporting the procedure in case of very high damping or noisy data and further improving the modal estimates. Especially, when only the kth principal value is dominant, i.e. it reaches the maximum near a modal frequency ω_k, the response PSD matrix can be approximated by a unitary rank matrix [14]:

$$\mathbf{G}_{yy}^{\mathrm{T}}(\omega_i = \omega_k) \simeq \mathrm{s}_k \mathbf{u}_{k1} \mathbf{u}_{k1}^{\mathrm{H}} \tag{3.21}$$

where the first singular value s_k at the kth resonance frequency leads to an estimate, with unitary normalization, of the related mode shape $\hat{\boldsymbol{\phi}}_k = \mathbf{u}_{k1}$. The identified mode shape is then compared to the others in its proximity [13], by making basic reference to the classical MAC (Modal Assurance Criterion) index [1]:

$$\mathrm{MAC}\left(\boldsymbol{\phi}_r, \boldsymbol{\phi}_s\right) = \frac{\left|\boldsymbol{\phi}_r^{\mathrm{H}} \boldsymbol{\phi}_s\right|^2}{\left|\boldsymbol{\phi}_r^{\mathrm{H}} \boldsymbol{\phi}_r\right| \left|\boldsymbol{\phi}_s^{\mathrm{H}} \boldsymbol{\phi}_s\right|} \tag{3.22}$$

The MAC index represents the square of the correlation between two modal vectors $\boldsymbol{\phi}_r$, $\boldsymbol{\phi}_s$. If the MAC index is 1, the two compared vectors can be considered as identical; if 0, clearly distinct (orthogonal). As long as a principal vector related to a frequency around the modal peak displays a high MAC value (near 1, say larger than for example $0.8 \div 0.9$), related to the estimated mode shape, the corresponding principal value locates a subset of SV that belongs to the SDoF density function [14, 15]. Further indices based on MAC Eq. (3.22) are also used later in the algorithm (see Section 3.4.3), with the purpose to assess the validity of the estimated modal parameters.

3.3 Modal damping ratio estimates by refined FDD

After the evaluation of the natural damped frequencies and mode shapes estimates, as delineated in previous Section 3.2.4, the rFDD algorithm is further extended, by accounting for consistent estimates of the modal damping ratios and of the undamped natural frequencies, through a development of the classical Enhanced FDD algorithm. Following Section 3.3.1 presents the classical FDD method, while Section 3.3.2 outlines in detail the original procedure developed in the rFDD algorithm, and Section 3.3.3 finally develops the coupled Chebyshev Type II filters procedure for the

estimate improvements, especially as concerning the modal damping ratios.

3.3.1 Classical Enhanced FDD algorithm

With the classical EFDD algorithm [14, 42] modal damping ratios and undamped natural frequencies can be estimated. The main features of this procedure are reported below. The SDoF power spectral density function associated to the kth mode is identified around the corresponding resonance peak, by comparing the associate estimated mode shape to those at the frequency lines in its proximity, in terms of MAC filtering [42, 130]. This phase is usually referred to as spectral bell identification. As a sample of the procedure, in Fig. 3.7a the peak picking technique on the first SV is represented, while in Fig. 3.7b the spectral bell identification of the first mode is depicted.

The located subset of singular values in the spectral bell is taken back to the time domain by Inverse Discrete Fourier Transform (IDFT), by obtaining an estimate of the SDoF auto-correlation function related to the resonance peak. In this process, remaining parts of the PSD function that lay outside the frequency window of the spectral bell are set to zero [14].

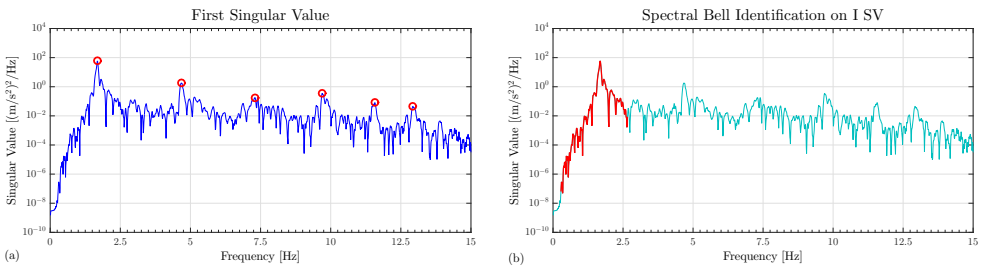

Figure 3.7: *Display of the peak-picking technique on the first singular value and of the spectral bell identification of the first mode; six-storey frame, L'Aquila earthquake.*

All extrema, i.e. peaks and valleys, that shall represent the free decay of a damped SDoF system, are identified within an appropriate time window, as it can be seen in Fig. 3.8a. Through a peak-picking of peaks and valleys in the selected time window, it is possible to evaluate the logarithmic decrement δ as:

$$\delta = \frac{2}{k} \ln \left(\frac{r_0}{|r_k|} \right) \tag{3.23}$$

where k is an integer index counter of the kth extreme of the auto-correlation function, $k = 1, 2, \ldots$, while r_0 and r_k are the initial and the kth extreme value of the auto-correlation function, respectively. Then, a linear

relation can be obtained in terms of counter k [12]:

$$2\ln\left(|r_k|\right) = \ln\left(r_0\right) - \delta k \tag{3.24}$$

which can be plotted and fitted with a straight line (see a sample in Fig. 3.8b). Its slope provides an estimate of the logarithmic decrement δ, through a linear regression on k and $2\ln\left(|r_k|\right)$. Finally, from the estimated logarithmic decrement $\delta = \delta_q$ of mode q the corresponding modal damping ratio ζ_q can be classically evaluated as [14]:

$$\zeta_q = \frac{\delta_q}{\sqrt{4\pi^2 + \delta_q^2}} \tag{3.25}$$

Then, knowing the estimated modal damping ratio ζ_q and the estimated damped frequency, the undamped natural frequency can be obtained [14]. Summarizing, the standard EFDD algorithm sets fixed values for the MAC index (for example 0.6) used to perform the spectral bell identification and the peaks of the auto-correlation within 90% to 20% of the maximum amplitude are selected to perform the subsequent regression operations. More details on the standard procedure can be found in [12, 14, 73].

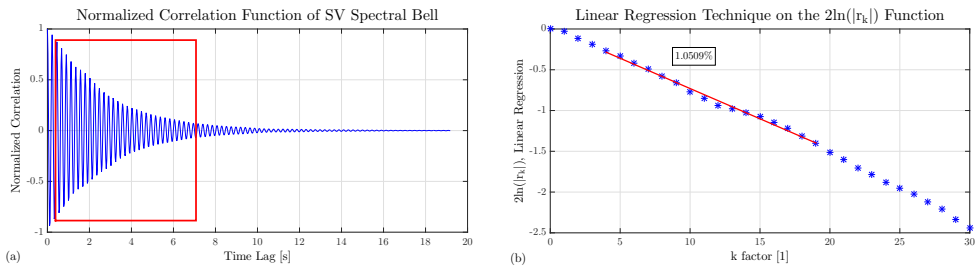

Figure 3.8: *Selected time window of the normalized IDFT and linear regression technique for the estimate of the modal damping ratio; first mode, six-storey frame, L'Aquila earthquake.*

3.3.2 Damping estimates by refined FDD: iterative loop and optimization algorithm

The refined FDD technique evaluates the modal damping ratios by an advanced optimization algorithm, in order to achieve reliable estimates, especially in the case of seismic input and heavy damping, which negatively affect the results achievable from classical EFDD algorithms. Mainly, the adoption of preselected fixed parameters (i.e. MAC value for the bell identification and selected range of amplitudes for the ACF, as explained in Section 3.3.1), as usually done in standard EFDD, suffers for these tough conditions [12, 73]. Also, the present use of seismic input makes it harder

for the correct detection of the SDoF system associated to the identified mode. Besides, the use of the following procedure automates the estimation of the modal damping ratios and does not require the interaction with an expert operator. The selection of the correct time window on the SDoF Auto-Correlation Function (ACF) represents the most difficult part of the algorithm, which, jointly with the spectral bell identification, derive from truncated data, introducing errors in the damping estimates [125]. This disadvantage must be taken into account, especially with closely spaced modes [130]. An inspection about contents, decimation and frequency resolution of adopted signals must be necessary to achieve well-defined time window representations. Besides, the correct outcome of the aforementioned linear regression is directly connected to the adequacy of the time window selection. These two steps, jointly with the choice of the spectral bell, shall be performed by an *iterative operation of advanced optimization*, according to the following procedure:

1. The spectral bell identification of the qth mode of vibration is performed first with a 0.9 MAC index, selecting the $\mathbf{S}_Q$ subset of SVs directly from Eq. (3.18):

$$\mathbf{S}_Q(\omega) = \mathbf{S}_Q(\omega_i = \omega_q) = \left[\, 0 \ \mathrm{s}_l \ \ldots \ \mathrm{s}_q \ \ldots \ \mathrm{s}_u \ 0 \,\right]^{\mathrm{T}} \tag{3.26}$$

   where s_l and s_u are the lower and upper values of the spectral bell.

2. The identified set of SV is taken back to time domain by Inverse Fourier Transform and normalized, by obtaining the related SDoF Auto-Correlation Function (ACF), $\mathbf{R}_{yy,Q}(\tau)$:

$$\begin{aligned} \mathbf{R}_{yy,Q}(\tau) = \mathcal{F}^{-1}\big\{\mathbf{S}_Q(\omega)\big\} &= \frac{1}{m}\sum_{j=0}^{m-1} \mathbf{S}_Q(\omega) e^{-\frac{2\pi \mathrm{i}}{m} jl} = \\ &= \left[\, \mathrm{r}_l \ \ldots \ \mathrm{r}_m \,\right]^{\mathrm{T}}, \quad l = 1, \ldots, m-1 \end{aligned} \tag{3.27}$$

3. On the normalized SDoF Auto-Correlation Function (ACF) two exponential decays are fitted, both on peaks and valleys of the ACF, defining terms $\hat{\mathbf{y}}_p$ and $\hat{\mathbf{y}}_v$, respectively:

$$\hat{\mathbf{y}}^p = \mathrm{A}^p \exp\big(\mathrm{B}^p \mathbf{x}^p\big), \quad \hat{\mathbf{y}}^v = \mathrm{A}^v \exp\big(\mathrm{B}^v \mathbf{x}^v\big) \tag{3.28}$$

   where A^i and B^i are the parameters to be fitted, while $\mathbf{x}^i$ represent the peak and valley time instant vectors (superscript i denotes peaks p, and valleys v, respectively). These parameters can be calculated by the minimization of the R_i function, wherein the points are equally

weighted (with respect to classical exponential best-fit, where greater weights to small y values are given):

$$\mathrm{R}_i^2(\mathrm{a}^i, \mathrm{b}^i) = \sum_{j=1}^{m} \mathrm{y}_j^i \left[\ln\left(\mathrm{y}_j^i\right) - \left(\mathrm{a}^i + \mathrm{b}^i \mathrm{x}_j^i\right) \right]^2$$
$$\Rightarrow \begin{cases} \mathrm{J}_{\mathrm{a},i} = \dfrac{\partial\left(\mathrm{R}_i^2\right)}{\partial\, \mathrm{a}^i} = 0 \\ \mathrm{J}_{\mathrm{b},i} = \dfrac{\partial\left(\mathrm{R}_i^2\right)}{\partial\, \mathrm{b}^i} = 0 \end{cases} \tag{3.29}$$

where $\mathrm{J}_{\mathrm{a},i}$ and $\mathrm{J}_{\mathrm{b},i}$ are the terms of the Jacobian matrix $\mathbf{J}$, while superscript i again denotes peaks and valleys, respectively. The fitting coefficients a^i and b^i may be computed as $\mathrm{a}^i = \ln(\mathrm{A})^i$ and $\mathrm{b}^i = \mathrm{B}^i$. Solving for a^i and b^i, it is possible to obtain the estimates of the exponential decays as in Eq. (3.28).

4. All ACF extrema ranging from $r_0 = 90\%$ to $r_n = 30\%$ of the maximum amplitude are selected within an appropriate time window, by obtaining the normalized ACF subset $\mathbf{R}_{yy,Q}(\tau_{\mathrm{sub}})$:

$$\mathbf{R}_{yy,Q}(\tau_{\mathrm{sub}}) = \left[\ \mathrm{r}_0\ \ldots\ \mathrm{r}_n\ \right]^{\mathrm{T}} \subseteq \mathbf{R}_{yy,Q}(\tau) \tag{3.30}$$

5. Subsequent operations of regression, according to classical EFDD procedures, are performed and the modal damping ratio ζ_q is estimated.

6. The exponential decays of Eq. (3.28) included in the time window of the ACF are compared with the classical damping trends, arising from SDoF free damped vibrations:

$$\mathbf{y}^p = \exp\left(-\zeta_q \frac{\omega_{dq}}{\sqrt{1-\zeta_q^2}} \mathbf{x}^p\right), \quad \mathbf{y}^v = \exp\left(-\zeta_q \frac{\omega_{dq}}{\sqrt{1-\zeta_q^2}} \mathbf{x}^v\right) \tag{3.31}$$

where the maximum amplitude of the motion is set equal to 1 for the normalized ACF, ζ_q is the estimated modal damping ratio (point 5) and ω_{dq} is the qth estimated damped frequency.

7. The computed exponential decays of Eqs. (3.31) are compared, by calculating the residuals $\hat{\boldsymbol{\varepsilon}}^i$ with the fitted decays of point 3:

$$\hat{\boldsymbol{\varepsilon}}^p = \mathbf{y}^p - \hat{\mathbf{y}}^p, \quad \hat{\boldsymbol{\varepsilon}}^v = \mathbf{y}^v - \hat{\mathbf{y}}^v \tag{3.32}$$

These residuals are compared for each peak and valley of the ACF considered time window.

8. The developed algorithm works in order to minimize these residuals, by recalibrating the time window parameters (i.e. the minimum and maximum amplitudes selected on the ACF, r_0 and r_n) and the MAC index at each step, with an iterative loop from point 1 to point 7, until a reliable estimate of ζ_q is obtained. This means that the residuals must be less than a fixed parameter, for example $\hat{\boldsymbol{\varepsilon}}^i < 0.01$ in the present analyses. The MAC index is the first value recalibrated by the algorithm, ranging from 0.70 to 0.99, while r_0 and r_n, secondarily, shall assume values between $0.7 \leq r_0 \leq 1.0$ and $0.1 \leq r_n \leq 0.4$, by expanding or contracting the time window, until the residuals have been minimized.

The optimization algorithm adopted for the residuals minimization adopts two sources of information, i.e. the classical damping trends $\mathbf{y}^p$, $\mathbf{y}^v$ and the exponential fitted decays $\hat{\mathbf{y}}^p$, $\hat{\mathbf{y}}^v$. Either these data depend on the adopted MAC index and on the ACF time window parameters. The minimization of the residuals, allowing for a most effective evaluation of the modal damping ratio ζ_q, is measured in terms of an appropriate objective function $\mathrm{P}(\mathbf{z})$, defined as follows:

$$\begin{aligned} \mathrm{P}(\mathbf{z}) &= \left[\alpha \left(\frac{y_i^p - \hat{y}_i^p}{y_i^p} \right)^2, (1-\alpha) \left(\frac{y_i^v - \hat{y}_i^v}{y_i^v} \right)^2 \right]^{\mathrm{T}} = \\ &= \left[\alpha \left(\frac{\hat{\boldsymbol{\varepsilon}}_i^p}{y_i^p} \right)^2, (1-\alpha) \left(\frac{\hat{\boldsymbol{\varepsilon}}_i^v}{y_i^v} \right)^2 \right]^{\mathrm{T}} \end{aligned} \tag{3.33}$$

where $\mathbf{z}$ is the (3×1) vector including the parameters to be optimized with respect to the $i = 1, \ldots, n$ ACF points, and $\alpha \in [0, 1]$ represents a weighting coefficient, set to 0.5 in the present work. The minimization of the residuals in the objective function is achieved by using a non-linear least-squares algorithm through the "lsqnonlin" function of the Matlab Optimization Toolbox [116].

The procedure described above conceptually derives from classical EFDD algorithms [14, 42] but considers a refined and improved procedure with an optimization loop, limiting possible errors and inaccuracies in the estimates, with respect to classical EFDD implementations of the literature (see the results presented in [91] for further details). Despite the iterative approach, rather limited computing time has been added to the computational effort of a classical EFDD algorithm, in the order of 20%. Finally, an example of the ACF curve fittings that may be achieved from the adoption of the present procedure is depicted in Fig. 3.9 (structural features of the adopted frames are going to be presented in Chapters 4).

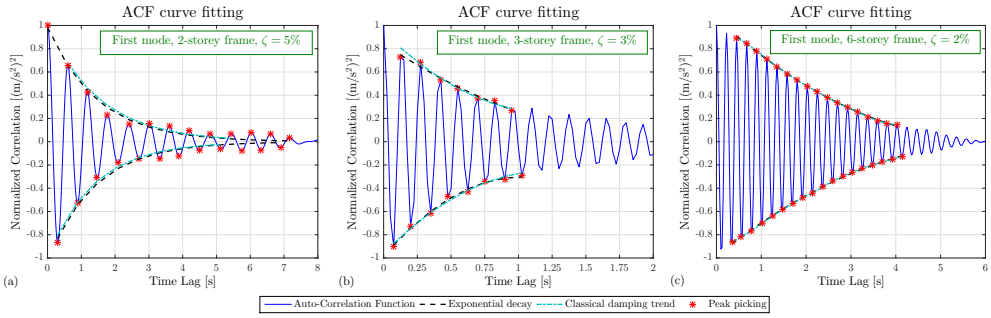

Figure 3.9: *ACF curve fitting for the 1st mode of vibration of a two-, three- and six-storey frame, Kocaeli b) (12082), Superstition Hills b) (12122) and Chi-Chi a) (12141) earthquakes, NS component.*

3.3.3 Enhancement of modal parameter estimates via coupled Chebyshev Type II bandpass filters

When tough seismic input and heavy damping conditions apply, i.e. especially when the adopted structural responses exhibit stronger non-stationary or heavy-damped conditions, in terms of FDD identification challenge (namely when $\zeta > 1 \div 2\%$, see [17]), this technique may be further improved with a novel computational procedure. This method is based on coupled Chebyshev Type II bandpass filters, in order to achieve much effective estimation of natural frequencies, mode shapes and damping ratios.

These filters have been adopted in order to enhance the SDoF spectral bells related to the identified mode and to isolate their frequency content, with respect to that of the remaining spectrum. This is because, when earthquakes characterized by strong non-stationary are adopted as input excitations, the harmonics brought about by themselves (around the modal peaks) may influence the correct outcomes of the rFDD algorithm. Therefore, the need was that of seeking for an appropriate filter that was capable to extract the correct modal information from the SVs, without loss of data content.

The choice had fallen on Chebyshev Type II filters since, after several trials and simulations, this kind of filter showed to be the most effective one for the sought enhancement of the SDoF spectral bells, without affecting the main characteristics of the original signal in the frequency interval of interest (i.e. within the range of the considered modal peak). Chebyshev II filters are characterized by a flat (monotonic) passband magnitude and equiripple response in the stopband. They do not roll off as fast as Type I filters, and they are free of passband ripple. In addition, they minimize the error between the idealized filter and the actual filter characteristics, over the range of the filter itself [79].

An example of the outcome of the adopted Chebyshev Type II filter is represented in Fig. 3.10, where magnitude and phase responses are depicted for the enhancement of the second mode SDoF spectral bell, for a two-storey frame (see later description in Chapter 4).

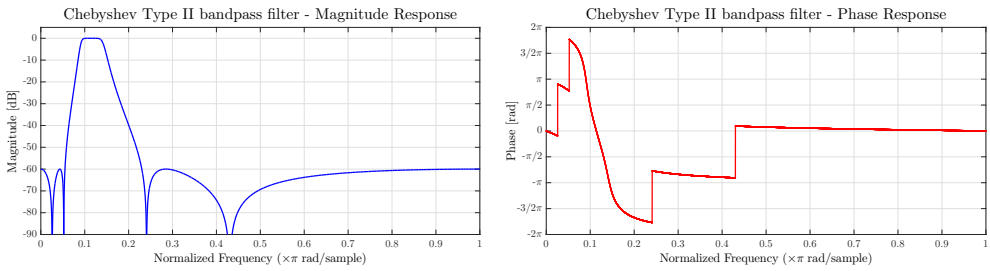

Figure 3.10: *Magnitude and phase response of the adopted Chebyshev Type II bandpass filter for the enhancement of the II mode SDoF spectral bell, two-storey frame.*

Basically, the Chebyshev Type II bandpass filter procedure may be outlined as follows:

1. A first run of the rFDD method is performed on the original earthquake-induced response signals, which are adopted as input channels for the identification algorithm, including for the iterative procedure for the modal damping ratio estimates (see Section 3.3.2). This is necessary to extract all the modal peaks, i.e. all the resonance frequencies $\omega_i = 1, \ldots, k, \ldots, n$ of the structure under analysis, whose modal estimates are going to be improved through the present coupled filter method.
2. From the iterative procedure in Section 3.3.2, a well-suited set of MAC indexes can be achieved, leading to an appropriate detection of the spectral bells. For the kth mode of vibration, the spectral bell may be selected from the $\mathbf{S}_k$ subset of the SVs as:

$$\mathbf{S}_K(\omega) = \mathbf{S}_K(\omega_i = \omega_k) = \left[\, 0 \; \mathrm{s}_l \; \ldots \; \mathrm{s}_k \; \ldots \; \mathrm{s}_u \; 0 \,\right]^{\mathrm{T}} \tag{3.34}$$

   where s_l and s_u are the lower and upper values of the spectral bell, to which lower and upper frequencies ω_l and ω_u defining the spectral bell correspond. These extreme values can be extracted by comparing the kth frequency peak with the frequency lines in its proximity, in terms of singular vectors, with a MAC index set equal to the one achieved from the iterative procedure in Section 3.3.2.
3. Lower and upper frequencies ω_l and ω_u are used for the definition of the lower and upper bounds, i.e. the stopband edge frequencies of a Chebyshev Type II bandpass filter [79]:

$$\omega_L = 0.80\,\omega_l, \quad \omega_U = 1.20\,\omega_u \tag{3.35}$$

where ω_L and ω_U are the lower and higher stopband frequencies of the filter, which are calculated by taking $\pm 20\%$ of the original lower and upper frequencies, as adopted for all the analyses in the present work. The attempts that were performed for the selection of the appropriate boundary values showed that these are, on average, the best values that can be adopted in the following steps. Generally, ω_L and ω_U may vary between $0.70 < \omega_L/\omega_l < 0.90$ and $1.10 < \omega_U/\omega_u < 1.30$, respectively, as a function of the modal damping ratio under target. In fact, the modal damping ratio directly affects the width of the SDoF spectral bell. For light damping, i.e. for ζ in the order of $1 \div 2\%$, normalized values of 0.90 and 1.10 can be used, leading to a narrow interval. On the other hand, for damping values in the order of $5 \div 10\%$, it is necessary to adopt a wider interval, i.e. with extreme normalized values of 0.70 and 1.30.

4. Then, the Chebyshev Type II filter is defined as a 4th-order (N = 4) bandpass filter with an $A_s = 60\,\text{dB}$ stopband attenuation and ω_L, ω_U lower and higher stopband frequencies. For the present analysis, the filter order and the stopband attenuation specifications have been selected, after several trials, as the more suitable ones to achieve the best trade-off among passband width, transition band steepness and stopband attenuation. As for ω_L and ω_U, order and stopband attenuation may vary between $3 < N < 5$ and $50\,\text{dB} < A_s < 70\,\text{dB}$, as a function of the modal damping ratio under target. The higher values show to be more suitable for light damping, while lower values need to be used at increasing damping. In the present form, the Chebyshev II filter is implemented within MATLAB via a Transfer Function design as a zero-phase digital filter [79], by using the "*cheby2*" filter design and the "*filtfilt*" digital filter environment.

5. The so-defined Chebyshev II filter is applied to all the original earthquake-induced response signals, in order to compute the filtered signals for each mode (detected in Step 1), which are used then as input channels for the rFDD algorithm. An example of the achievable filtered responses (in terms of accelerations) and their FFT after the application of the Chebyshev II filter is depicted in Fig. 3.11, where the filtering on the I and II mode is applied on the 1st-storey response. The rFDD procedure shall be applied in all its computational steps, until the SVD of the output PSD matrix is achieved (see Eq. (3.20)). In this way, a set of n SDoF filtered spectral bells can be obtained, by sequentially applying present Steps 2-5, for each of the previously-defined modal peaks $\omega_i = 1, \ldots, k, \ldots, n$.

6. Obviously, each kth SDoF filtered spectral bell has components on

the different SV lines, obtained through the application of the SVD. An example of the Singular Value Decomposition obtained from the Chebyshev II filtering applied on the I and II mode of vibration is represented in Fig. 3.12. Finally, the achieved set of n SDoF filtered spectral bells is recomposed over the original SVs, in order to obtain the new set of filtered SVs that is going to constitute the basis for the modal parameter identification. The filtered set of SVs can be reconstructed by taking into account the overlapping points between the data coming from different SDoF filtered spectral bells. The remaining parts that do not compete to the kth modal peaks are then removed from the final SV curves.

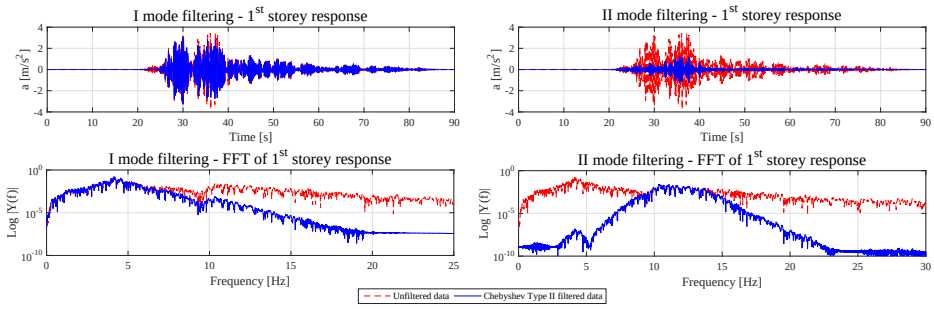

Figure 3.11: *Chebyshev Type II bandpass filtering on the I and II mode on the 1st-storey responses and FFT of the responses, Chi-Chi a) (12141) earthquake, NS component, two-storey frame.*

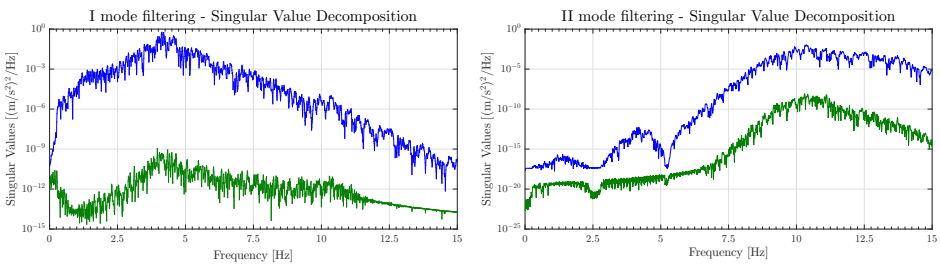

Figure 3.12: *Singular Value Decomposition obtained from the Chebyshev Type II bandpass filtering on the first and second mode, Chi-Chi a) (12141) earthquake, NS component, two-storey frame.*

Then, the achieved set of reconstructed filtered SVs is used for modal identification, by applying the estimation steps of the rFDD algorithm (see Section 3.2). Samples of the resulting SVs are depicted in Fig. 3.13a and 3.13b, for a two- and a three-storey frame (frame properties are described in Chapter 4). The support of this innovative strategy enhances the modal parameter estimates, with respect to those achievable by the

basic rFDD algorithm, especially when the adopted earthquakes exhibit stronger non-stationary and critical features for the rFDD validity. In fact, some earthquakes carry several strong harmonics in correspondence of the structural frequencies, which trouble the correct detection of the resonance peaks and lead to more difficult estimates. That feature, in addition to heavy damping (in terms of FDD identification challenge), may bring to failures or to consistent errors, when using traditional FDD methods. Then, the application of the current procedure shows to be able to isolate the modal information of the spectral peaks from the remaining frequency lines of the spectra. Further descriptions and numerical examples from this procedure can be found in [97].

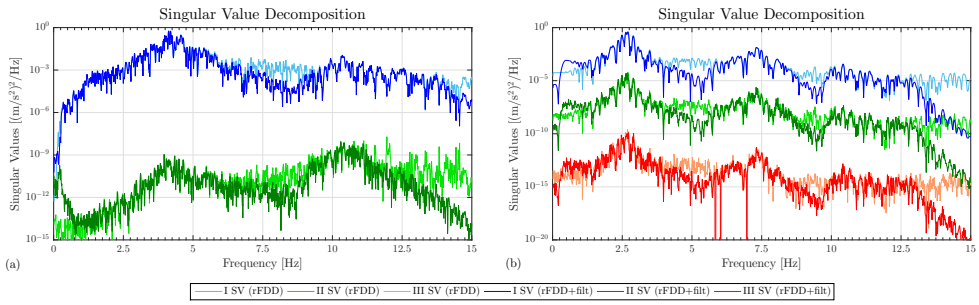

Figure 3.13: *Singular Value Decomposition obtained from basic rFDD and rFDD+filter for: (a) two-storey frame, Chi-Chi a) (12141) earthquake, NS component; (b) three-storey frame, Superstition Hills b) (12122) earthquake, NS component.*

3.4 Further rFDD computational procedures at seismic input and heavy damping

3.4.1 Reconstruction of the original SDoF spectral bells

With the adoption of ambient input excitations, i.e. of classically-used white noise, modal peaks may be detected all on the first Singular Value (SV) curve, which contains all the necessary modal information towards natural frequency, mode shape and modal damping ratio estimations. With white noise input, the adoption of the remaining SVs curves is not necessary, since they are characterized by greatly lower energetic levels, bringing to an increase of the bias level of the estimates.

That is no longer true with seismic input, since they display different characteristics with respect to the white noise signals. Then, the integrated approach for PSD matrix computation, explained before in Section 3.2.3, leads to the possibility of having the modal information, and

then the modal peaks, on different SV curves. In this case, the different energy levels of the SV curves with seismic input bring to less biased estimations by adopting also the SV curves beyond the first one.

Then, the integrated PSD matrix computation suggested by the refined FDD procedure (Section 3.2.3), shall lead to substantial help in the location of the correct resonance peaks at seismic input and also at heavy damping. With this procedure, the estimate of the modal parameters becomes feasible by operating at the same time on different SVs: an example is shown in following Fig. 3.14a, where the SVD of the PSD matrix calculated with the Corr method is represented. It is possible to see that resonance peaks can be found on different SVs, thanks to the clearer representation offered by the procedure. Moreover, the use of the SV product plot, i.e. the representation of the product between various SVs for each frequency line, is complementary (see [88, 89]).

Then, in case of very noisy SVs (e.g. especially with heavy damping) or some seismic input, a partial overlapping of SVs is also possible. The individuation of the spectral bells can be originally made as an envelope composition of different SVs portions, similarly to the common overlapping technique [64], by building a fictitious SDoF SV, as it is shown in Fig. 3.14b. Then, the use of Blind Source Separation [29] is not necessary at this stage.

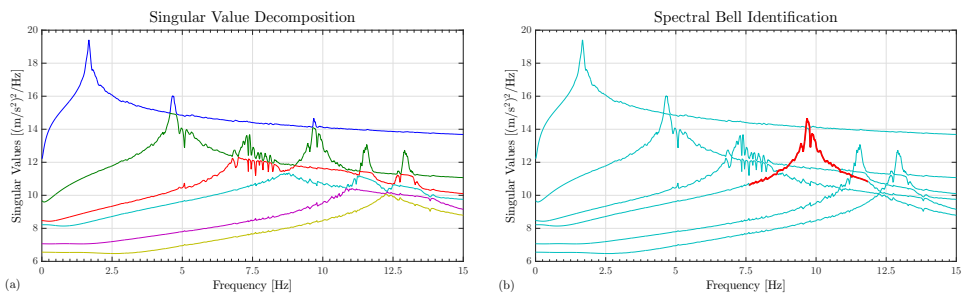

Figure 3.14: *Display of the SVD and of the fictitious SV related to the fourth vibration mode, six-storey frame, L'Aquila earthquake.*

So, a fictitious SDoF SV can be built to help the modal parameter estimates, especially as concerning the identification of the modal damping ratios. The example reported in Fig. 3.14b, where the spectral bell related to the fourth mode of vibration is composed as a fictitious SV from portions of different SVs (in this case the I, II, III and IV modes are adopted). Also, the peaks related to the III, V and VI modes can be found on the second SV curve, and the spectral bells can be similarly composed. This feature differs from the chance offered by classical EFDD algorithms, which allow for the overlapping of SVs based upon the use of

a modal peak positioned on the first SV. The presence of resonance peaks on different SVs may produce severe working conditions for traditional EFDD algorithms, which are supported here by the strategies of the current refined FDD procedure [91,92]. Then, by starting from the SV curve reconstruction related to a particular mode of vibration, all the remaining rFDD computational procedures may be thoroughly applied.

3.4.2 Frequency resolution enhancement

Another important issue concerns the frequency resolution (f_s). Seismic input signals display very limited registrations with respect to ambient recordings, and this may reduce the frequency resolution adopted for the PSD matrix evaluation. In fact, the PSD's frequency resolution is another fundamental issue towards achieving reliable estimates, especially for the damping ratios, where the frequency resolution directly affects the number of points which can be used during the linear regressions (see Section 3.3.2), and consequently the reliability of the results. Also the remaining modal parameters are affected by the adopted frequency resolution, since a low frequency sampling f_s may truncate the modal peaks in the SV curves, leading to less accurate natural frequency and mode shape estimates, or even introducing noise and errors in the estimates.

Then, the adopted frequency resolution looks an essential feature for the adoption of seismic input, whose intrinsic short duration (with respect to ambient recordings) may definitely affect the achievable estimates. Then, it is possible to enhance the frequency resolution by acting on two parameters: the time sampling Δt or the total number of points N_{points} adopted for the PSD matrix computation. Both directly depend on the total time length of the structural response recording.

Time sampling and total time length of the recording depends on the duration of the seismic signal and on the characteristics of the adopted instrumentation. So, the way implemented with the rFDD algorithm to avoid the lacking of frequency resolution is to increase the number of points used for the PSD matrix computations through an interpolation of the spectrum; this can be done by adding a zero-solicitation time window at the end of the earthquake acquisitions, thus increasing the length of recordings with an operation similar to that known as zero-padding in classical signal analysis [36].

Starting from the original seismic response recording, which has its own total time length t_f, total number of points N_{points} and time sampling Δt as:

$$t_f = N_{\text{points}} \cdot \Delta t \tag{3.36}$$

it is possible to add a zero-solicitation time window t_0, i.e. a series of

zeros N_{zeros}, such that time length t_f may be incremented until time length t_{ft}, necessary to obtain the desired frequency resolution. Than, it is possible to obtain:

$$t_{ft} = t_f + t_0 = (N_{\text{points}} + N_{\text{zeros}}) \cdot \Delta t \tag{3.37}$$

With the new number of points N_p:

$$N_p = N_{\text{points}} + N_{\text{zeros}} = \frac{t_{ft}}{\Delta t} \tag{3.38}$$

The new increased frequency resolution which is going to be adopted for the PSD computation is the following:

$$\Delta f = \frac{1}{\Delta t} \cdot \frac{1}{N_p} = \frac{1}{t_{ft}} \tag{3.39}$$

More specifications and some practical examples may be found in [89, 92], where some case studies relating the record length to the modal estimates are considered, too. In the literature, it is generally said that registration lengths of about $1000 - 2000$ times the first natural period often result to be appropriate [13, 104]. So, this issue is fundamental to reach consistent estimates of the modal parameters, especially for the modal damping ratios, even for the low damping cases, where a fine frequency resolution is necessary to correctly score the very sharp peaks.

3.4.3 Modal detection and validation via MAC indexes and complexity analysis

Towards modal detection and modal validation purposes, the present rFDD algorithm adopts the combined use of different MAC indexes [91,93]. The use of Modal Assurance Criterion (MAC) and Modal Phase Collinearity (MPC) indexes (also in their Auto-MAC and Auto-MPC meanings) comes after a preliminary "peak-picking" on the available SVs [92], and becomes necessary to discern "spurious peaks" from true (physical) modal ones. In particular, these indexes may be used to discard spurious peaks that exhibit a complex-number character (i.e. displaying modal deflection phases that significantly deviate from 0 or π).

Fig. 3.15 represents, for an applicative case, the associated Modal Assurance Criterion (MAC), Auto-Modal Assurance Criterion (Auto-MAC) and Auto-Modal Phase Collinearity (Auto-MPC) indices [1]. The MAC index was outlined in previous Section 3.2.4. Its purpose is that of comparing two different mode shapes towards modal validation (when target modal parameters are available), and to support modal peak and spectral bell detection for the modal damping ratio estimation.

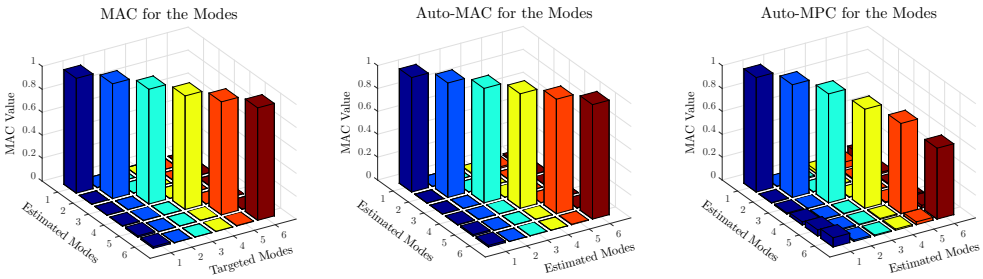

Figure 3.15: *Modal Assurance Criterion, Auto-Modal Assurance Criterion and Auto-Modal Phase Collinearity for the estimated mode shapes; six-storey frame, L'Aquila earthquake ($\zeta_k = 1\%$).*

The Auto-MAC index is a version of the MAC index in which the estimated mode shapes are correlated with themselves, Auto-MAC = $\mathrm{MAC}(\boldsymbol{\phi}_{k,\mathrm{est}}, \boldsymbol{\phi}_{k,\mathrm{est}})$; especially, the Auto-MAC matrix is useful to detect if some modes are not orthogonal to each-other. All diagonal terms are unitary by definition, while off-diagonal terms, due to the orthogonality hypothesis between the modes, shall be at around zero. The existence of non-zero off-diagonal terms (e.g. larger than 0.4) can be taken as a sign of little degree of correlation.

Finally, the Auto-MPC is an index that checks the degree of complexity of a mode, by evaluating the functional linear relation between imaginary and real parts of the mode shape components [1, 104]. This index is based on variance-covariance matrix computations applied to the estimated mode shapes, and can be calculated as the MAC index among an estimated mode shape and its complex conjugate, Auto-MPC = $\mathrm{MAC}(\boldsymbol{\phi}_{k,\mathrm{est}}, \overline{\boldsymbol{\phi}}_{k,\mathrm{est}})$. An MPC index greater than, say, 0.5 may be interpreted as if the mode shape vector components are all in-phase (and then the estimates are considered to be suitable), while a lower value suggests anomalous fluctuations of the phases (related, for example, to unreliable mode shapes, or to potential structural damage). Also, a visual inspection of the mode shapes complexity is possible at this stage [93].

Either the Auto-MAC and Auto-MPC indexes help with the modal identification when no target parameters are available for comparison purposes [1]. The existence of non-zero off-diagonal terms also indicates a little degree of correlation between some of the modes, i.e. some of them are not correctly estimated (or in some cases the estimates may not be reliable).

Chapter 4

Refined Frequency Domain Decomposition: main results

As it concerns the developed identification analyses and results, in the present thesis only selected outcomes are reported, from the whole bulge of cases that have been analysed in seminal works [88–90] and in more recent works [38–40,91–95,97,98,100] and all along the whole development of this doctoral dissertation.

In particular, in present Chapter 4 the focus falls on two different structures, i.e. a reference three-storey shear-type frame and a more realistic ten-storey shear-type frame, with regards to the use of synthetic earthquake-induced structural response signals. Both structures are characterized by heavy damping, and they are analysed through the adoption of a set of ten earthquake base excitations. These structures and earthquakes are going to be adopted for all the three proposed methods explored in this thesis, namely rFDD (present Chapter 4), SSI-DATA (Chapter 6) and FDCIM (Chapter 7), in order to make it possible for a detailed comparison among these algorithms within the Earthquake Engineering range.

For the rFDD algorithm only – the most deepened and analysed algorithm in the present work – additional results are going to be presented both in present Chapter 4 (Section 4.3) and in Chapter 5, representing an extensive analysis based on the adoption of the FEMA P695 earthquake database with three different shear-type frame structures and a further analysis with structures subjected to Soil-Structure Interaction effects, additionally to the earthquake excitation input and the heavy damping conditions, respectively.

Then, as a final and conclusive analysis framework, some results with the adoption of real earthquake-induced structural response signals will be reported in Chapter 8, where all the three OMA methods are going to be used for final comparison purposes.

4.1 Adopted earthquake dataset and numerical models

The input response channels to be fed to the present OMA output-only algorithms are first obtained from calculated synthetic structural response signals of linear multi-storey frames. Storey accelerations are considered as input for the identification algorithms. These numerical response recordings are generated prior to the modal identification by taking as base acceleration an earthquake from a set of ten selected seismic ground motions (see Table 4.1).

The adopted earthquakes have been chosen as representative ones from a wide variety of seismic events, with rather different characteristics, i.e. time-frequency spectra, duration, sampling, magnitude and PGA. Also, they have been specifically selected as expected challenging instances for the present rFDD, SSI-DATA and FDCIM identification purposes, given their non-stationary nature.

The simulated structural responses are calculated by direct time integration of the equations of motion, via Newmark's (average acceleration) method [27]. The use of synthetic signals shall fulfil a first necessary condition for the algorithms' effectiveness, since modal parameters are determined via direct modal analysis before identification and adopted as known targets for validation purposes.

Earthquake	*Date*	*Station*	*Dur.* [s]	f_s [Hz]	M	*Comp.*	*PGA* [g]
(AQ) L'Aquila	06/04/2009	AQV	100	200	5.8	WE	0.659
(CH) Maule	27/02/2010	Angle S/N 760	180	100	8.8	WE	0.697
(EC) El Centro	18/05/1940	0117	40	100	7.1	NS	0.312
(IV) Imperial Valley	15/10/1979	01260	58	100	6.4	NS	0.331
(KO) Kobe	17/01/1995	Nishi Akashi	41	100	6.9	WE	0.510
(LP) Loma Prieta	17/10/1989	47459	40	50	7.0	WE	0.359
(NO) Northridge	17/02/1994	24436	60	50	6.7	WE	1.778
(NZ) Christchurch	03/09/2010	163541	82	50	7.1	NS	0.752
(TA) Tabas	16/09/1978	70 Boshrooyeh	43	50	7.3	WE	0.929
(TO) Tohoku	11/03/2011	MYG004	300	100	9.0	NS	2.699

Table 4.1: *Main features of the adopted set of ten selected earthquake base excitations.*

The frame structure that has been adopted first for initial verification is a reference three-storey shear-type frame, subjected to each single base excitation instance from the above adopted set of ten strong ground motions. This reference 3-DoF case has been characterized by a modal damping ratio $\zeta_k = 7\%$, for all the structural modes, a rather high value for the present OMA identification purposes, especially within the seismic engineering scenario. Structural and modal dynamic characteristics of the

adopted three-storey frame [92] are reported in Table 4.2.

Floor	1	2	3
Stiffness $\times 10^3$ [kN/m]	202.83	202.83	202.83
Mass $\times 10^3$ [kg]	144	144	144
Mode	1	2	3
Natural frequency [Hz]	2.658	7.448	10.76
Mode shape [1]	$\begin{Bmatrix} 0.328 \\ 0.591 \\ 0.737 \end{Bmatrix}$	$\begin{Bmatrix} -0.737 \\ -0.328 \\ 0.591 \end{Bmatrix}$	$\begin{Bmatrix} 0.591 \\ -0.737 \\ 0.328 \end{Bmatrix}$
Assumed modal damping ratio [%]	7%	7%	7%

Table 4.2: *Properties of the analysed reference three-storey frame [92].*

Then, after the reference 3-storey frame, the focus goes to the analyses and results that can be achieved by adopting a realistic ten-storey RC frame, taken from the work of Villaverde and Koyama [123]. This shear-type frame is subjected to each single earthquake excitation from the set of strong ground motions reported in Table 4.1 and synthetic seismic response signals are calculated before the subsequent identification process. Structural and modal dynamic characteristics of this 10-DoF frame are reported in Table 4.3 (mode shapes are not reported for compactness purposes; however, they may be found in [82]).

Floor	1	2	3	4	5	6	7	8	9	10
Stiffness $\times 10^3$ [kN/m]	62.47	59.26	56.14	53.02	49.91	46.79	43.70	40.55	37.43	34.31
Mass $\times 10^3$ [kg]	179	170	161	152	143	134	125	116	107	98
Mode	1	2	3	4	5	6	7	8	9	10
Natural frequency [Hz]	0.500	1.326	2.151	2.934	3.653	4.292	4.836	5.272	5.590	5.787
Modal damping ratio [%]	2.50%	3.50%	5.16%	6.83%	8.40%	9.81%	11.01%	11.98%	12.69%	13.13%

Table 4.3: *Properties of the analysed realistic ten-storey frame [123].*

The use of this 10-DoFs frame represents a rather challenging case for the modal identification, since the building is characterized by very close modes (the ten natural frequencies are contained within a 5 Hz interval). As concerning to the damping modelling, Rayleigh proportional damping (i.e. a linear combination of stiffness and mass matrices) has been adopted, by setting $\zeta_1 = 2.5\%$ and $\zeta_2 = 3.5\%$ for the first two modes, respectively. In this way, the modal damping ratios become rather high, in terms of identification challenge for the present OMA algorithms, raising up to values of ζ_i at around 10% for half of the modes of vibration.

4.2 Results from synthetic output-only modal dynamic identification

4.2.1 Analyses and results with a reference three-storey frame

By taking as base excitation the single instances from the set of ten selected earthquake recordings presented in Section 4.1 (Table 4.1), modal dynamic identification analyses have been performed with the rFDD algorithm (Chapter 3), in order to identify all strong ground motion modal parameters.

The rFDD identification method adopts constant time series lengths of 400 s and a 0.0025 Hz frequency resolution, by applying the method outlined in Section 3.4.2, which allows to increase the frequency resolution of the recordings, despite for the shortness of the seismic histories.

As concerning to the present rFDD method, the following parameters have been adopted for the performed analyses:

- Butterworth low-pass filtering, order 8, cutting frequency 15 Hz, applied to the earthquake-induced structural response signals (input channels for the rFDD algorithm);
- No decimation, decimation of order 2 and of order 5 of the response signals, as a function of the frequency sampling of the recordings, i.e. 50 Hz, 100 Hz and 200 Hz, respectively;
- Integrated PSD matrix computation through both Welch's Modified Periodogram, generally set with 1024-points Hanning smoothing windows and 66.7% overlapping (2048-points Hanning smoothing windows when no decimation is applied), and Wiener-Khinchin method, set with a de-trended biased correlation matrix (see [91] for more details).

As concerning to the achievable rFDD outcomes, the three modal peaks are detectable from the frequency lines on the first SV. Also, modal peaks are repeated on the remaining SVs, which is a clear index of existence of the related mode of vibration. Anyway, MAC and MPC indexes may be simultaneously adopted towards modal peak selection and validation, as extensively outlined in [91, 92].

Thus, by the strategies and settings reported above, complete synthetic output-only analyses with the rFDD method have been performed. A synopsis from all the achieved results is reported in Fig. 4.1, where the estimates in terms of absolute deviations of rFDD identified natural frequencies and modal damping ratios and achieved MAC indexes for the

estimated mode shapes are depicted. Estimates are reported in terms of absolute deviations of estimated natural frequencies Δf and modal damping ratios $\Delta\zeta$ from the target parameters, and of achieved MAC indexes for the estimated mode shapes on the target ones, calculated as follows:

$$\Delta f = \frac{|f_{est} - f_{targ}|}{f_{targ}} \tag{4.1a}$$

$$\Delta\zeta = \frac{|\zeta_{est} - \zeta_{targ}|}{\zeta_{targ}} \tag{4.1b}$$

$$\mathrm{MAC} = \frac{|\boldsymbol{\phi}_{est}^{\mathrm{H}}\boldsymbol{\phi}_{targ}|^2}{|\boldsymbol{\phi}_{est}^{\mathrm{H}}\boldsymbol{\phi}_{est}|\,|\boldsymbol{\phi}_{targ}^{\mathrm{H}}\boldsymbol{\phi}_{targ}|} \tag{4.1c}$$

The rFDD estimated frequencies show deviations that are always below 5%, except for the last modes of the NO, LP and TA earthquake cases (Table 4.1), where deviations increase up to 9%. The estimated modal damping ratios display very low deviations, at around 10% as a mean. Then, the frequency and damping estimates from these analysed rFDD cases show to be very close to the target values. Then, also MAC values are always higher than 0.91, for all the modes, by confirming the goodness of the achieved results.

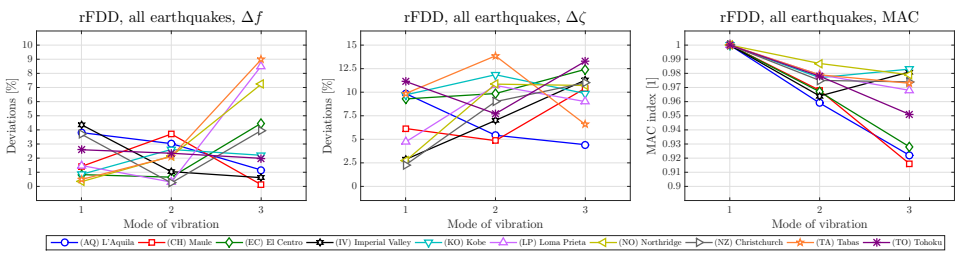

Figure 4.1: *Deviations of estimated natural frequencies and modal damping ratios, and MAC indexes, three-storey frame, synthetic response signals, rFDD algorithm, complete considered earthquake dataset.*

Then, global results on the achieved modal estimates are further summarized in Fig. 4.2, where the absolute deviations of the estimated natural frequencies and modal damping ratios, and the MAC indexes are represented, in terms of suitably-designed dispersion diagrams [97]. The synthetic estimates for the adopted three-storey frame have been condensed all together, by displaying the minimum, the mean and the maximum (absolute) deviations, in blue, black and red coloured lines and markers, respectively. Then, the normalized truncated Gaussian Probability Density Functions (PDF) related to the dispersion of the estimates have

been depicted for each mode, jointly with an indication of the standard deviation σ of the estimated values. In the present case, frequency and modal damping ratio deviations shall turn out strictly positive (since absolute percentage deviations are adopted), while MAC indexes shall vary between 0 and 1. By taking into account such boundaries, truncated Gaussians are fitted on the achieved estimates, for each examined case. A demonstration of the possible use of truncated Gaussians is further going to be reported in Chapter 5, where the performed analysis with the FEMA P695 earthquake database is going to be addressed.

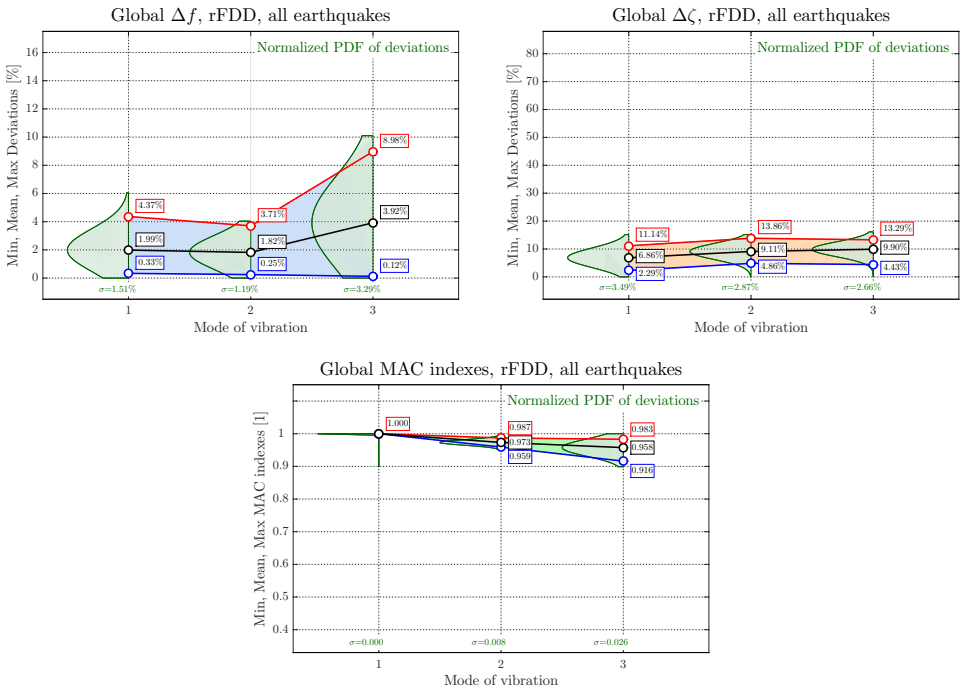

Figure 4.2: *Dispersion diagrams for the deviations of estimated natural frequencies and modal damping ratios, and for the MAC indexes, three-storey frame, synthetic response signals, rFDD algorithm, complete considered earthquake dataset. Minimum, mean and maximum values, and standard deviations are indicated.*

These truncated Gaussians represent the probability of appearance of a certain deviation, as associated to each estimate, between the minimum and the maximum value, and are centred on the mean value. As it is possible to be appreciated, the maximum deviations are always on the Gaussian tails, while the minimum deviations lay in the Gaussian center. This confirms the goodness of the achieved rFDD modal identification estimates.

Finally, the achieved results are also synoptically reported in statistical

form in Fig. 4.3, through appropriate *boxplots*. In these representations, each boxplot relates to the natural frequencies, modal damping ratios and MAC values estimated from the performed analyses. In each boxplot the inner rectangular box represents the central 50% of the identified parameters, while the centred line indicates their median. Then, the right and left boundary segments depict the 25% and 75% quantiles of the related statistical distributions. Finally, the vertical through-plot dashed green lines mark the known targeted modal parameters for the identification procedure.

The presented boxplots confirm again the goodness of the achieved rFDD results. Natural frequency estimates show to substantially catch the expected target values. Also, MAC indexes reveal very good mode shape estimates, even for the last modes of vibration. Finally, modal damping ratios display again very good estimates, by showing a rather contained dispersion.

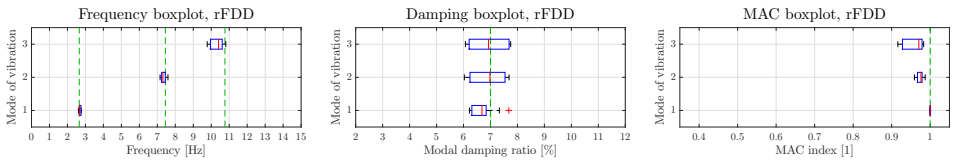

Figure 4.3: *Boxplot diagrams for estimated natural frequencies, modal damping ratios and MAC indexes, three-storey frame, synthetic response signals, rFDD algorithm, complete considered earthquake dataset.*

4.2.2 Further synthetic identification analyses with a realistic ten-storey frame

In the present section, the focus goes to the analyses and results that can be achieved by adopting the realistic ten-storey RC frame introduced in Section 4.1 (see Table 4.3). The adopted settings for the rFDD identification procedure are the same as those employed before, except than for the Butterworth low-pass filtering, whose cutting frequency now has been taken equal to 7.5 Hz.

Thus, by adopting the present realistic ten-storey frame, synthetic output-only analyses with the present rFDD algorithm have been performed. As it was previously done in Section 4.2.1, a synopsis from all the achieved results is depicted in Fig. 4.4. Again, the absolute deviations of the rFDD identified natural frequencies and modal damping ratios and the achieved MAC indexes are reported in the following representations.

The estimated frequencies from rFDD show deviations that are always below 7%, except for the fifth and sixth modes of the IV earthquake case

(Table 4.1), where deviations increase up to 8.11%. The most demanding seismic excitations turn out to be the EC, IV and NO cases.

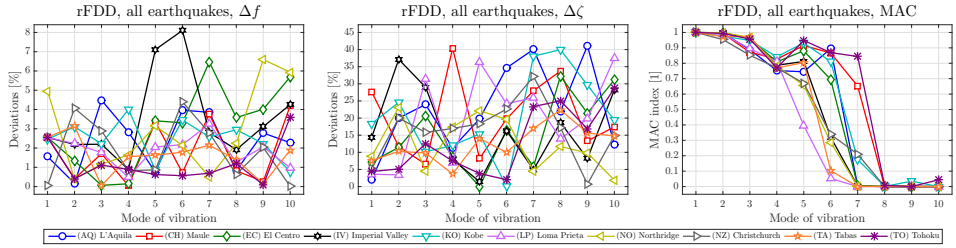

Figure 4.4: *Deviations of estimated natural frequencies and modal damping ratios, and MAC indexes, ten-storey frame, synthetic response signals, rFDD algorithm, complete considered earthquake dataset.*

The rFDD estimated modal damping ratios display good (low) deviations, at around 20%. Maximum deviations show to be lower than 42%, for all the cases. Deviations show to be higher than for the three-storey frame; however, it should be recalled that really demanding heavy-damping identification conditions have been challenged here, with ζ_i up to 13%. As it was seen with the previous 3-DoF case, rFDD frequency and damping estimates for the present 10-DOF case show to be very close to the target values.

MAC values are always higher than 0.70 for the first five modes, except for the fifth mode of the LP, NO and NZ cases, where they go down to 0.396, 0.657 and 0.670, respectively. Anyway, especially for the lowest MAC values, they show to be rather isolate instances. For the remaining modes, MACs show to be acceptable for most cases, until for the seventh mode, after which MAC values go to rather unacceptable values.

Thus, in terms of strong ground motion modal parameters at heavy damping, rFDD shows to be very consistent, for the present MDoF realistic case, at the present stage of development and implementation.

As before, Fig. 4.5 summarizes the global results on the achieved modal estimates for the ten-storey frame, where the absolute deviations of the estimated natural frequencies and modal damping ratios, and the MAC indexes are represented in terms of appropriate dispersion diagrams. The truncated Gaussian distributions show once again that maximum deviations lay always on the Gaussian tails, while minimum deviations are located near the Gaussian centres. This confirms the goodness of the achieved rFDD modal identification estimates, despite for the rather challenging scenario. In fact, it is clearly visible that rFDD Gaussians are very narrow, especially as concerning to the natural frequencies and the modal damping ratios. This is again an indication of the effective performance

of the rFDD algorithm in the present context and implementation.

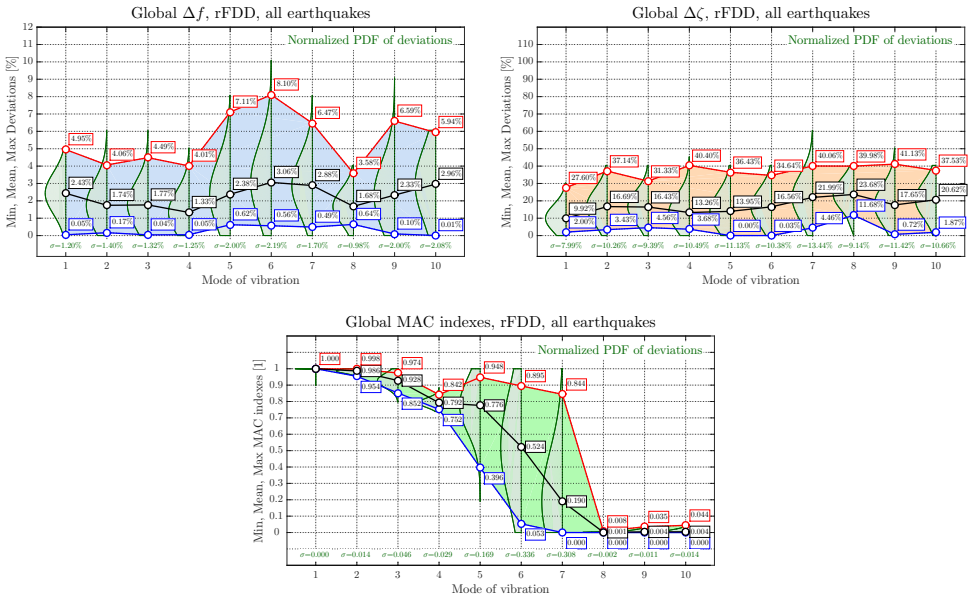

Figure 4.5: *Dispersion diagrams for the deviations of estimated natural frequencies and modal damping ratios, and for the MAC indexes, ten-storey frame, synthetic response signals, rFDD algorithm, complete considered earthquake dataset. Minimum, mean and maximum values, and standard deviations are indicated.*

Finally, the results achieved from the realistic ten-storey frame are also synoptically reported in Fig. 4.6, in terms of statistical boxplots. Here, natural frequencies, modal damping ratios and MAC values estimated from the performed synthetic analyses are represented.

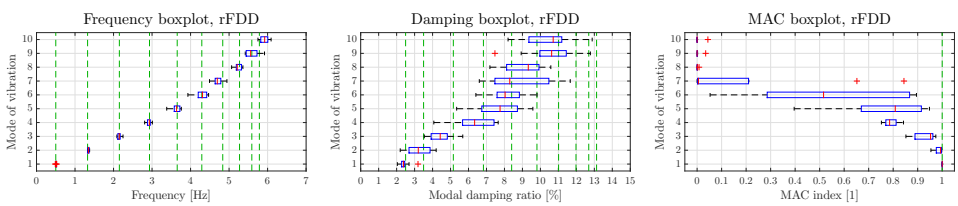

Figure 4.6: *Boxplot diagrams for estimated natural frequencies, modal damping ratios and MAC indexes, ten-storey frame, synthetic response signals, rFDD algorithm, complete considered earthquake dataset.*

The proposed boxplots confirm again the goodness of the rFDD achieved results. Despite for the very high modal damping ratios reached by the present case, in terms of rFDD identification challenge, modal

parameter estimates show to be very close to the target values. Again, natural frequency estimates turn out very close to the expected target values. Also MAC indexes reveal very good mode shape estimates until the fifth mode of vibration, i.e. a more than adequate number of modes, in order to describe the dynamical behaviour of the structure, specifically under seismic excitation. Finally, also modal damping ratios display very good estimates, by showing rather contained dispersions for all the modes.

4.3 Extensive validation with the FEMA P695 earthquake database

4.3.1 Adopted FEMA P695 seismic database

Towards reaching a conclusive validation of the effectiveness of the present rFDD algorithm, specifically for the targeted context of earthquake-induced structural responses (accelerations adopted as input channels for the identification process) and simultaneous heavy damping, the codified FEMA P695 seimic database [37] has been considered as a source for the base-excitation instances of structural input.

This database was developed by the US Federal Emergency Management Agency (FEMA) as a selection of ground motion records, towards the collapse assessment of structures using nonlinear dynamic analysis methods [37]. Nowadays, its use is widely established in the earthquake engineering research field, whether for structural analysis, dynamics or identification purposes.

The ground motion record database includes a set of ground motions recorded at sites located at a distance greater than or equal to 10 km from fault rupture, referred to as "Far-Field" record set (22 NS and 22 WE individual components for 22 seismic events), recordings adopted for the present identification analysis, and a set of ground motions recorded at sites laying less than 10 km from fault rupture, referred to as "Near-Field" record set (28 NS and 28 WE individual components for 28 seismic events).

Seismic records in the database have been selected according to the following criteria [37]:

- *Source magnitude:* ground motions with a magnitude M larger than 6.5;
- *Source type:* ground motions from earthquakes with either strike-slip or reverse (thrust) sources;
- *Site conditions:* ground motions recorded on either soft rock (Site Class C) or stiff soil (Site Class D) sites;
- *Site-source:* the source-to-site distance was taken as the average of

Campbell and Joyner-Boore fault distances provided in the PEER NGA database;

- *Number of records per event:* to avoid potential event-based bias in record sets, no more than two records were taken from any one earthquake for a record set;
- *Strongest ground motion records:* PGA and PGV greater than 0.2 g and 15 cm/s, respectively;
- *Strong-motion instrument capability:* ability to record long-period vibrations is required;
- *Strong-motion instrument location:* only instruments located in a free-field location or on a ground floor of a small building have been used.

Subset	*EQ ID*	*Earthquake*						*Station Name - Owner*
		M	PGA [g]	*Year*	*Name*	*Dur.* [s]	f_s [Hz]	
	12011	6.7	0.52	1994	Northridge, USA	29.99	100	Bev. Hills, Mulhol - USC
	12012	6.7	0.48	1994	Northridge, USA	19.99	100	Canyon Country - USC
	12041	7.1	0.82	1999	Duzce, Turkey	55.90	100	Bolu - ERD
	12052	7.1	0.34	1999	Hector Mine, USA	45.31	100	Hector, SCSN
	12061	6.5	0.35	1979	Imperial Valley, USA	99.92	100	Delta - UNAMUCSD
(1/2)	12062	6.5	0.38	1979	Imperial Valley, USA	39.035	200	El Centro Arr. #11 - USGS
	12071	6.9	0.51	1995	Kobe, Japan	40.96	100	Nishi-Akashi - CUE
	12072	6.9	0.24	1995	Kobe, Japan	40.96	100	Shin-Osaka - CUE
	12081	7.5	0.36	1999	Kocaeli, Turkey	27.085	200	Duzce - ERD
	12082	7.5	0.22	1999	Kocaeli, Turkey	30.00	200	Arcelik - KOERI
	12091	7.3	0.24	1992	Landers, USA	44.00	50	Yermo Fire Stat. - CDMG
	12092	7.3	0.42	1992	Landers, USA	27.965	300	Coolwater - SCE
	12101	6.9	0.53	1989	Loma Prieta, USA	39.955	200	Capitola - CDMG
	12102	6.9	0.56	1989	Loma Prieta, USA	39.945	200	Gilroy Array #3 - CDMG
	12111	7.4	0.51	1990	Manjil, Iran	53.52	50	Abbar - BHRC
	12121	6.5	0.36	1987	Superstition Hills, USA	40.00	200	El Centro Imp. Co. - CDMG
(2/2)	12122	6.5	0.45	1987	Superstition Hills, USA	22.30	100	Poe Road (temp) - USGS
	12132	7.0	0.45	1992	Cape Mendocino, USA	36.00	50	Rio Dell Overpass - CDMG
	12141	7.6	0.44	1999	Chi-Chi, Taiwan	90.00	200	CHY101 - CWB
	12142	7.6	0.51	1999	Chi-Chi, Taiwan	90.00	200	TCU045 - CWB
	12151	6.6	0.21	1971	San Fernando, USA	28.00	100	LA Hollywood Stor - CDMG
	12171	6.5	0.35	1976	Friuli, Italy	36.345	200	Tolmezzo

Table 4.4: *Main characteristics of the 22 Far-Field set of earthquakes, FEMA P695 [37]. Subsets (1/2) and (2/2) refer to the graphs later reported in Section 4.3.2.*

Table 4.4 summarizes the main characteristics of the adopted set of Far-Field seismic records (44 recordings) considered as base excitations for the present identification analyses. PGA is referred here as the maximum value registered among the NS and WE components, for each considered earthquake instance. These signals have been used as base excitation for the calculation of the linear structural response of chosen shear-type frame

structures (Section 4.3.2). The subdivision of seismic signals in Table 4.4 into two further subsets (indicated as (1/2) and (2/2)) becomes necessary, at this stage, to better appreciate the outcomes of the forthcoming investigation and their graphical representation. Thus, such partition refers just to achieving a clearer reading of the graphs that are going to be reported in following Section 4.3.2.

4.3.2 Numerical rFDD identification results

A series of multi-storey shear-type frames have been analysed, specifically a two-, a three- and a six-storey shear-type frame. The structural features of these three frames are resumed in Table 4.5. The undamped modal parameters of the frames have been determined first, via direct modal analysis, before starting the identification process, to constitute then the benchmark reference to be targeted by the present rFDD modal identification procedure.

Frame	*Floor*	1	2	3	4	5	6
Two-storey	*Stiffness* $\times 10^3$ [kN/m]	130	124				
	Mass $\times 10^3$ [kg]	70	70				
Three-storey	*Stiffness* $\times 10^3$ [kN/m]	202.83	202.83	202.83			
	Mass $\times 10^3$ [kg]	144	144	144			
Six-storey	*Stiffness* $\times 10^3$ [kN/m]	304.25	283.96	263.68	243.40	223.11	202.83
	Mass $\times 10^3$ [kg]	144	144	144	144	144	144

Table 4.5: *Structural properties of the adopted two-, three- and six-storey shear-type frames (adopted also in [92]).*

In the present work, the modal damping ratios of the frames have been set as constant for all their structural modes. Specifically, within the present section, the following values of modal damping ratios have been assumed: $\zeta_i = 5\%$ for the two-storey frame, $\zeta_i = 3\%$ for the three-storey frame and $\zeta_i = 2\%$ for the six-storey frame. The modal features, namely natural frequencies and modal damping ratios, of the three adopted frames, are reported in Table 4.6.

Within following Section 4.3.3, instead, only the six-storey frame is going to be considered for further validation, though with a very high value of modal damping ratio, i.e. $\zeta_i = 10\%$, for all the six modes of the frame.

For the sake of representation and discussion, only selected and synoptic identification results from the whole bulge of generated identification outcomes are reported and commented here, in view of deciphering global identification trends.

Frame	*Mode*	1	2	3	4	5	6
Two-storey	*Natural frequency* [Hz]	4.211	10.91				
	Modal damping ratio [%]	5%	5%				
Three-storey	*Natural frequency* [Hz]	2.658	7.448	10.76			
	Modal damping ratio [%]	3%	3%	3%			
Six-storey	*Natural frequency* [Hz]	1.667	4.674	7.451	9.793	11.59	13.09
	Modal damping ratio [%]	2%	2%	2%	2%	2%	2%

Table 4.6: *Modal properties of the adopted two-, three- and six-storey shear-type frames (adopted also in [92]).*

As said, the numerical input to be fed to the rFDD output-only identification algorithm is constituted by synthetic earthquake-induced response signals, generated numerically prior to dynamic identification. The above presented $22 + 22 = 44$ Far-Field seismic records (Table 4.4) have been adopted as base excitation instances for the structural response calculation of the considered frame structures, through standard time integration (Newmark's average acceleration method) [27]. Then, the input channels for the rFDD identification arise from the achieved simulated structural responses (all storey accelerations are considered as input channels).

Although the duration and sampling frequency of each seismic record vary, the rFDD dynamic identification analyses have been performed with the same time series lengths and frequency resolutions, as reported in Table 4.7 (see Section 3.4.2 in Chapter 3 and [92] for more details).

Table 4.7: *Processing parameters for the adopted seismic response signals and considered frame structures.*

Frame	*Length of time series* t [s]	*Sampling frequency* f_s [Hz]	*Adopted frequency resolution* Δf [Hz]
Two-storey	400	$50 - 300$	0.0025
Three-storey	600	$50 - 300$	0.00167
Six-storey	1000	$50 - 300$	0.001

Despite for the non-stationary seismic input characteristics and the concurrent heavy damping condition (in terms of identification challenge), all structural modes have been excited enough to be consistently identified all. Fundamental support has been especially brought about by the developed integrated PSD matrix computation (Section 3.2.3), implementing simultaneously both Wiener-Khinchin and Welch's modified periodogram methods, and by all the remaining rFDD procedures outlined in Chapter 3.

Detailed syntheses from all the achieved results are depicted in Figs. 4.7-4.9, where the estimates in terms of absolute deviations of rFDD identified natural frequencies and modal damping ratios, and achieved

MAC indexes for the estimated mode shapes are reported. As referred to above, for the sake of representation, the adopted FEMA P695 "Far Field" set has been subdivided into two further subsets (indicated as (1/2) and (2/2)), for each of the spatial NS and WE components of the earthquake recordings. In the present section, a total of $(22 + 22) \times 3 = 132$ cases with the Far-Field FEMA P695 database (both 44 NS and WE components) and the three frames has been analysed.

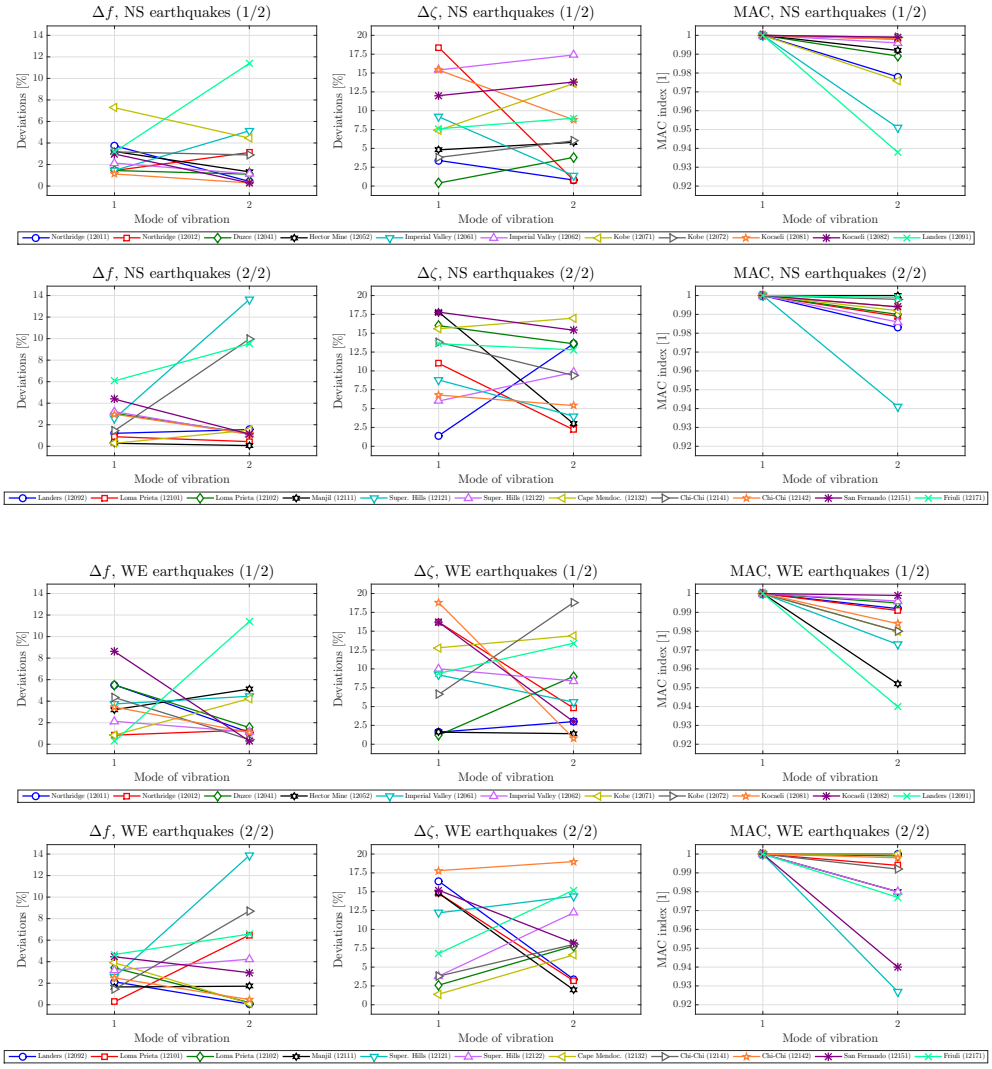

Figure 4.7: *Deviations of estimated natural frequencies and modal damping ratios, and MAC indexes, two-storey frame, $\zeta_i = 5\%$, Far-Field FEMA P695 database, NS and WE components. Results from the adopted (1/2) and (2/2) subsets of the Far-Field set are individually reported, for each of the 22 NS and 22 WE components (Table 4.4).*

Estimates are reported in terms of absolute deviations of estimated natural frequencies Δf and of estimated modal damping ratios $\Delta\zeta$ from the target parameters, and of achieved MAC indexes for the estimated mode shapes on the target ones (see Eqs. 4.1a-4.1c).

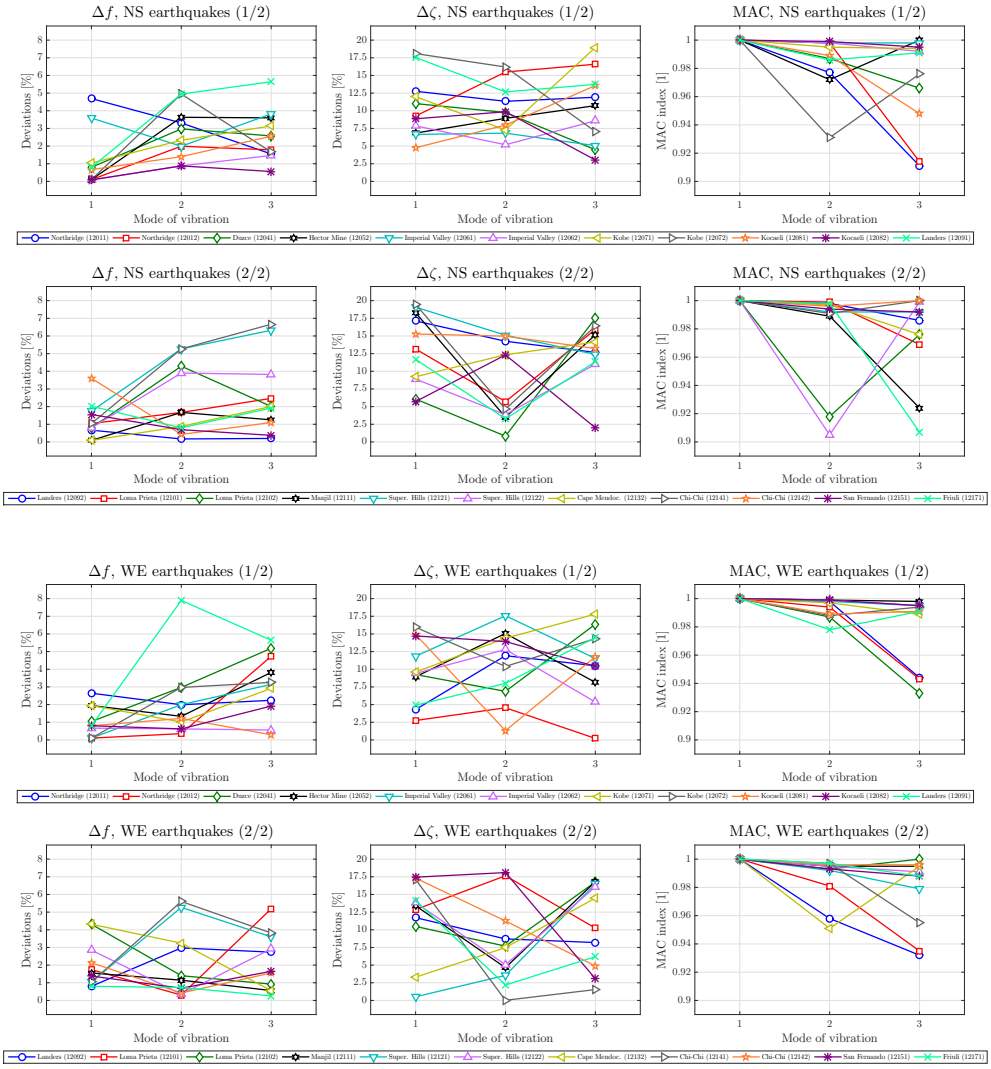

Figure 4.8: *Deviations of estimated natural frequencies and modal damping ratios, and MAC indexes, three-storey frame, $\zeta_i = 3\%$, Far-Field FEMA P695 database, NS and WE components. Results from the adopted (1/2) and (2/2) subsets of the Far-Field set are individually reported, for each of the 22 NS and 22 WE components (Table 4.4).*

Maximum deviations of the estimated frequencies turn out below 10%, 5% and 10% for the first mode of vibration, for the two-, three- and six-

storey frames, respectively. Also for the subsequent modes, maxima of deviations are reasonably contained, showing peaks of 13.86%, 7.9% and 16.24% for the second, second and sixth modes of vibration of the two-, three- and six-storey frames. In general, the larger deviations on the last modes arise from Landers a) (12091), Manjil (12111) and Cape Mendocino (12132) earthquakes, characterized by a lower frequency sampling of 50 Hz (Table 4.4). Also Kocaeli b) (12082), Superstition Hills b) (12122) and Chi-Chi a) (12141) earthquakes lead to larger deviations, with respect to those achieved from the other seismic records. This is directly related to the exhibited stronger non-stationarity of such earthquake signals.

However, these larger deviations appear only as isolated instances, among the remaining ones. In fact, deviations have shown to be very limited, by proving that these slightly higher deviations rather behave as outliers, as compared to the values of the mean deviations. In general terms, as it could be expected, deviations increase from the first to the last modes of vibration, for all the three considered frames and selected forty-four earthquake FEMA P695 "Far-Field" excitations. Further, at increasing modal damping values, modal identification becomes much challenging, giving rise to higher deviations, with respect to the identification results achieved for the cases with lower damping.

Modal damping ratio deviations show to be always less than 20%, for all the analysed cases. In general terms, this modal parameter displays well-distributed estimates, with respect to those achieved for the natural frequencies, in the sense that it reveals to be less sensitive to the variation of the adopted frame and considered earthquake in the identification analysis. This is due to the achieved possibility of always identifying correctly the spectral bells, namely by selecting the correct SVs instances with an appropriate MAC filtering, in the surroundings of the selected modal frequency [96].

Finally, a very good agreement between estimated and targeted mode shapes is demonstrated by the achieved MAC indexes. MACs are always unitary for the first mode of vibration, for all the considered cases. For the second and third modes of vibration (for the three- and six-storey frames only), MACs show to be always higher than 0.9. For the six-storey frame, the fourth mode displays MACs always higher than 0.8. Only the fifth and sixth modes start to be less accurate, but anyway acceptable in engineering terms, by referring to their mean values. The worse cases, i.e. for the fifth and sixth modes of the six-storey frame, are related again to Kocaeli b) (12082), Superstition Hills b) (12122) and Chi-Chi a) (12141) earthquakes, by confirming their critical features, as concerning to the adoption of the present rFDD approach with seismic response input, at raising structural damping.

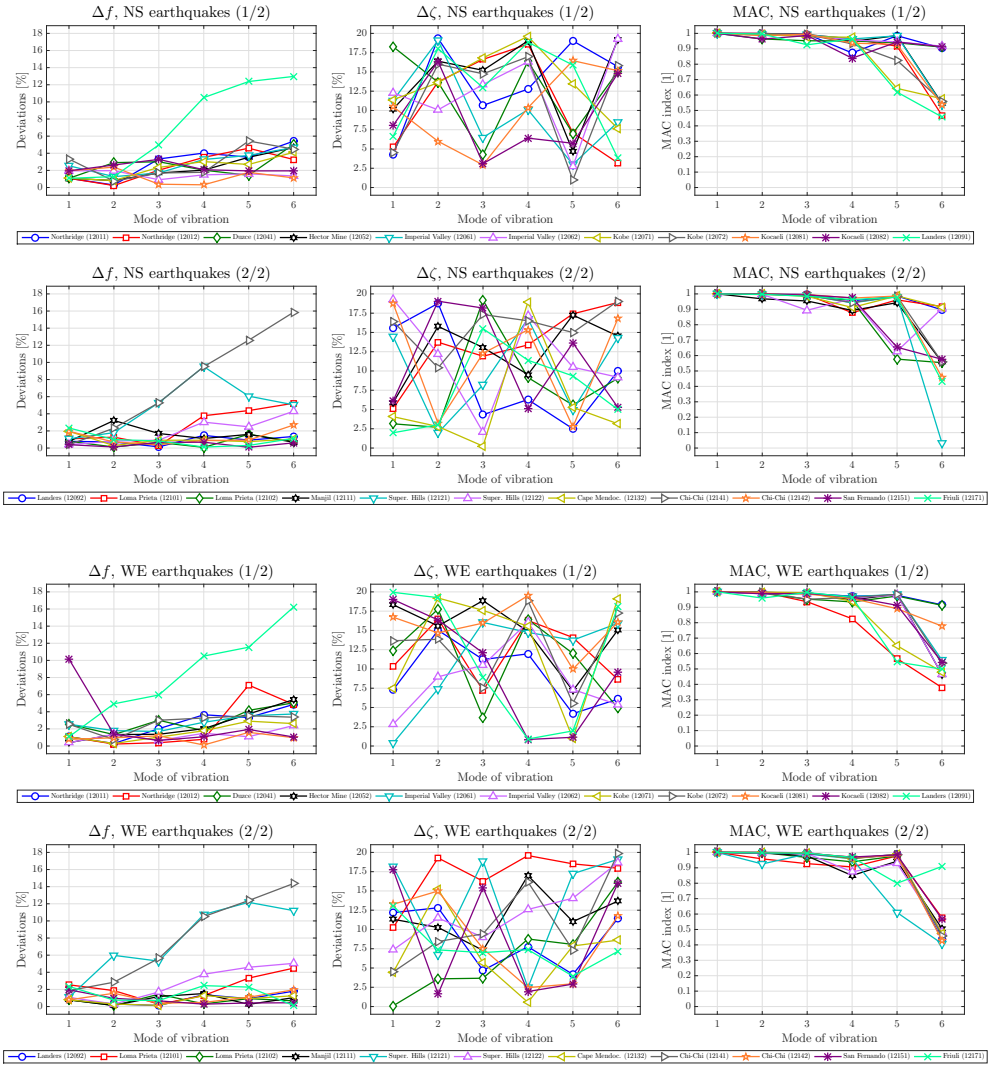

Figure 4.9: *Deviations of estimated natural frequencies and modal damping ratios, and MAC indexes, six-storey frame, $\zeta_i = 2\%$, Far-Field FEMA P695 database, NS and WE components. Results from the adopted (1/2) and (2/2) subsets of the Far-Field set are individually reported, for each of the 22 NS and 22 WE components (Table 4.4).*

Additionally, a summary of all the analysed cases is reported in Figs. 4.11-4.14, in terms of suitably-developed dispersion diagrams, as it was previously done in Sections 4.2.1 and 4.2.2. The estimates for the adopted two-, three- and six-storey frames have been condensed, by displaying the minimum, the mean and the maximum (absolute) deviations, in blue, black and red coloured lines and markers, respectively. The absolute deviations are represented on the y-axis, for each adopted frame, as a function of the considered mode of vibration, which is depicted on

the x-axis. The achieved estimates are reported in three groups for each frame, i.e. by summarizing the results from the North-South (NS), from the West-East (WE) and from the full set of all the analysed cases (both spatial components).

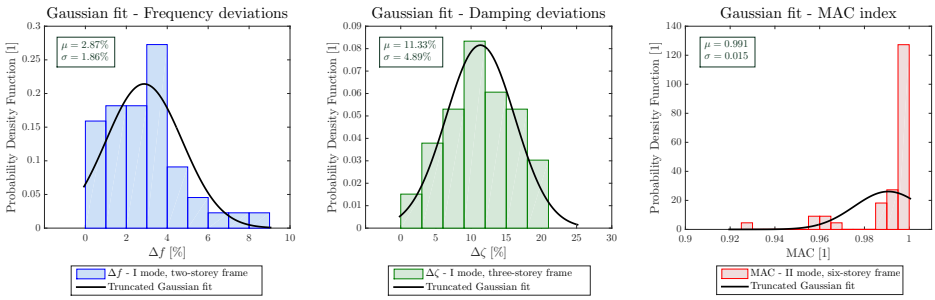

Figure 4.10: *Histograms and truncated Gaussian fit of frequency and damping deviations and of MAC indexes for three sample cases, two-, three- and six-storey frames, Far-Field FEMA P695 database, NS and WE components. Mean value μ and standard deviation σ are reported. MAC index is reported for the II mode since estimates on the I mode do not show significant dispersion from value 1.*

Then, the normalized truncated Gaussian Probability Density Functions (PDF) related to the dispersion of the estimation results for each mode have been depicted, jointly with an indication of the standard deviation σ of the estimated values. The truncated Gaussian PDF is the probability distribution of a normally-distributed variable whose value is bounded either from below or above (or from both) [58]. In the present case, frequency and damping ratio deviations must be strictly positive (since absolute percentage deviations are adopted), while MAC indexes shall vary between 0 and 1. By taking into account these boundaries, truncated Gaussians are fitted on the achieved estimates, for each examined case. The truncated Gaussians showed to be a good approximation of the estimated deviations, as it can be seen in Fig. 4.10, where three fitting examples are reported. In particular, a Gaussian fitting over the histogram of the Δf (I mode) of the $\Delta\zeta$ (I mode) and of the MAC indexes (II mode, since for the I mode all MACs are unitary) are reported, for the two-storey, three-storey and six-storey frame, respectively. Also, the advantage in using the Gaussian distribution is that the PDF exhibits the same mean value (μ) and standard deviation (σ) of the achieved data.

These truncated Gaussians represent the probability of appearing of a certain deviation associated to each estimate between the maximum and the minimum value, and are centred on the mean value. As it is possible to be appreciated, the maximum deviations are always on the Gaussian tails, while the minimum deviations lay in the center. This confirms the goodness of the achieved rFDD estimates.

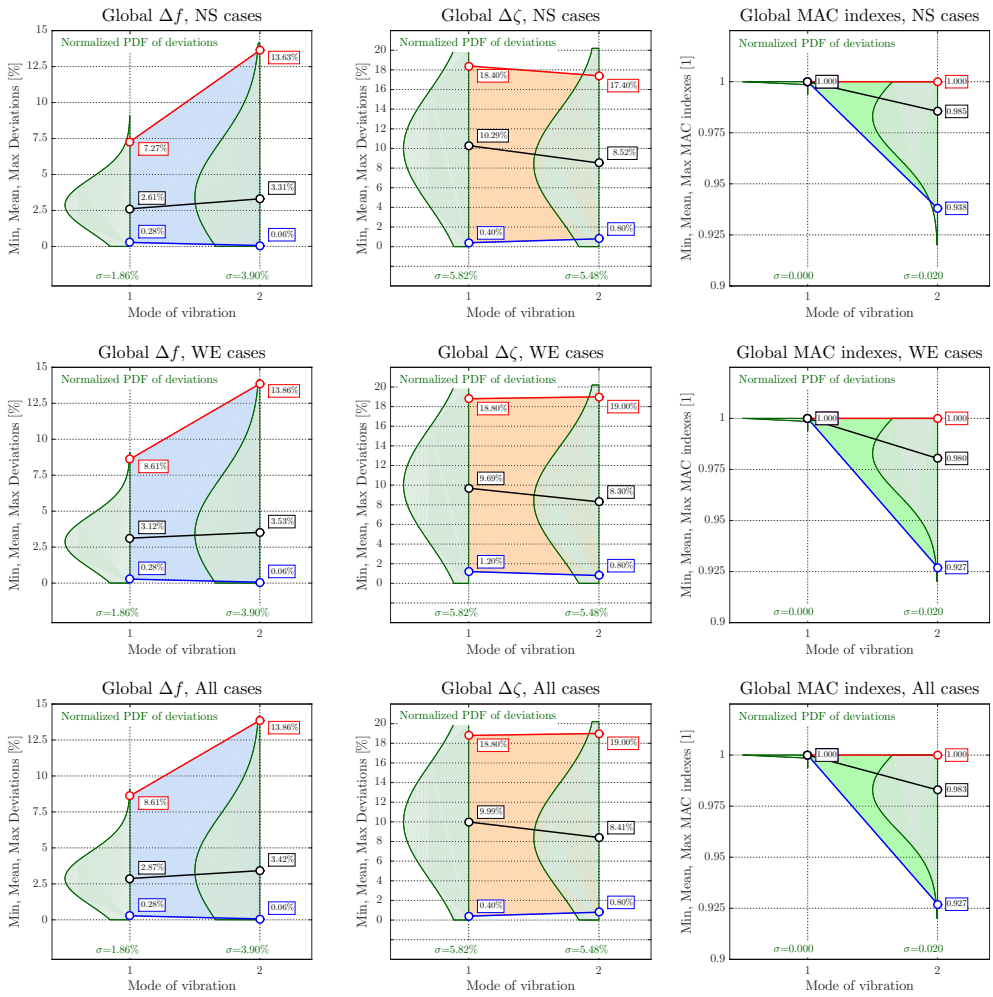

Figure 4.11: *Dispersion diagrams for the deviations of estimated natural frequencies and modal damping ratios, and for the MAC indexes, two-storey frame, $\zeta_i = 5\%$, Far-Field FEMA P695 database, NS component (1st row), WE component (2nd row), NS and WE components (3rd row). Minimum, mean and maximum values, and standard deviations are indicated.*

By looking in detail to Figs. 4.11-4.14, it is possible to see that mean values of the frequency deviation are always less than 4.5%. For the two-storey cases, no notable differences may be appreciated among the NS and WE cases. Then, as expected (and previously recorded also in Figs. 4.7-4.9), mean deviations increase from the first to the last modes, for all the cases. This is true also at increasing damping values, since identification becomes more challenging, giving rise to higher deviations with respect to the low-damped cases. This can be especially observed from the frequency deviations achievable from the two-storey frame, characterized by $\zeta_i = 5\%$

for all the modes. In fact, these become the higher deviations (especially by looking at the mean values) which can be observed from the analysis of the first two modes of vibration. By looking at the remaining frames and analyses, the deviations gradually decrease for the three- and six-storey frames, characterized by $\zeta_i = 3\%$ and $\zeta_i = 2\%$ for all the modes, respectively.

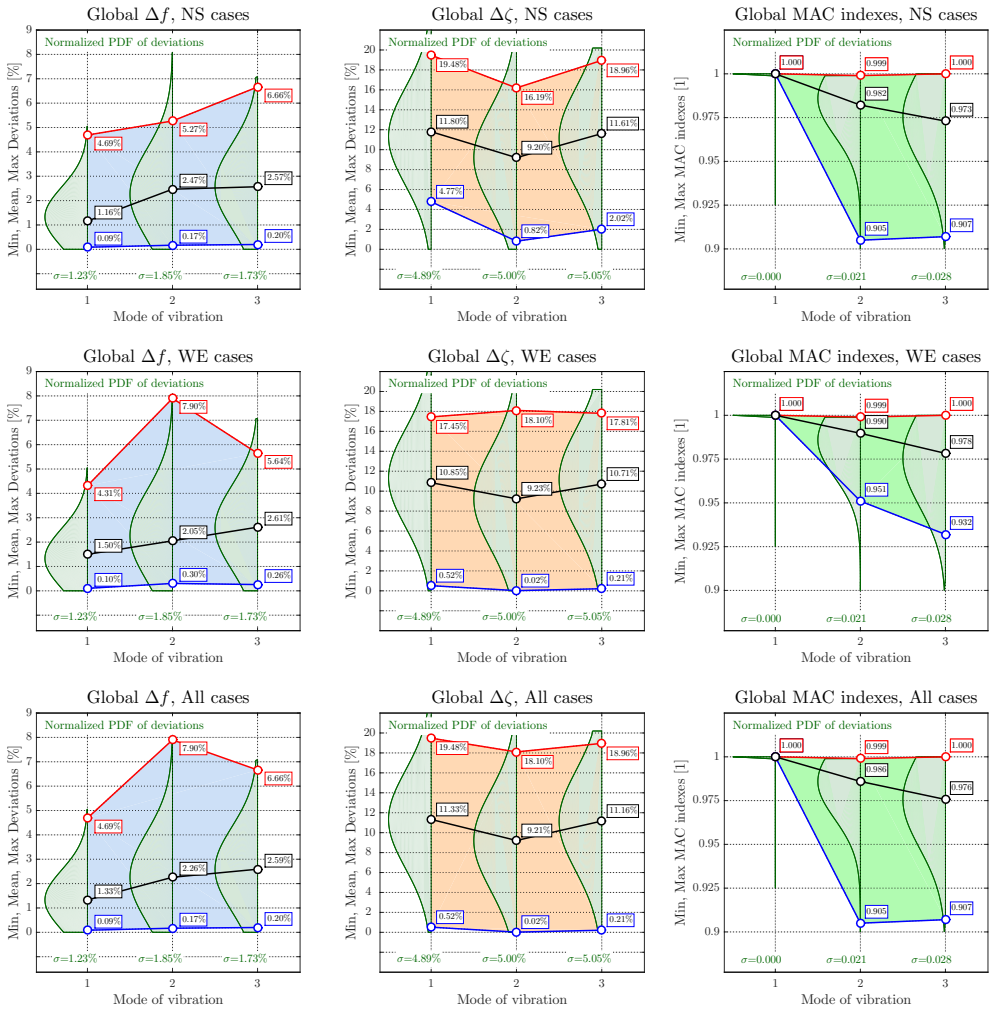

Figure 4.12: *Dispersion diagrams for the deviations of estimated natural frequencies and modal damping ratios, and for the MAC indexes, three-storey frame, $\zeta_i = 3\%$, Far-Field FEMA P695 database, NS component (1st row), WE component (2nd row), NS and WE components (3rd row). Minimum, mean and maximum values, and standard deviations are indicated.*

As concerning to the achieved modal damping ratios, mean values show to be very targeted, with deviations around 10% for all the cases. In partic-

ular, the two-storey frame displays accurate results, despite for the heavy damping for structural identification ($\zeta_i = 5\%$). The achieved estimates show well-distributed cases with respect to the natural frequencies, due to the possibility of always identifying correctly the spectral bells.

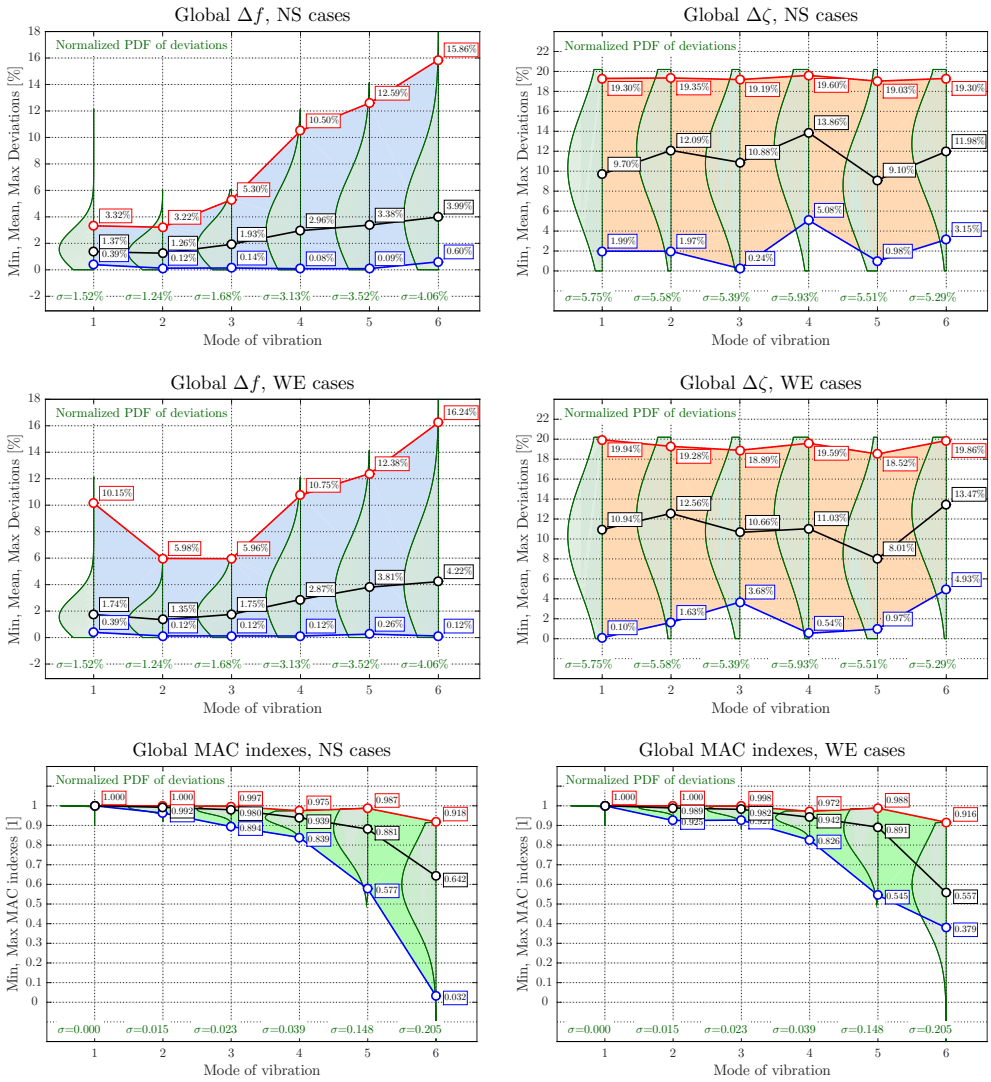

Figure 4.13: *Dispersion diagrams for the deviations of estimated natural frequencies and modal damping ratios, and for the MAC indexes, six-storey frame, $\zeta_i = 2\%$, Far-Field FEMA P695 database, NS component (1st column), WE component (2nd column). Minimum, mean and maximum values, and standard deviations are indicated.*

Finally, about the achieved MAC indexes, the combined use of different MAC indexes (see Section 3.4.3) also helps with the modal identification,

in order to detect the correct modal peaks and to discern between physical peaks and complex spurious peaks. In fact, MACs display the achieved effective estimation of the mode shapes, especially on the first modes of vibration. For the six-storey frame, only the fifth and sixth modes start to be less accurate, but anyway acceptable in engineering terms, with mean values that turn out to be equal to 0.886 and 0.600.

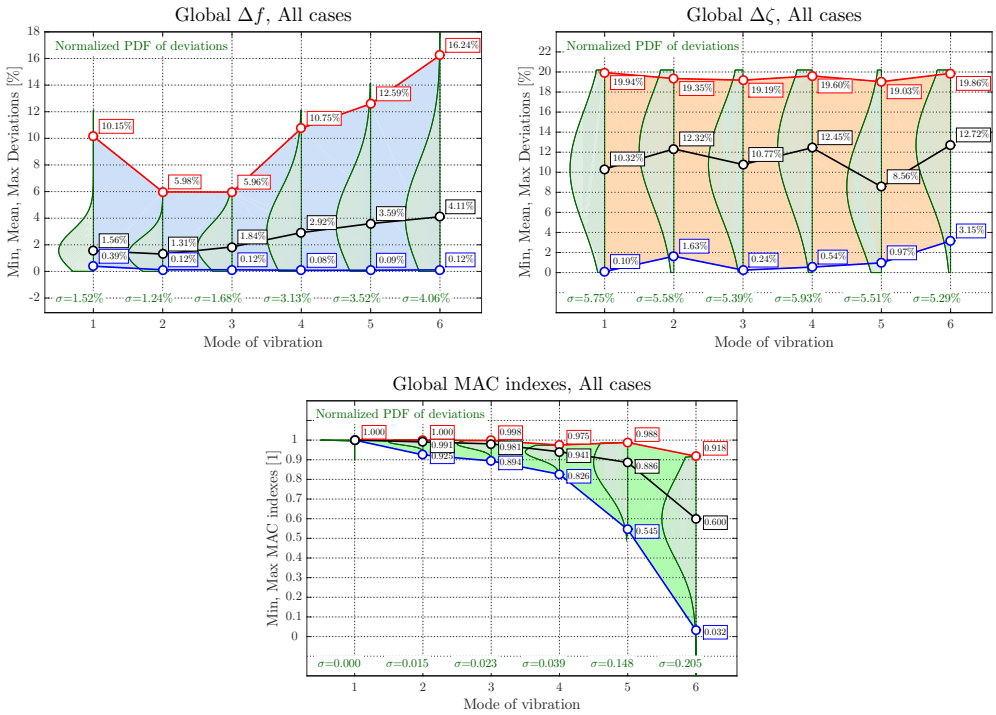

Figure 4.14: *Dispersion diagrams for the deviations of estimated natural frequencies and modal damping ratios, and for the MAC indexes, six-storey frame, $\zeta_i = 2\%$, Far-Field FEMA P695 database, NS and WE components. Minimum, mean and maximum values, and standard deviations are indicated.*

Concerning the higher deviations (of natural frequencies and, in particular, of MAC indexes) which can be observed on the last modes of vibration (the 5th and especially the 6th mode), these do not appear critical in engineering terms, since the effective modal mass associated to them is very small. A demonstration of this statement can be found in [97].

In conclusion, all the obtained estimates confirm the effectiveness of the developed rFDD algorithm, towards detecting correct strong ground motion modal parameters, in the linear range of dynamic response, also at concurrent heavy damping, with modal damping ratios ranging from 2% to 5%. Further details on this wide analysis and systematically-generated

rough preliminary results on all cases, regenerated, refined and further post-processed here, are available in [19,97,100]. In following Section 4.3.3, a further inspection on the identification results from the most demanding earthquakes will be considered, by simultaneously adopting a very high value of the modal damping ratios, namely $\zeta_i = 10\%$.

4.3.3 Further rFDD identification analyses at heavy damping

In the present section, a new further rFDD identification analysis is proposed, with the individuated most demanding earthquakes from the previous identification campaign and for very high values of the modal damping ratios. As revealed by the results in Section 4.3.2, the most challenging earthquakes have revealed to be Landers a) (12091), Manjil (12111) and Cape Mendocino (12132) cases, characterized by a sampling frequency of 50 Hz, and Kocaeli b) (12082), Superstition Hills b) (12122) and Chi-Chi a) (12141) ones, characterized by higher sampling frequencies (Table 4.4) but by stronger non-stationary features (see Time-Frequency plots in [97]).

Both NS and WE spatial components of such six earthquake signals are now considered, for a total of 12 seismic excitations selected from the FEMA P695 database. The adopted building is the six-storey frame (see Tables 4.5 and 4.6), namely the MDoF frame with the higher number of DoFs among the considered shear-type frames. The modal damping ratios of the frame are set to $\zeta_i = 10\%$ for all the six modes of vibration. This value of ζ_i is to be considered very high in terms of rFDD identification challenge, since classical FDD techniques usually deal with ζ_i in the order of 1% only [15]. Further, the present analysis shall be considered as innovative in the dedicated FDD literature, because such high values of modal damping ratios, set fixed for all the modes and for structures with more than three DoFs seem to have been never considered so far, specifically in the Earthquake Engineering range.

As it was previously done, estimates are again reported in terms of absolute deviations of estimated natural frequencies Δf and modal damping ratios $\Delta\zeta$ from the target parameters, and of achieved MAC indexes, as it can be newly appreciated in Fig. 4.15.

The estimated natural frequencies display deviations that are always less than 13%, except for an isolated value of 16.73% for the first mode with the earthquake of Manjil, WE component. Anyway, deviations show mean values at around 4-5%, i.e. rather suitable values in engineering terms, despite for the really challenging identification analysis. Concerning the NS components, the most demanding earthquakes turn out to be Landers and Cape Mendocino ones, especially for the last modes of vibration. Conversely, Manjil and Kocaeli earthquakes become the most challenging

ones on the WE ground motions, especially concerning the estimation of the first modes of vibration.

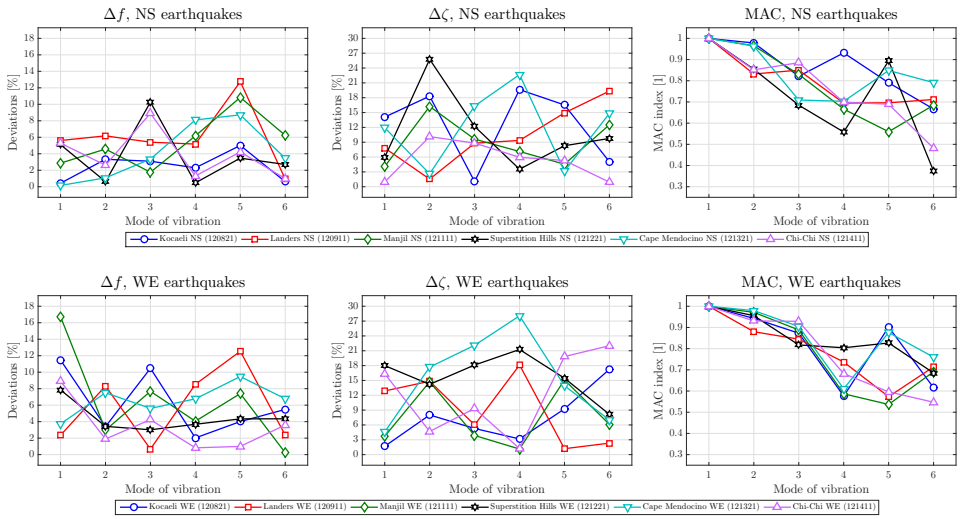

Figure 4.15: *Deviations of estimated natural frequencies and modal damping ratios, and MAC indexes, six-storey frame, $\zeta_i = 10\%$, indicated selected six-earthquakes from the FEMA P695 dataset, NS and WE components.*

Modal damping ratio deviations display higher values with respect to those from the previous cases (see Section 4.3.2), but still always less than 28%, for all the examined instances. As before, the achieved modal damping ratio estimates show to be well-distributed, with respect to the outcomes from the natural frequencies (in terms of variability as a function of adopted earthquake excitation), by showing mean deviations that are always in the order of 6-7%. This is rather astonishing, considering the challenging identification scenario provided by the assumed $\zeta_i = 10\%$.

Furthermore, a very good agreement between estimated and targeted mode shapes is again proven by the achieved MAC indexes, despite again for the very high value assumed for the modal damping ratios ($\zeta_i = 10\%$). For the first mode of vibration, MACs show to be always unitary. For the second mode, MACs turn out to be always higher than 0.80. The same happens for the third mode, with only two isolated cases where MAC values lower down to at around 0.70. The last three modes show mean values that come down to around 0.60-0.70, with only a few isolated cases where MACs go to even less reliable values in engineering terms.

Finally, the achieved results are also synoptically reported in statistical form in Fig. 4.16, through appropriate *boxplots*. In these representations, each boxplot relates to the natural frequencies, modal damping ratios and MAC values estimated from the performed analyses. In each boxplot the

inner rectangular box represents the central 50% of the identified parameters, while the centred line indicates their median. Then, the right and left boundary segments depict the 25% and 75% quantiles of the related statistical distributions. Finally, the vertical through-plot dashed green lines mark the known targeted modal parameters for the identification procedure.

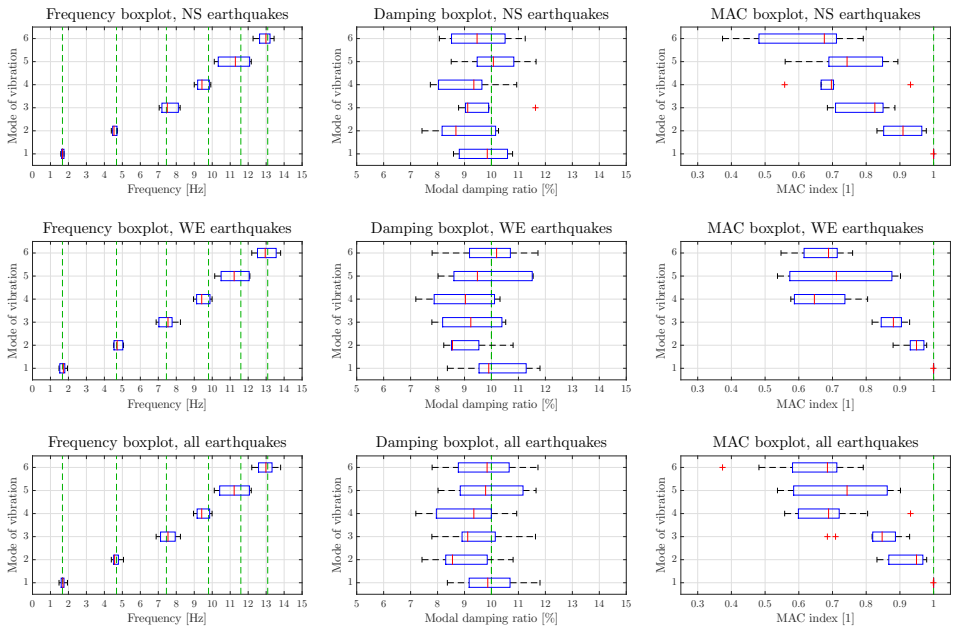

Figure 4.16: *Boxplot diagrams for estimated natural frequencies, modal damping ratios and MAC indexes, six-storey frame, $\zeta_i = 10\%$, selected six earthquakes from the FEMA P695 dataset (Figure 4.15), NS, WE and all (both NS and WE) components.*

Presented boxplots confirm again the goodness of the achieved results, since the deviations of the estimated parameters show to be reasonably well contained, for all the modes of vibration and associated modal parameters. Clearly, deviations increase by passing from the first to the last mode of vibration. Concerning the natural frequencies, these are the parameters that are subjected to less deviation, among all the achieved estimates, especially concerning the first modes of vibration. Also MAC indexes reveal very good mode shape estimates, also for the last modes of vibration. These are obviously more dispersed, since some troubles start to appear, especially in relation to the fifth and sixth mode shapes. Finally, modal damping ratios display again very good estimates, by showing a rather contained dispersion, for all the modes of vibration, despite for the heavy damping conditions set by assuming $\zeta_i = 10\%$ for all the modal damping ratios of the considered six-storey frame.

Chapter 5

Further rFDD results with Soil-Structure Interaction under earthquake-induced structural response signals

After the rFDD analyses developed in previous Chapter 4, where the focus fell on a reference three-storey shear-type frame and a more realistic ten-storey shear-type frame, now the attention moves to the adoption of synthetic earthquake-induced structural response signals coming from a five-storey shear-type frame under Soil-Structure Interaction conditions. All the structures are characterized by heavy damping, and they are analysed by rFDD through the adoption of the earlier set of ten earthquake base-excitations (Table 4.1).

5.1 Soil-Structure Interaction and structural response modeling

The input response channels to be fed to the rFDD algorithm, i.e. storey accelerations, are obtained from calculated structural response signals in the linear range. These synthetic recordings are generated by taking the set of ten selected seismic ground motions (see Table 4.1) as base excitation acting on the underlying bedrock of a five-storey shear-type frame with a Sway-Rocking (SR) foundation model adapted from [28, 43].

The simulated structural responses are calculated again by direct time integration of the equations of motion, via Newmark's (average acceleration) method [27]. As adopted in previous Chapter 4, the use of simulated signals shall fulfil a first, necessary condition for rFDD algorithm's efficiency, since flexible- and fixed-base modal parameters are determined via modal analysis before identification, and then adopted as known targets for validation purposes. The theoretical bases of the Sway-Rocking

Soil-Structure Interaction model are outlined in Section 5.1.1, while the adopted numerical example is introduced in Section 5.1.2.

5.1.1 Idealization of a shear-type frame with Soil-Structure Interaction effects

An n-storey shear-type superstructure with an underlying Sway-Rocking (SR) Soil-Structure Interaction model [28, 52, 70] is adopted as a benchmark structure-foundation system for this study. For the present application, a SR Soil-Structure Interaction model from the literature [52, 70] is taken, adapted and reformulated, as outlined in the following. In Fig. 5.1, the initial geometry, the lumped-mass scheme and the displacements DoFs of the SR model are sketched.

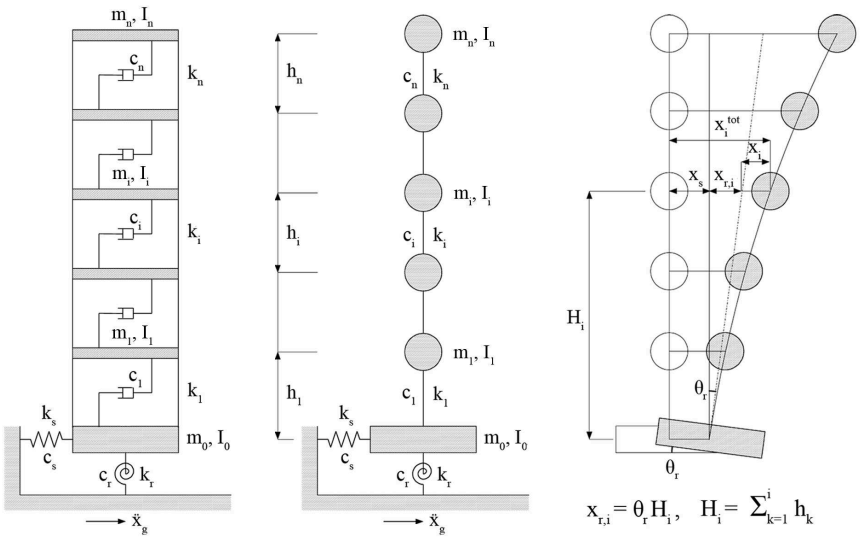

Figure 5.1: *Adopted linear Sway-Rocking Soil-Structure Interaction model of a multi-storey shear-type frame.*

Specifically, m_i, c_i, k_i, I_i and x_i are the mass, damping, stiffness, mass moment of inertia and displacement of the ith shear-type frame floor, respectively, with $i = 1, \ldots, n$. The foundation displays mass m_0 and mass moment of inertia $I_0 = m_0 r^2/4$, and is modeled as a rigid circular disc footing (with radius r) of a negligible thickness, attached to the surface of a linear elastic halfspace, representing the underlying soil [28].

With respect to the reference fixed-base model with no Soil-Structure Interaction effects, the Sway-Rocking model shall be described by two additional dynamical degrees of freedom (Fig. 5.1), i.e. horizontal sway $x_s = x_0$ (with associated k_s and c_s stiffness and damping coefficients) and

system rocking $\theta_r = \theta_0$ (with associated k_r and c_r stiffness and damping coefficients). Here, label 0 is meant to mark DoFs at the ground (0) level. Then, $\ddot{x}_g$ represents the horizontal acceleration related to free-field ground motion displacement x_g, to which the building-foundation system is subjected to. The total horizontal displacement x_i^{tot} along the ith translational storey DoF may be then computed as $x_i^{tot} = x_g + x_0 + x_{r,i} + x_i$ (Fig. 5.1). Finally, h_i and H_i are the ith relative and absolute floor heights, respectively.

The $n+2$ equations of motion of the so-assembled SR Soil-Structure Interaction model may be written by the following system of second-order ordinary differential equations:

$$\begin{cases} \mathbf{M}\left(\ddot{\mathbf{x}} + \mathbf{r}\ddot{x}_g + \mathbf{r}\ddot{x}_0 + \mathbf{z}\ddot{\theta}_0\right) + \mathbf{C}\dot{\mathbf{x}} + \mathbf{K}\mathbf{x} = \mathbf{0} & (5.1) \\ \mathbf{r}^{\mathrm{T}}\mathbf{M}\left(\ddot{\mathbf{x}} + \mathbf{r}\ddot{x}_g + \mathbf{r}\ddot{x}_0 + \mathbf{z}\ddot{\theta}_0\right) + m_0\left(\ddot{x}_g + \ddot{x}_0\right) + c_s\dot{x}_0 + k_s x_0 = 0 & (5.2) \\ \mathbf{z}^{\mathrm{T}}\mathbf{M}\left(\ddot{\mathbf{x}} + \mathbf{r}\ddot{x}_g + \mathbf{r}\ddot{x}_0 + \mathbf{z}\ddot{\theta}_0\right) + I_t\ddot{\theta}_0 + c_r\dot{\theta}_0 + k_r\theta_0 = 0 & (5.3) \end{cases}$$

where $\mathbf{M}$, $\mathbf{C}$ and $\mathbf{K}$ are the $n \times n$ mass, damping and stiffness matrices of the superstructure (shear-type frame), $\mathbf{x}$ is the $n \times 1$ vector collecting displacements x_i of the superstructure itself, with $\dot{\mathbf{x}}$ and $\ddot{\mathbf{x}}$ their time derivatives, namely velocities and accelerations. Then, $\mathbf{r}$ is a horizontal rigid body motion vector of unitary components $(n \times 1)$, $\mathbf{z}$ is the vector of absolute floor heights H_i $(n \times 1)$, $I_t = I_0 + \sum_{i=1}^{n} I_i$ is the sum of the mass moment of inertia of the foundation-superstructure system. Superscript 'T' marks transpose. Eqs. (5.2) and (5.3) represent the translational and rotational dynamical equilibriums of the entire structure-foundation system, respectively, that shall be written (and satisfied at each time instant) in order to complement the dynamic equilibrium of the system superstructure, as represented by Eq. (5.1).

The system of $n+2$ second-order differential equations may be rewritten in simpler global matrix notation as follows:

$$\boldsymbol{\mathcal{M}}\ddot{\mathbf{x}}_t + \boldsymbol{\mathcal{C}}\dot{\mathbf{x}}_t + \boldsymbol{\mathcal{K}}\mathbf{x}_t = \mathbf{f}(t) = -\boldsymbol{\rho}\ddot{x}_g \tag{5.4}$$

where $\boldsymbol{\mathcal{M}}$, $\boldsymbol{\mathcal{C}}$ and $\boldsymbol{\mathcal{K}}$ are the $(n+2) \times (n+2)$ mass, damping and stiffness block matrices of the foundation-structure system, $\mathbf{x}_t$ is the $(n+2) \times 1$ vector collecting displacements $x_{i,t}$ of the entire system, with $\dot{\mathbf{x}}_t$ and $\ddot{\mathbf{x}}_t$ their time derivatives, namely velocities and accelerations, and $\boldsymbol{\rho}$ is a mass vector useful to represent the structural effect of the base excitation. These terms may be defined as:

$$
\begin{aligned}
\boldsymbol{\mathcal{M}} &= \underbrace{\begin{bmatrix} \mathbf{M}_{n\times n} & \mathbf{M}\mathbf{r}_{n\times 1} & \mathbf{M}\mathbf{z}_{n\times 1} \\ \mathbf{r}^{\mathrm{T}}\mathbf{M}_{1\times n} & \mathbf{r}^{\mathrm{T}}\mathbf{M}\mathbf{r}+m_0 & \mathbf{r}^{\mathrm{T}}\mathbf{M}\mathbf{z} \\ \mathbf{z}^{\mathrm{T}}\mathbf{M}_{1\times n} & \mathbf{z}^{\mathrm{T}}\mathbf{M}\mathbf{r} & \mathbf{z}^{\mathrm{T}}\mathbf{M}\mathbf{z}+I_t \end{bmatrix}}_{(n+2)\times(n+2)}, \\
\boldsymbol{\mathcal{C}} &= \underbrace{\begin{bmatrix} \mathbf{C}_{n\times n} & \mathbf{0}_{n\times 1} & \mathbf{0}_{n\times 1} \\ \mathbf{0}_{1\times n} & c_s & 0 \\ \mathbf{0}_{1\times n} & 0 & c_r \end{bmatrix}}_{(n+2)\times(n+2)}, \qquad \boldsymbol{\mathcal{K}} = \underbrace{\begin{bmatrix} \mathbf{K}_{n\times n} & \mathbf{0}_{n\times 1} & \mathbf{0}_{n\times 1} \\ \mathbf{0}_{1\times n} & k_s & 0 \\ \mathbf{0}_{1\times n} & 0 & k_r \end{bmatrix}}_{(n+2)\times(n+2)}, \\
\boldsymbol{\rho} &= \underbrace{\begin{Bmatrix} \mathbf{M}\mathbf{r}_{n\times 1} \\ \mathbf{r}^{\mathrm{T}}\mathbf{M}\mathbf{r}+m_0 \\ \mathbf{z}^{\mathrm{T}}\mathbf{M}\mathbf{r} \end{Bmatrix}}_{(n+2)\times 1}, \qquad \mathbf{x}_t = \underbrace{\begin{Bmatrix} \mathbf{u}_{n\times 1} \\ u_0 \\ \theta_0 \end{Bmatrix}}_{(n+2)\times 1}
\end{aligned}
\tag{5.5}
$$

Then, starting from the system of differential equations of motion in Eq. (5.4), the responses of the linear structure-foundation Sway-Rocking model may be calculated numerically, i.e. by Newmark's direct integration (average acceleration), by solving for each of the $n+2$ DoFs of the dynamical system.

5.1.2 Adopted numerical models

The analytical model proposed in Section 5.1.1 is adopted for the numerical analyses on a five-storey shear-type building with underlying Sway-Rocking foundation. The superstructure is assumed to be laying on four different types of soil, i.e. *very soft, soft, medium and dense*, as represented by different characteristic soil parameters. The standard fixed-base frame (like an infinitely-stiff soil) is considered as a basic reference, too. The achieved structural dynamic characteristics include close modes and heavy damping, in terms of modal identification challenge (realistic structural damping in terms of practical applications).

The inter-storey height is assumed to be equal to 4 m. The floor mass and mass moment of inertia of each floor are taken as $m_i = 3\times 10^5$ kg and $I_i = 7.5\times 10^6\,\mathrm{kg\,m^2}$. Inter-storey stiffness, from the first to the fifth, are assumed as $7k$, $5k$, $3k$, $2k$ and k, respectively, where $k = 5\times 10^7$ N/m.

Important, as a matter of modelling the inherent structural damping in a comprehensive way, two separate cases of superstructure damping have been investigated, characterized by different damping distributions over the various modes of vibration:

- (ζ_{M}): Mass-proportional damping, with $\zeta_{\mathrm{M}} = 10\%$ set for the first mode;

- (ζ_{R}): Rayleigh damping (linear combination of mass and stiffness matrices), with $\zeta_{\mathrm{R}} = 2\%$ and 2.25% set for the first and second modes, respectively.

Mass-proportional damping means that stiffness matrix $\mathbf{C}$ is proportional to mass matrix $\mathbf{M}$ only, namely $\mathbf{C} = \alpha\mathbf{M}$. In the present case, $\alpha = 1.3970$ is set, in order to have $\zeta_{\mathrm{I,M}} = 10\%$ for the first mode of vibration. Instead, Rayleigh damping assumes that $\mathbf{C}$ is a linear combination of both mass and stiffness matrices, i.e. $\mathbf{C} = \alpha\mathbf{M}+\beta\mathbf{K}$. Then, $\alpha = 0.1761$ and $\beta = 0.0021$ are set, in order to have $\zeta_{\mathrm{I,R}} = 2\%$ and $\zeta_{\mathrm{II,R}} = 2.25\%$ for the 1st and 2nd mode, respectively. For all the damping values, related also to the adopted soil type, the resulting modal damping ratios are reported later in Section 5.2.

These two damping cases bring to different responses, and then to different identification challenges. In fact, the energy contribution of the higher modes with ζ_{R} is much lower than those of the lower modes, a fact that makes difficult the estimations related to the higher modes. Mass-proportional damping, instead, displays a light damping in the higher modes, bringing to less problems for their identification. Identification of the first modes, instead, becomes more challenging, due to the heavy damping associated to them. The separate consideration of both damping models brings then to such a variety of possible cases and challenges during rFDD modal dynamic identification.

Thus, five structure-foundation system cases with two different damping distributions are considered, thus 10 structure-foundation instances, with 10 underlying earthquake excitations, for a total of 100 analysed modal identification cases.

The circular foundation adopted to explore Soil-Structure Interaction effects displays the following characteristics: $r = 10\,\mathrm{m}$, $m_0 = 5 \times 10^5\,\mathrm{kg}$ and $I_0 = m_0 r^2/4 = 7.5 \times 10^6\,\mathrm{kg\,m^2}$. The spring and dashpot coefficients for the SR model are obtained from the frequency-dependent impedance function of the soil [81, 127], for the static case (frequency-dependence is removed):

$$k_s = \frac{8\,\mathrm{G}\,r}{2-\nu}, \quad c_s = \frac{4.6}{2-\nu}\,\rho\,V_s\,r^2; \qquad k_r = \frac{8\,\mathrm{G}\,r^3}{3\,(1-\nu)}, \quad c_r = \frac{0.4}{1-\nu}\,\rho\,V_s\,r^4 \tag{5.6}$$

where G, ν, ρ and $V_s = \sqrt{\mathrm{G}/\rho}$ are shear modulus, Poisson's ratio, mass density and shear-wave velocity of the adopted soil.

Table 5.1 summarizes the assumed mechanical parameters of the analysed soils and the stiffness and damping characteristics of the Sway-Rocking model, as taken and re-elaborated from [70]. Obviously, by taking

$k_s, k_r \to \infty$ and $c_s, c_r \to 0$, the SR model is traced back to a standard fixed-base model (no Soil-Structure Interaction effects).

Soil type	ν [1]	G [MPa]	ρ [kg/m^3]	V_s [m/s]	k_s [N/m]	k_r [N m]	c_s [N s/m]	c_r [N s m]
Very soft	0.49	4	1600	50	2.12×10^8	2.09×10^{10}	2.44×10^7	6.27×10^8
Soft	0.49	18	1800	100	9.54×10^8	9.41×10^{10}	5.48×10^7	1.41×10^9
Medium	0.48	171	1900	300	9.00×10^9	8.77×10^{11}	1.73×10^8	4.38×10^9
Dense	0.33	600	2400	500	2.87×10^{10}	2.39×10^{12}	3.31×10^8	7.16×10^9

Table 5.1: *Characteristic mechanical parameters of the soil-foundation SR system for the four adopted soil types.*

As concerning the vast outcomes of simulated Soil-Structure Interaction effects in the present structure-foundation modelling (100 analysed cases), sample results are presented and discussed below, in order to show typical observed characteristic features of the recorded seismic responses in the presence of Soil-Structure Interaction effects.

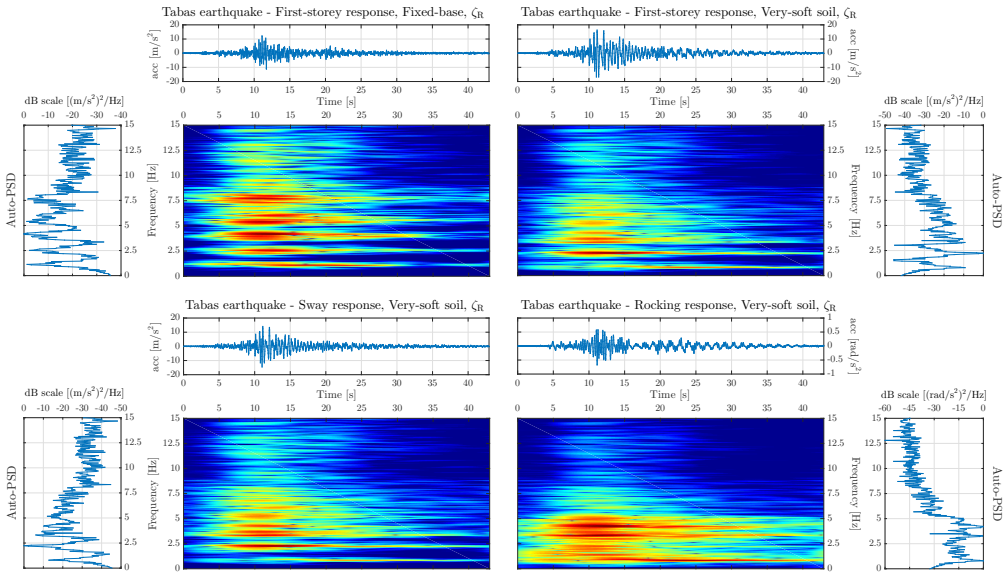

Figure 5.2: *Acceleration, Auto-PSD and Gabor Wavelet Transform of the structural response to Tabas earthquake, Rayleigh damping (ζ_R). First row: first-storey response of fixed-base and very-soft soil cases. Second row: horizontal sway and system rocking of the very-soft soil case.*

Fig. 5.2 displays an example of how Soil-Structure Interaction may affect the building structural response, by examining the response of the structure within Time, Frequency and Time-Frequency domains, under

Tabas earthquake excitation. Specifically, the response related to the first storey (fixed-base and very-soft cases) and to the horizontal sway and system rocking (very-soft cases only) are reported, in terms of acceleration (Time), Auto-PSD (Frequency) and Gabor Wavelet Transform [11] (Time-Frequency). Due to the presence of Soil-Structure Interaction, the first-storey response for the very-soft soil case is noticeably amplified. Also, the frequency shift that Soil-Structure Interaction involves into the structural response is clearly visible, along with the appearance of structural frequencies into the foundation motions (as well as for soil, non-structural, frequencies, in the above structural motions).

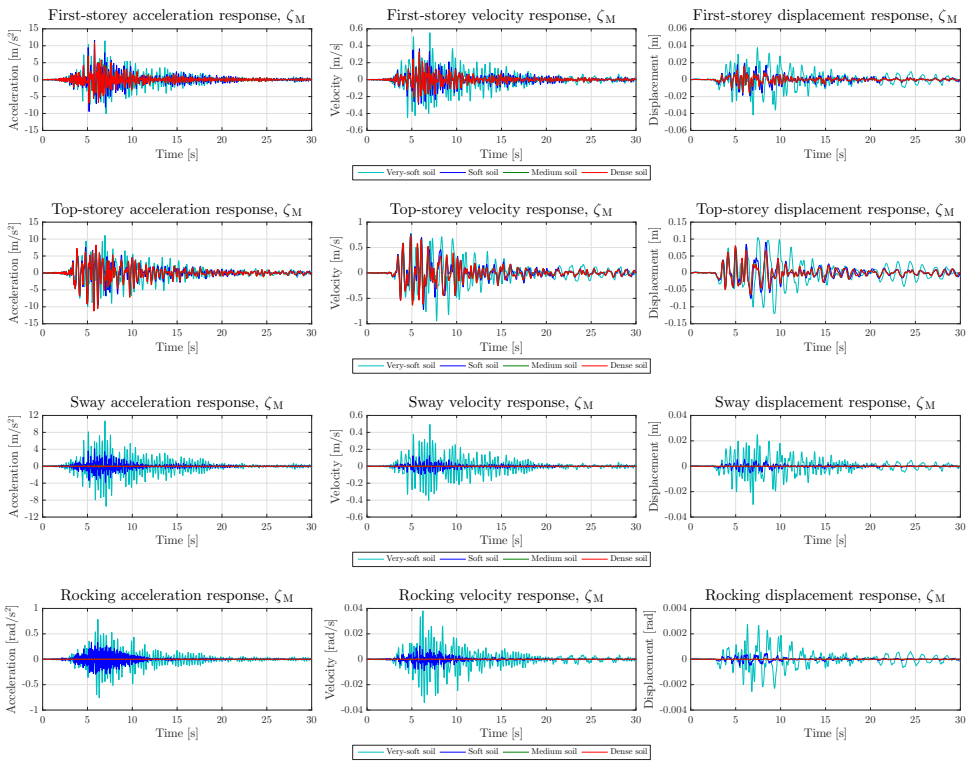

Figure 5.3: *Acceleration, velocity and displacement structural responses to Loma Prieta earthquake, Soil-Structure Interaction flexible-base cases (at different soil type), Mass-proportional damping (ζ_M). First row: first-storey responses. Second row: top-storey responses. Third row: horizontal sway responses. Fourth row: system rocking responses.*

Further, Fig. 5.3 depicts an example of the collected structural responses, in terms of accelerations, velocities and displacements. The simulated first-storey, top-storey, horizontal-sway and system-rocking responses are shown for all flexible-base cases (i.e. for all four soil types),

for the Loma Prieta earthquake taken as base excitation and for assumed Mass-proportional (ζ_{M}) damping. The earthquake instances of Tabas and Loma Prieta have been selected here because the associated identification estimates reveal to be among the most challenging between all the considered seismic cases, as it will be reported and discussed in Section 5.2. The different behaviours of the structural responses are clearly visible, in particular on the soil-foundation DoFs.

Then, the rFDD technique outlined in Chapter 3 is innovatively applied to a shear-type building under Soil-Structure Interaction effects. The target is the identification of flexible-base modal parameters from earthquake-induced structural response signals only, as it will be demonstrated in Section 5.2. Originally, the rFDD method is expanded to further work under OMAX conditions, by aiming at a quantification of Soil-Structure Interaction effects, i.e. at the identification of underlying fixed-base modal parameters, too (see later Section 5.3). There, the numerical results arising from the application of the rFDD-OMAX algorithm are presented, focusing specifically on the evaluation of Soil-Structure Interaction effects and on their implications on the targeted modal dynamic identification.

5.2 Results from synthetic output-only modal dynamic identification under Soil-Structure Interaction

By taking the earlier set of 10 selected earthquake recordings (Table 4.1) as base excitation, modal dynamic identification has been performed with the rFDD algorithm, in order to estimate the modal parameters under flexible-base conditions. Constant time series lengths of 400 s and 0.0025 Hz frequency resolution have been adopted, by applying the method outlined in [92]. In this first step, flexible-base modal parameters have been estimated by using only storey accelerations (superstructure responses, i.e. 5 channels). In forthcoming Section 5.3, instead, also sway and rocking accelerations will be taken into account, thus by applying OMAX conditions to the Soil-Structure Interaction identification (7 channels), in order to identify fixed-base superstructural properties too.

By considering flexible-base conditions, every soil case takes different target parameters. Reference natural frequencies of the structural system are reported in Table 5.2. Clearly, the first five modes are related to be modes of vibration of the superstructure, while the 6th and 7th modes are related to the additional soil SR DoFs (indicated in slanted in Table 5.2). The 6th and 7th modes increase from the softer (very-soft) to the harder (dense) soils, since these are directly related to the soil (sway and rocking) stiffness parameters. The higher they are, the more the last two modal frequencies are detached from the structural ones. Obviously, the fact that

here soil frequencies are the last ones in the model is directly related to the fine balance between soil and structural parameters. With different soils and structural parameters (or structures) it is possible that soil frequencies could be within the structural frequency range, instead that over their upper bound limit, as in the present case.

In Tables 5.3 and 5.4, target superstructure modal damping ratios ζ_i, for both Mass-proportional ζ_{M} and Rayleigh ζ_{R} damping modellings (Section 5.1.2), respectively, may be found. Here, only superstructure modal damping ratios are reported, since foundation damping parameters are calculated apart, as indicated in Section 5.1.2.

Mode, f_n [Hz]	1	2	3	4	5	*6*	*7*
Very-soft soil	0.8002	2.2035	3.3550	4.1185	5.1056	*6.7280*	*9.2036*
Soft soil	1.0169	2.4687	3.8872	5.4386	7.4337	*7.8733*	*11.159*
Medium soil	1.1004	2.5499	4.0301	5.6424	8.0882	*22.393*	*28.124*
Dense soil	1.1076	2.5578	4.0416	5.6579	8.1204	*36.773*	*49.567*
Fixed-base model	1.1115	2.5601	4.0570	5.6650	8.1345	–	–

Table 5.2: *Targeted natural frequencies of the five-storey SR frame at variable soil properties.*

Mode, $\zeta_{\mathrm{M},n}$ [%]	1	2	3	4	5
Very-soft soil	10.00	3.63	2.38	1.94	1.57
Soft soil	10.00	4.12	2.62	1.87	1.37
Medium soil	10.00	4.32	2.73	1.95	1.36
Dense soil	10.00	4.33	2.74	1.96	1.36
Fixed-base model	10.00	4.34	2.75	1.96	1.37

Table 5.3: *Targeted modal damping ratios of the five-storey SR frame at variable soil properties, Mass-proportional damping (ζ_{M}).*

Mode, $\zeta_{\mathrm{R},n}$ [%]	1	2	3	4	5
Very-soft soil	2.00	2.25	3.00	3.55	4.28
Soft soil	2.00	2.25	3.04	4.03	5.35
Medium soil	2.00	2.25	3.04	4.02	5.58
Dense soil	2.00	2.25	3.04	4.02	5.58
Fixed-base model	2.00	2.25	3.04	4.01	5.58

Table 5.4: *Targeted modal damping ratios of the five-storey SR frame at variable soil properties, Rayleigh damping (ζ_{R}).*

Then, target mode shapes of the structural system are depicted in Fig. 5.4. For every mode shape, from the 1st to the 7th, the different soil types are indicated with different colors and markers. The distinct effect

of the different soil types is clearly visible, especially at increasing mode of vibration, in comparison to those of standard fixed-base model. In particular, the soft and very-soft soil mode shapes are truly detached from the fixed-base case and from the most rigid soil cases. In their mode shapes the Soil-Structure Interaction effect is remarkable, since both superstructure and soil DoFs participate for every mode of vibration. Obviously, for the fixed-base system the last two modes of vibration, related to the soil DoFs, are not available.

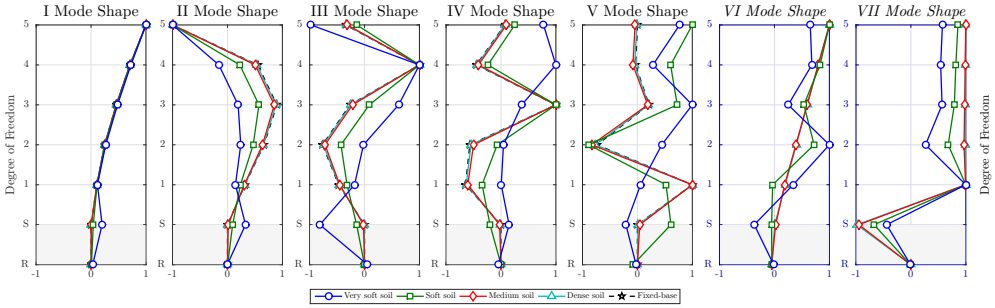

Figure 5.4: *Targeted mode shapes of the five-storey Sway-Rocking frame at variable soil properties.*

An example of the achievable modal estimates is reported in Fig. 5.5, obtained for L'Aquila earthquake excitation. The estimates in terms of absolute deviations of the estimated natural frequencies Δf and modal damping ratios $\Delta\zeta$ from the target parameters, and of the achieved MAC indexes for the estimated mode shapes are reported (see Chapter 4 for their calculation). In turn, the target parameters, namely natural frequencies, modal damping ratios and mode shapes, refer to the adopted soil case. The fixed-base case is reported too, as a fundamental (no Soil-Structure Interaction) reference case for comparison purposes.

The rFDD estimated frequencies show deviations that are always below 4%, except for the first modes of the ζ_{M} cases, where deviations increase up to 7%, due to the related heavy damping ($\zeta = 10\%$) associated to that mode of vibration. The estimated modal damping ratios display suitable deviations, at around 10%, for all the soil cases. Only isolated maxima of about $20 \div 25\%$ can be detected in a few cases, which still looks acceptable in engineering terms, especially considering the present heavy-damping identification conditions. The frequency and damping deviations for the flexible-base cases show to be close to those achieved from the fixed-base case.

Moreover, MAC values are always higher than 0.8 for the first three modes, for all the soil cases. With the exception of the soft and very-soft

soil cases, the last two mode shapes turn out to be quite reliable. In fact, only the last modes show rather inaccurate values for these cases, where tough soil conditions (and simultaneous earthquake excitations) make it harder for the correct mode shape detection. Generally, the first modes of the ζ_R cases show better MAC indexes, while the same happens for the last modes of the ζ_M instances. This is directly related to the heavy damping reached by the first modes and last modes of the ζ_M and ζ_R cases, respectively. This clearly affects the achievable rFDD estimates.

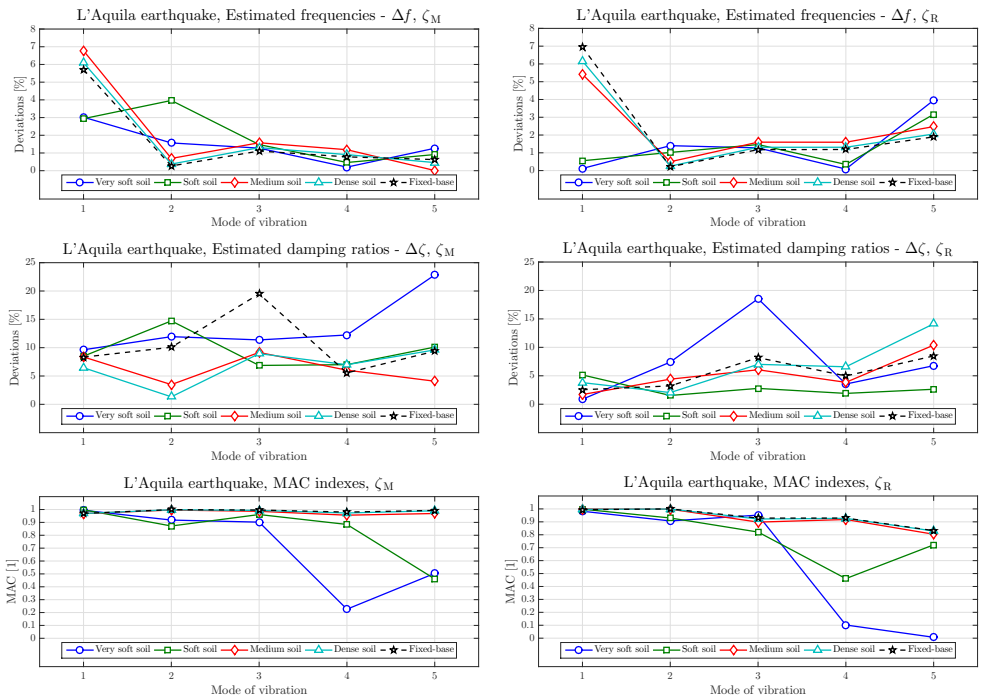

Figure 5.5: *Deviations of rFDD estimated natural frequencies (first row) and modal damping ratios (second row) for the flexible-base models, MAC calculated between rFDD estimated and target flexible-base mode shapes (third row), L'Aquila earthquake, Mass-proportional (ζ_M) with $\zeta_{M,I} = 10\%$ (first column) and Rayleigh damping (ζ_R) with $\zeta_{R,I} = 2\%$ and $\zeta_{R,II} = 2.25\%$ (second column). Corresponding targeted modal damping ratios are reported in Tables 5.3 and 5.4, respectively.*

Finally, a synthesis from all the achieved results on the total of 100 analysed cases is reported in Figs. 5.6 and 5.7. There, the estimates in terms of absolute deviations of the rFDD identified natural frequencies and modal damping ratios from the target values, and of the achieved MAC indexes for the rFDD estimated mode shapes are depicted. All the rFDD estimated values for each of the adopted earthquakes and soil cases

are reported, for both Mass-proportional (ζ_{M}) and Rayleigh damping (ζ_{R}), respectively.

By looking at these figures, the estimated frequencies show maximum deviations that are always below 8%. On average, deviations reveal to be around $3 \div 4\%$, for both ζ_{M} and ζ_{R} cases. The first modes of the ζ_{M} cases are affected by higher deviations, due to the related heavy damping reached for the first mode (10%). The same happens for the last two modes of the ζ_{R} cases, where again quite heavy damping occurs ($\simeq 5\%$). In relation to the adopted earthquakes, the LP, NO, NZ and TA cases (i.e. the seismic events characterized by $f_s = 50\,\mathrm{Hz}$) show to be the most challenging, in terms of estimated natural frequencies (and of achieved absolute deviations). In particular, the LP earthquake makes it difficult for the correct detection of the 4th and 5th modal frequencies, for all the cases. The AQ earthquake, instead, leads to some troubles for the estimation of the 1st natural frequency for the medium, dense and fixed-base cases, ζ_{R} damping.

The estimated modal damping ratios display deviations at around 10%, for all the analysed cases. Isolated maxima of about $20 \div 25\%$ can be detected in a few cases, which may still look acceptable. This since the identification of damping is very challenging, especially with FDD methods, and in the presence of Soil-Structure Interaction effects. Additionally, the presence of heavy damping adds a further difficulty. The present work pushes hard on that and seeks to study the limit conditions for the present rFDD algorithm, by assuming high damping ratios, to be targeted. Within such a frame, even relatively high percentage deviations of about $20 \div 25\%$ may be considered as a rather surprising identification success. Then, noticeable is the fact that increasing and decreasing trends of the achieved absolute deviations may be read from the graphs, for ζ_{M} and ζ_{R}, respectively. This is related to the different damping distribution implemented on the two cases. In general terms, slightly-less accurate results are obtained again for the LP, NO, NZ and TA cases.

MAC values are always higher than 0.8 for the first three modes, except for a few isolated cases, where they still remain greater than an acceptable value of 0.7. Only the last modes of vibration show rather inaccurate values for some cases, especially in relation to the very-soft soil. In general, the ζ_{M} cases show to be more accurate on the last modes, while the same happens for the first modes of the ζ_{R} cases. This is again related to the different behaviour and distribution of the damping assumed along the modes. In detail, the most challenging earthquakes reveals to be NE, NO and NZ for the ζ_{M} cases (especially for the 2nd and 5th modes of vibration). Instead, for ζ_{R} damping, the most demanding seismic excitations show to be CH, NE, NO and TA (especially for the 4th and 5th modes of vibration).

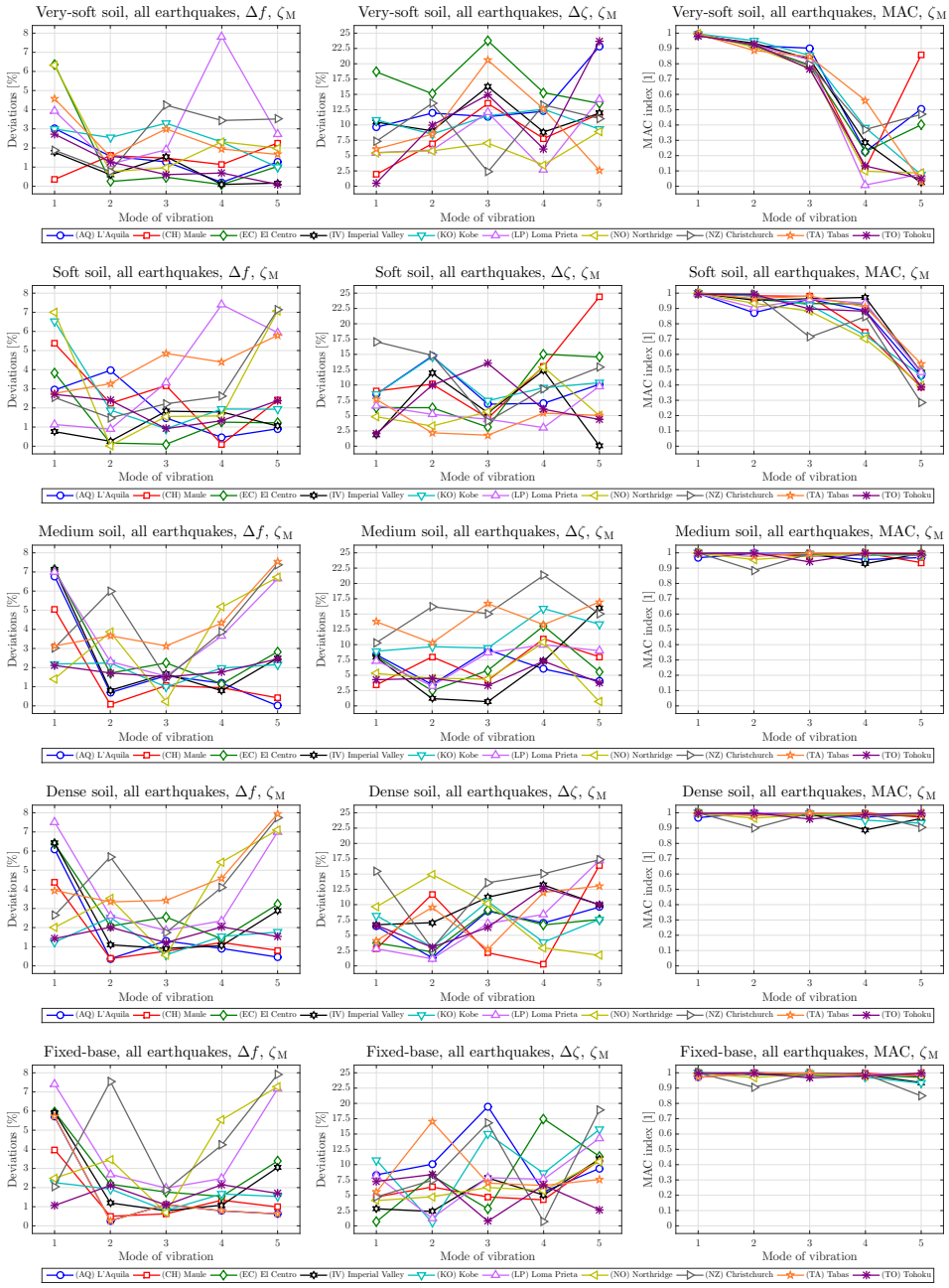

Figure 5.6: *Deviations of estimated natural frequencies and modal damping ratios, and MAC indexes for the flexible-base models, complete earthquake dataset, Mass-proportional damping (ζ_M) with $\zeta_{M,I} = 10\%$ (corresponding targeted modal damping ratios in Table 5.3).*

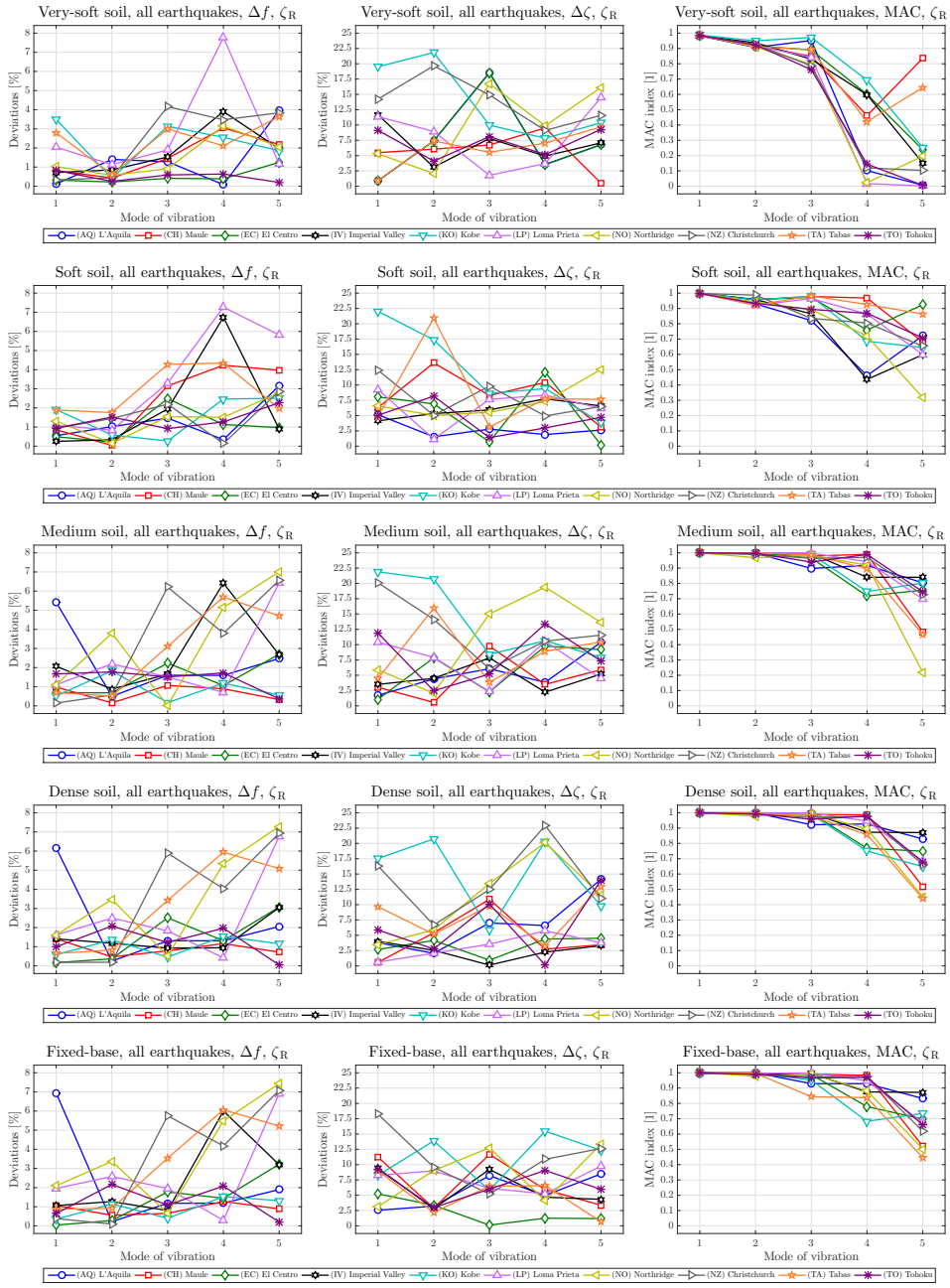

Figure 5.7: *Deviations of estimated natural frequencies and modal damping ratios, and MAC indexes for the flexible-base models, complete earthquake dataset, Rayleigh damping (ζ_R) with $\zeta_{R,I} = 2\%$ and $\zeta_{R,II} = 2.25\%$ (corresponding targeted modal damping ratios in Table 5.4).*

Notice that the estimated frequencies show deviations that vary among the different earthquakes and from the targeted values. This is expected and confirmed also by the trends for the modal damping ratios. The MAC indexes, instead, generally remain on high values for the first three to four modes, while they decrease for the remaining ones, especially for the soft and very-soft soil cases. This feature may be appreciated also by looking at Fig. 5.8, where the estimated mode shapes for the soft soil case are reported.

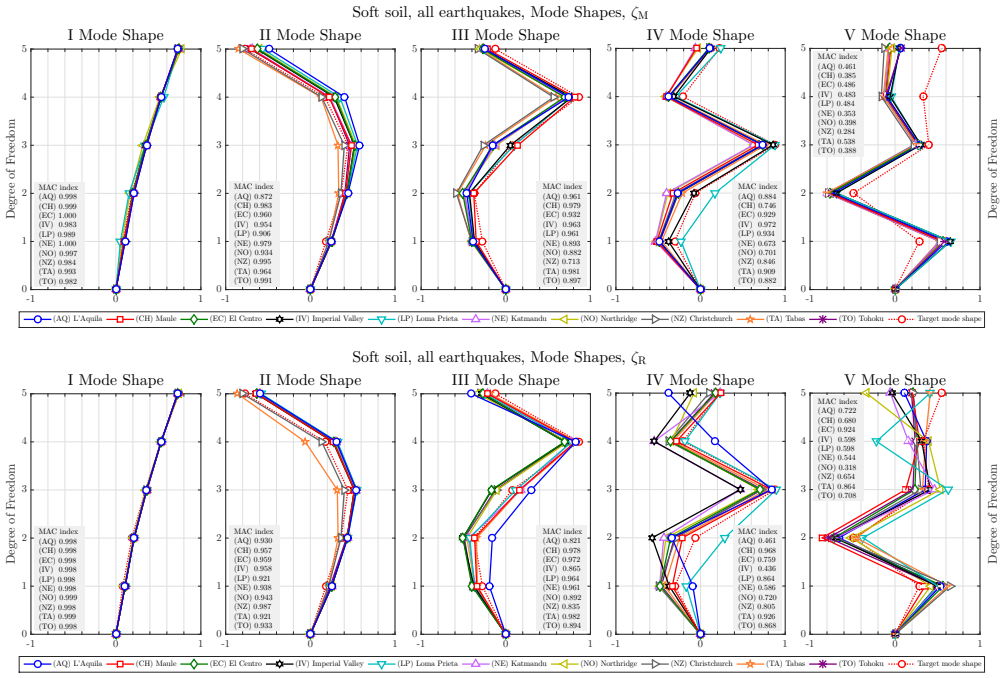

Figure 5.8: *Estimated mode shapes for the soft soil case, complete earthquake dataset, Mass-proportional (ζ_M) with $\zeta_{M,I} = 10\%$ (first row) and Rayleigh damping (ζ_R) with $\zeta_{R,I} = 2\%$ and $\zeta_{R,II} = 2.25\%$ (second row). Corresponding targeted mode shapes and calculated MAC indexes are reported, too (see also Fig. 5.4).*

Here, the complete earthquake dataset is considered, with both Mass-proportional (ζ_M) and Rayleigh damping (ζ_R) cases. In the achieved representation, the corresponding targeted mode shapes and the calculated MAC indexes for every mode and earthquake instance are also reported (see Fig. 5.4). By observing this figure in detail, it is clear that mode shape estimates remain very effective, especially for the first three to four modes. Independently from the adopted earthquake, mode shapes are caught with accuracy, by tracing the target ones with a very good approximation. Also for the fifth mode, despite for the lower MAC indexes, the targeted mode shape is more or less caught, in its form. This is again

a confirmation of the goodness of the MAC as a global validation index, as well as of the efficacy of the present rFDD algorithm in detecting also mode shapes in the present such challenging framework with heavy damping and Soil-Structure Interaction effects, under earthquake excitation.

In conclusion, all the obtained results confirm the effectiveness of the developed rFDD algorithm for the detection of Soil-Structure Interaction flexible-base structural modal parameters, by adopting earthquake-induced structural response signals and heavy structural damping (in terms of identification challenge).

5.3 OMAX evaluation of Soil-Structure Interaction effects

The evaluation of Soil-Structure Interaction effects now operates through an expansion of the rFDD algorithm within an OMAX environment [48], as earlier described in Section 5.1. At this stage, the foundation (Sway and Rocking) recordings (2 signals) and the output-only superstrucure responses of the floors (5 signals) are simultaneously processed by the present rFDD-OMAX algorithm. The tools adopted for Soil-Structure Interaction detection, which are embedded into the rFDD approach, are taken and adapted from works [107,108]. These tools rely on two different approaches, as detailed in the following two subsections. Reference fixed-base modal properties can then be estimated.

5.3.1 Identification of Soil-Structure Interaction conditions

Specifically, from the recordings of the foundation sway and of the upper-storey acceleration, a first immediate procedure may refer to the extraction of the natural frequencies of the fixed-base building and of the foundation. This is possible since the ratio of the Fourier amplitude spectra between storey and foundation accelerations allows for the identification of fixed-base building natural frequencies, as demonstrated in [108], for a simplified SDoF system (while here a MDoF superstructure is originally considered).

This is obtained by starting from the following relation [108]:

$$|\mathrm{R}| = \frac{|\mathcal{H}_{b,i}|}{|\mathcal{H}_{f,k}|} = \frac{|\mathscr{F}\left\{\ddot{x}_{b,i}\right\}|}{|\mathscr{F}\left\{\ddot{x}_{f,k}\right\}|} \tag{5.7}$$

where $|\mathrm{R}|$ is the absolute value (or amplitude) of the ratio of the system Transfer Functions (TF), $|\mathcal{H}_{b,i}|$ and $|\mathcal{H}_{f,k}|$ are the building and foundation TF amplitudes (referred to the selected $x_{b,i}$ and $x_{f,k}$ building and foundation DoFs), $\mathscr{F}$ represents Fourier Transform and $\ddot{x}_{b,i}$, $\ddot{x}_{f,k}$ are the accelerations of the selected DoFs. In the present work, implications of study [108] are thus extended to MDoF systems. The selected DoFs from

which acceleration data are considered are the top-storey displacement and the foundation sway.

In Fig. 5.9 a clear representation of the Fourier transform and of the TF modulus can be appreciated, by taking Mass-proportional damping (ζ_M), for the very-soft soil and for the fixed-base cases. It has been demonstrated [108] that |R| is not influenced by the dynamic characteristics of the foundation, and it always displays a peak at or near the fundamental frequency of the fixed-base building. Thus, |R| describes the characteristics of the fixed-base building, and always peaks at or near the fixed-base building frequencies, for structures characterized by low damping.

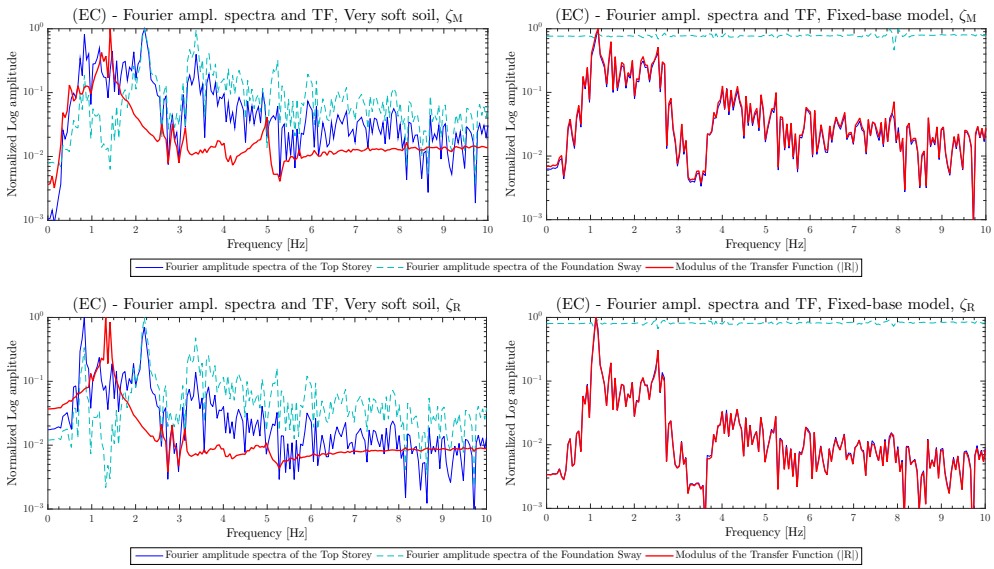

Figure 5.9: *Fourier amplitude spectra of top-storey and foundation-sway accelerations and their Ratio |R| for the very-soft soil and for the fixed-base cases, El Centro earthquake (EC), ζ_M and ζ_R dampings.*

Instead, the coupling between building and foundation is present in the true TF, which is a complex-valued quantity and incorporates both building and foundation properties. Then, such coupling alters the phase of the TF, but not its amplitude. That is the reason because the coupling can be detected on the true TF, but not on its amplitude. This is feasible by observing the curves represented under normalized log scale in Fig. 5.9, where the El Centro earthquake is considered for the Mass-proportional (ζ_M) and Rayleigh (ζ_R) damping cases, respectively.

For the fixed-base model, the two Fourier amplitudes and the modulus of the TF are overlapped. Also, they clearly mark the same frequency, that is the fundamental frequency of this case (first mode of vibration, at around 1.1 Hz). For the very-soft soil model, instead, the fundamen-

tal frequencies of the three curves are clearly decoupled, suggesting the presence of Soil-Structure Interaction effects. Also, the modulus of the Transfer Function (in red color) indicates some frequency peaks for the fixed-base model. In particular, a unitary amplitude may be detected in correspondence to the fundamental mode of vibration (first mode) of the fixed-base model.

This feature is also confirmed by the results achieved for all the remaining flexible-base models and earthquakes, which are not reported here, proving the effectiveness of the present rFDD-OMAX identification methodology in handling fixed-base conditions too.

5.3.2 Empirical method for the estimation of Soil-Structure Interaction effects

A second rFDD-OMAX approach belongs to a simplified empirical method for assessing seismic Soil-Structure Interaction effects on shear-type buildings, proposed by Renzi et al. [107]. They performed a parametric study in the linear range of seismic Soil-Structure Interaction effects on a large number of numerical shear-type buildings, by making comparisons with the related fixed-base conditions. The analysed structures were first modeled as an equivalent single degree of freedom (SDoF) system and dynamic analyses were then performed. The outcomes of the numerical analyses were used as a base, in order to obtain a simple analytical non-dimensional relationship, to be applied for each mode to estimate seismic Soil-Structure Interaction effects, in terms of modified period (and attached natural frequency) [107].

From this method, the statistical model describing the relationship between fixed-base (unknown) and flexible-base (known, estimated) periods, T_i and $\tilde{T}_i$, respectively, for the ith mode of vibration, may be deduced as [107]:

$$y_i = \frac{\tilde{T}_i}{T_i} = 1 + 0.7698 \left(\frac{h_{eq,i}}{T_i\, V_s}\right)^{1.663} \left(\frac{r}{H_{dep}}\right)^{-0.1359} \left(\frac{h_{eq,i}}{r}\right)^{0.8443} \tag{5.8}$$

where $h_{eq,i} = (\mathbf{H}^{\mathrm{T}}\mathbf{M}\boldsymbol{\phi}_i)/(\mathbf{r}^{\mathrm{T}}\mathbf{M}\boldsymbol{\phi}_i)$ is the equivalent height of the SDoF system for the ith mode [27], being $\boldsymbol{\phi}_i$ the ith mode shape, V_s the shear-wave velocity, r the radius of the foundation and H_{dep} the depth assumed for the bedrock.

Anyhow, as it could be seen from Eq. (5.8), period T_i of the fixed-base system appears on both sides of the equality, which makes it difficult for the use of this formulation towards estimation purposes. For the application of the method to the outcomes of the present rFDD algorithm (flexible-base parameters), a specific procedure has been developed here,

in order to obtain the related rFDD-OMAX fixed-base parameters. This procedure shall be performed for each estimated flexible-base frequency f_i.

Through the rFDD-OMAX algorithm, the determination of the fixed-base frequencies can be achieved by the following computational steps:

1. From the previous application of the rFDD algorithm, flexible-base natural frequency estimates $\tilde{f}_i$ (and consequently periods $\tilde{T}_i$ and mode shapes $\tilde{\boldsymbol{\phi}}_i$) can be achieved, for the estimated i^{th} mode of vibration.

2. The equivalent SDoF system height, for the ith mode, is computed as:
$$h_{eq,i} = \frac{\mathbf{H}^{\mathrm{T}}\mathbf{M}\tilde{\boldsymbol{\phi}}_i}{\mathbf{r}^{\mathrm{T}}\mathbf{M}\tilde{\boldsymbol{\phi}}_i} \tag{5.9}$$
where $\tilde{\boldsymbol{\phi}}_i$ is the ith mode shape estimate, coming from rFDD identification above.

3. Some parameters about the soil characteristics need to be known, or at least estimated, i.e. shear-wave velocity V_s and bedrock depth H_{dep}; in the present work, they have been taken as $V_s = V_{s,k}$, where k is the adopted soil case (see data in Table 5.1), while H_{dep} has been assumed as $H_{dep} = 50\,\mathrm{m}$, a value which was selected, after several assessments, as the physical parameter that was able to ensure the best fixed-base estimates.

4. Estimation of fixed-base period T_i, via recursive solution of the following equation, derived from Eq. (5.8):
$$\begin{aligned} T_i &= \frac{\tilde{T}_i}{y_i} = \\ &= \tilde{T}_i \left[1 + 0.7698 \left(\frac{h_{eq,i}}{T_i\, V_s} \right)^{1.663} \left(\frac{r}{H_{dep}} \right)^{-0.1359} \left(\frac{h_{eq,i}}{r} \right)^{0.8443} \right]^{-1} \end{aligned} \tag{5.10}$$
This model provides a frequency correction, to be applied to the original rFDD flexible-base period $\tilde{T}_i$, in order to get the underlying fixed-base one. The latter equation needs to be solved recursively, since sought fixed-base period T_i appears in both equality terms. In this study, a value $T_i^0 = \tilde{T}_i^0$ has been taken as a starting point for the recursions, until convergence of the solution has been reached. This means that the residual $\varepsilon = |(T_i^j - T_i^{j-1})/T_i^{j-1}| < \bar{\varepsilon}$, at j^{th} iteration, becomes lower than a given tolerance $\bar{\varepsilon}$. For the present analyses convergence tolerance $\bar{\varepsilon}$ has been taken as $\bar{\varepsilon} = 10^{-4}$.

The estimation of original fixed-base frequencies f_i may be directly related to ambient vibration conditions, which, jointly with the flexible-base features (seismic Soil-Structure Interaction effects) of the analysed structures, aims at a complete determination of their dynamic behaviour.

Fig. 5.10 presents an example of the estimated (flexible-base) and of the corrected (fixed-base) frequency deviations, with respect to the target frequencies of the fixed-base model. The El Centro earthquake is taken as a sample, for both Mass-proportional (ζ_{M}) and Rayleigh (ζ_{R}) damping. As it is clearly visible, the deviations, especially for the first modes, take significant benefit from the application of this OMAX correction. In fact, the deviation on the 1st fixed-base frequency estimate is brought to less than 15%, starting from an initial value of 25%. This certainly aims at a closer representation of the fixed-base conditions and also of the Soil-Structure Interaction effects read on the superstructure.

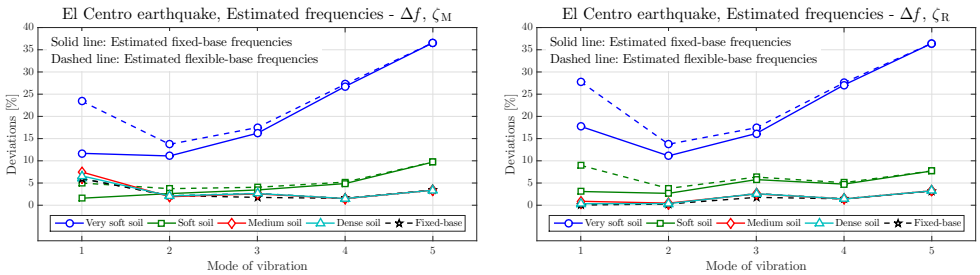

Figure 5.10: *Deviations of rFDD-OMAX estimated flexible-base and fixed-base natural frequencies with respect to the targets computed for the fixed-base model.*

5.4 Remarks and conclusions for the rFDD algorithm in the presence of Soil-Structure Interaction

The present Chapter 5 has outlined several informative results towards the use of a rFDD(-OMAX) identification algorithm for the determination of flexible- and fixed-base modal properties of linear frame buildings under earthquake excitation with Soil-Structure Interaction effects. Real seismic input and heavy-damping cases (in terms of identification challenge, though very realistic in practical cases) have been considered, getting closer to real earthquake engineering application scenarios. A five-storey shear-type frame with a Sway-Rocking foundation model has been analysed, by taking a set of ten earthquake excitations at bedrock's base and two types of superstructural damping models (Mass-proportional and Rayleigh damping), for a total of 100 analysed cases.

The effectiveness of the achieved results demonstrates the validity of the present identification methodology, standing from the goodness of the

estimated natural frequencies, modal damping ratios and mode shapes, for both flexible- and fixed-base conditions. This proves that the rFDD(-OMAX) technique can be used for up-to-date detection of building modal properties in the earthquake engineering range, considering Soil-Structure Interaction effects, within a linear context.

Summarizing main outcomes and results of the present study, the following salient issues may be briefly outlined:

- The rFDD algorithm proves to be a reliable identification method towards the estimation of Soil-Structure Interaction flexible-base modal parameters, i.e. natural frequencies, mode shapes and modal damping ratios under pure output-only conditions, with seismic response input and simultaneous heavy damping in terms of identification challenge. This kind of modal dynamic identification shall be innovative in the present dedicated literature.

- Flexible-base modal parameter estimates show to be accurate, despite for the presence of Soil-Structure Interaction effects. The computational steps of the rFDD algorithm demonstrated to be very effective under these tough identification conditions.

- The rFDD-OMAX condition belongs to the joint use of output-only response signals and foundation recordings (and/or free-field/ downhole acquisitions), towards estimating also fixed-base frequencies.

- The detection of Soil-Structure Interaction effects, by adapting method [108] (conceived for a SDoF system) to the present conditions (MDoF system, Section 5.3.1), results to be quite reliable in engineering terms.

- The quantification of Soil-Structure Interaction effects, by improving method [107], shows to be rather effective towards the estimation of fixed-base modal frequencies, i.e. for the explicit quantification of Soil-Structure Interaction effects.

Chapter 6

Data-Driven Stochastic Subspace Identification: theory and results

6.1 Fundamentals of the Data-Driven Stochastic Subspace Identification technique

Data-Driven Stochastic Subspace methods are parametric Time Domain approaches for system identification, which start from the use of discrete time state-space models. That without the need of covariance sequencies, thus relying just on the available data histories. OMA subspace methods, in particular, are based on obtaining the Kalman Filter (KF) states from the given output-only data, by using linear algebra tools and geometric concepts only [121]. So, once KF states are known, the identification problem becomes a linear least squares problem in the unknown system matrices. Typical underlying hypotheses of SSI-DATA methods are: (stationary) white noise input (so that process noise w_k and measurement noise v_k are not identically zero) and adequately long structural response signals (so that the number of measurements goes to infinity $j \to \infty$). Light damping (modal damping ratios in the order of $1 \div 2\%$) generally leads to better and less noisy estimates [106, 121].

The present SSI-DATA implementation attempts to clear these issues, when dealing with challenging earthquake-induced structural response signals. In the present section, all crucial steps of the theoretical framework of the SSI-DATA algorithm are exposed, basically relying on theoretical work [84, 85, 121] (Section 6.1.1). Then, the main workflow and novelties of the present SSI-DATA algorithm are introduced and explained in Section 6.1.3.

6.1.1 Main theoretical background of the SSI-DATA algorithm

A classical system of m second-order differential equations of motion of a linear dynamical structural system may be written as (*spatial model*):

$$\mathbf{M}\ddot{\mathbf{u}}(t) + \mathbf{C}\dot{\mathbf{u}}(t) + \mathbf{K}\mathbf{u}(t) = \bar{\mathbf{B}}\mathbf{f}'(t) \tag{6.1}$$

where $\mathbf{M}$, $\mathbf{C}$ and $\mathbf{K} \in \mathcal{R}^{m\times m}$ are the mass, damping and stiffness matrices, matrix $\bar{\mathbf{B}} \in \mathcal{R}^{m\times m}$ defines the location of the input channels, $\mathbf{f}'(t) \in \mathcal{R}^{m\times 1}$ is the input force vector and $\ddot{\mathbf{u}}(t)$, $\dot{\mathbf{u}}(t)$ and $\mathbf{u}(t) \in \mathcal{R}^{m\times 1}$ are the vectors of acceleration, velocity and displacement structural responses.

By switching to *State-Space* form, the m second-order differential equations of motion in Eq. (6.1) can be rewritten into $2m$ first-order differential equations as [121]:

$$\begin{cases} \dot{\mathbf{x}}(t) = \mathbf{A}_c\mathbf{x}(t) + \mathbf{B}_c\mathbf{f}'(t) \\ \mathbf{y}(t) = \mathbf{C}_c\mathbf{x}(t) + \mathbf{D}_c\mathbf{f}'(t) \end{cases} \tag{6.2}$$

being the first equation the *state equation*, in terms of *state vector* of responses $\mathbf{x}(t) \in \mathcal{R}^{2m\times 1}$, $\mathbf{x}(t) = \{\mathbf{u}(t)\ \dot{\mathbf{u}}(t)\}^{\mathrm{T}}$ and its time derivative $\dot{\mathbf{x}}(t) = \{\dot{\mathbf{u}}(t)\ \ddot{\mathbf{u}}(t)\}^{\mathrm{T}}$, and the second equation the *observer equation*, in terms of *observer vector* of responses $\mathbf{y}(t) \in \mathcal{R}^{m\times 1}$ (either displacements, velocities and/or, typically, accelerations). From Eq. (6.2), *state matrix* $\mathbf{A}_c \in \mathcal{R}^{2m\times 2m}$, input matrix $\mathbf{B}_c \in \mathcal{R}^{2m\times m}$, *output matrix* $\mathbf{C}_c \in \mathcal{R}^{m\times 2m}$ and *feed-through matrix* $\mathbf{D}_c \in \mathcal{R}^{m\times m}$ are defined as follows, where subscript c denotes continuous time [121]:

$$\begin{aligned} \mathbf{A}_c &= \begin{bmatrix} \mathbf{0}_{n\times n} & \mathbf{I}_{n\times n} \\ -\mathbf{M}^{-1}\mathbf{K} & -\mathbf{M}^{-1}\mathbf{C} \end{bmatrix}, & \mathbf{B}_c &= \begin{bmatrix} \mathbf{0}_{n\times n} \\ \mathbf{M}^{-1}\bar{\mathbf{B}} \end{bmatrix} \\ \mathbf{C}_c &= \begin{bmatrix} -\mathbf{M}^{-1}\mathbf{K} & -\mathbf{M}^{-1}\mathbf{C} \end{bmatrix}, & \mathbf{D}_c &= \mathbf{M}^{-1}\bar{\mathbf{B}} \end{aligned} \tag{6.3}$$

Here, the structures of matrices $\mathbf{C}_c$ and $\mathbf{D}_c$ refer to the adoption of acceleration responses for the observer vector, namely $\mathbf{y}(t) = \ddot{\mathbf{u}}(t)$.

In the OMA context, structures are excited by unmeasurable input excitations; this means that the information from excitation $\mathbf{f}'(t)$ is not available. Also, experimental tests yield measurements taken at discrete time instants, while Eqs. (6.1)-(6.3) are actually expressed in continuous time. For a given sampling time interval Δt, continuous-time equations can be discretized and solved at discrete time instants $t_k = k\Delta t, k = 1, \ldots, N$, with N being the total number of sampling points of the signal.

By taking into account the kth time instant and assuming unknown/unmeasured input (treated as white noise), classical SSI-DATA theory takes as a typical starting point of the identification process the following OMA Stochastic State-Space model in discrete-time notation [121]:

$$\begin{cases} \mathbf{x}_{k+1} = \mathbf{A}\mathbf{x}_k + \mathbf{w}_k \\ \mathbf{y}_k = \mathbf{C}\mathbf{x}_k + \mathbf{v}_k \end{cases} \tag{6.4}$$

being $\mathbf{x}_k = \{\mathbf{u}_k \ \mathbf{u}_{k+1}\}^{\mathrm{T}}$ the *state vector* of responses and its time derivative $\mathbf{x}_{k+1} = \{\mathbf{u}_{k+1} \ \mathbf{u}_{k+2}\}^{\mathrm{T}}$, and $\mathbf{y}_k$ the *observer vector* of responses (either displacements, velocities and/or, typically, accelerations, as considered here). Notation $\mathbf{u}_{k+1}$, $\mathbf{u}_{k+1}$ and $\mathbf{u}_{k+1}$ refers to the discrete-time counterparts of continuous-time vectors of displacement $\mathbf{u}(t)$, velocity $\dot{\mathbf{u}}(t)$ and acceleration $\ddot{\mathbf{u}}(t)$ responses, respectively. There, $\mathbf{A}$ and $\mathbf{C}$ are discrete-time counterparts of the $\mathbf{A}_c$ and $\mathbf{C}_c$ matrices, while vectors $\mathbf{w}_k$ and $\mathbf{v}_k \in \mathcal{R}^{2m\times 1}$ are zero mean, stationary white noise stochastic processes, representing process noise and measurement noise, respectively [121]. These $\mathbf{w}_k$ and $\mathbf{v}_k$ stochastic processes become necessary and shall be included, in order to describe real measurement data, which are also driven by uncertainty and noise.

Then, the salient mathematical and computational steps described in the following summarize the main workflow of the present SSI-DATA algorithm.

The first step of classical SSI-DATA identification algorithms is the computation of the so-called *block Hankel matrix* $\boldsymbol{H}_{0|2i-1} \in \mathcal{R}^{2mi\times j}$ of responses, which is directly calculated from the measurement data [121], i.e. system structural responses $\mathbf{y}_k$ (in the present case, accelerations), as:

$$\boldsymbol{H}_{0|2i-1} = \frac{1}{\sqrt{j}} \begin{bmatrix} \mathbf{y}_0 & \cdots & \mathbf{y}_{j-1} \\ \vdots & \ddots & \vdots \\ \mathbf{y}_{i-1} & \cdots & \mathbf{y}_{i+j-2} \\ \mathbf{y}_i & \cdots & \mathbf{y}_{i+j-1} \\ \vdots & \ddots & \vdots \\ \mathbf{y}_{2i-1} & \cdots & \mathbf{y}_{2i+j-2} \end{bmatrix} = \begin{bmatrix} \boldsymbol{Y}_{0|i-1} \\ \boldsymbol{Y}_{i|2i-1} \end{bmatrix} = \begin{bmatrix} \boldsymbol{Y}_p \\ \boldsymbol{Y}_f \end{bmatrix} \tag{6.5}$$

where the two partition sub-matrices refer to past $\boldsymbol{Y}_p = \boldsymbol{H}_{0|i-1}$ and future $\boldsymbol{Y}_f = \boldsymbol{H}_{i|2i-1}$ output channel matrices, where subscripts on the lefthand and righthand sides of delimiter | denote the first and the last element of the first column, respectively, of block Hankel matrix $\boldsymbol{H}_{0|2i-1}$. So, matrices $\boldsymbol{Y}_p$ and $\boldsymbol{Y}_f$ are defined by splitting matrix $\boldsymbol{H}_{0|2i-1}$ in two equal parts of i block rows, where number of block rows i shall be determined in agreement with condition $m \cdot i \geq n$ [83], being m the number of output (acquisition) channels and n the so-called *system order* (i.e. the dimension of square matrix $\mathbf{A}$ in the identification process, i.e. the rank of diagonal matrix $\boldsymbol{\Sigma}_1$ defined below). Number of columns j of block Hankel matrix $\boldsymbol{H}_{0|2i-1}$ is usually taken as $j = N - 2i + 1$, which implies that all recorded data

samples are used [121]. Thus, all following quantities showing subscript i refer to the assumed number of block rows. By observing Eq. (6.5), it is clear that the block Hankel matrix consists of the repetition of the same element in each anti-diagonal term.

The second computational step is based on the calculation of *projection matrix* $\boldsymbol{P}_i \in \mathcal{R}^{mi \times mi}$, i.e. the orthogonal projection of the row space of future output channels $\boldsymbol{Y}_f$ into the row space of past output channels $\boldsymbol{Y}_p$, which can be expressed as [121]:

$$\boldsymbol{P}_i = \boldsymbol{Y}_f / \boldsymbol{Y}_p = \boldsymbol{Y}_f \boldsymbol{Y}_p^{\mathrm{T}} (\boldsymbol{Y}_p \boldsymbol{Y}_p^{\mathrm{T}})^{\dagger} \boldsymbol{Y}_p = \boldsymbol{O}_i \hat{\boldsymbol{S}}_i \tag{6.6}$$

where symbol † indicates Moore-Penrose pseudo-inverse, whilst the factorization of projection matrix $\boldsymbol{P}_i$ into the product of *observability matrix* $\boldsymbol{O}_i \in \mathcal{R}^{mi \times n}$ and *Kalman filter state sequence* $\hat{\boldsymbol{S}}_i \in \mathcal{R}^{n \times mi}$ defines a main theorem of SSI-DATA [106, 121], where n is the selected system order, as detailed in the following.

Then, observability matrix $\boldsymbol{O}_i$ and Kalman filter state sequence $\hat{\boldsymbol{S}}_i$ may be defined as follows [106, 121]:

$$\boldsymbol{O}_i = \begin{bmatrix} \boldsymbol{C} \\ \boldsymbol{C}\boldsymbol{A} \\ \vdots \\ \boldsymbol{C}\boldsymbol{A}^{i-1} \end{bmatrix}, \quad \hat{\boldsymbol{S}}_i = \begin{bmatrix} \hat{\boldsymbol{s}}_i & \hat{\boldsymbol{s}}_{i+1} & \cdots & \hat{\boldsymbol{s}}_{i+j-1} \end{bmatrix} \tag{6.7}$$

where $(q+1)^{th}$ column $\hat{\boldsymbol{s}}_{i+q}$ of matrix $\hat{\boldsymbol{S}}_i$ represents the state estimate based on i output values $\mathbf{y}_q, \ldots, \mathbf{y}_{i+q-1}$ [121].

Furthermore, through the application of specific weighting matrices $\boldsymbol{W}_1$ and $\boldsymbol{W}_2$ to projection matrix $\boldsymbol{P}_i$, a SVD may be derived, by holding non-zero singular values only [106, 121], as:

$$\boldsymbol{W}_1 \boldsymbol{P}_i \boldsymbol{W}_2 = [\mathbf{U}_1 \mathbf{U}_2] \begin{bmatrix} \boldsymbol{\Sigma}_1 & \mathbf{0} \\ \mathbf{0} & \mathbf{0} \end{bmatrix} \begin{bmatrix} \mathbf{V}_1^{\mathrm{T}} \\ \mathbf{V}_2^{\mathrm{T}} \end{bmatrix} = \mathbf{U}_1 \boldsymbol{\Sigma}_1 \mathbf{V}_1^{\mathrm{T}} \tag{6.8}$$

where $\mathbf{U}_k$ and $\mathbf{V}_k \in \mathcal{R}^{mi \times n}$, $k = 1, 2$ are the singular vector matrices, and $\boldsymbol{\Sigma}_1 \in \mathcal{R}^{n \times n}$ is the diagonal matrix holding the non-zero singular values (which allows to estimate the rank of matrix $\boldsymbol{P}_i$). The selection of the dimension (n) of square diagonal matrix $\boldsymbol{\Sigma}_1$ fixes system order n of the State-Space model, which is adopted for the subsequent computational steps.

As concerning weighting matrices $\boldsymbol{W}_1 \in \mathcal{R}^{mi \times mi}$ and $\boldsymbol{W}_2 \in \mathcal{R}^{mi \times mi}$, they may be defined according to different weighting proposals [121], namely Principal Component (PC), Unweighted Principal Component (UPC) and Canonical Variate Analysis (CVA). Accordingly, the corresponding weighting matrices can be defined as follows [121]:

- for the Principal Component (PC) weighting:

$$\boldsymbol{W}_1 = \mathbf{I}, \quad \boldsymbol{W}_2 = \boldsymbol{Y}_p^{\mathrm{T}} \left(\frac{1}{j} \boldsymbol{Y}_p \boldsymbol{Y}_p^{\mathrm{T}} \right)^{-\frac{1}{2}} \boldsymbol{Y}_p; \tag{6.9}$$

- for the Unweighted Principal Component (UPC) weighting:

$$\boldsymbol{W}_1 = \mathbf{I}, \quad \boldsymbol{W}_2 = \mathbf{I}; \tag{6.10}$$

- for the Canonical Variate Analysis weighting (CVA) (of a main use in the following):

$$\boldsymbol{W}_1 = \left(\frac{1}{j} \boldsymbol{Y}_f \boldsymbol{Y}_f^{\mathrm{T}} \right)^{-\frac{1}{2}}, \quad \boldsymbol{W}_2 = \mathbf{I}. \tag{6.11}$$

where j is again the number of columns of block Hankel matrix $\boldsymbol{H}_{0|2i-1}$ (taken as $j = N - 2i + 1$ in the present case, i.e. all recorded data samples are used) [121]).

As a practical rule, literature references suggest that the UPC SSI-DATA should be used in the presence of modes of equal strength and data with a good signal-to-noise ratio. On the contrary, CVA SSI-DATA should be used in the presence of noisy data and modes characterized by widely different strengths. Finally, the PC SSI-DATA variant may be considered as a compromise between the chioce of UPC and CVA algorithms [106, 121].

Then, starting from Eq. (6.8), observability matrix $\boldsymbol{O}_i$ and Kalman filter state sequence $\hat{\boldsymbol{S}}_i$ may be computed as:

$$\boldsymbol{O}_i = \mathbf{U}_1 \boldsymbol{\Sigma}_1^{1/2} \mathbf{T}, \quad \hat{\boldsymbol{S}}_i = \boldsymbol{O}_i^{\dagger} \boldsymbol{P}_i \tag{6.12}$$

where $\mathbf{T} \in \mathcal{R}^{n \times n}$ is a further possible weighting matrix, generally taken as an identity matrix, $\mathbf{T} = \mathbf{I}$ (as done here). By taking into account Eqs. (6.6) and (6.12), Kalman filter state sequence $\hat{\boldsymbol{S}}_{i+1}$ and output sequence $\boldsymbol{Y}_{i|i}$ may be calculated as shown in [121]. Especially, $\boldsymbol{Y}_{i|i}$ comes directly from a different partition of block Hankel matrix $\boldsymbol{H}_{0|2i-1}$:

$$\boldsymbol{H}_{0|2i-1} = \begin{bmatrix} \boldsymbol{Y}_{0|i-1} \\ \boldsymbol{Y}_{i|i} \\ \boldsymbol{Y}_{i+1|2i-1} \end{bmatrix} = \begin{bmatrix} \boldsymbol{Y}_{0|i} \\ \boldsymbol{Y}_{i+1|2i-1} \end{bmatrix} = \begin{bmatrix} \boldsymbol{Y}_p^{+} \\ \boldsymbol{Y}_f^{-} \end{bmatrix} \tag{6.13}$$

where superscript symbols $+$ and $-$ stay for addition and for subtraction of one block row to the original $\boldsymbol{Y}_p$ and $\boldsymbol{Y}_f$ matrices. Then, from projection matrix $\boldsymbol{P}_{i-1}$ it is possible to obtain:

$$\boldsymbol{P}_{i-1} = \boldsymbol{Y}_f^- / \boldsymbol{Y}_p^+ = \boldsymbol{Y}_f^- \boldsymbol{Y}_p^{+\mathrm{T}} (\boldsymbol{Y}_p^+ \boldsymbol{Y}_p^{+\mathrm{T}})^\dagger \boldsymbol{Y}_p^+ = \boldsymbol{O}_{i-1} \hat{\boldsymbol{S}}_{i+1} \tag{6.14}$$

where observability matrix $\boldsymbol{O}_{i-1}$ may be directly obtained from $\boldsymbol{O}_i$ by deleting the last m rows, while Kalman filter state sequence $\hat{\boldsymbol{S}}_{i+1}$ can be determined as:

$$\hat{\boldsymbol{S}}_{i+1} = \boldsymbol{O}_{i-1}^\dagger \boldsymbol{P}_{i-1} \tag{6.15}$$

At this stage, discrete-time State-Space matrices $\mathbf{A}$ and $\mathbf{C}$ may be computed through an asymptotically-unbiased least squares estimate as [121]:

$$\begin{bmatrix} \mathbf{A} \\ \mathbf{C} \end{bmatrix} = \begin{bmatrix} \hat{\boldsymbol{S}}_{i+1} \\ \boldsymbol{Y}_{i|i} \end{bmatrix} \hat{\boldsymbol{S}}_i^\dagger \tag{6.16}$$

Then, the eigenvalue decomposition of discrete-time state matrix $\mathbf{A}$ allows for the estimation of the modal parameters, by passing through an eigenvalue decomposition and a conversion from discrete- to continuous-time of the eigenvalues themselves.

6.1.2 Implemented SSI-DATA algorithm: computational steps

Block Hankel matrix $\boldsymbol{H}_{0|2i-1}$ may be further processed via LQ factorization [45], in order to efficiently compute several contributes of the main SSI-DATA workflow:

$$\boldsymbol{H}_{0|2i-1} = \boldsymbol{L}\boldsymbol{Q} \tag{6.17}$$

so that the Hankel matrix $\boldsymbol{H}_{0|2i-1}$ may be expressed as the product of a lower triangular matrix $\boldsymbol{L} \in \boldsymbol{R}^{2mi \times 2mi}$ and an orthonormal matrix $\boldsymbol{Q} \in \boldsymbol{R}^{2mi \times j}$:

$$\boldsymbol{L} = \begin{bmatrix} \boldsymbol{L}_{11} & \mathbf{0} & \mathbf{0} \\ \boldsymbol{L}_{21} & \boldsymbol{L}_{22} & \mathbf{0} \\ \boldsymbol{L}_{31} & \boldsymbol{L}_{32} & \boldsymbol{L}_{33} \end{bmatrix}, \quad \boldsymbol{Q} = \begin{bmatrix} \boldsymbol{Q}_1^T \\ \boldsymbol{Q}_2^T \\ \boldsymbol{Q}_3^T \end{bmatrix} \tag{6.18}$$

That in order to obtain the projection matrices $\boldsymbol{P}_i$ and $\boldsymbol{P}_{i-1}$ of the row space of future output channels into the row space of past output channels directly from the LQ decomposition terms [106]:

$$\boldsymbol{P}_i = \boldsymbol{Y}_f / \boldsymbol{Y}_p = \begin{bmatrix} \boldsymbol{L}_{21} \\ \boldsymbol{L}_{31} \end{bmatrix} \boldsymbol{Q}_1^T \tag{6.19}$$

$$\boldsymbol{P}_{i-1} = \boldsymbol{Y}_f^- / \boldsymbol{Y}_p^+ = \begin{bmatrix} \boldsymbol{L}_{31} & \boldsymbol{L}_{32} \end{bmatrix} \begin{bmatrix} \boldsymbol{Q}_1^T \\ \boldsymbol{Q}_2^T \end{bmatrix} \tag{6.20}$$

Moreover, output sequence $\boldsymbol{Y}_{i|i}$, instead than from a partition of block Hankel matrix $\boldsymbol{H}_{0|2i-1}$, may be expressed as:

$$\boldsymbol{Y}_{i|i} = \begin{bmatrix} \boldsymbol{L}_{21} & \boldsymbol{L}_{22} \end{bmatrix} \begin{bmatrix} \boldsymbol{Q}_1^T \\ \boldsymbol{Q}_2^T \end{bmatrix} \tag{6.21}$$

So, Kalman filter state sequences $\hat{\boldsymbol{S}}_i$ and $\hat{\boldsymbol{S}}_{i+1}$, by substituting Eqs. (6.19) and (6.20) into Eqs. (6.12) and (6.15), can be calculated as:

$$\hat{\boldsymbol{S}}_i = \left(\mathbf{U}_1 \boldsymbol{\Sigma}_1^{1/2} \mathbf{T}\right)^{\dagger} \begin{bmatrix} \boldsymbol{L}_{21} \\ \boldsymbol{L}_{31} \end{bmatrix} \boldsymbol{Q}_1^T \tag{6.22}$$

$$\hat{\boldsymbol{S}}_{i+1} = \left(\mathbf{U}_1 \boldsymbol{\Sigma}_1^{1/2} \mathbf{T}\right)^{\uparrow\dagger} \begin{bmatrix} \boldsymbol{L}_{31} & \boldsymbol{L}_{32} \end{bmatrix} \begin{bmatrix} \boldsymbol{Q}_1^T \\ \boldsymbol{Q}_2^T \end{bmatrix} \tag{6.23}$$

where apex symbol $\uparrow$ denotes that the last m rows have been deleted from the $\mathbf{U}_1 \boldsymbol{\Sigma}_1^{1/2} \mathbf{T}$ matrix product.

Then, the State-Space matrices can be generally derived according to three different approaches, as outlined in detail in [121]. They differ for the capability to ensure the positive realness of covariance sequences.

For the present SSI-DATA algorithm, the first approach is adopted. It directly uses the state sequences to estimate the State-Space matrices. In fact, once the Kalman filter state sequences $\hat{\boldsymbol{S}}_i$ and $\hat{\boldsymbol{S}}_{i+1}$ have been estimated according to Eqs. (6.22) and (6.23), while output sequence $\boldsymbol{Y}_{i|i}$ has been calculated from Eq. (6.21), state matrices $\boldsymbol{A}$ and $\boldsymbol{C}$ may be computed from the following overdetermined set of linear equations, obtained by stacking the State-Space models for the time instants from i up to $i+j-1$:

$$\begin{bmatrix} \hat{\boldsymbol{S}}_{i+1} \\ \boldsymbol{Y}_{i|i} \end{bmatrix} = \begin{bmatrix} \boldsymbol{A} \\ \boldsymbol{C} \end{bmatrix} \hat{\boldsymbol{S}}_i + \begin{bmatrix} \boldsymbol{\rho}_w \\ \boldsymbol{\rho}_v \end{bmatrix} \tag{6.24}$$

where Kalman filter residuals $\boldsymbol{\rho}_w$ and $\boldsymbol{\rho}_v$ (also named innovations) are uncorrelated with Kalman filter state sequences $\hat{\boldsymbol{S}}_i$. Thus, this set of equations can be solved in a least squares sense. In fact, by taking into account that the least squares residuals are orthogonal and, therefore, uncorrelated with regressors $\hat{\boldsymbol{S}}_i$. In this way, an asymptotically-unbiased least squares estimate of $\boldsymbol{A}$ and $\boldsymbol{C}$ may be obtained from previously exposed Eq. (6.16):

$$\begin{bmatrix} \mathbf{A} \\ \mathbf{C} \end{bmatrix} = \begin{bmatrix} \left(\mathbf{U}_1 \boldsymbol{\Sigma}_1^{1/2} \mathbf{T}\right)^{\uparrow\dagger} \begin{bmatrix} \boldsymbol{L}_{31} & \boldsymbol{L}_{32} \end{bmatrix} \\ \begin{bmatrix} \boldsymbol{L}_{21} & \boldsymbol{L}_{22} \end{bmatrix} \end{bmatrix} \left[\left(\mathbf{U}_1 \boldsymbol{\Sigma}_1^{1/2} \mathbf{T}\right)^{\dagger} \begin{bmatrix} \boldsymbol{L}_{21} \\ \boldsymbol{L}_{31} \end{bmatrix} \right]^{\dagger} \tag{6.25}$$

where all quantities on the right hand side of Eq. (6.25) may be expressed in terms of the LQ factors [106]. As a result of their orthonormality, the

Q factors wipe out from Eq. (6.25), leading to a significant data reduction coming from the adoption of the L factors only.

Once matrices $\mathbf{A}$ and $\mathbf{C}$ have been determined, modal parameters may be obtained from the eigenvalue decomposition of discrete-time state matrix $\mathbf{A}$:

$$\mathbf{A} = \mathbf{\Psi}\mathcal{M}\mathbf{\Psi}^{-1} \tag{6.26}$$

where matrices $\mathbf{\Psi}$ and $\mathcal{M}$ hold the discrete-time eigenvectors $\boldsymbol{\psi}_r$ and eigenvalues μ_r, respectively.

Thus, the rth mode shape estimate of the system may be obtained as:

$$\boldsymbol{\phi}_r = \mathbf{C}\boldsymbol{\psi}_r \tag{6.27}$$

Afterwards, discrete-time eigenvalues μ_r are converted to continuous time eigenvalues λ_r (or system poles) as:

$$\mu_r = e^{\lambda_r \Delta t} \Rightarrow \lambda_r = \frac{\ln(\mu_r)}{\Delta t} \tag{6.28}$$

Finally natural frequency, damped modal frequency and modal damping ratio of rth mode may be computed as [106]:

$$f_r = \frac{|\lambda_r|}{2\pi}, \quad f_{r,d} = \frac{\mathrm{Im}(\lambda_r)}{2\pi}, \quad \zeta_r = -\frac{\mathrm{Re}(\lambda_r)}{|\lambda_r|} \tag{6.29}$$

6.1.3 Novelties of the present SSI-DATA algorithm

Main assumptions of classical SSI-DATA methods consist of (stationary) white noise input (so that process noise w_k and measurement noise v_k are not identically zero) and adequately long structural response signals (so that the number of measurements goes to infinity $j \to \infty$), to achieve a suitable *stabilization* of the estimated poles. Light damping (modal damping ratios in the order of $1 \div 2\%$) leads to better estimates, too, since it may reduce the occurrence of noise poles or of mathematical poles (e.g. false stable poles characterized by a positive real part and a negative damping ratio) [106, 121].

The present SSI-DATA algorithm, whose original theoretical background comes from the general formulation in [83, 121], as outlined in earlier Section 6.1.1, may be intended as a first implementation attempt, for SSI-DATA algorithms, to deal with earthquake-induced structural response signals, at concurrent heavy structural damping in terms of modal identification challenge.

Therefore, the following paragraphs summarize the main steps and issues related to the present SSI-DATA implementation.

6.1.3.1 Definition of the weighting matrices

A first issue is to appropriately define weighting matrices $\boldsymbol{W}_1$ and $\boldsymbol{W}_2$ that pre- and post-multiply projection matrix $\boldsymbol{P}_i$. After first extensive simulations performed in [82], under white noise input or seismic excitation, it was shown that the Canonical Variate Analysis weighting (CVA) [121], with weighting matrices $\boldsymbol{W}_1$ and $\boldsymbol{W}_2$ as given in Eq. (6.11), turns out to be the most stable and performing weighting option towards achieving reliable estimates at seismic response input and concurrent heavy damping. This feature was demonstrated also in [94, 98], where both synthetic and real earthquake-induced structural response signals were adopted towards identification purposes, also with simultaneous heavy damping, in terms of identification challenge.

The Canonical Variate Analysis weighting (CVA) weighting, as opposed to widely-used Principal Component (PC) (Eq. (6.9)) and Unweighted Principal Component (UPC) (Eq. (6.10)) weightings, returns even less noise or mathematical poles and looks mostly able to separate true physical modes from possible spurious earthquake harmonics.

Then, jointly with the selection of the CVA weighting, several features help in returning much reliable modal parameter estimates under seismic response input. Among those, Butterworth low-pass filtering, generally set with order 8 and cutting frequency 25 Hz, without decimation of the signals. Then, the Block Hankel matrix is generally set with number of block rows equal to $i = 50$ (usually adopted as variable in the range $30 \leq i \leq 80$) and number of columns $j = N - 2i + 1$.

6.1.3.2 Specifically-developed stabilization diagrams

For the correct selection of system order n and for the determination of the stable poles (i.e. the poles where frequency, mode shape and modal damping ratio estimates show to be stable and not deriving from noise or mathematical poles), a *stabilization diagram* may be constructed from the SSI-DATA identification outcomes [18, 84]. It displays the poles that are obtained according to different considered system orders, as a function of the estimated frequency lines. The Singular Value (SV) curves extracted from SVD of SSI-DATA output spectral matrix $\mathbf{G}_{yy}(\omega)$ may be reported too, within the same stabilization diagram. This matrix may be typically calculated from the estimated SSI model as outlined in [83], by adopting the estimated *next state-output covariance matrix* and the *output covariance matrix* [106] as:

$$\mathbf{G}_{yy}(z) = \mathbf{C}(z\mathbf{I} - \mathbf{A})^{-1}\mathbf{G} + \mathbf{R}_o + \mathbf{G}^{\mathrm{T}}(z^{-1}\mathbf{I} - \mathbf{A}^{\mathrm{T}})^{-1}\mathbf{C}^{\mathrm{T}}|_{z=e^{\mathrm{i}\omega\Delta t}}. \quad (6.30)$$

where $\mathbf{G}$ is the *next state-output covariance matrix*, which corresponds to

the last m columns of the reversed controllability matrix $\mathbf{\Gamma}_i$ [121]:

$$\mathbf{\Gamma}_i = \boldsymbol{O}_i^{\dagger} \frac{1}{j} \boldsymbol{Y}_f \boldsymbol{Y}_p^{\mathrm{T}} \tag{6.31}$$

and $\mathbf{R}_o$ is the *output covariance matrix*, defined as [106]:

$$\boldsymbol{R}_0 = \frac{1}{j} \boldsymbol{Y}_{i|i} \boldsymbol{Y}_{i|i}^{\mathrm{T}} \tag{6.32}$$

The expression in Eq. (6.30) can be evaluated for any number of the unit circle $z = e^{\mathrm{i}\omega\Delta t}$, where ω can be any frequency of interest [83].

As an original alternative of the present work, a novel integrated arrangement considers instead the use of SV curves, which are computed from the SVD of direct output spectral matrix $\mathbf{G}_{yy}(\omega)$. This is calculated through a routine of the previous rFDD algorithm, by adopting Welch's modified periodogram [93], here reported for added clarity:

$$\mathbf{G}_{yy}(\omega) \simeq \frac{1-r}{K} \sum_{k=1}^{K/(1-r)} \frac{\left[\sum_{t=0}^{L-1} \overline{\mathbf{y}}_k(t) \mathrm{W}(t) e^{-\mathrm{i}\omega \frac{t}{L}}\right] \left[\sum_{t=0}^{L-1} \mathbf{y}_k^{\mathrm{T}}(t) \mathrm{W}(t) e^{-\mathrm{i}\omega \frac{t}{L}}\right]}{\left[\sum_{t=0}^{L-1} \mathrm{W}(t)^2\right]} \tag{6.33}$$

where K is the number of segments of length L and overlapping r ($r = 2/3$ in the present work) in which initial signal $\mathbf{y}(t)$ has been divided, $\mathbf{y}_k(t)$ is the kth segment of the original signal and $\mathrm{W}(t)$ is the considered windowing function (a Hanning window in the present work [9]).

Such proposed integration of SSI and FDD information demonstrates to provide a reliable tool to support the individuation of the stable SSI poles within the stabilization diagram, especially when dealing with earthquake-induced structural response signals and at concurrent heavy damping, as handled here.

Further, the generally adopted stabilization diagram parameters are a maximum order $n = 150$ (in general, adopted as $n = m \cdot i$, as a function of number of response channels m and number of block rows i), while the detection of stable poles is set with tolerance levels equal to $\Delta f_k = |f_k - f_{k+1}|/f_k < 0.01$, $\Delta\zeta_k = |\zeta_k - \zeta_{k+1}|/\zeta_k < 0.075$ and $\Delta\mathrm{MAC}_k = 1 - \mathrm{MAC}(\boldsymbol{\phi}_k, \boldsymbol{\phi}_{k+1}) < 0.02$ for frequencies, modal damping ratios and MACs, respectively, being k the current model order. Than, the stabilization diagram SVs are computed through SVD of the PSD matrix as estimated via Welch's Modified Periodogram (Eq. (6.33), set with 2048-points Hanning smoothing windows and 66.7% overlapping.

6.1.3.3 System order selection and modal dynamic identification

Anyway, the most severe issue in the present SSI identification keeps lying in the fact that seismic response signals are characterized by rather short durations (specifically with respect to ambient vibration recordings), while as a basilar assumption the method requires $j \to \infty$. This directly affects the achievable estimates, since the poles intrinsically display a harder stabilization.

So, the maximum system order employed in the analysis shall be incremented, jointly with a careful setting of the adopted number of block rows in the Hankel matrix. This has been specifically pursued in the present implementation (see also preliminary investigation results in [82,98]). In this way, better natural frequency and mode shape estimates may be achieved. As regarding to the modal damping ratios, they appear to be the most challenging parameters to be detected by the present SSI identification, especially in relation to the cited very short durations of the seismic response signals.

Finally, a sample of the outcomes from the SSI-DATA algorithm is compared with the rFDD outcomes in Fig. 6.1, operating here at seismic response input and concurrent heavy damping. In this representation, the Singular Value Decomposition with peak-picking of the modes of vibration (left) and the *Global stabilization diagram* with the first rFDD Singular Value, representing rFDD and SSI-DATA all together (right) are respectively depicted. The Global stabilization diagram displays the stable poles, at increasing system order n, concerning frequency, damping ratio and mode shape. Stable poles are selected as poles with a stable frequency, damping ratio and mode shape, between two consecutive system orders (they are marked with blue circles in Fig. 6.1).

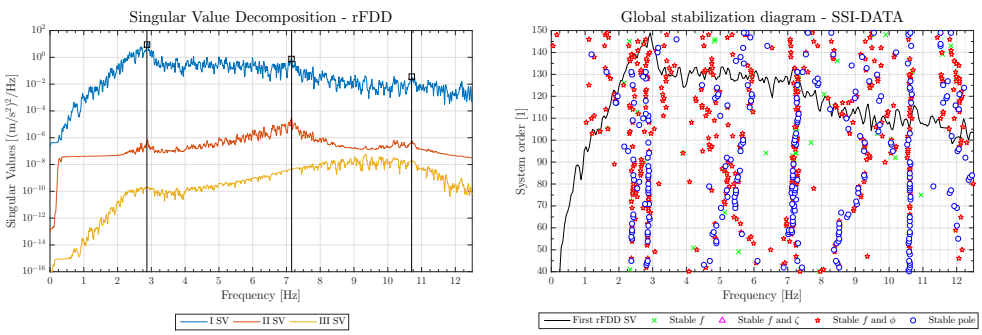

Figure 6.1: *Singular Value Decomposition and peak-picking of the modes of vibration by rFDD (left) and Global Stabilization Diagram with 1st rFDD SV by SSI-DATA (right), three-storey frame, synthetic response signals, earthquake of Maule (CH).*

Then, a sample of the outcomes from the SSI-DATA algorithm is compared to the rFDD outcomes in Fig. 6.2 , by adopting real earthquake-induced structural response data coming from the local Loma Prieta earthquake excitation on the San Bruno six-storey office building (see Chapter 8 for more details). In this figure, the Singular Value Decomposition with modal peak-picking and the Global Stabilization Diagram with the first rFDD Singular Value, for the NS response component, are depicted. Despite for the real seismic-induced responses, the first three modes of vibration can still be detected from the graphs.

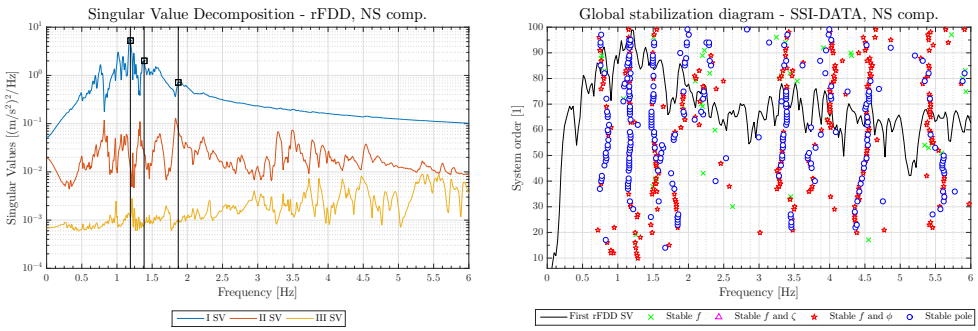

Figure 6.2: *Singular Value Decomposition and peak-picking of the modes of vibration by rFDD (left) and Global Stabilization Diagram with 1st rFDD SV by SSI-DATA (right), San Bruno six-storey office building, real response signals, earthquake of Loma Prieta (LP), NS component.*

6.2 Results from synthetic output-only modal dynamic identification

In the present section, selected analyses and results are going to be presented, taken from the whole bulge of cases that have been analysed [82, 94, 98].

As seen in Chapter 4, the focus falls again on two different structures, namely a reference three-storey shear-type frame (Table 4.2) and a more realistic ten-storey shear-type frame (Table 4.3), both characterized by heavy damping. As before, these structures are analysed through the adoption of a set of ten earthquake base-excitations (Table 4.1). Since these structures and earthquakes are adopted for all the three proposed methods, namely rFDD (Chapter 4), SSI-DATA (present Chapter 6) and FDCIM (Chapter 7), a detailed comparison among these algorithms in the Earthquake Engineering range is gradually approached.

6.2.1 Analyses and results with a reference three-storey frame

By taking as base excitation the single instances from the set of ten selected earthquake recordings presented in Section 4.1 (Table 4.1), modal dynamic identification analyses have been performed with the present SSI-DATA algorithm, in order to identify all strong ground motion modal parameters.

As concerning to the present SSI-DATA algorithm, the performed analyses adopted the following settings:

- Butterworth low-pass filtering, order 8, cutting frequency 25 Hz, no decimation of the signals (earthquake-induced structural response signals – input channels for the SSI-DATA algorithm);
- Block Hankel matrix parameters: number of block rows set to $i = 50$ (in general, adopted as variable in the range $30 \leq i \leq 80$), number of columns $j = N - 2i + 1$, for all the analysed cases;
- Stabilization diagram parameters: maximum order $n = 150$ (in general, adopted as $n = m \cdot i$, as a function of number of response channels m and number of block rows i), detection of stable poles with tolerance levels set to $\Delta f_k = |f_k - f_{k+1}|/f_k < 0.01$, $\Delta\zeta_k = |\zeta_k - \zeta_{k+1}|/\zeta_k < 0.075$ and $\Delta\mathrm{MAC}_k = 1 - \mathrm{MAC}(\boldsymbol{\phi}_k, \boldsymbol{\phi}_{k+1}) < 0.02$ for frequencies, modal damping ratios and MACs, respectively, being k the current model order;
- Stabilization diagram SVs computed through SVD of the PSD matrix, as estimated via Welch's Modified Periodogram, set with 2048-points Hanning smoothing windows and 66.7% overlapping.

Regarding SSI-DATA outcomes, the achieved Global Stabilization Diagrams, coupled with the representation of the 1st rFDD SV (see Section 6.1.3), shows three clear lines of stabilization of the poles. These lines may be discerned from the remaining poles, which are spurious poles coming from earthquake harmonics or from numerical or mathematical poles. The use of the rFDD SV considerably helps in the selection of the correct stable poles, since it provides a better indication with respect to classically adopted PSDs within the stabilization diagrams. See the extensive analysis and details reported in [82, 98].

Thus, by the strategies and settings reported above, complete synthetic output-only analyses with the SSI-DATA method have been performed. A synopsis from all the achieved results is reported in Fig. 6.3, where the estimates in terms of absolute deviations of SSI-DATA identified natural

frequencies Δf and modal damping ratios $\Delta\zeta$ and achieved MAC indexes for the estimated mode shapes are depicted (see Eqs. 4.1a-4.1c).

The SSI-DATA estimated frequencies show quite scattered deviations, with deviations up to 14%, higher than the maximum deviation of 5% registered for the rFDD algorithm. The estimated modal damping ratios display higher deviations with respect to those from the previous rFDD outcomes, with modal damping ratios discrepancies raising up to 70%. By this method, the order of magnitude is more or less caught, but deviations look much higher and often rather unacceptable in engineering terms. However, it should be recalled that really tough heavy-damping identification conditions have been considered here. Generally, the frequency and damping estimates from the rFDD cases show to be much closer to the target values than from the SSI-DATA ones. In this sense, Frequency Domain rFDD appears superior to Time Domain SSI-DATA, within the considered seismic engineering scenario at simultaneous heavy damping, according to the present implementation and achieved level of refinement.

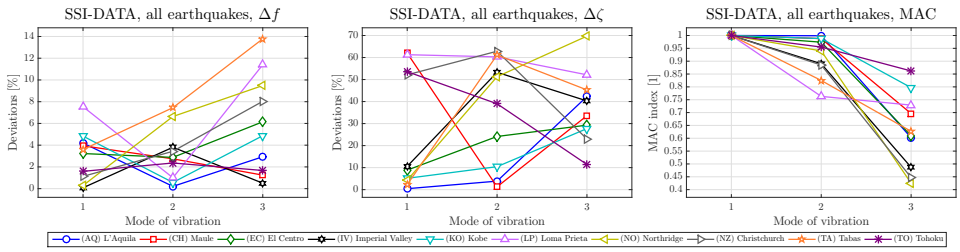

Figure 6.3: *Deviations of estimated natural frequencies and modal damping ratios, and MAC indexes, three-storey frame, synthetic response signals, SSI-DATA algorithm, complete considered earthquake dataset.*

MAC indexes perform slightly less well with the present SSI-DATA algorithm, than with the rFDD method. For the first two modes, MAC values are always higher than 0.75, with acceptable values in engineering terms. The third modes, instead, show to display some problems, especially with the IV, NO and NZ cases (Table 4.1), which return quite unreliable mode shapes. Thus, also in terms of mode shape estimates, rFDD performs better than SSI-DATA, in the present seismic and heavy damping context.

Then, global results on the achieved modal estimates are further summarized in Fig. 6.4, where the absolute deviations of the estimated natural frequencies and the modal damping ratios, and the MAC indexes are represented, in terms of suitably-designed dispersion diagrams [97], as adopted earlier in Chapter 4.

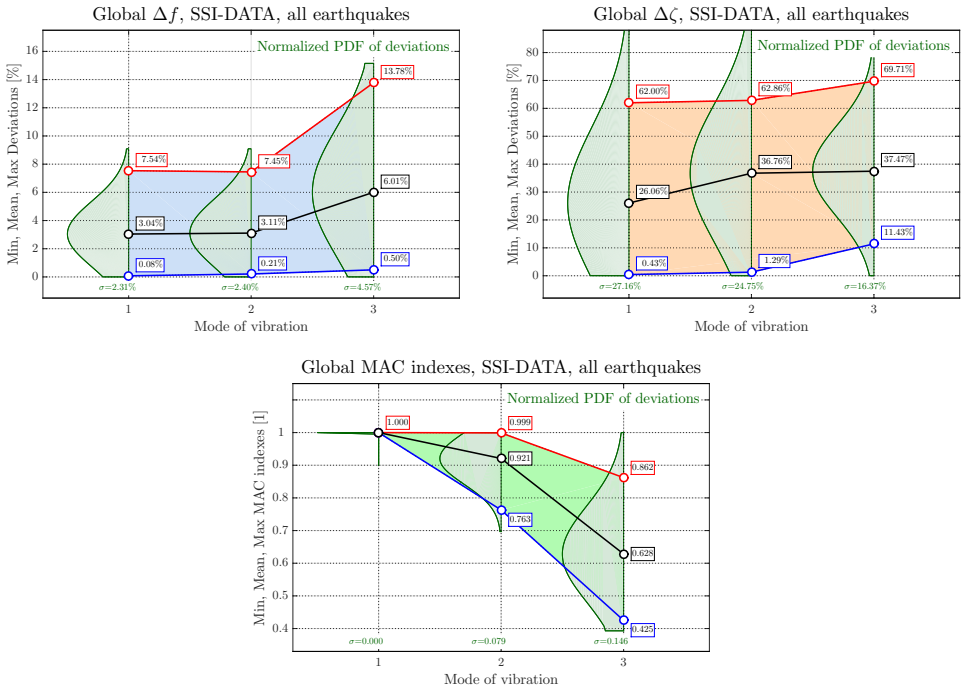

Figure 6.4: *Dispersion diagrams for the deviations of estimated natural frequencies and modal damping ratios, and for the MAC indexes, three-storey frame, synthetic response signals, SSI-DATA algorithm, complete considered earthquake dataset. Minimum, mean and maximum values, and standard deviations are indicated.*

As before, these truncated Gaussians represent the probability of appearance of a certain deviation, as associated to each estimate, between the minimum and the maximum value, and are centred on the mean value. Again, maximum deviations are always on the Gaussian tails, while the minimum deviations lay in the Gaussian center. This confirms the goodness of the achieved SSI-DATA modal identification estimates, too.

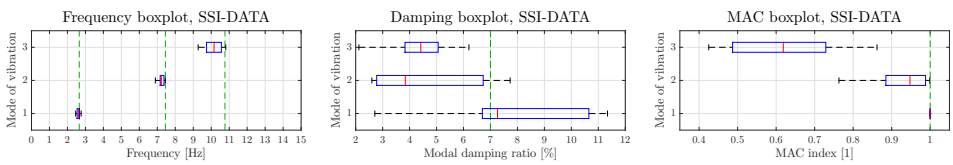

Figure 6.5: *Boxplot diagrams for estimated natural frequencies, modal damping ratios and MAC indexes, three-storey frame, synthetic response signals, SSI-DATA algorithm, complete considered earthquake dataset.*

Finally, the achieved results are also synoptically reported in statistical form in Fig. 6.5, by making use of appropriate boxplots, as previously

adopted in Chapter 4. The presented boxplots confirm also the goodness of the achieved SSI-DATA estimates. Natural frequency estimates show to substantially catch the expected target values. Also MAC indexes reveal reliable mode shape estimates, including for the last modes of vibration, although SSI-DATA returns less accurate results than rFDD, though still acceptable in engineering terms. Finally, concerning the modal damping ratio estimates with the SSI-DATA, some troubles appear, especially on the second and third modes of vibration.

6.2.2 Further synthetic identification analyses with a realistic ten-storey frame

In the present section, as seen in Section 4.2.2, the focus goes again to the analyses and results that can be achieved by adopting the realistic ten-storey RC frame adopted in Section 4.1 (Table 4.3). The settings for the SSI-DATA identification procedure are the same as those employed before, except than for the Butterworth low-pass filtering, whose cutting frequency has been now taken equal to 12.5 Hz.

Thus, by adopting the present realistic ten-storey frame, synthetic output-only analyses with the present SSI-DATA algorithm have been performed. One may notice that, out of the achieved SSI results within the present case, in general a low number of block rows i in the Hankel matrix ($30 \leq i \leq 50$) allows to achieve better stabilization diagrams, and consequently better identification estimates.

As it was previously done in Section 6.2.1, a synopsis from all the achieved results is depicted in Fig. 6.6. Again, the absolute deviations of SSI-DATA identified natural frequencies and modal damping ratios and the achieved MAC indexes are reported in the subsequent representations.

Estimated SSI-DATA frequencies, show slightly higher deviations with respect to rFDD outcomes, with a maximum of 11.04% for the third mode of the LP case. The most challenging earthquakes reveal to be the KO, IV, LP and NO cases, especially as concerning to the estimates of the first modes of vibration.

As concerning the modal damping ratios, deviations for the SSI-DATA algorithm grow up to 96%, with discrepancies that become at around 50% as a mean. The order of magnitude of the damping ratios is more or less caught, but deviations look rather high in most cases. However, it should be recalled that really demanding heavy-damping identification conditions have been challenged here, with ζ_i up to 13%. As it was seen with the previous 3-DoF case, rFDD frequency and damping estimates for the present 10-DOF case show to be much closer to the target values than for SSI ones.

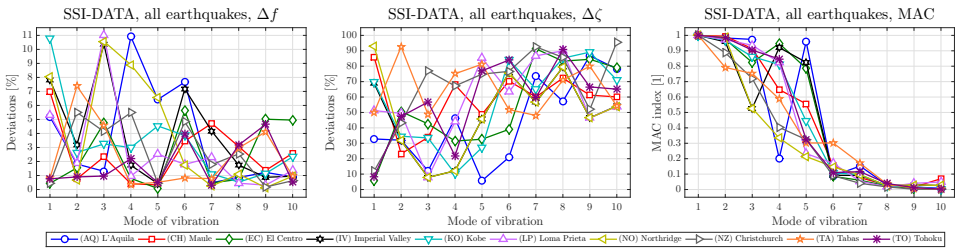

Figure 6.6: *Deviations of estimated natural frequencies and modal damping ratios, and MAC indexes, ten-storey frame, synthetic response signals, SSI-DATA algorithm, complete considered earthquake dataset.*

MAC indexes with SSI-DATA perform once again slightly less well than with rFDD. For the first three modes, MAC values are always higher than 0.70, except for the IV and NO cases, where they go down to 0.527 and 0.525, respectively. From the fourth modes, some problems in the correct mode shape identification start to appear. From the sixth mode, mode shapes start to be badly identified.

Thus, in terms of strong ground motion modal parameters at heavy damping, rFDD show again to be superior than SSI-DATA, for the present MDoF realistic case, at the present stage of development and implementation.

As before, Fig. 6.7 summarizes the global results on the achieved modal estimates for the ten-storey frame, where the absolute deviations of the estimated natural frequencies and modal damping ratios, and the MAC indexes are represented in terms of appropriate dispersion diagrams. The truncated Gaussian distributions show once again that maximum deviations lay always on the Gaussian tails, while minimum deviations are located near the Gaussian centres. This confirms the reliability of the achieved SSI-DATA modal identification estimates too, despite for the rather challenging scenario. SSI-DATA Gaussians are less narrower than previous rFDD ones, especially as concerning to the natural frequencies and the modal damping ratios. This is again an indication of the superior rFDD performance with respect to SSI-DATA in the present context and implementation.

Finally, the results achieved from the realistic ten-storey frame are also synoptically reported in Fig. 6.8, in terms of statistical boxplots. Here, natural frequencies, modal damping ratios and MAC values estimated from the performed synthetic analyses are represented.

The proposed boxplots confirm also the goodness of the SSI-DATA estimates. Despite for the very high modal damping ratios considered in the present case, in terms of SSI-DATA identification challenge, modal

parameter estimates show to be close to the target values. Again, natural frequency estimates show to be very close to the expected target values. Also MAC indexes reveal very good mode shape estimates until the fifth mode of vibration, i.e. a more than adequate number of modes, in order to describe the dynamical behaviour of the structure, specifically under seismic excitation. Finally, modal damping ratios display less accurate estimates, where much problems appear, especially as concerning to the last modes of vibration.

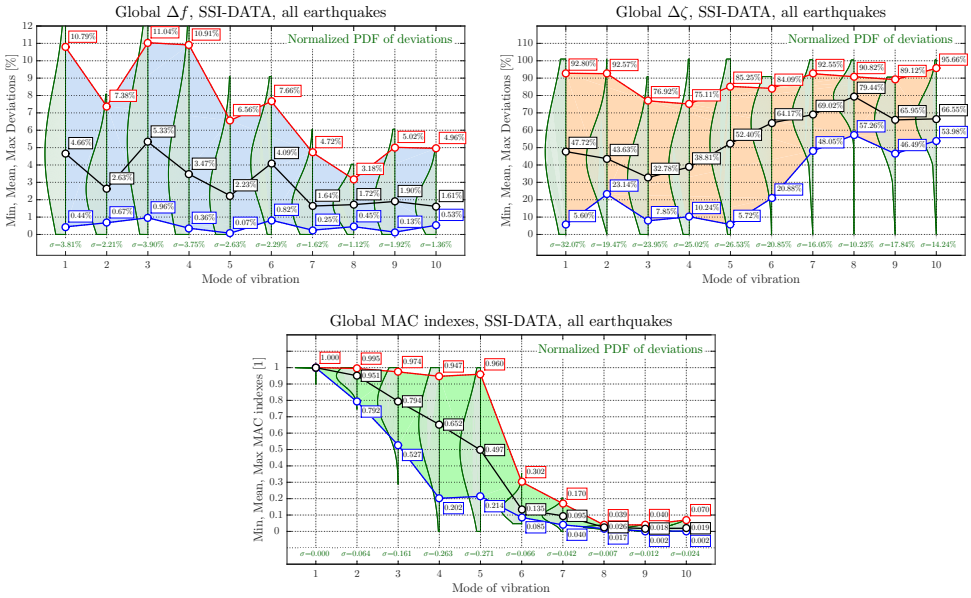

Figure 6.7: *Dispersion diagrams for the deviations of estimated natural frequencies and modal damping ratios, and for the MAC indexes, ten-storey frame, synthetic response signals, SSI-DATA algorithm, complete considered earthquake dataset. Minimum, mean and maximum values, and standard deviations are indicated.*

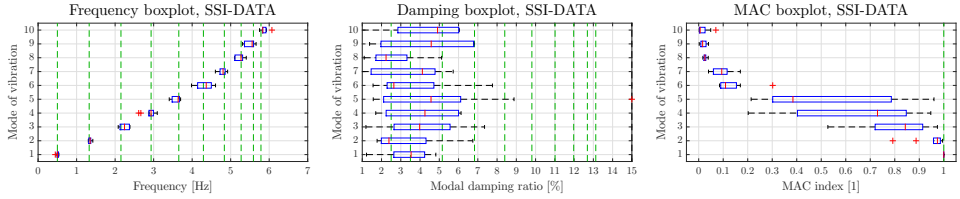

Figure 6.8: *Boxplot diagrams for estimated natural frequencies, modal damping ratios and MAC indexes, ten-storey frame, synthetic response signals, SSI-DATA algorithm, complete considered earthquake dataset.*

Chapter 7

Full Dynamic Compound Inverse Method: theory and results

7.1 Fundamentals of the Full Dynamic Compound Inverse Method

The present innovative method, hereafter named *Full Dynamic Compound Inverse Method (FDCIM)*, extending the terminology DCIM first introduced by Chen et al. [24] in *Computational Mechanics*, is a complete element-level system identification and input estimation algorithm.

This is specifically developed here to operate with earthquake-induced response signals, collected from seismically-excited MDoF shear-type frames. The identification method releases strong assumptions implied by earlier techniques, especially the required knowledge of the full mass matrix (or at least of its specific elements), to provide an effective identification of the modal parameters of the system, i.e. natural frequencies, mode shapes and modal damping ratios, of the excitation input and of realizations of the state matrices. In fact, the present FDCIM algorithm requires the knowledge of structural response signals only, while mass, damping and stiffness matrices, and the exciting earthquake input, may be completely unknown.

Accurate estimations of the input ground motion time history and of the states at the element-level are provided through a two-stage iterative algorithm. This method works jointly with a Statistical Average technique, a modification process and a parameter projection strategy, which are adopted at each iteration to provide correct and stronger constraints for the estimates, allowing for faster and much reliable convergence.

Moreover, the proposed FDCIM method (as opposed to other methods operating within the stochastic framework) appears to be completely deterministic and it is fully developed in *State-Space form*. It does not

require transformations from continuous-time to discrete-time and it does not depend on the adopted initial conditions or on the state estimation, in order to identify the modal parameters and the input ground motion. Further, all structural features as element-level mass, damping and stiffness matrices, may be accurately identified by knowing merely any single component of one of these matrices, or even by relying on an estimate of a global structural parameter, like for instance the total mass of the building. Then, the adopted formulation is suitable for integration or support to other common output-only methods working with State-Space parametric Time Domain frameworks.

Main assumptions of the present FDCIM implementation are: shear-type frame structures (or, generally, structures compatible with a diagonal mass matrix and a tridiagonal symmetric stiffness matrix), excited by ground motion excitation at the base (it could be an earthquake-induced excitation, or any other input, even though applied as base excitation to the considered structures). The simultaneous knowledge of acceleration, velocity and displacement structural responses may be useful, though the missing recordings may be directly calculated from the available responses (e.g. if only acceleration responses are available, velocities and displacements may be obtained from integration of the accelerations themselves).

In Section 7.1.1, the basic mathematical model underlying the FDCIM method is described, while the associated two-stage identification algorithm and the element-level identification procedure are presented in Sections 7.1.2 and 7.1.3. Finally, the adoption of General or Rayleigh damping is addressed in Section 7.2, where the modified basic mathematical model, the upgraded two-stage identification algorithm and the procedure for the Rayleigh damping coefficients estimation are outlined, in Sections 7.2.1, 7.2.2 and 7.2.3, respectively.

7.1.1 Basic mathematical model of the FDCIM algorithm

The response of a linear MDoF shear-type building subjected to earthquake base excitation, characterized by ground acceleration $\ddot{u}_g(t)$, is governed by the following classical set of second-order time-differential equations:

$$\mathbf{M}\ddot{\mathbf{u}}(t) + \mathbf{C}\dot{\mathbf{u}}(t) + \mathbf{K}\mathbf{u}(t) = \mathbf{f}(t) = -\mathbf{M}\ddot{\mathbf{u}}_g(t) = -\mathbf{M}\mathbf{r}\ddot{u}_g(t) \tag{7.1}$$

where $\mathbf{M}$, $\mathbf{C}$ and $\mathbf{K} \in \mathcal{R}^{n\times n}$ are the mass, damping and stiffness matrices of the structural system, respectively, with the following classical definitions:

$$
\mathbf{M} = \begin{bmatrix} m_1 & 0 & 0 & \dots & 0 \\ 0 & m_2 & 0 & \dots & 0 \\ 0 & 0 & m_3 & \dots & 0 \\ \vdots & \vdots & \vdots & \ddots & \vdots \\ 0 & 0 & 0 & \dots & m_n \end{bmatrix} \text{[kg]},
$$

$$
\mathbf{C} = \begin{bmatrix} c_1 + c_2 & -c_2 & 0 & \dots & 0 \\ -c_2 & c_2 + c_3 & -c_3 & \dots & 0 \\ 0 & -c_3 & c_3 + c_4 & \dots & 0 \\ \vdots & \vdots & \vdots & \ddots & \vdots \\ 0 & 0 & 0 & \dots & c_n \end{bmatrix} \text{[Ns/m]}, \tag{7.2}
$$

$$
\mathbf{K} = \begin{bmatrix} k_1 + k_2 & -k_2 & 0 & \dots & 0 \\ -k_2 & k_2 + k_3 & -k_3 & \dots & 0 \\ 0 & -k_3 & k_3 + k_4 & \dots & 0 \\ \vdots & \vdots & \vdots & \ddots & \vdots \\ 0 & 0 & 0 & \dots & k_n \end{bmatrix} \text{[N/m]}
$$

where n is the number of floors, m_i are the floor masses, c_i and k_i $(i = 1, \dots, n)$ are the lateral column damping and stiffness coefficients, respectively, between the ith and the $(i-1)^{th}$ floor. Matrix $\mathbf{M}$ is diagonal and matrices $\mathbf{C}$, $\mathbf{K}$ share a tridiagonal (symmetric) structure. Vector $\mathbf{u} = [u_1 \ u_2 \ u_3 \ \dots \ u_n]^{\mathrm{T}} \in \mathcal{R}^{n \times 1}$ gathers the absolute (relative to the ground) displacements of each floor. Consistently, vectors $\dot{\mathbf{u}}$ and $\ddot{\mathbf{u}}$ represent absolute (relative to the ground) velocities and accelerations. Finally, the input force vector $\mathbf{f}(t) \in \mathcal{R}^{n \times 1}$ is the vector containing the acting excitation input, here coming from the ground acceleration $\ddot{u}_g$. It is defined as $\mathbf{f}(t) = -\mathbf{M}\ddot{\mathbf{u}}_g = -\mathbf{M}\mathbf{r}\ddot{u}_g$, where $\mathbf{r} = [1 \ 1 \ 1 \ \dots \ 1]^{\mathrm{T}} \in \mathcal{R}^{n \times 1}$ is the influence coefficient (rigid body motion) vector for the analysed case and $\ddot{\mathbf{u}}_g = \mathbf{r}\ddot{u}_g$ is the ground acceleration vector. Fig. 7.1 sketches the initial geometry, the lumped-mass scheme and the displacements of the adopted shear-type model, where h_i represent the relative floor heights.

By switching to State-Space form, the n second-order differential equations of motion in Eq. (7.1) can be rewritten into $2n$ first-order differential equations, in terms of *state equation* $\dot{\mathbf{x}}(t)$ and *observer equation* $\mathbf{y}(t)$, by sticking to classical literature definitions (see e.g. [34]):

$$
\begin{cases} \dot{\mathbf{x}}(t) = \mathbf{A}\mathbf{x}(t) + \mathbf{B}\mathbf{f}(t) \\ \mathbf{y}(t) = \mathbf{C}_o\mathbf{x}(t) + \mathbf{D}\mathbf{f}(t) \end{cases} \tag{7.3}
$$

where $\mathbf{x}(t) = [\mathbf{u}(t) \ \dot{\mathbf{u}}(t)]^{\mathrm{T}} \in \mathcal{R}^{2n \times 1}$ is the *state vector* and $\dot{\mathbf{x}}(t)$ its derivative, while $\mathbf{y}(t) \in \mathcal{R}^{n \times 1}$ is the *output vector*. Moreover, $\mathbf{A} \in \mathcal{R}^{2n \times 2n}$ is the

state matrix, $\mathbf{B} \in \mathcal{R}^{2n\times n}$ the *input matrix*, $\mathbf{C}_o \in \mathcal{R}^{n\times 2n}$ the *output matrix* and $\mathbf{D} \in \mathcal{R}^{n\times n}$ the *feed-through matrix*, which can be defined as follows:

$$\begin{aligned} \mathbf{A} &= \begin{bmatrix} \mathbf{0}_{n\times n} & \mathbf{I}_{n\times n} \\ -\mathbf{M}^{-1}\mathbf{K} & -\mathbf{M}^{-1}\mathbf{C} \end{bmatrix}, \quad \mathbf{B} = \begin{bmatrix} \mathbf{0}_{n\times n} \\ \mathbf{M}^{-1} \end{bmatrix} \\ \mathbf{C}_o &= \begin{bmatrix} -\mathbf{M}^{-1}\mathbf{K} & -\mathbf{M}^{-1}\mathbf{C} \end{bmatrix}, \quad \mathbf{D} = \mathbf{M}^{-1} \end{aligned} \tag{7.4}$$

Matrix terms $\mathbf{0}_{n\times n}$ and $\mathbf{I}_{n\times n} \in \mathcal{R}^{n\times n}$ indicate zero and identity matrices of the specified dimensions, respectively.

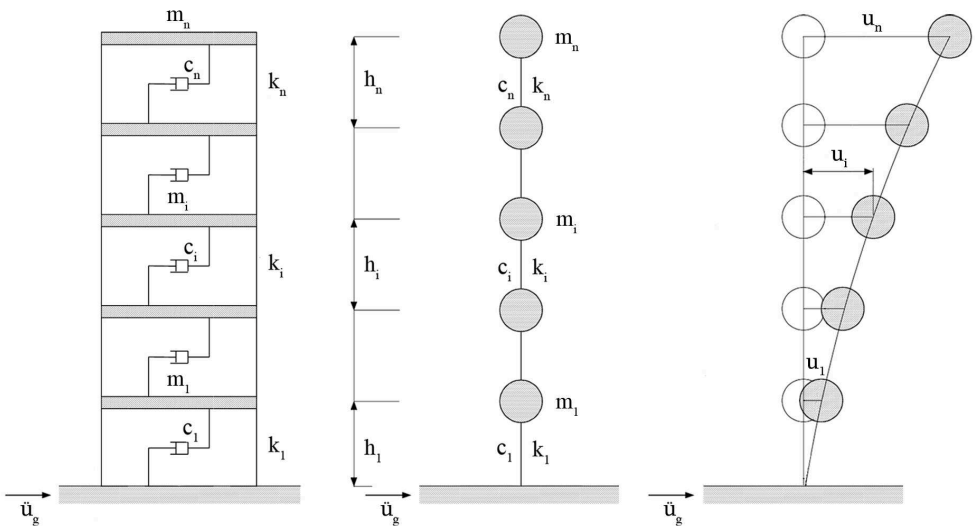

Figure 7.1: *Lumped mass structural model of the adopted shear-type frame subjected to ground motion base excitation* $\ddot{\mathbf{u}}_g$.

In the present identification implementation, the known quantities are only the dynamic responses, i.e. $\mathbf{x}(t)$ and $\dot{\mathbf{x}}(t)$ state vectors, while state matrices (i.e. $\mathbf{A}$, $\mathbf{B}$, $\mathbf{C}_o$ and $\mathbf{D}$ matrices) and input vector $\mathbf{f}(t)$ are the unknown variables to be identified. Accordingly, by switching back to physical space, the parameters which will be estimated are the modal characteristics, the seismic ground acceleration and the mass, damping and stiffness matrices (i.e. their coefficients).

Thus, while typically Eqs. (7.1) or (7.3) are conceived to be formed and solved for the unknown structural responses, in the present identification process the role of given information and unknown variables is reversed and effective algebraic rewriting of the equations of motion, leading to appropriate identification equations, is sought, in view of expressing the new role of the unknown variables (the identification variables). This is pursued next.

It can be noticed that the estimation problem, by taking into account the desired unknowns, turns out to be undetermined, in the sense that it

is going to be revealed in the following. In order to handle this issue, from Eq. (7.1) it is possible to write the two following concatenated relations, namely the two basic equations on which the present recursive algorithm is built:

$$\mathbf{C}\dot{\mathbf{u}}(t) + \mathbf{K}\mathbf{u}(t) = -\mathbf{M}\Big(\ddot{\mathbf{u}}(t) + \ddot{\mathbf{u}}_g(t)\Big) \tag{7.5}$$

$$\mathbf{M}^{-1}\Big(\mathbf{C}\dot{\mathbf{u}}(t) + \mathbf{K}\mathbf{u}(t)\Big) = -\ddot{\mathbf{u}}(t) - \ddot{\mathbf{u}}_g(t) \tag{7.6}$$

where Eq. (7.6) may be derived directly from Eq. (7.5), by a $\mathbf{M}^{-1}$ pre-multiplication. Notice that mass matrix $\mathbf{M}$ can always be inverted, since it is taken as a diagonal, non-singular matrix. The switching of Eqs. (7.5) and (7.6) to State-Space representation is immediate, and leads to the following formulations:

$$\mathbf{G}_{ck}\mathbf{x}(t) = \mathbf{N}_{ck}\dot{\mathbf{x}}(t) + \mathbf{L}_{ck}\mathbf{f}(t) = \mathbf{N}_{ck}\dot{\mathbf{x}}(t) - \mathbf{L}_{ck}\mathbf{M}\ddot{\mathbf{u}}_g(t) \tag{7.7}$$

$$\mathbf{G}_m\mathbf{x}(t) = -\dot{\mathbf{x}}(t) - \mathbf{L}_m\ddot{\mathbf{u}}_g(t) \tag{7.8}$$

where $\mathbf{G}_{ck} \in \mathcal{R}^{2n\times 2n}$, $\mathbf{N}_{ck} \in \mathcal{R}^{2n\times 2n}$, $\mathbf{L}_{ck} \in \mathcal{R}^{2n\times n}$, $\mathbf{G}_m \in \mathcal{R}^{2n\times 2n}$ and $\mathbf{L}_m \in \mathcal{R}^{2n\times n}$ are matrices to be specifically assembled, defined as follows:

$$\mathbf{G}_{ck} = \begin{bmatrix} \mathbf{0}_{n\times n} & \mathbf{I}_{n\times n} \\ \mathbf{K} & \mathbf{C} \end{bmatrix}, \quad \mathbf{N}_{ck} = \begin{bmatrix} \mathbf{I}_{n\times n} & \mathbf{0}_{n\times n} \\ \mathbf{0}_{n\times n} & -\mathbf{M} \end{bmatrix}, \quad \mathbf{L}_{ck} = \begin{bmatrix} \mathbf{0}_{n\times n} \\ \mathbf{I}_{n\times n} \end{bmatrix} \tag{7.9a}$$

$$\mathbf{G}_m = \begin{bmatrix} \mathbf{0}_{n\times n} & -\mathbf{I}_{n\times n} \\ \mathbf{M}^{-1}\mathbf{K} & \mathbf{M}^{-1}\mathbf{C} \end{bmatrix}, \qquad \mathbf{L}_m = \begin{bmatrix} \mathbf{0}_{n\times n} \\ \mathbf{I}_{n\times n} \end{bmatrix} \tag{7.9b}$$

Then, Eq. (7.7) can be rewritten, with the purpose of a first stage identification (described in subsequent Section 7.1.2), in the following form (see [67]):

$$\mathbf{H}_{ck}(t)\boldsymbol{\theta}_{ck} = \mathbf{P}_{ck}(t) \quad \Rightarrow \quad \underbrace{\begin{bmatrix} \mathbf{H}^1_{ck}(t) & \mathbf{0}_{n\times 2n} \\ \mathbf{0}_{n\times n} & \mathbf{H}^2_{ck}(t) \end{bmatrix}}_{2n\times 3n} \underbrace{\begin{Bmatrix} \boldsymbol{\theta}^1_{ck} \\ \boldsymbol{\theta}^2_{ck} \end{Bmatrix}}_{3n\times 1} = \underbrace{\begin{Bmatrix} \mathbf{P}^1_{ck}(t) \\ \mathbf{P}^2_{ck}(t) \end{Bmatrix}}_{2n\times 1} \tag{7.10}$$

Last Eq. (7.10) is defined for every time instant $t = t_i$, $i = 1, \ldots, L$, being L the total number of points of the acquired input signals, i.e. the length of the signal. By collecting together all the sampling time instants, the subsequent formulation can be reached:

$$\underbrace{\mathbf{H}_{ck}}_{(L\times 2n)\times 3n} \underbrace{\boldsymbol{\theta}_{ck}}_{3n\times 1} = \underbrace{\mathbf{P}_{ck}}_{(L\times 2n)\times 1} \tag{7.11}$$

where:

$$\mathbf{H}_{ck} = [\mathbf{H}_{ck}(t_1)\ \mathbf{H}_{ck}(t_2)\ \ldots\ \mathbf{H}_{ck}(t_L)]^{\mathrm{T}} \tag{7.12a}$$

$$\boldsymbol{\theta}_{ck} = \{\underbrace{1\ 1\ 1\ \ldots\ 1}_{1\times n},\ \underbrace{c_1\ c_2\ c_3\ \ldots\ c_i\ \ldots\ c_n}_{1\times n},\ \underbrace{k_1\ k_2\ k_3\ \ldots\ k_i\ \ldots\ k_n}_{1\times n}\}^{\mathrm{T}} \tag{7.12b}$$

$$\mathbf{P}_{ck} = \{\mathbf{P}_{ck}(t_1)\ \mathbf{P}_{ck}(t_2)\ \ldots\ \mathbf{P}_{ck}(t_L)\}^{\mathrm{T}} \tag{7.12c}$$

Then, $\mathbf{H}_{ck}(t)$ is a matrix containing the (known) velocity and displacement responses, $\boldsymbol{\theta}_{ck}$ is a vector containing all the (unknown, to be identified) damping and stiffness parameters and $\mathbf{P}_{ck}(t)$ is a vector related to the (unknown) mass terms, containing both (known) acceleration responses and (unknown) input ground motion excitation. Their elements can be computed, at the generic time instant t_i, as:

$$\mathbf{H}^1_{ck}(t_i) = \underbrace{\begin{bmatrix} \dot{u}_1 & 0 & 0 & \cdots & 0 \\ 0 & \dot{u}_2 & 0 & \cdots & 0 \\ 0 & 0 & \dot{u}_3 & \cdots & 0 \\ \vdots & \vdots & \vdots & \ddots & \vdots \\ 0 & 0 & 0 & \cdots & \dot{u}_n \end{bmatrix}}_{n\times n},\ \boldsymbol{\theta}^1_{ck} = \underbrace{\begin{Bmatrix} 1 \\ 1 \\ 1 \\ \vdots \\ 1 \end{Bmatrix}}_{n\times 1},\ \mathbf{P}^1_{ck}(t_i) = \underbrace{\begin{Bmatrix} \dot{u}_1 \\ \dot{u}_2 \\ \dot{u}_3 \\ \vdots \\ \dot{u}_n \end{Bmatrix}}_{n\times 1} \tag{7.13}$$

$$\mathbf{H}^2_{ck}(t_i) = \underbrace{\begin{bmatrix} \dot{u}_1 & \dot{u}_1-\dot{u}_2 & 0 & \cdots & 0 & u_1 & u_1-u_2 & 0 & \cdots & 0 \\ 0 & \dot{u}_2-\dot{u}_1 & \dot{u}_2-\dot{u}_3 & \cdots & 0 & 0 & u_2-u_1 & u_2-u_3 & \cdots & 0 \\ 0 & 0 & \dot{u}_3-\dot{u}_2 & \cdots & 0 & 0 & 0 & u_3-u_2 & \cdots & 0 \\ \vdots & \vdots & \vdots & \ddots & \vdots & \vdots & \vdots & \vdots & \ddots & \vdots \\ 0 & 0 & 0 & \cdots & \dot{u}_n-\dot{u}_{n-1} & 0 & 0 & 0 & \cdots & u_n-u_{n-1} \end{bmatrix}}_{n\times 2n} \tag{7.14a}$$

$$\boldsymbol{\theta}^2_{ck} = \{\underbrace{c_1\ c_2\ c_3\ \ldots\ c_i\ \ldots\ c_n,\ k_1\ k_2\ k_3\ \ldots\ k_i\ \ldots\ k_n}_{1\times 2n}\}^{\mathrm{T}} \tag{7.14b}$$

$$\mathbf{P}^2_{ck}(t_i) = \underbrace{\begin{Bmatrix} -m_1(\ddot{u}_1+\ddot{u}_g) \\ -m_2(\ddot{u}_2+\ddot{u}_g) \\ -m_3(\ddot{u}_3+\ddot{u}_g) \\ \vdots \\ -m_n(\ddot{u}_n+\ddot{u}_g) \end{Bmatrix}}_{n\times 1} \tag{7.14c}$$

Finally, the $\boldsymbol{\theta}_{ck}$ parameters may be estimated by applying a Least-Squares technique on previous Eq. (7.11):

$$\boldsymbol{\theta}_{ck} = \mathbf{H}^{\dagger}_{ck}\mathbf{P}_{ck} = \left(\left[\mathbf{H}^{\mathrm{T}}_{ck}\mathbf{H}_{ck}\right]^{-1}\mathbf{H}^{\mathrm{T}}_{ck}\right)\mathbf{P}_{ck} \tag{7.15}$$

where superscript symbol † indicates the Moore-Penrose pseudo-inverse.

Similarly, for a second identification stage (see Section 7.1.2), Eq. (7.8) can be rewritten, for every time instant $t = t_i$, $i = 1, \ldots, L$, as:

$$\mathbf{H}_m(t)\boldsymbol{\theta}_m = \mathbf{P}_m(t) \quad \Rightarrow \quad \underbrace{\begin{bmatrix} \mathbf{H}_m^1(t) & \mathbf{0}_{n\times n} \\ \mathbf{0}_{n\times n} & \mathbf{H}_m^2(t) \end{bmatrix}}_{2n\times 2n} \underbrace{\begin{Bmatrix} \boldsymbol{\theta}_m^1 \\ \boldsymbol{\theta}_m^2 \end{Bmatrix}}_{2n\times 1} = \underbrace{\begin{Bmatrix} \mathbf{P}_m^1(t) \\ \mathbf{P}_m^2(t) \end{Bmatrix}}_{2n\times 1} \tag{7.16}$$

By collecting the sampling time instants all together one has:

$$\underbrace{\mathbf{H}_m}_{(L\times 2n)\times 2n} \underbrace{\boldsymbol{\theta}_m}_{2n\times 1} = \underbrace{\mathbf{P}_m}_{(L\times 2n)\times 1} \tag{7.17}$$

where:

$$\mathbf{H}_m = [\mathbf{H}_m(t_1)\ \mathbf{H}_m(t_2)\ \ldots\ \mathbf{H}_m(t_L)]^{\mathrm{T}} \tag{7.18a}$$

$$\boldsymbol{\theta}_m = \{\underbrace{1\ 1\ 1\ \ldots\ 1}_{1\times n},\ \underbrace{1/m_1\ 1/m_2\ 1/m_3\ \ldots\ 1/m_i\ \ldots\ 1/m_n}_{1\times n}\}^{\mathrm{T}} \tag{7.18b}$$

$$\mathbf{P}_m = \{\mathbf{P}_m(t_1)\ \mathbf{P}_m(t_2)\ \ldots\ \mathbf{P}_m(t_L)\}^{\mathrm{T}} \tag{7.18c}$$

So, $\mathbf{H}_m(t)$ is again a matrix containing the (known) velocity and displacement responses, $\boldsymbol{\theta}_m$ is a vector containing all the inverse of the (unknown, to be identified) mass parameters and $\mathbf{P}_m(t)$ is a vector collecting the (known) acceleration responses and the (unknown) input ground motion excitation. By considering a generic time instant t_i, each of their elements can be calculated as:

$$\mathbf{H}_m^1(t_i) = -\underbrace{\begin{bmatrix} \dot{u}_1 & 0 & 0 & \cdots & 0 \\ 0 & \dot{u}_2 & 0 & \cdots & 0 \\ 0 & 0 & \dot{u}_3 & \cdots & 0 \\ \vdots & \vdots & \vdots & \ddots & \vdots \\ 0 & 0 & 0 & \cdots & \dot{u}_n \end{bmatrix}}_{n\times n}, \quad \boldsymbol{\theta}_m^1 = \underbrace{\begin{Bmatrix} 1 \\ 1 \\ 1 \\ \vdots \\ 1 \end{Bmatrix}}_{n\times 1}, \quad \mathbf{P}_{ck}^1(t_i) = -\underbrace{\begin{Bmatrix} \dot{u}_1 \\ \dot{u}_2 \\ \dot{u}_3 \\ \vdots \\ \dot{u}_n \end{Bmatrix}}_{n\times 1} \tag{7.19}$$

$$\mathbf{H}_m^2(t_i) = \underbrace{\mathbf{K}\begin{bmatrix} u_1 & 0 & 0 & \cdots & 0 \\ 0 & u_2 & 0 & \cdots & 0 \\ 0 & 0 & u_3 & \cdots & 0 \\ \vdots & \vdots & \vdots & \ddots & \vdots \\ 0 & 0 & 0 & \cdots & u_n \end{bmatrix} + \mathbf{C}\begin{bmatrix} \dot{u}_1 & 0 & 0 & \cdots & 0 \\ 0 & \dot{u}_2 & 0 & \cdots & 0 \\ 0 & 0 & \dot{u}_3 & \cdots & 0 \\ \vdots & \vdots & \vdots & \ddots & \vdots \\ 0 & 0 & 0 & \cdots & \dot{u}_n \end{bmatrix}}_{n\times n} \tag{7.20a}$$

$$\boldsymbol{\theta}_m^2 = \{\underbrace{1/m_1\ 1/m_2\ 1/m_3\ \ldots\ 1/m_i\ \ldots\ 1/m_n}_{1\times n}\}^{\mathrm{T}} \tag{7.20b}$$

$$\mathbf{P}_m^2(t_i) = \underbrace{\begin{Bmatrix} -(\ddot{u}_1 + \ddot{u}_g) \\ -(\ddot{u}_2 + \ddot{u}_g) \\ -(\ddot{u}_3 + \ddot{u}_g) \\ \vdots \\ -(\ddot{u}_n + \ddot{u}_g) \end{Bmatrix}}_{n\times 1} \tag{7.20c}$$

As seen in Eq. (7.15), the mass parameters collected in $\boldsymbol{\theta}_m$ can be estimated by applying a Least-Squares technique on Eq. (7.17):

$$\boldsymbol{\theta}_m = \mathbf{H}_m^{\dagger}\mathbf{P}_m = \left(\left[\mathbf{H}_m^{\mathrm{T}}\mathbf{H}_m\right]^{-1}\mathbf{H}_m^{\mathrm{T}}\right)\mathbf{P}_m \tag{7.21}$$

Notice that, as commented earlier right after Eq. (7.4), the achieved algebraic representations in Eqs. (7.11) and (7.17) invert the role of unknown parameters and given quantities, as in Eqs. (7.1) and (7.3), so as to allow for solving the identification process in the unknown quantities to be identified, for a total number of $3n$ unknown structural parameters and unknown input ground motion signal.

By summarizing the introduced problem and its formulation so far, it can be noted that it does not look one of a simple solution, since unknown quantities are collected inside $\mathbf{P}_{ck}$ and $\mathbf{H}_m$. Then, a two-stage iterative solution provided by the present Full Dynamic Compound Inverse Method (FDCIM) is innovatively developed below, to deal with the present identification inverse problem, as it is presented in the next section.

7.1.2 Two-stage identification algorithm

The developed Full Dynamic Compound Inverse Method (FDCIM) is an algorithm that, by working with a State-Space representation, allows for the estimation, in series, of modal parameters, input ground motion and structural characteristics at the element-level. This is possible through a

two-stage iterative algorithm, which consists of a Least-Squares (LS) optimization technique for parameter identification [62], and of a Statistical Average (SA) method [24], which make the estimated input excitation to comply with the dynamic equilibrium of the considered frame, at each time instant, and rely on a modification process, allowing for faster convergence.

The only known quantities are the time histories acquired from the building responses; especially, only acceleration responses may be known, since velocities and displacements may be integrated numerically from accelerations, see [30]. Then, the development of the FDCIM algorithm, divided in two subsequent stages, may be summarized in the computational steps outlined below.

- **First stage (realization of stiffness and damping parameters):**

1.1 For the first iteration, since both $\boldsymbol{\theta}_{ck}$, $\boldsymbol{\theta}_m$ and $\ddot{u}_g$ are unknown quantities, each parameter vector must be assigned to an arbitrary initial value, for example ${}^0\boldsymbol{\theta}_{ck} = \{1\ 1\ 1\ \ldots\ 1\}^{\mathrm{T}}$, ${}^0\boldsymbol{\theta}_m = \{1\ 1\ 1\ \ldots\ 1\}^{\mathrm{T}}$, where left apex symbol 0 stays for initial starting value. For the subsequent recursions, a similar left apex i denotes the current iteration. Notice that the performance of the method is not sensitive to these initial values, which may be whatever between, say, 10^{-6} and 10^6. Then, initial matrices ${}^0\mathbf{M}$, ${}^0\mathbf{C}$, ${}^0\mathbf{K}$ (through Eqs. (7.2)) and ${}^0\mathbf{H}_{ck}$ (through Eq. (7.12a)) can be computed.

1.2 An estimate of vector $\mathbf{P}_{ck}$ can be calculated by using the terms of Step 1, from Eq. (7.11), getting ${}^0\tilde{\mathbf{P}}_{ck} = {}^0\mathbf{H}_{ck}{}^0\boldsymbol{\theta}_{ck}$. Overmarking symbol $\sim$ stays here for estimated value.

1.3 By using ${}^0\tilde{\mathbf{P}}_{ck}$, matrix $\mathbf{G}_{ck}$ can be estimated from the following Least-Squares expression:

$$ {}^0\tilde{\mathbf{G}}_{ck} = {}^0\tilde{\mathbf{P}}_{ck}\mathbf{X}^{\dagger} = {}^0\tilde{\mathbf{P}}_{ck}\left(\left[\mathbf{X}^{\mathrm{T}}\mathbf{X}\right]^{-1}\mathbf{X}^{\mathrm{T}}\right) \tag{7.22} $$

where $\mathbf{X} = \{\mathbf{x}(t_1)\ \ \mathbf{x}(t_2)\ \ldots\ \mathbf{x}(t_L)\}^{\mathrm{T}} \in \mathcal{R}^{(L\times 2n)\times 1}$ is the global state matrix, accounting for all L time instants.

1.4 Knowing ${}^0\boldsymbol{\theta}_m$, ${}^0\tilde{\mathbf{N}}_{ck}$ can be reconstructed from Eq. (7.9a).

1.5 Starting from Eq. (7.7), an estimate of the input ground motion vector ${}^0\ddot{\mathbf{u}}_{g,k}(t)$ can be obtained:

$$ {}^0\tilde{\ddot{\mathbf{u}}}_{g,ck}(t) = -\Big(\mathbf{L}_{ck}{}^0\mathbf{M}\Big)^{\dagger}\Big({}^0\tilde{\mathbf{G}}_{ck}\mathbf{x}(t) - {}^0\tilde{\mathbf{N}}_{ck}\dot{\mathbf{x}}(t)\Big) \tag{7.23} $$

where ${}^0\tilde{\ddot{\mathbf{u}}}_{g,ck}(t) = \{{}^0\tilde{\ddot{u}}^{(1)}_{g,ck}(t) \quad {}^0\tilde{\ddot{u}}^{(2)}_{g,ck}(t) \quad \dots \quad {}^0\tilde{\ddot{u}}^{(i)}_{g,ck}(t) \quad \dots \quad {}^0\tilde{\ddot{u}}^{(n)}_{g,ck}(t)\}^{\mathrm{T}}$ contains the estimate of the input ground motion relative to each storey $i = 1, \dots, n$ and for every time instant $t = t_j$, $j = 1, \dots, L$.

1.6 Then, a Statistical Average (SA) process is introduced in the algorithm, since the nth ground accelerations ${}^0\tilde{\ddot{u}}^{(i)}_{g,ck}(t)$ obtained from previous Eq. (7.23) should be the same for every storey, at each time instant $t = t_j$. Actually, this is not true because of the difference between the assumed initial values ${}^0\boldsymbol{\theta}_{ck}$, ${}^0\boldsymbol{\theta}_m$ and their true values. So, the SA method can be applied as follows, by computing the average (mean value) ${}^0\bar{\ddot{u}}_{g,ck}(t_j)$ between the n different ${}^0\tilde{\ddot{u}}^{(i)}_{g,ck}(t_j)$, at each time instant $t = t_j$:

$$ {}^0\bar{\ddot{u}}_{g,ck}(t_j) = \frac{1}{n}\sum_{i=1}^{n} {}^0\tilde{\ddot{u}}^{(i)}_{g,ck}(t_j), \quad j = 1, \dots, L \tag{7.24} $$

1.7 After the computation of the average ground motion ${}^0\bar{\ddot{u}}_{g,ck}(t)$, a modified version of vector $\mathbf{P}_{ck}(t)$ may be reconstructed, by using the following modification procedure:

$$ {}^0\hat{\mathbf{P}}_{ck}(t) = {}^0\tilde{\mathbf{N}}_{ck}\dot{\mathbf{x}}(t) - \mathbf{L}_{ck}\,{}^0\mathbf{M}\mathbf{r}\,{}^0\bar{\ddot{u}}_{g,ck}(t) \tag{7.25} $$

where superscript $\wedge$ means modified value.

1.8 Finally, an improved estimation of the $\boldsymbol{\theta}_{ck}$ parameters can be computed by the use of the modified ${}^0\hat{\mathbf{P}}_{ck}$ vector, leading to estimates of damping and stiffness parameters at iteration 1 as follows:

$$ {}^1\boldsymbol{\theta}_{ck} = {}^0\mathbf{H}^{\dagger}_{ck}\,{}^0\tilde{\mathbf{P}}_{ck} = \left(\left[{}^0\mathbf{H}^{\mathrm{T}}_{ck}\,{}^0\mathbf{H}_{ck}\right]^{-1}\,{}^0\mathbf{H}^{\mathrm{T}}_{ck} \right){}^0\tilde{\mathbf{P}}_{ck} \tag{7.26} $$

1.9 On the latter Least-Squares formulation, a parameter projection technique is adopted, in order to arrive at strictly-positive estimates of $\left({}^1\boldsymbol{\theta}_{ck}\right)_{ij}$ parameters, i.e. of c_i and k_i terms, when $i = j$ (i.e. for the diagonal terms of the damping and stiffness matrices), without the need of solving constrained LS problems:

$$ \left({}^1\boldsymbol{\theta}_{ck}\right)_{ij} = \mathrm{sgn}\left[\left({}^1\boldsymbol{\theta}_{ck}\right)_{ij}\right]\left({}^1\boldsymbol{\theta}_{ck}\right)_{ij}, \quad \forall i, j = 1, \dots, n \tag{7.27} $$

where sgn[...] represents the sign function, that is the odd mathematical function which extracts the sign of the real number in its argument.

Then, from the estimate of ${}^1\boldsymbol{\theta}_{ck}$, updated estimates ${}^1\mathbf{C}$ and ${}^1\mathbf{K}$ of the damping and stiffness matrices can be computed.

• **Second stage (realization of mass parameters):**
Similarly to what seen for the first stage, the second stage will be outlined by the following computational steps.

2.1 The first iteration of the second identification stage starts from the achieved estimates of ${}^1\boldsymbol{\theta}_{ck}$, ${}^1\mathbf{C}$ and ${}^1\mathbf{K}$, aiming at the computation of the ${}^0\mathbf{H}_m$ matrix, through Eq. (7.18a).

2.2 Vector $\mathbf{P}_m$ can be estimated by using the terms of Step 2.1, from Eq. (7.17) to ${}^0\tilde{\mathbf{P}}_m = {}^0\mathbf{H}_m{}^0\boldsymbol{\theta}_m$, where ${}^0\boldsymbol{\theta}_m$ was defined in previous Step 1.1.

2.3 Matrix $\mathbf{G}_m$ can be estimated, through the estimated value of ${}^0\tilde{\mathbf{P}}_m$, from the Least-Squares problem:

$$ {}^0\tilde{\mathbf{G}}_m = {}^0\tilde{\mathbf{P}}_m\mathbf{x}^\dagger = {}^0\tilde{\mathbf{P}}_m\Big(\left[\mathbf{x}^{\mathrm{T}}\mathbf{x}\right]^{-1}\mathbf{x}^{\mathrm{T}}\Big) \tag{7.28} $$

Notice that from matrix $\mathbf{G}_m$, an estimate of state matrix $\mathbf{A}$ can be directly computed, leading to ${}^0\tilde{\mathbf{A}}$ (see Eq. (7.9b) for more details).

2.4 The input ground motion vector ${}^0\ddot{\mathbf{u}}_{g,c}(t)$ can be again estimated, by taking into account previous Eq. (7.8), as:

$$ {}^0\tilde{\ddot{\mathbf{u}}}_{g,m}(t) = -\mathbf{L}_m^\dagger\Big({}^0\tilde{\mathbf{G}}_m\mathbf{x}(t) - \dot{\mathbf{x}}(t)\Big) \tag{7.29} $$

where, again, vector ${}^0\tilde{\ddot{\mathbf{u}}}_{g,m}(t)$ holds the input ground motion estimates for each storey $i = 1, \ldots, n$ and for every time instant $t = t_j$, $j = 1, \ldots, L$.

2.5 As in previous Step 1.6, the Statistical Average method is applied, at each time instant $t = t_j$, to the n different ${}^0\tilde{\ddot{u}}_{g,m}^{(i)}(t_j)$ ground motion accelerations:

$$ {}^0\bar{\ddot{u}}_{g,m}(t_j) = \frac{1}{n}\sum_{i=1}^{n}{}^0\tilde{\ddot{u}}_{g,m}^{(i)}(t_j), \quad j = 1, \ldots, L \tag{7.30} $$

2.6 Through the following modification procedure, the modified version of vector $\mathbf{P}_m(t)$ can be reconstructed as:

$$ {}^0\hat{\mathbf{P}}_m(t) = -\dot{\mathbf{x}}(t) - \mathbf{L}_{ck}\mathbf{r}\,{}^0\bar{\ddot{u}}_{g,c}(t) \tag{7.31} $$

2.7 Then, through the use of modified vector ${}^{0}\hat{\mathbf{P}}_m$, the improved estimation of $\boldsymbol{\theta}_m$ can be computed, by giving rise to iteration 1 for the second identification stage:

$$ {}^{1}\boldsymbol{\theta}_m = {}^{0}\mathbf{H}_m^{\dagger}\,{}^{0}\tilde{\mathbf{P}}_m = \Big(\left[{}^{0}\mathbf{H}_m^{\mathrm{T}}\,{}^{0}\mathbf{H}_m\right]^{-1}\,{}^{0}\mathbf{H}_m^{\mathrm{T}}\Big)\mathbf{P}_m \tag{7.32} $$

2.8 As before, on previous Eq. (7.32) the parameter projection technique is implemented, towards getting strictly-positive estimations of the $\left({}^{1}\boldsymbol{\theta}_m\right)_{ij}$ parameters $\forall i,j = 1,\ldots,n$ (since mass matrix elements must be all strictly-positive), without the use of constrained LS problems:

$$ \left({}^{1}\boldsymbol{\theta}_m\right)_{ij} = \mathrm{sgn}\Big[\left({}^{1}\boldsymbol{\theta}_m\right)_{ij}\Big]\left({}^{1}\boldsymbol{\theta}_m\right)_{ij} \quad \forall i,j = 1,\ldots,n \tag{7.33} $$

Then, from the ${}^{1}\boldsymbol{\theta}_m$ estimate, the updated estimate of mass matrix ${}^{1}\mathbf{M}$ can be computed.

2.9 In the end, ${}^{0}\mathbf{M}$, ${}^{0}\mathbf{C}$, ${}^{0}\mathbf{K}$, ${}^{0}\boldsymbol{\theta}_{ck}$ and ${}^{0}\boldsymbol{\theta}_m$ can be replaced by updated parameters ${}^{1}\mathbf{M}$, ${}^{1}\mathbf{C}$, ${}^{1}\mathbf{K}$, ${}^{1}\boldsymbol{\theta}_{ck}$ and ${}^{1}\boldsymbol{\theta}_m$ in Step 1.1.

The two-stage recursive algorithm iterates then from Step 1.2 to Step 2.8, until the following convergence criteria are met:

$$ \max\left|\frac{{}^{i}\boldsymbol{\theta}_{ck}(p) - {}^{i-1}\boldsymbol{\theta}_{ck}(p)}{{}^{i}\boldsymbol{\theta}_{ck}(p)}\right| < \varepsilon_\theta, \qquad \max\left|\frac{{}^{i}\boldsymbol{\theta}_{m}(q) - {}^{i-1}\boldsymbol{\theta}_{m}(q)}{{}^{i}\boldsymbol{\theta}_{m}(q)}\right| < \varepsilon_\theta \tag{7.34a} $$

$$ \max\left\|\frac{{}^{i}\tilde{\ddot{u}}_{g,ck}^{(r)}(t_j) - {}^{i}\bar{\ddot{u}}_{g,ck}(t_j)}{{}^{i}\bar{\ddot{u}}_{g,ck}(t_j)}\right\| < \varepsilon_g, \quad \max\left\|\frac{{}^{i}\tilde{\ddot{u}}_{g,m}^{(r)}(t_j) - {}^{i}\bar{\ddot{u}}_{g,m}(t_j)}{{}^{i}\bar{\ddot{u}}_{g,m}(t_j)}\right\| < \varepsilon_g \tag{7.34b} $$

where left superscript i indicates the current iteration step (and $i-1$ the previous one), and p and q are the pth and q^{th} elements of vectors $\boldsymbol{\theta}_{ck}$ and $\boldsymbol{\theta}_m$, respectively. Superscript r is the rth DOF of the estimated ground motion, while j indicates the jth time instant of interest. Finally, ε_θ and ε_g represent the selected tolerances, which generally can be chosen to be between 10^{-4} and 10^{-6}. Of course, ε_θ refers to a convergence criterion on the structural parameters, while ε_g refers to a convergence criterion on the estimated input ground motion.

For the analyses presented here, convergence tolerances have been generally set to $\varepsilon_\theta = 10^{-6}$ and $\varepsilon_g = 10^{-4}$. For the ground motion, a lower

convergence level is selected, since the estimation error is "diluted" over a considerable greater amount of values, with respect to that for the vector parameters. A stopping criterion is set if after 2000 iterations the convergence criteria have not reached at least $\varepsilon_\theta = 10^{-4}$ and $\varepsilon_g = 10^{-2}$. Then, the algorithm definitively stops if after 5000 iterations convergence has not been reached, or if any of the θ_i identified parameters goes to zero or to infinity.

Once the iterations made on the two stages of the algorithm go to convergence, the final $\boldsymbol{\theta}_{ck}$ and $\boldsymbol{\theta}_m$ render realizations of the final mass, damping and stiffness matrices, jointly with realizations of state matrix $\mathbf{A}$ and output matrix $\mathbf{C}_0$, which can be directly derived from $\mathbf{G}_m$. At a glance, a realization of the State-Space model can be reconstructed from these matrices. Then, the average value $\bar{\ddot{u}}_{g,m}(t)$ obtained from Step 2.5 represents the estimated time history of the ground motion.

7.1.3 Element-level identification procedure

As previously explained, from the FDCIM, estimates of the modal parameters, of the input ground motion excitation and of the structural (mass, damping and stiffness) matrices at the element-level can be achieved. These matrices, as well as the identified State-Space matrices ($\mathbf{A}$, $\mathbf{B}$, $\mathbf{C}_0$ and $\mathbf{D}$), represent a realization of the system under investigation, i.e. a possible combination of matrices which is able to reconstruct the acquired structural responses $\mathbf{u}(t)$, $\dot{\mathbf{u}}(t)$ and $\ddot{\mathbf{u}}(t)$, known the input ground motion excitation $\ddot{u}_g(t)$. The latter can be estimated from Step 2.5, as exposed earlier.

Then, from the estimated realization of state and output matrices ($\mathbf{A}$ and $\mathbf{C}_0$) or, equivalently, of mass, damping and stiffness matrices, the modal properties (natural frequencies, mode shapes and modal damping ratios) can be obtained in a straight-forward manner [27, 31].

The last issue concerns the accurate identification of the *element-level* values, since by this iterative procedure matrices $\mathbf{M}$, $\mathbf{C}$ and $\mathbf{K}$ are identified correctly, unless for a real positive multiplying parameter δ, hereafter called *Fixing Factor*. This means that the proper orders of magnitude between each element are preserved, and only a multiplying parameter δ is required to restore the real amount of each mass, damping and stiffness element. In other words, different realizations of matrix $\mathbf{M}$, $\mathbf{C}$ and $\mathbf{K}$ differ only for an unknown proportionality factor.

The Fixing Factor δ can be computed through the knowledge (or at least, the evaluation) of a single structural parameter, allowing then for rescaling the realizations. For instance, the total mass of the building under exam may be known or estimated, or any other single parameter of

one of three matrices $\mathbf{M}$, $\mathbf{C}$ and $\mathbf{K}$ (namely any single parameter among m_i, c_i and k_i). Basically, one of these comparison values P comes from its knowledge (or estimation) from the real building (P_{real}), while the other is taken from the estimated model (P_{est}). So, the Fixing Factor can be simply computed as the ratio between them:

$$\delta = \frac{P_{real}}{P_{est}}, \quad \text{being } P = m_{tot},\ m_i,\ c_i \text{ or } k_i \tag{7.35}$$

Then, by multiplying the estimated mass, damping and stiffness matrices by the Fixing Factor, the real value of the element-level identified parameters is achieved. In the present work and in [96, 99], the element-level estimates achieved from the analysed cases adopt always $P = m_{tot}$ as rescaling parameter (a parameter that may be judged in practical cases, based on several types of information that may be known for the building).

7.2 Full Dynamic Compound Inverse Method with General and Rayleigh damping

7.2.1 FDCIM mathematical model with General and Rayleigh damping

With viscous damping, as treated in previous Section 7.1, damping matrix $\mathbf{C}$ shares the same tridiagonal symmetric structure as for matrix $\mathbf{K}$ (see Eq. 7.2), with n damping coefficients c_i, leading to a matrix where damping coefficients c_{ij} are coupled to each other. This damping matrix definition is not able to describe more general damping behaviours, where the damping characteristics are spread all over the structure, and do not depend only on the lateral column dissipative coefficients between floor i and $(i-1)$. A particular case of the General damping behaviour above is well-known Rayleigh damping, where damping matrix $\mathbf{C}$ is made by a linear combination of stiffness and mass matrices $\mathbf{C} = \alpha\mathbf{M} + \beta\mathbf{K}$.

So, this modification of the FDCIM algorithm is implemented to deal with the attached implementation issues, in order to achieve an effective element-level system identification and input estimation procedure. In the following of the present section, fundamental changes in the FDCIM equations are highlighted. The first expedient to bypass the coupling of the damping coefficients c_{ij} comes from a different writing of damping matrix $\mathbf{C}$, with an augmented number of damping coefficients:

$$\mathbf{C} = \underbrace{\begin{bmatrix} c_1 + c_2 & -c_2 & 0 & \dots & 0 \\ -c_2 & c_2 + c_3 & -c_3 & \dots & 0 \\ 0 & -c_3 & c_3 + c_4 & \dots & 0 \\ \vdots & \vdots & \vdots & \ddots & \vdots \\ 0 & 0 & 0 & \dots & c_n \end{bmatrix}}_{n \text{ parameters } c_i} [\text{Ns/m}]$$

$$\Rightarrow \mathbf{C} = \underbrace{\begin{bmatrix} c_{11} & c_{12} & 0 & \dots & 0 \\ c_{21} & c_{22} & c_{23} & \dots & 0 \\ 0 & c_{32} & c_{33} & \dots & 0 \\ \vdots & \vdots & \vdots & \ddots & \vdots \\ 0 & 0 & 0 & \dots & c_{nn} \end{bmatrix}}_{2n-1 \text{ parameters } c_{ij}=c_{ji}} [\text{Ns/m}] \tag{7.36}$$

In this way, the tridiagonal symmetric structure of matrix $\mathbf{C}$ with n coefficients c_i $(i = 1, \dots, n)$, which is in common with stiffness matrix $\mathbf{K}$, may be neglected, on behalf of a more general (still symmetric) tridiagonal structure, where $2n+1$ coefficients c_{ij} $(i, j = 1, \dots, n)$ are generic damping parameters, decoupled from each other and thanks to the symmetry of the $\mathbf{C}$ matrix, decrease to $2n - 1$ different coefficients. Thus, this is the first step when dealing with General or Rayleigh damping (or when hypotheses on damping behaviour cannot be made).

The adoption of Rayleigh damping, as a particular case of General damping, is actually very interesting and rather challenging from the inverse analysis point of view, since it brings to a set of non-linear identification equations in terms of the unknown stiffness and mass parameters. Thus, it is brought to light below how the $\mathbf{C}$ matrix formulation of Eq. (7.36) can be the adopted to address such an identification issue for Rayleigh damping.

By adopting Rayleigh damping $\mathbf{C} = \alpha\mathbf{M} + \beta\mathbf{K}$, the n equations of motion (Eq. (7.1)) may be rewritten as:

$$\mathbf{M}\left[\ddot{\mathbf{u}}(t) + \alpha\dot{\mathbf{u}}(t)\right] + \mathbf{K}\left[\beta\dot{\mathbf{u}}(t) + \mathbf{u}(t)\right] = -\mathbf{M}\ddot{\mathbf{u}}_g(t) \tag{7.37}$$

Previous Eqs. (7.1) and (7.37) can be rewritten in State-Space (SS) form, by switching their n second-order differential equations of motion into $2n$ first-order differential equations [31], in terms of *state equation* and *observer equation* (see Eqs. (7.3) and (7.4)).

With the purpose of FDCIM system identification, structural dynamic responses $\mathbf{u}(t)$, $\dot{\mathbf{u}}(t)$ and $\ddot{\mathbf{u}}(t)$ are the only known quantities. Mass $\mathbf{M}$, damping $\mathbf{C}$ (with Rayleigh damping coefficients α and β) and stiffness $\mathbf{K}$

matrices and seismic ground acceleration $\ddot{u}_g(t)$ are the unknown variables to be identified.

Thus, by following the theoretical background of FDCIM (Section 7.1.1 and [97]), the two basic identification equations for the present Rayleigh damping case may be written from Eq. (7.37) as:

$$(\alpha\mathbf{M} + \beta\mathbf{K})\,\dot{\mathbf{u}}(t) + \mathbf{K}\mathbf{u}(t) = -\mathbf{M}\Big(\ddot{\mathbf{u}}(t) + \ddot{\mathbf{u}}_g(t)\Big) \tag{7.38}$$

$$\mathbf{M}^{-1}\Big[\,(\alpha\mathbf{M} + \beta\mathbf{K})\,\dot{\mathbf{u}}(t) + \mathbf{K}\mathbf{u}(t)\Big] = -\ddot{\mathbf{u}}(t) - \ddot{\mathbf{u}}_g(t) \tag{7.39}$$

From Eqs. (7.38) and (7.39) it is possible to see that they constitute a set of non-linear identification equations in terms of the unknown structural parameters, since unknown coefficients α and β are strictly coupled to the unknown stiffness and mass terms in matrices $\mathbf{K}$ and $\mathbf{M}$, respectively. Thus, the identification problem based on Eqs. (7.38) and (7.39) is quite difficult to be handled by FDCIM (and, in general, by DCIM methods). Then, the general formulation below is adopted. In this way, Rayleigh damping may be treated as a special case of a more general formulation, with Rayleigh damping coefficients that may be estimated as outlined later in Section 7.2.3.

Thus, the expedient to bypass the set of non-linear identification equations comes exactly from the different writing of damping matrix $\mathbf{C}$ exposed in Eq. (7.36). The derivation goes back to that from now on.

Accordingly, Eqs. (7.38) and (7.39) may be brought back to the definitions made in Eqs. (7.5) and (7.6), which constitute the basic concatenated relations on which the present recursive FDCIM method is built.

By following the treatment developed in Section 7.1.1, subsequent steps may be adapted and modified in order to arrive at the equations of the *two identification stages* in case of General damping or Rayleigh damping. Then, Eq. (7.5) – the origin of the first stage of the FDCIM identification method – may be rewritten from Eq. (7.10):

$$\mathbf{H}_{ck}(t)\boldsymbol{\theta}_{ck} = \mathbf{P}_{ck}(t) \quad \Rightarrow \quad \underbrace{\begin{bmatrix} \mathbf{H}^1_{ck}(t) & \mathbf{0}_{n\times(3n-1)} \\ \mathbf{0}_{n\times n} & \mathbf{H}^2_{ck}(t) \end{bmatrix}}_{2n\times(4n-1)} \underbrace{\begin{Bmatrix} \boldsymbol{\theta}^1_{ck} \\ \boldsymbol{\theta}^2_{ck} \end{Bmatrix}}_{(4n-1)\times 1} = \underbrace{\begin{Bmatrix} \mathbf{P}^1_{ck}(t) \\ \mathbf{P}^2_{ck}(t) \end{Bmatrix}}_{2n\times 1} \tag{7.40}$$

where zero matrices have dimensions as suggested by the related subscripts. In earlier Eq. (7.40), matrix $\mathbf{H}_{ck}(t)$ contains the velocity and displacement responses (known quantities, input for the identification algorithm), vector $\boldsymbol{\theta}_{ck}$ contains all c_{ij} damping and k_i stiffness parameters (unknowns, to be identified) and vector $\mathbf{P}_{ck}(t)$ is related to the m_i mass

terms (unknowns, to be identified), containing both velocity and acceleration responses (known quantities) and input ground motion excitation $\ddot{u}_g(t)$ (unknown, to be identified). At a generic time instant $t = t_i$, $i = 1, \ldots, L$, being L the length of the recorded input signal, $\mathbf{H}^1_{ck}(t_i)$, $\boldsymbol{\theta}^1_{ck}$, $\mathbf{P}^1_{ck}(t_i)$ and $\mathbf{P}^2_{ck}(t_i)$ elements can be expressed as reported by Eqs. (7.13) and (7.14c), while $\mathbf{H}^2_{ck}(t_i)$ and $\boldsymbol{\theta}^2_{ck}$ takes a different expression, which may be computed as:

$$\mathbf{H}^2_{ck}(t_i) = \underbrace{\begin{bmatrix} \dot{u}_1 & \dot{u}_2 & 0 & 0 & 0 & \cdots & 0 & u_1 & u_1-u_2 & 0 & \cdots & 0 \\ 0 & \dot{u}_1 & \dot{u}_2 & \dot{u}_3 & 0 & \cdots & 0 & 0 & u_2-u_1 & u_2-u_3 & \cdots & 0 \\ 0 & 0 & 0 & \dot{u}_2 & \dot{u}_3 & \cdots & 0 & 0 & 0 & u_3-u_2 & \cdots & 0 \\ \vdots & \vdots & \vdots & \vdots & \vdots & \ddots & \vdots & \vdots & \vdots & \vdots & \ddots & \vdots \\ 0 & 0 & 0 & 0 & 0 & \cdots & \dot{u}_n & 0 & 0 & 0 & \cdots & u_n-u_{n-1} \end{bmatrix}}_{n\times(3n-1)} \tag{7.41a}$$

$$\boldsymbol{\theta}^2_{ck} = \{\underbrace{c_{11}\ c_{12}\ c_{22}\ \ldots\ c_{ij}\ \ldots\ c_{nn},\ k_1\ k_2\ k_3\ \ldots\ k_i\ \ldots\ k_n}_{1\times(3n-1)}\}^{\mathrm{T}} \tag{7.41b}$$

The definitions of terms contained in Eq. (7.40) may be expressed also by gathering the sampling time instants all together as:

$$\underbrace{\mathbf{H}_{ck}}_{(L\times 2n)\times(4n-1)} \quad \underbrace{\boldsymbol{\theta}_{ck}}_{(4n-1)\times 1} = \underbrace{\mathbf{P}_{ck}}_{(L\times 2n)\times 1} \tag{7.42}$$

where the full matrix components take the subsequent definitions:

$$\mathbf{H}_{ck} = [\mathbf{H}_{ck}(t_1)\ \mathbf{H}_{ck}(t_2)\ \ldots\ \mathbf{H}_{ck}(t_L)]^{\mathrm{T}} \tag{7.43a}$$

$$\boldsymbol{\theta}_{ck} = \{\underbrace{1\ \ 1\ 1\ \ldots\ 1}_{1\times n},\ \underbrace{c_{11}\ c_{12}\ c_{22}\ \ldots\ c_{ij}\ \ldots\ c_{nn}}_{1\times(2n-1)},\ \underbrace{k_1\ k_2\ k_3\ \ldots\ k_i\ \ldots\ k_n}_{1\times n}\}^{\mathrm{T}} \tag{7.43b}$$

$$\mathbf{P}_{ck} = \{\mathbf{P}_{ck}(t_1)\ \mathbf{P}_{ck}(t_2)\ \ldots\ \mathbf{P}_{ck}(t_L)\}^{\mathrm{T}} \tag{7.43c}$$

In the end, the unknown parameters of vector $\boldsymbol{\theta}_{ck}$ may be estimated via Least-Squares, on the full matrix definitions of Eqs. (7.43a)-(7.43c), by adopting the formulation of previous Eq. (7.15).

In a similar way, the second identification stage (Section 7.2.2) can be deduced from Eq. (7.6), by retracing all the steps, definitions and equations starting from Eq. (7.16) to Eq. (7.21).

The so-formulated identification problem is not one of a simple solution, since the unknown parameters are contained not only into the $\boldsymbol{\theta}_{ck}$ and $\boldsymbol{\theta}_m$ vectors, but also into the $\mathbf{P}_{ck}$, $\mathbf{H}_m$ and $\mathbf{P}_m$ matrices. Obviously, the price to be paid for the possibility of identifying also Generally-damped and Rayleigh-damped systems is the increase of the number of unknowns from $3n$ to $4n-1$ and $4n+1$, respectively. Besides, convergence is guaranteed

and results turn out to be very effective, as presented in [99]. Then, the $4n-1$ unknown structural parameters (which becomes $4n+1$ in case of Rayleigh damping, with the additional α and β Rayleigh damping coefficients, i.e. two unknowns more) and the unknown input ground motion signal may be identified by this modification of the two-stage iterative algorithm of the Full Dynamic Compound Inverse Method (FDCIM). This is treated in the next section.

7.2.2 FDCIM two-stage identification algorithm with General and Rayleigh damping

Through a modification of the two-stage iterative Least-Squares (LS) algorithm seen in Section 7.1.2, the FDCIM technique aims at estimating modal parameters, structural features at the element-level, Rayleigh damping coefficients and input ground motion excitation, when General or Rayleigh damping occur.

Then, the FDCIM algorithm with General or Rayleigh damping can be developed through the same two subsequent stages outlined in Section 7.1.2, where some new steps are necessary in the formulation and are then highlighted from the main workflow of the original FDCIM.

As it concerns to the *first stage of identification*, which allows for the realization of stiffness and damping parameters, the FDCIM novelty is the adopted parameter projection technique, which is necessary after the estimation of damping and stiffness parameters at iteration 1. This step is different from that in Step 1.9 of Section 7.1.2, and it is necessary in order to achieve strictly-positive estimations of some selected $\left({}^1\boldsymbol{\theta}_{ck}\right)_{ij}$ parameters, without the need of solving constrained LS problems. This because the diagonal c_{ij} terms and all the k_{ij} terms need to be positive, while non-diagonal terms c_{ij} can be free to assume their own signs and values:

$$\left({}^1\boldsymbol{\theta}_{ck}\right)_{ij} = \begin{cases} \operatorname{sgn}\left[\left({}^1\boldsymbol{\theta}_{ck}\right)_{ij}\right] \cdot \left({}^1\boldsymbol{\theta}_{k}\right)_{ij} & \text{for } \left({}^1\boldsymbol{\theta}_{ck}\right)_{ij} = c_{ij}, \text{ if } i=j \\ \left({}^1\boldsymbol{\theta}_{ck}\right)_{ij} & \text{for } \left({}^1\boldsymbol{\theta}_{ck}\right)_{ij} = c_{ij}, \text{ if } i \neq j \\ \operatorname{sgn}\left[\left({}^1\boldsymbol{\theta}_{ck}\right)_{ij}\right] \cdot \left({}^1\boldsymbol{\theta}_{k}\right)_{ij} & \text{for } \left({}^1\boldsymbol{\theta}_{ck}\right)_{ij} = k_{ij}, \ \forall i,j = 1,\ldots,n \end{cases} \tag{7.44}$$

where $\operatorname{sgn}[\ldots]$ is again the sign function, i.e. the odd function which aims at extracting the sign of its argument.

Then, as it concerns to the *second stage of identification*, which allows for the realization of the mass parameters, computational steps do not require variations from the original version of FDCIM (see Section 7.1.2). Again, normalized convergence tolerances are represented by ε_θ and ε_g, which are generally selected between 10^{-4} and 10^{-6}.

For the present cases, normalized convergence tolerances for the structural parameters and the input ground motion have been generally set to $\varepsilon_\theta = 10^{-6}$ and $\varepsilon_g = 10^{-4}$. After 2000 iterations, a stopping criteria is set to block the algorithm if convergence criterion do not satisfy at least values $\varepsilon_\theta = 10^{-4}$ and $\varepsilon_g = 10^{-2}$. After 5000 iterations without convergence, or if any of the θ_i identified parameters goes to zero or to infinity, the algorithm stops.

Once convergence is reached, the final $\boldsymbol{\theta}_{ck}$ and $\boldsymbol{\theta}_m$ estimates return a realization of state matrix $\mathbf{A}$ and output matrix $\mathbf{C}_0$ (see Eq. (7.4)), together with a realization of final mass, damping and stiffness matrices. The averaged input vector $\bar{\ddot{u}}_{g,m}(t)$ obtained from Step 2.5 of Section 7.1.2, represents the estimated time history of the ground motion excitation. Finally, Rayleigh damping coefficients α and β may be estimated as outlined in following Section 7.2.3, while the element-level identification procedure follows exactly the same steps previously outlined in Section 7.1.3.

7.2.3 Estimation of Rayleigh damping coefficients

After the computation of the final $\boldsymbol{\theta}_{ck}$ and $\boldsymbol{\theta}_m$ vectors, i.e. of the final mass, damping and stiffness matrices, it is possible to estimate the Rayleigh damping coefficients via the following procedure. The subsequent important comments apply:

- The present procedure may be applied not only to specific Rayleigh-damped systems, as a particular case of General damping, but also to systems characterized by General damping itself, as discussed in Section 7.2.1.

- Thus, in case of the broader case of General damping, the present procedure will return the best possible estimate of the α and β Rayleigh damping coefficients related to the estimated modal and structural properties of the system under investigation.

First, starting from the realizations of mass $\mathbf{M}$, damping $\mathbf{C}$ and stiffness $\mathbf{K}$ matrices, it is possible to calculate the modal properties, i.e. natural frequencies f_i, mode shapes $\boldsymbol{\phi}_i$ and modal damping ratios ζ_i, as usually done in classical modal anaysis [31], i.e. through the solution of the eigenvalue problem, or by operating with State-Space matrices $\mathbf{A}$ and $\mathbf{C}_0$.

By knowing eigenvector matrix $\boldsymbol{\Phi}$, gathering all $i = 1, \ldots, n$ eigenvectors $\boldsymbol{\phi}_i$ as columns, modal mass $\mathcal{M}$, modal damping $\mathcal{C}$ and modal stiffness $\mathcal{K}$ matrices can be classically calculated as:

$$\mathcal{M} = \boldsymbol{\Phi}^{\mathrm{T}}\mathbf{M}\boldsymbol{\Phi}, \quad \mathcal{C} = \boldsymbol{\Phi}^{\mathrm{T}}\mathbf{C}\boldsymbol{\Phi}, \quad \mathcal{K} = \boldsymbol{\Phi}^{\mathrm{T}}\mathbf{K}\boldsymbol{\Phi} \tag{7.45}$$

where $\mathcal{M} = \text{diag}[m_i]$, $\mathcal{C} = \text{diag}[c_i]$ and $\mathcal{K} = \text{diag}[k_i]$ are the diagonal modal matrices related to the estimated system.

So, by starting from the definition of Rayleigh damping coefficients α and β in modal coordinates, i.e. $\mathcal{C} = \alpha\mathcal{M} + \beta\mathcal{K}$, the following relations may be obtained:

$$\begin{aligned} \boldsymbol{z}_{i,j} &= \begin{bmatrix} \alpha_{i,j} \\ \beta_{i,j} \end{bmatrix} = \begin{bmatrix} m_i & k_i \\ m_j & k_j \end{bmatrix}^{-1} \cdot \begin{bmatrix} c_i \\ c_j \end{bmatrix}, \quad \forall\, i,j = 1,\ldots,n \\ \Rightarrow \mathcal{Z} &= \begin{bmatrix} \boldsymbol{z}_{1,2} & \boldsymbol{z}_{1,3} & \boldsymbol{z}_{2,2} & \ldots & \boldsymbol{z}_{i,j} & \ldots & \boldsymbol{z}_{n,n} \end{bmatrix} \end{aligned} \tag{7.46}$$

where the solutions of the previous linear system, made by the calculated modal mass, damping and stiffness as known terms, are the unknown Rayleigh coefficients, for every possible combination of i and j indexes. Then, matrix $\mathcal{Z} \in \mathcal{R}^{2\times r}$ collects each of the r $\boldsymbol{z}_{i,j}$, being r the number of possible combinations without repetitions of indexes i and j, which can be calculated as:

$$r = \mathscr{C}_{n,2} = \frac{n!}{2!(n-2)!} \tag{7.47}$$

Finally, the estimation of the α and β coefficients may be evaluated as the mean value of such r collected parameters:

$$\alpha = \frac{1}{r}\sum_{i,j=1}^{r} \alpha_{i,j}, \quad \beta = \frac{1}{r}\sum_{i,j=1}^{r} \beta_{i,j} \tag{7.48}$$

With reference to the analysed case, this type of estimation of the Rayleigh damping coefficients demonstrated to be very effective, as it was also shown in the results produced in [99].

7.3 Results from synthetic output-only modal dynamic identification

In the present section, the same cases adopted in previous Chapters 4 and 6 are going to be addressed, namely a reference three-storey shear-type frame (Table 4.2) and a more realistic ten-storey shear-type frame (Table 4.3), both characterized by heavy damping. As before, these structures are analysed through the adoption of a set of ten earthquake base-excitations (Table 4.1). Since these structures and earthquakes are adopted for all the three proposed methods, namely rFDD (Chapter 4), SSI-DATA (present Chapter 6) and present FDCIM (Chapter 7), a conclusive comparison among these algorithms in the Earthquake Engineering range may be finally pursued.

Further, representative and exhaustive results, also with variable adopted number of signal points and with added noise to the response signals, are reported in [96, 99].

7.3.1 Analyses and results with a reference three-storey frame

By taking as base excitation the single instances from the set of ten selected earthquake recordings presented in Section 4.1 (Table 4.1), modal dynamic identification analyses have been performed here with the present FDCIM algorithm, in order to identify all strong ground motion modal parameters.

In order to make the FDCIM modal dynamic identification even more challenging, Rayleigh damping ($\mathbf{C} = \alpha\mathbf{M} + \beta\mathbf{K}$) is adopted at this stage, with modal damping ratios set to $\zeta_1 = 7\%$, $\zeta_2 = 7\%$ and $\zeta_3 = 8.73\%$ for the three modes of vibration, respectively.

As concerning to the present FDCIM algorithm, the performed analysis adopted the following settings:

- Butterworth low-pass filtering, order 8, cutting frequency 20 Hz, no decimation of the signals (earthquake-induced structural response signals – input channels for the FDCIM algorithm);
- Adopted number of points set to the entire response signals, for all the earthquake instances;
- Initial values of the iterating vectors set to ${}^0\boldsymbol{\theta}_{ck} = \{1\ 1\ 1\ \ldots\ 1\}^{\mathrm{T}}$ and ${}^0\boldsymbol{\theta}_m = \{1\ 1\ 1\ \ldots\ 1\}^{\mathrm{T}}$;
- Convergence tolerances set both to $\varepsilon_\theta = 10^{-6}$ and $\varepsilon_g = 10^{-6}$, in order to achieve the best estimates as possible, despite for the possible increase of the total number of iterations;
- Stopping criterion set after 30000 iterations, if the convergence criteria have not reached at least $\varepsilon_\theta = 10^{-4}$ and $\varepsilon_g = 10^{-2}$;
- Stop after 100000 iterations if convergence has not been reached, or if any of the θ_i identified parameters goes to zero or to infinity;
- Fixing Factor δ computed through the total mass of the building under exam m_{tot}, namely $\delta = P_{real}/P_{est} = m_{tot,real}/m_{tot,est}$.

In the present context, the analysed cases represent very challenging instances for the present FDCIM algorithm, since all the m_i and k_i structural parameters turn out to be equal one each other, respectively (i.e. $m_1 = m_2 = m_3$ and $k_1 = k_2 = k_3$), by representing the worst case for a good

and fast convergence of the algorithm. In addition, also Rayleigh damping is taken into account. Then, this leads to a necessary enlargement of the required number of iterations, and consequently of the stopping criterion, in order to respect the set convergence tolerances. Despite those issues, estimate results turn out the be very effective, as outlined in the following.

Thus, by adopting the present FDCIM algorithm, with the settings reported above, complete synthetic output-only analyses have been performed. A synopsis from all the achieved modal parameter estimates is reported in Fig. 7.2, where the estimates in terms of absolute deviations of FDCIM identified natural frequencies Δf and modal damping ratios $\Delta\zeta$ and achieved MAC indexes for the estimated mode shapes are depicted (see Eqs. 4.1a-4.1c).

The FDCIM estimated frequencies show to be very effective, with maximum deviations equal to 0.0611%, 0.0063% and 0.0197% for the three natural frequencies, respectively. These deviations are all related to the earthquake of Kobe (KO), the worst case to be analysed with the present three-storey shear-type frame with the FDCIM algorithm. Jointly with the Kobe earthquake, the most challenging seismic cases are related to the earthquakes of Christchurch (NZ) and Northridge (NO). Modal damping ratios display a bit higher deviations with respect to those for the natural frequencies, but they are estimated again in a very effective way. In fact, maximum deviations are equal to 1.2923%, 0.0530% and 0.4445%, for the three modal damping ratios, respectively. These deviations are all related to the Imperial Valley (IV) seismic event, which represents a challenging case for the modal damping ratio identification, together with the earthquakes of Kobe (KO) and Northridge (NO). Finally, mode shapes are estimated in an extremely effective way, by showing always unitary MAC indexes.

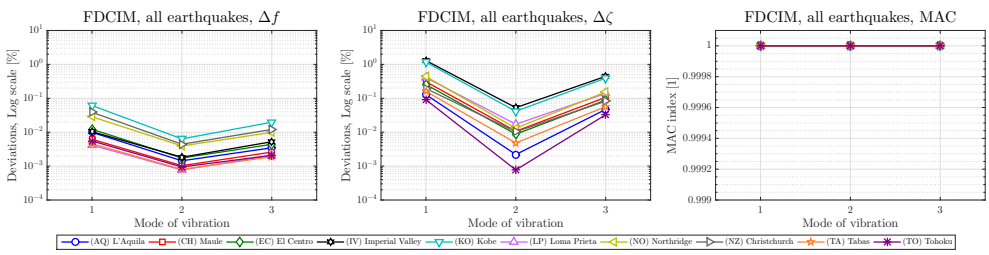

Figure 7.2: *Deviations of estimated natural frequencies and modal damping ratios, and MAC indexes, three-storey frame, synthetic response signals, FDCIM algorithm, Rayleigh damping, complete considered earthquake dataset.*

With the present FDCIM algorithm is then possible to achieve very accurate modal parameter estimates, for all the cases. In terms of all the

achieved estimates, FDCIM performs better than rFDD and SSI-DATA, in the present seismic and heavy damping context, by showing the closest estimates to the target values. In this sense, the two-stage iterative Time Domain FDCIM algorithm appears superior to the non-parametric Frequency Domain rFDD and to the parametric Time Domain Data-Driven SSI. The hypotheses made on the matrix structural behaviour and the totally deterministic framework display to be the key features in order to achieve these very effective modal parameter estimates.

Then, global results on the achieved modal estimates are further summarized in Fig. 7.3, where the absolute deviations of estimated natural frequencies and modal damping ratios, and the MAC indexes are represented, in terms of suitably-designed dispersion diagrams [97], as adopted before in Chapters 4 and 6.

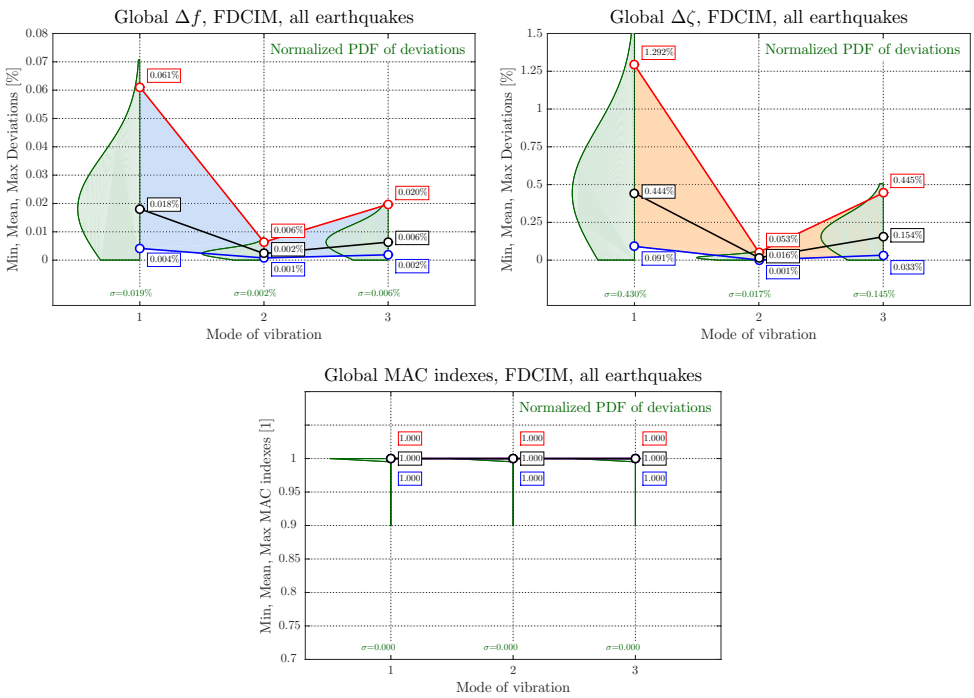

Figure 7.3: *Dispersion diagrams for the deviations of estimated natural frequencies and modal damping ratios, and for the MAC indexes, three-storey frame, synthetic response signals, FDCIM algorithm, Rayleigh damping, complete considered earthquake dataset. Minimum, mean and maximum values, and standard deviations are indicated.*

As before, these truncated Gaussians represent the probability of appearance of a certain deviation, as associated to each estimate, between the minimum and the maximum value, and are centred on the mean value.

Gaussians show to be very narrow, especially for the MAC indexes, and maximum deviations are always on the Gaussian tails, while the minimum deviations lay in the Gaussian center. This confirms again the accuracy of the achieved FDCIM modal identification estimates.

Finally, the achieved results are also synoptically reported in statistical form in Fig. 7.4, by making use of appropriate boxplots, as previously adopted in Chapters 4 and 6. Presented boxplots confirm again the accuracy of the achieved FDCIM estimates. All modal parameters, namely natural frequencies, modal damping ratios and MAC indexes, display to catch exactly the target values.

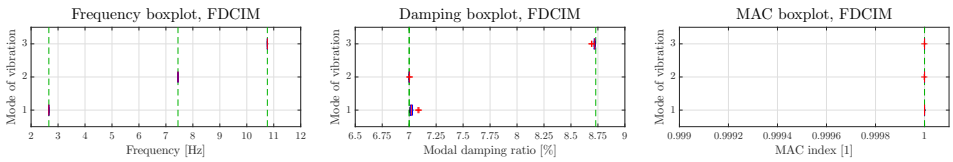

Figure 7.4: *Boxplot diagrams for estimated natural frequencies, modal damping ratios and MAC indexes, three-storey frame, synthetic response signals, FDCIM algorithm, Rayleigh damping, complete considered earthquake dataset.*

7.3.1.1 Element-level identification estimates for a three-storey frame

Additionally to the estimation of the modal parameters, the FDCIM method is able to identify also the structural parameters at the element-level, the Rayleigh damping coefficients and the seismic ground motion base-excitation.

The structural features of the frame are reported in Chapter 4 (see Table 4.2), where the frame is revised here to take into account Rayleigh damping. This is implemented by setting the first two modal damping ratios equal to $\zeta_1 = \zeta_2 = 7\%$, resulting in a third modal damping ratio $\zeta_3 = 8.73\%$. The corresponding Rayleigh damping coefficients are $\alpha = 1.723328$ and $\beta = 0.002205$.

For all the analysed cases, absolute percentage deviations of the estimated mass m_i, damping c_{ij} and stiffness k_i element-level parameters are reported in Fig. 7.5 (calculated for each Par parameter as $\Delta\text{Par} = |\text{Par}_{i,id} - \text{Par}_{i,targ}|/\text{Par}_{i,targ} \cdot 100$, as seen in Eqs. (4.1a)-(4.1b) for f_i and ζ_i).

As it concerns the estimated element-level parameters, maximum deviations are equal to 0.1281%, 0.0366% and 0.1648% for the mass parameters (all related to the Kobe (KO) earthquake), 0.1563% (IV), 1.0897%, 0.2364%, 0.7842% (KO) and 0.1865% (IV) for the damping coefficients and 0.0990%, 0.0359% and 0.0645% (KO) for the stiffness coefficients. As before, the most challenging earthquakes are the Kobe (KO), Christ-

church (NZ) and Northridge (NO) seismic events. Then, also the element-level structural parameters are estimated always in an extremely effective way, by showing very limited deviations.

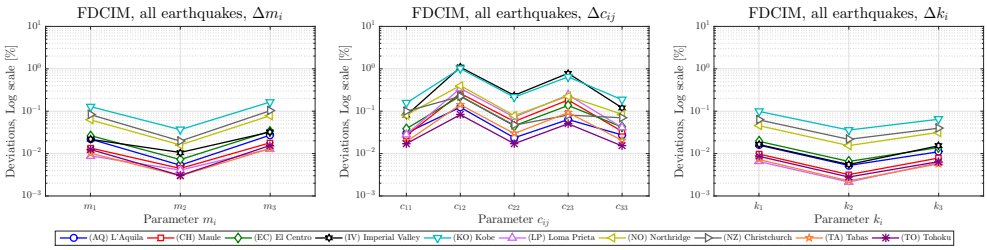

Figure 7.5: *Deviations of identified mass m_i, damping c_i and stiffness k_i parameters, three-storey frame, synthetic response signals, FDCIM algorithm, Rayleigh damping, complete considered earthquake dataset.*

Furthermore, in Fig. 7.6 the achieved absolute deviations of the results for the Rayleigh damping coefficients and for the earthquake input excitation are represented, for each considered seismic excitation. For the Rayleigh damping coefficients, maximum deviations are 2.4114% (IV) and 0.8607% (IV) for the α and β parameters, respectively. In general, parameter α performs slightly better than parameter β. Then, for the estimated earthquake input base excitation, the maximum deviations show to be 0.0984% (IV) for the Peak Ground Acceleration (PGA) and 0.1330% (IV) for the Root Mean Square (RMS). Anyway, they perform more or less equally. Again, as demonstrated also with the other estimates, all the identified results for the Rayleigh coefficients and the input ground motion excitation prove the reliability and effectiveness of the present FDCIM algorithm.

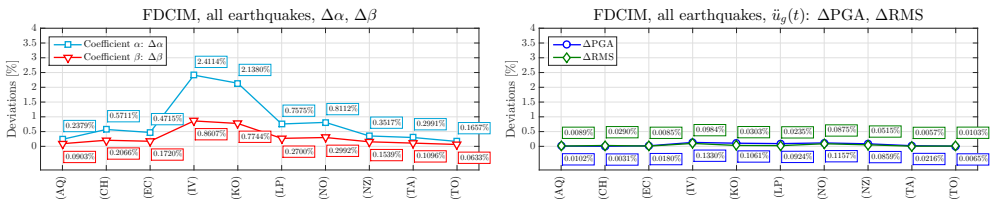

Figure 7.6: *Deviations of identified α and β Rayleigh damping coefficients and estimated input ground motion excitation in terms of PGA and RMS, three-storey frame, synthetic response signals, FDCIM algorithm, Rayleigh damping, complete considered earthquake dataset.*

Then, global results on the achieved element-level parameters are fur-

ther summarized in Fig. 7.7, where the absolute deviations of estimated element-level mass, damping and stiffness structural parameters are represented, in terms of suitably-designed dispersion diagrams [97].

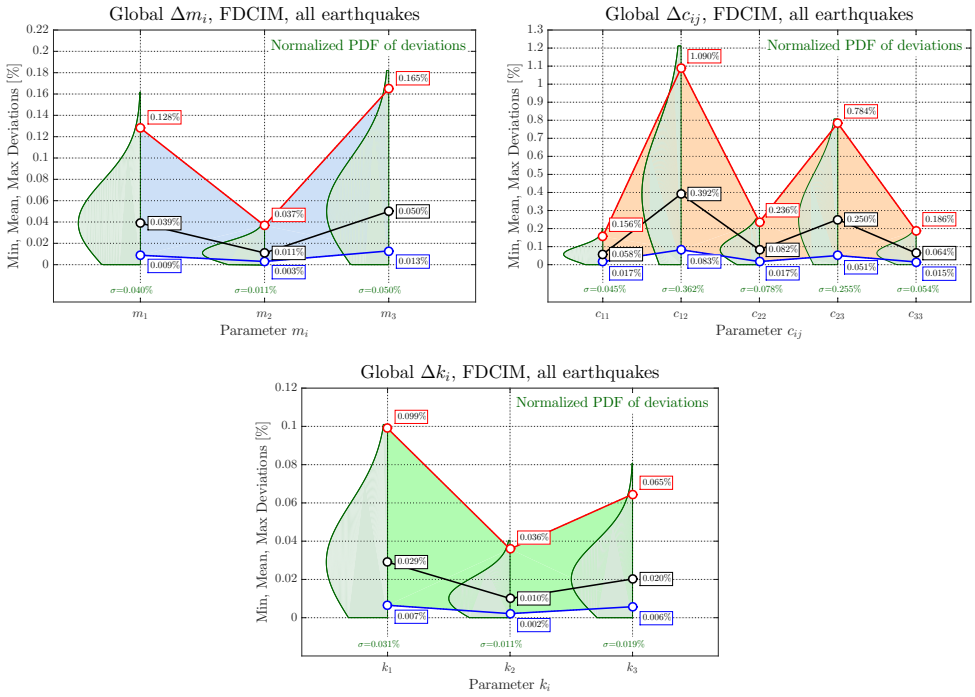

Figure 7.7: *Dispersion diagrams for the deviations of identified mass m_i, damping c_i and stiffness k_i parameters, three-storey frame, synthetic response signals, FDCIM algorithm, Rayleigh damping, complete considered earthquake dataset. Minimum, mean and maximum values, and standard deviations are indicated.*

As it was expected, stiffness parameters are the most accurate, while deviations increase a little bit for mass and damping parameters, in the order of increasing deviations.

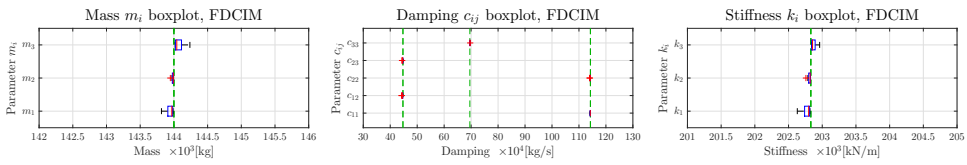

Figure 7.8: *Boxplot diagrams for identified mass m_i, damping c_i and stiffness k_i parameters, three-storey frame, synthetic response signals, FDCIM algorithm, Rayleigh damping, complete considered earthquake dataset.*

Finally, the achieved element-level parameters are also synoptically re-

ported in statistical form in Fig. 7.8, by making use of appropriate boxplots, as previously adopted in Chapters 4 and 6. Presented boxplots confirm again the accuracy of the achieved FDCIM estimates. All structural parameters, namely element-level mass, damping and stiffness features, catch exactly the target values.

7.3.2 Further synthetic identification analyses with a realistic ten-storey frame

In the present section, as seen in Sections 4.2.2 and 6.2.2, the focus goes again to the analyses and results that can be achieved by adopting the realistic ten-storey RC frame adopted before (Table 4.3). The settings for the FDCIM identification procedure are the same as those employed earlier, except than for the following points:

- Butterworth low-pass filtering, order 8, cutting frequency 10 Hz, no decimation of the signals (earthquake-induced structural response signals – input channels for the FDCIM algorithm);
- Stopping criterion set after 2000 iterations, if convergence criteria have not reached at least $\varepsilon_\theta = 10^{-4}$ and $\varepsilon_g = 10^{-2}$;
- Stop after 5000 iterations if convergence has not been reached, or if any of the θ_i identified parameters goes to zero or to infinity.

As it was previously done in Section 7.3.1, a synopsis from all the achieved results is depicted in Fig. 7.9. The absolute deviations of FDCIM identified natural frequencies and modal damping ratios and the achieved MAC indexes are reported in this representations.

As before, the FDCIM estimated frequencies show to be very effective, with a maximum deviation equal to 0.0034%, related to the 7th natural frequency with the NZ earthquake. This time, the most challenging seismic cases are related to the Christchurch (NZ) and Loma Prieta (LP) earthquakes. Modal damping ratios display a bit higher deviations with respect to natural frequencies, but they are estimated again in a very effective way. In fact, the maximum deviation is equal to 0.0074%, related to the 1st modal damping ratio with the TO earthquake. This time, the higher deviations are related to the Christchurch (NZ) and to the Tohoku (TO) seismic events. Finally, mode shapes are again estimated in an extremely effective way, by showing always unitary MAC indexes.

As seen with the three-storey frame, with the present FDCIM algorithm is then possible to achieve very accurate modal parameter estimates, for all the cases. Rather, the adoption of ten input (response) channels allows for a better and faster convergence of the two-stage iterative algorithm.

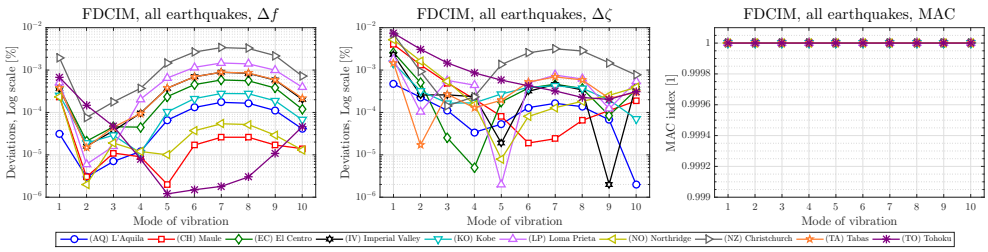

Figure 7.9: *Deviations of estimated natural frequencies and modal damping ratios, and MAC indexes, ten-storey frame, synthetic response signals, FDCIM algorithm, Rayleigh damping, complete considered earthquake dataset.*

Then, FDCIM performs even much better than rFDD and SSI-DATA, in the present seismic and heavy damping context, by showing the closest estimates to the target values.

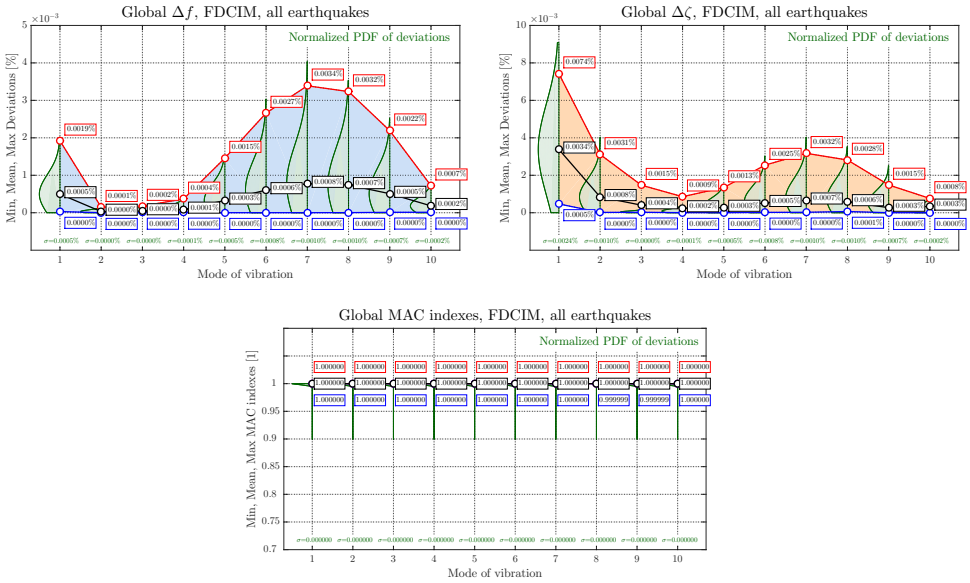

Figure 7.10: *Dispersion diagrams for the deviations of estimated natural frequencies and modal damping ratios, and for the MAC indexes, ten-storey frame, synthetic response signals, FDCIM algorithm, Rayleigh damping, complete considered earthquake dataset. Minimum, mean and maximum values, and standard deviations are indicated.*

Then, as before, Fig. 7.10 summarizes the global results on the achieved modal estimates for the ten-storey frame, where the absolute deviations of the estimated natural frequencies and modal damping ratios, and the MAC indexes are represented in terms of appropriate dispersion diagrams.

The truncated Gaussian distributions show once again that maximum deviations lay always on the Gaussian tails, while minimum deviations are located near the Gaussian centres. This confirms once again the reliability of the achieved FDCIM modal identification estimates.

Finally, the results achieved from the realistic ten-storey frame are also synoptically reported in Fig. 7.11, in terms of statistical boxplots. Here, natural frequencies, modal damping ratios and MAC values estimated from the performed synthetic analyses are represented. The proposed boxplots confirm again the effectiveness of the FDCIM estimates, by showing that estimated instances are very close to the target modal parameters.

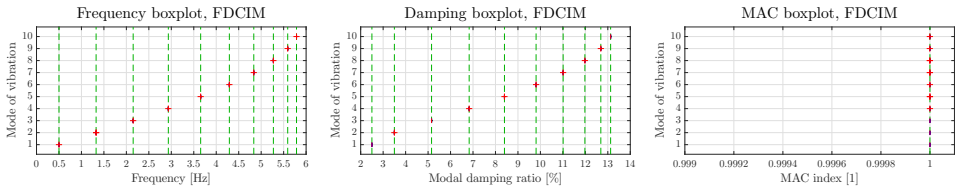

Figure 7.11: *Boxplot diagrams for estimated natural frequencies, modal damping ratios and MAC indexes, ten-storey frame, synthetic response signals, FDCIM algorithm, Rayleigh damping, complete considered earthquake dataset.*

7.3.2.1 Element-level identification estimates for a ten-storey frame

As previously done with the three-storey frame, structural parameters at the element-level, the Rayleigh damping coefficients and the seismic ground motion base-excitation estimates are now addressed also for the ten-storey frame.

The structural features of the ten-storey frame are reported in Chapter 4 (see Table 4.3). The Rayleigh damping coefficients corresponding to those parameters are $\alpha = 0.086478$ and $\beta = 0.007155$.

For all the analysed cases, absolute percentage deviations of the estimated mass m_i, damping c_{ij} and stiffness k_i element-level parameters are reported in Fig. 7.9.

For the estimated element-level parameters, maximum deviations are equal to 0.0250% for the mass parameters (9th mass parameter for the NZ earthquake), 0.0202% (last damping parameter for the NZ earthquake) and 0.0222% (last stiffness parameter for the NZ earthquake) for the stiffness coefficients. The most challenging earthquakes reveals to be the Loma Prieta (LP), Christchurch (NZ) and Tohoku (TO) seismic events. Again, the element-level structural parameters are estimated always in an extremely effective way, by showing very limited deviations. They take ad-

vantage of the increased number of input (response) channels, as seen previously for the modal parameters.

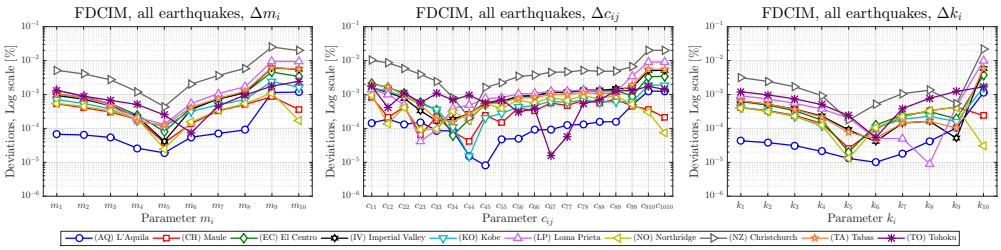

Figure 7.12: *Deviations of identified mass m_i, damping c_i and stiffness k_i parameters, ten-storey frame, synthetic response signals, FDCIM algorithm, Rayleigh damping, complete considered earthquake dataset.*

Then, in Fig. 7.13 the achieved absolute deviations of the results for the Rayleigh damping coefficients and for the earthquake input excitation are represented, for each considered seismic excitation. For the Rayleigh damping coefficients, maximum deviations are 0.0804% and 0.0013% for the α and β parameters, respectively, for the NZ earthquake. As before, parameter α performs slightly better than parameter β. Then, for the estimated earthquake input base excitation, the maximum deviations show to be 0.00010% for the PGA and 0.00029% for the RMS, both for the LP earthquake. Again, they perform more or less equally.

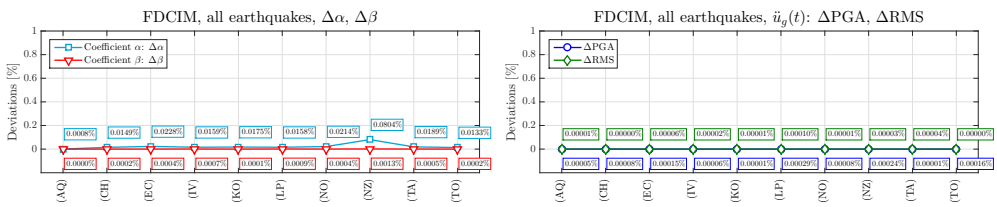

Figure 7.13: *Deviations of identified α and β Rayleigh damping coefficients and estimated input ground motion excitation in terms of PGA and RMS, ten-storey frame, synthetic response signals, FDCIM algorithm, Rayleigh damping, complete considered earthquake dataset.*

Additionally, global results on the achieved element-level parameters are summarized in Fig. 7.14, where the absolute deviations of estimated element-level mass, damping and stiffness structural parameters are represented, in terms of suitably-designed dispersion diagrams [97].

Notice that for the last element-level parameters there is an increase of the deviations, for all the cases. Nevertheless, deviations remain very

limited, in the order of 0.025%.

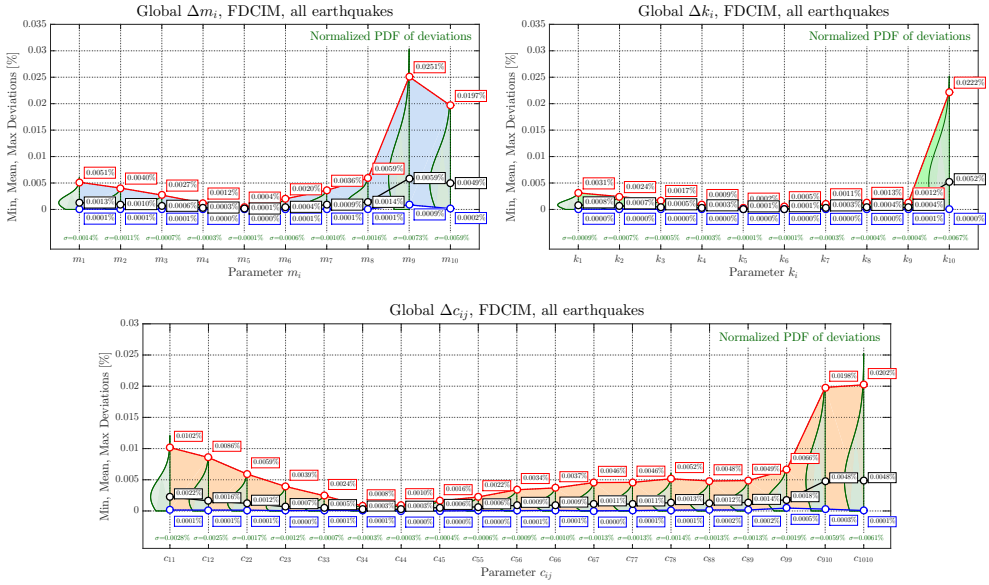

Figure 7.14: *Dispersion diagrams for the deviations of identified mass m_i, damping c_i and stiffness k_i parameters, ten-storey frame, synthetic response signals, FDCIM algorithm, Rayleigh damping, complete considered earthquake dataset. Minimum, mean and maximum values, and standard deviations are indicated.*

Finally, the achieved element-level parameters are synoptically reported in statistical form in Fig. 7.11. Presented boxplots confirm again the accuracy of the achieved FDCIM estimates. All element-level structural parameters, namely mass m_i, damping c_{ij} and stiffness k_i coefficients, catch exactly the target values. This is again the confirmation of the exceptional effectiveness of the present FDCIM algorithm with synthetic earthquake-induced response signals.

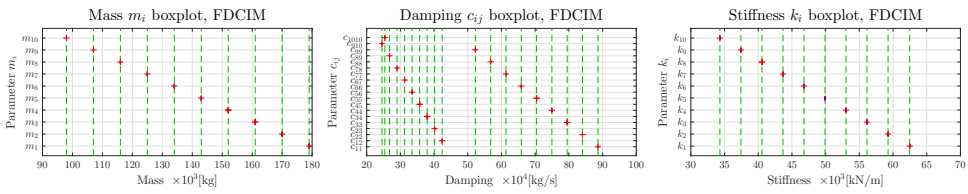

Figure 7.15: *Boxplot diagrams for identified mass m_i, damping c_i and stiffness k_i parameters, ten-storey frame, synthetic response signals, FDCIM algorithm, Rayleigh damping, complete considered earthquake dataset.*

Chapter 8

Analysis and comparison between the three investigated OMA techniques

In the present synoptic chapter, a detailed comparison between the three developed OMA identification methods, namely a Frequency Domain refined Frequency Domain Decomposition (rFDD) technique, a Time Domain Data-Driven Stochastic Subspace Identification (SSI-DATA) procedure and a Time Domain Full Dynamic Compound Inverse Method (FDCIM) is developed (Section 8.1). In particular, after the separate analyses with synthetic earthquake-induced structural response signals already addressed in Chapters 4, 6 and 7, the focus moves now on the further challenging use of real seismic responses, for all the three OMA methods. Some preliminary results with the adoption of real seismic response signals were selectively given in [93, 98].

8.1 rFDD, SSI-DATA and FDCIM analyses with real earthquake-induced structural response signals

8.1.1 Real case study description

Next to the numerical analyses earlier reported in Chapters 4, 6 and 7, where synthetic earthquake-induced structural response signals have been first adopted, as a necessary validation condition, the present rFDD, SSI-DATA and FDCIM OMA approaches are now applied to real earthquake-induced structural response data. The selected structural system is the San Bruno six-storey office building (in short SBOB), California (Fig. 8.1).

Data are taken from the Center of Engineering Strong Motion Data (CESMD) online database [22], and represent a well-documented case, already studied in the dedicated EMA literature [20, 76] (notice that here more challenging OMA is attempted).

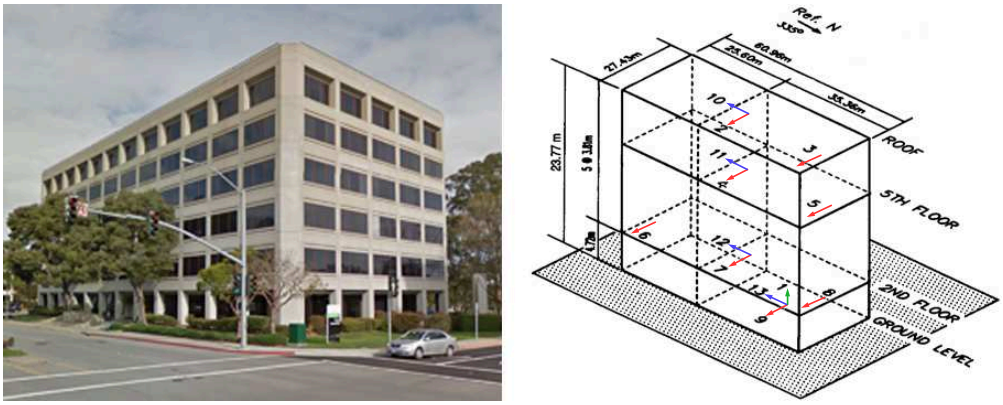

Figure 8.1: *External view of the San Bruno six-storey office building (SBOB), California, and three-dimensional sensor layout (adapted from [76]). Input data are taken from the CESMD database (storey acceleration responses).*

This six-storey building is constituted by RC moment resisting frames, located in the city of San Bruno, in the metropolitan area of San Francisco. The design was made in 1978 and displays a plan of 60.96 m × 27.43 m, and a height of 23.77 m. In particular, this building contains precast, post-tensioned floor beams acting integrally with the floor slabs, while the perimeter columns are cast in cavities formed by the precast wall panels. A heavily reinforced WE interior frame is located 4.88 m South of the geometric center of the building. This eccentricity introduces a twisting component to the WE response. The foundation consists of individual spread footings located just below the ground floor, which is a slab on grade. More information on the building, its history and characteristics may be found in [20, 76].

Thanks to the California Strong Motion Instrumentation Program, the building was instrumented in 1985 (CSMIP Station n. 58490) [22]. The recording system consisted of 13 accelerometers, on four levels of the building: four channels were devoted to the NS direction, eight channels were devised to the WE direction and one channel was setup for the UP direction. Fig. 8.1 briefly represents the overall building dimensions and the instrumentation layout.

In this work, the adopted SBOB seismic response data refer to the local earthquake excitation of Loma Prieta (1989), already considered in the previous synthetic analyses (see Table 4.1), now with main local characteristics as recorded at the building site and reported in Table 8.1. Recorded data belong to the seven WE channels and to the three NS channels (the channels at the ground floor have not been considered, both for the OMA purposes of the present analysis and for their low signal-to-noise ratio).

Peak Ground Acceleration (PGA) and Peak Structural Acceleration (PSA) refer to the ground level and to the roof plan, respectively.

Adopted earthquake	*Date*	*Dur.* [s]	f_s [Hz]	*M*	*Dist.* [km]	*Comp.*	*PGA* [g]	*PSA* [g]
Loma Prieta (LP)	17/10/1989	60	50	7.0	81.0	NS	0.14	0.25
						WE	0.11	0.32

Table 8.1: *Main local characteristics and properties of the Loma Prieta earthquake (CESMD database [22]).*

8.1.2 Performed analyses and results

The developed rFDD, SSI-DATA and FDCIM algorithms have been adopted to analyse the real earthquake-induced structural response data coming from the local Loma Prieta earthquake excitation. In the following, the parameters adopted for the developed analyses are summarized, for each method.

For the rFDD method:

- Butterworth low-pass filtering, order 8, cutting frequency 10 Hz, no decimation of the response signals;
- Integrated PSD matrix computation through both Welch's Modified Periodogram, set with 1024-points Hanning smoothing windows and 66.7% overlapping, and Wiener-Khinchin method, set with a detrended biased correlation matrix.

For the SSI-DATA algorithm:

- Butterworth low-pass filtering, order 8, cutting frequency 15 Hz, no decimation of the response signals;
- Block Hankel matrix parameters: number of block rows set to $i = 50$, number of columns $j = N - 2i + 1$;
- Stabilization diagram parameters: maximum order $n = 150$, detection of stable poles with tolerance levels for frequencies, modal damping ratios and MACs, respectively, set to $\Delta f_k = |f_k - f_{k+1}|/f_k < 0.01$, $\Delta\zeta_k = |\zeta_k - \zeta_{k+1}|/\zeta_k < 0.075$ and $\Delta\mathrm{MAC}_k = 1 - \mathrm{MAC}(\boldsymbol{\phi}_k, \boldsymbol{\phi}_{k+1}) < 0.02$, being k the current model order;
- Stabilization diagram SVs computed through SVD of the PSD matrix as estimated via Welch's Modified Periodogram, set with 1024-points Hanning smoothing windows and 66.7% overlapping.

For the FDCIM algorithm:

- Butterworth low-pass filtering, order 8, cutting frequency 15 Hz, no decimation of the response signals;
- Adopted number of points corresponding to the entire response signals;
- Initial values of the iteration vectors set to ${}^0\boldsymbol{\theta}_{ck} = \{1\ 1\ 1\ \ldots\ 1\}^{\mathrm{T}}$ and ${}^0\boldsymbol{\theta}_m = \{1\ 1\ 1\ \ldots\ 1\}^{\mathrm{T}}$;
- Convergence tolerances ε_θ and ε_g set both to 10^{-3};
- Fixing Factor δ computed through the total mass of the building under exam m_{tot}, namely $\delta = P_{real}/P_{est} = m_{tot,real}/m_{tot,est}$.

Then, main results, in terms of estimated natural frequencies and modal damping ratios, are reported in Tables 8.2 and 8.3. The analyses and the resulting modal parameter estimates have been subdivided into the two horizontal spatial components of the excitation, namely the NS and the WE responses. The first three modes of vibration can be identified as well, and deviations between the three methods are reported, as $\Delta f = [(f_{\mathrm{Me,I}} - f_{\mathrm{Me,II}})/f_{\mathrm{Me,II}}]\%$ and $\Delta\zeta = [(\zeta_{\mathrm{Me,I}} - \zeta_{\mathrm{Me,II}})/\zeta_{\mathrm{Me,II}}]\%$, where Me, I and Me, II are the two methods under comparison, i.e. rFDD, SSI-DATA and FDCIM, in turn.

These deviations show to be suitable concerning the natural frequencies, with a maximum of 29.2% on the third natural frequency (SSI-FDCIM) for the NS case and of 29.2% on the second natural frequency (SSI-FDCIM) for the WE case. Despite that, the higher deviations are related to the last modes of vibration, while for the first one, the most important, deviations are more contained.

Then, concerning the modal damping ratios, deviations show to be contained between rFDD and SSI, with a maximum of about 30% for the first mode of the NS cases. The only exceptions are related to the second modes of vibration, where deviations increase, for both NS and WE components. In these cases, SSI-DATA shows much higher modal damping ratios than for rFDD; this is probably due to the presence of two very close modes of vibration, i.e. the first and the second, which may negatively affects the damping estimates.

Rather, for the FDCIM algorithm, modal damping ratio deviations show to be far higher, with different values with respect to rFDD and FDCIM in most cases. This is directly related to the representation of the damping behaviour that is assumed inside the FDCIM algorithm. In simple terms, the matrix behaviour selected for the damping matrix (and in general for the mass and stiffness matrices, too) affects the achievable

estimates, i.e. the identified values are the best values that may result from a representation of the structure via the adopted matrix entities.

	Mode	*Identified - Loma Prieta (NS)*			*Percentage deviations* Δ		
		rFDD	*SSI*	*FDCIM*	*rFDD-SSI*	*rFDD-FDCIM*	*SSI-FDCIM*
f_i [Hz]	1	1.185	1.187	1.048	−0.133%	−11.5%	−11.7%
	2	1.386	1.348	1.590	2.73%	14.8%	18.0%
	3	1.873	1.720	2.222	8.14%	18.7%	29.2%
ζ_i [%]	1	6.38%	8.37%	3.27%	−31.2%	−48.7%	−60.9%
	2	2.54%	7.83%	3.90%	−208%	53.2%	−50.2%
	3	4.55%	5.50%	1.56%	−20.9%	−65.6%	−71.6%

Table 8.2: *Identified natural frequencies f_i, modal damping ratios ζ_i and related deviations, computed among rFDD, SSI-DATA and FDCIM estimates, San Bruno six-storey office building, real response signals, earthquake of Loma Prieta (LP), NS component (Table 8.1).*

	Mode	*Identified - Loma Prieta (WE)*			*Percentage deviations* Δ		
		rFDD	*SSI*	*FDCIM*	*rFDD-SSI*	*rFDD-FDCIM*	*SSI-FDCIM*
f_i [Hz]	1	0.9957	0.9872	1.063	0.851%	7.13%	8.05%
	2	1.286	1.267	1.626	1.52%	27.2%	29.2%
	3	2.302	2.231	2.527	3.11%	9.85%	13.4%
ζ_i [%]	1	3.99%	3.51%	9.33%	12.2%	104%	132%
	2	4.96%	11.2%	11.4%	−125%	130%	2.34%
	3	6.06%	5.00%	2.35%	17.5%	−30.3%	−15.6%

Table 8.3: *Identified natural frequencies f_i, modal damping ratios ζ_i and related deviations, computed among rFDD, SSI-DATA and FDCIM estimates, San Bruno six-storey office building, real response signals, earthquake of Loma Prieta (LP), WE component (Table 8.1).*

Mode shapes, instead, are reported in terms of MAC indexes in Fig. 8.2. These are calculated among the three OMA methods outcomes, i.e. $\mathrm{MAC}(\boldsymbol{\phi}_{\mathrm{Me,I}}, \boldsymbol{\phi}_{\mathrm{Me,II}}) = |\boldsymbol{\phi}^{\mathrm{H}}_{\mathrm{Me,I}}\boldsymbol{\phi}_{\mathrm{Me,II}}|^2/(|\boldsymbol{\phi}^{\mathrm{H}}_{\mathrm{Me,I}}\boldsymbol{\phi}_{\mathrm{Me,I}}|\,|\boldsymbol{\phi}^{\mathrm{H}}_{\mathrm{Me,II}}\boldsymbol{\phi}_{\mathrm{Me,II}}|)$, where $\mathrm{Me,I}$ and $\mathrm{Me,II}$ are the two methods under comparison, i.e. rFDD, SSI-DATA and FDCIM, in turn. Here, 3D MAC barplots are made by combining rFDD vs. SSI, rFDD vs. FDCIM and SSI vs. FDCIM mode shapes, for each mode of vibration. For the rFDD vs. SSI mode shapes, on the diagonal terms, where the same modes are combined, MAC values turn out very close to one, as expected (since the first rFDD mode shape is combined with the first SSI mode shapes, and so on), while off-diagonal terms shall be close to zero, as effectively detected (since different modes are combined to each other, resulting to be orthogonal among them). For the remaining comparison, rFDD vs. FDCIM and SSI vs. FDCIM, the first mode shape display to be estimated with a reasonable accuracy, while some problems remain on the second and third mode shapes, that are not

very well detected. In fact, some issues remain on all the estimates concerning the second and third modes of vibration, for both the NS and WE components.

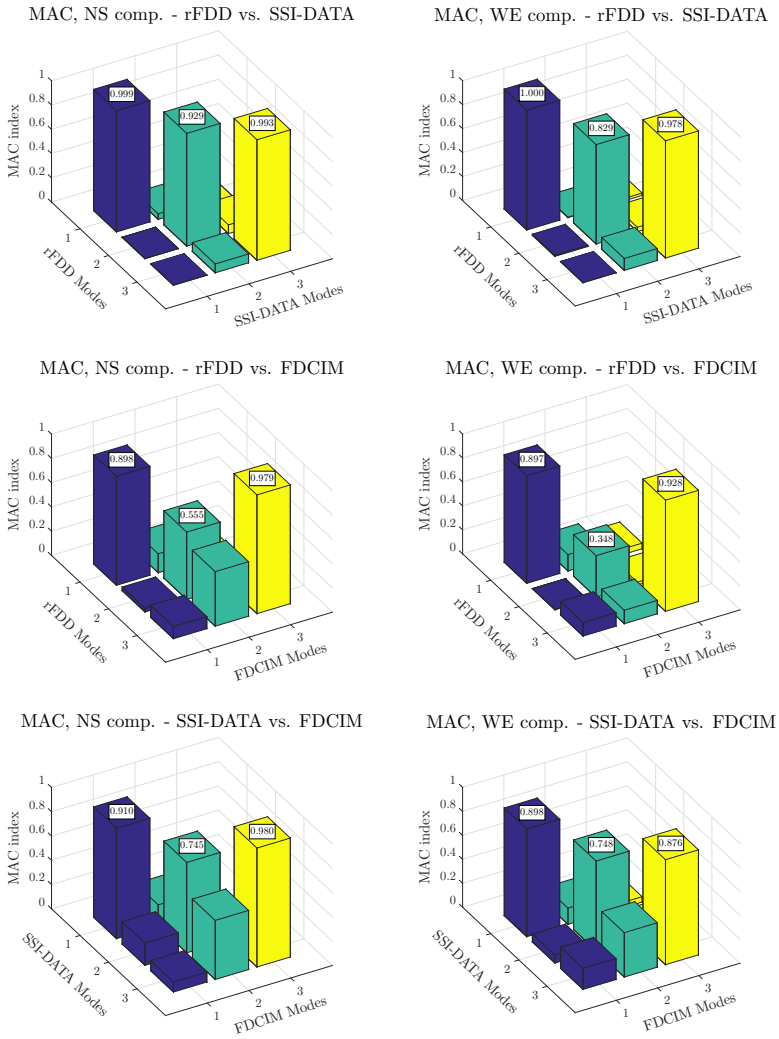

Figure 8.2: *MAC indexes for the estimated mode shapes, computed between rFDD vs. SSI-DATA (1st row), rFDD vs. FDCIM (2nd row) and SSI vs. FDCIM (3rd row) eigenvector estimates, San Bruno six-storey office building, real response signals, earthquake of Loma Prieta (LP), NS and WE components (Table 8.1).*

Notice that the direct comparison with the different OMA methods (with respect to natural frequencies, modal damping ratios and mode shapes), after the numerical analyses with synthetic response signals made in Chapters 4, 6 and 7, helps with the validation of the achieved strong ground motion modal parameters with real signals. In fact, by adopting

the validated method, it is possible to arrive at a set of rFDD, SSI-DATA and FDCIM modal parameters, which can be "self-compared", in order to reach final identification outcomes when structural features are unknown.

Finally, the barplots proposed in Fig. 8.3 represent the achieved natural frequencies and modal damping ratios, computed with the rFDD, SSI-DATA and FDCIM methods for the LP earthquake responses, NS and WE components. In particular, jointly with the estimated parameters, also the target ones are proposed, towards further comparison purposes. Target modal parameters are taken from [20, 76]. For the NS case, the first three natural frequencies and the first modal damping ratio are available, while for the WE case the first two natural frequencies and the first modal damping ratio are provided. These target parameters are marked in grey in Fig. 8.3, and deviations are calculated on them as $\Delta f = [(f_{\text{ID}} - f_{\text{TARGET}})/f_{\text{TARGET}}]\%$ and $\Delta\zeta = [(\zeta_{\text{ID}} - \zeta_{\text{TARGET}})/\zeta_{\text{TARGET}}]\%$.

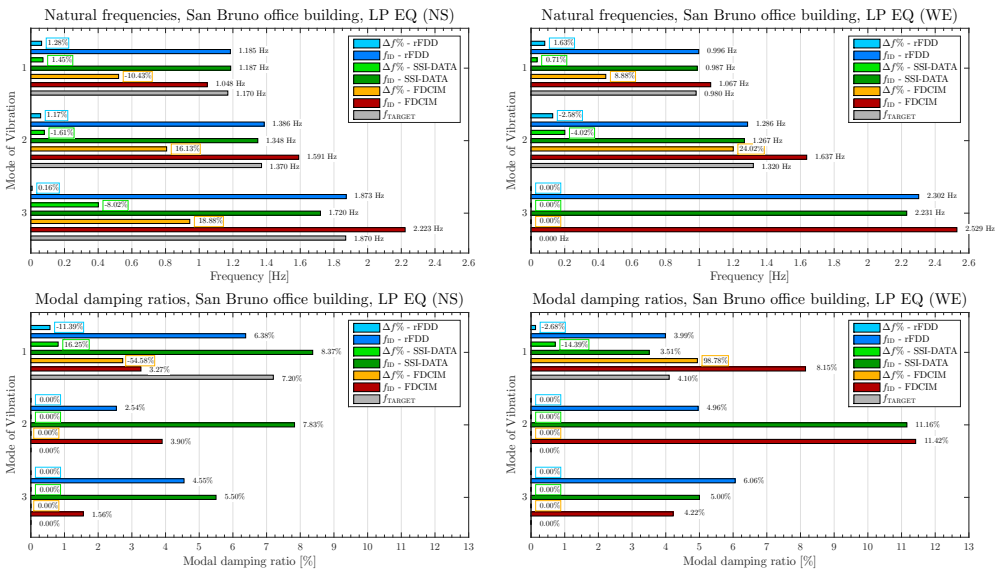

Figure 8.3: *Natural frequency and modal damping ratio barplots for rFDD, SSI-DATA and FDCIM, San Bruno six-storey office building, real response signals, earthquake of Loma Prieta (LP), NS and WE components (Table 8.1). Percentage deviations from the target values (where available) are indicated.*

The limited deviations, especially those related to the natural frequencies, between the estimated and the target values confirm once again the reliability of the proposed OMA techniques in detecting strong ground motion modal parameters with real earthquake-induced structural response signals. Notice that the FDCIM presents the higher deviations, especially for the modal damping ratio estimates. This may be expected, since the FDCIM method imposes, as a starting point of the present implementa-

tion, a specific matrix behaviour for mass, damping and stiffness matrices, which may be not be strictly pertinent for the analysed building. Then, as a consequence, the available estimates reflect the best possible approximation that is possible to be achieved, for the structure under analysis, with such assumed structural behaviours. Accordingly, the approximation improves, the more the supposed structural matrix behaviour becomes adherent to that of the real structure.

8.1.2.1 Element-level identification and input estimation via FDCIM

The FDCIM, further to the modal dynamic identification, allows also for the estimation of the element-level structural parameters and for the identification of the input ground motion excitation. Additionally, also the estimation of the Rayleigh damping parameters is possible. As described before, the total mass of the building is adopted as Fixing Factor parameter for the element-level identification, and is supposed here to be equal to $m_{tot} = 900 \cdot 10^3$ kg, as a first possible approximation based on the characteristics and information on the building.

In Table 8.4, identified values are presented for mass m_i, damping c_{ij} and stiffness k_i element-level structural features, α and β Rayleigh damping coefficients, and Peak Ground Acceleration (PGA) and Root Mean Square (RMS) of the identified seismic base excitation. Both NS and WE components are considered.

Parameter	*Estimated* LP (NS)	*Estimated* LP (WE)	*Parameter*	*Estimated* LP (NS)	*Estimated* LP (WE)
Mass parameters ($\times 10^3$ [kg])			*Stiffness parameters* ($\times 10^2$ [kN/m])		
m_1	676.80	622.20	k_1	754.06	716.53
m_2	172.30	206.90	k_2	187.74	294.67
m_3	50.90	70.90	k_3	35.34	50.75
Damping parameters ($\times 10^4$ [N s/m])			*Rayleigh damping coefficients* ([1])		
c_{11}	1451.74	3852.07	α	6.768792	15.39820
c_{12}	−198.07	−843.33	β	0.105504	0.286194
c_{22}	351.98	1307.15	*Estimated input ground motion* ([m/s^2])		
c_{23}	−37.28	−145.23	PGA	3.16 (0.32 g)	5.58 (0.57 g)
c_{33}	71.73	254.40	RMS	0.69 (0.07 g)	1.56 (0.16 g)

Table 8.4: *FDCIM identified mass m_i, damping c_i and stiffness k_i parameters, Rayleigh damping coefficients α and β, PGA and RMS three-storey frame, real response signals, earthquake of Loma Prieta (LP), NS and WE components (Table 8.1).*

As discussed before, the previous element-level identification and input estimation shall be taken as the best possible approximation for the real

data under analysis, on the basis of the supposed matrix structural behaviour. Then, some peculiar values at the element-level, as well as for the modal analysis, may appear from the FDCIM application. In addition, the present element-level structural features are representative of a 2D three-storey shear-type frame approximation of the original 3D six-storey real building. Than, in order to take into account more DoFs, as a future development issue, it would be possible to pass through a stochastic framework, with the adoption of a Kalman Filter based procedure.

8.2 Main conclusions on the performed OMA analyses

Earlier Chapters 4, 6 and 7 summarized the synthetic analyses performed with the three developed OMA methods, namely rFDD, SSI-DATA and FDCIM, under strong ground motion synthetic structural response signals and heavy damping. Linear frame structures were adopted. Starting from a reference three-storey frame, a ten-storey frame was then adopted, towards approaching even more realistic cases. That by considering base-excitation instances from a selected earthquake dataset of ten seismic signals. These earthquake recordings have been chosen also among ones that were expected to possibly lead to particular identification troubles, due to their intrinsic characteristic signal features and non-stationary.

Furthermore, in Chapter 4 an additional inspection with the FEMA P695 earthquake database was performed for the rFDD algorithm, by adopting all the 22×2 seismic recordings on three different shear-type frames (namely, a two-, a three- and a six-storey frame), for a total of 132 analysed cases. Also, in Chapter 5 a five-storey shear-type frame with an underlying Sway-Rocking Soil-Structure Interaction model was considered for studying fixed- and flexible-base conditions with the rFDD method.

Notice that, differently from rFDD and SSI-DATA, FDCIM is also able to extract element-level structural features (according to a pre-set structural model), Rayleigh damping parameters and input ground motion excitation, and the two adopted synthetic frames were adopted towards an inspection of these features, too.

Finally, present Chapter 8 proposed a comparison between the results achievable from the adoption of the three OMA techniques with real earthquake-induced structural response signals, coming from a real instrumented six-storey RC building in California. This in order to further investigate possible realistic Earthquake Engineering applications of the present output-only methods.

Thus, both synthetic and real earthquake-induced structural response signals have been adopted and consistently analysed in the present work, by adopting the three developed OMA methods. As concerning the syn-

thetic analyses, for all the examined cases the estimates are strongly consistent with the target values, in particular for the natural frequency identification. In the order, the best estimates come from FDCIM, then from rFDD and from SSI-DATA, although they are all characterized by very limited deviations from the targeted natural frequencies.

The other modal parameters are also estimated with quite limited errors, and this holds true as well for the heavy-damped cases, especially for the ten-storey frame. Mode shapes are always estimated with unitary MACs for FDCIM, while MACs slightly decrease for rFDD on the last modes. For SSI-DATA, instead, the last modes of vibration are characterized by lower MAC indexes; anyway, SSI-DATA also confirms a good agreement with the target values, proving its efficacy.

As concerning to the modal damping ratio estimations, FDCIM confirms its efficacy on all the adopted cases. Then, also rFDD is able to detect damping characteristics with very good accuracy. Just the SSI-DATA method reveals some problems with the damping estimation, and this may be the target of future inspections. Thus, the achieved outcomes have shown the present rFDD, SSI-DATA and FDCIM methodologies to turn out rather robust in terms of global modal identification capability, within the considered seismic engineering range, by allowing for objective and readable estimates of all the modal parameters.

Good results from synthetic seismic response signals have been then corroborated and validated by consistent outcomes from real seismic response recordings, especially for the adoption of rFDD and SSI-DATA. SSI-DATA, in the present form, needs to be further enhanced and refined, especially for the modal damping ratio estimates, while FDCIM needs to release the fully deterministic framework, towards a stochastic framework that may be able to reconstruct the missing channels, i.e. the unmonitored floors, of the buildings under analysis. That in order to getting even closer to the real structural behaviour of the buildings themselves.

That observation comes from the necessary consideration that the FDCIM method a-priori imposes a specific matrix structure for mass, damping and stiffness matrices, as a given starting point of the analysis. As a direct consequence, the available estimates reflect the best possible approximation that is possible to be achieved, for the structure under analysis, with such assumed ideal behaviours. Accordingly, the closer the FDCIM approximation is near to the representation of the real structure itself, the more the supposed structural matrix behaviour becomes closer to that of the real structure.

Then, as a specific identification outcome, within the considered and analysed cases, rFDD overall looks superior to SSI-DATA, both with synthetic and real structural recordings. Concerning synthetic data only, FD-

CIM reveals to be the better method among all, by allowing also for the element-level structural parameter and input estimations, but still suffers from some troubles when dealing with real earthquake-induced structural response signals.

Thus, these three OMA methodologies, within the present enhanced implementations, may be effectively used, either separately or all together, for the stated challenging identification purposes. The achieved results help in the understanding of the behaviour of the developed OMA algorithms, by varying the earthquake excitations and by taking as fixed the remaining structural parameters.

In following Chapter 9, main conclusions from the whole doctoral dissertation are summarized, jointly with the main outcomes, results and issues on the formulation and application of the present OMA identification approaches within the seismic engineering range.

Chapter 9

Conclusions

The present doctoral dissertation has outlined the outcomes of a research investigation attempted towards the characterization of Operational Modal Analysis (OMA) techniques within the Earthquake Engineering and Structural Health Monitoring range. In particular, the aim was that of adopting output-only techniques to characterize dynamical systems with the adoption of earthquake-induced structural response signals, also at simultaneous heavy damping (in terms of identification challenge). This since within the Earthquake Engineering field, the purpose will be not only that of knowing the modal dynamic characteristics of the systems under analysis at the pre- and post-earthquake stages (as usually done within classical OMA ambient vibration), but also that of inspecting current structural characteristics, along the development of main earthquake sequences and histories.

This may open up the way to a possible structural characterization and assessment during the earthquake sequences themselves, where modifications of the structures (i.e. damages, anomalous structural responses, Soil-Structure Interaction) may occur, too. Additionally, only structural response signals shall be used, in the assumption of unknown (seismic) input acting at the base of the structure, as it may be in most real practical cases (they may be available, in some cases, as foundation recordings, but possibly characterized by a low signal-to-noise ratio).

In Chapter 2, a brief literature review about Operational Modal Analysis techniques under strong ground motion structural response signals has been presented, to introduce the framework and motivations of the present analysis. In particular, the focus went to the main contributions and researches that have mostly inspired the development of the present implementations.

In theoretical Chapter 3, the novel refined Frequency Domain Decomposition (rFDD) algorithm, a main original subject of the present research

investigation, has been introduced and revealed in all its characteristic features. By starting from its main theoretical background, the attention has moved to the detail of all the computational steps and the adopted arrangements. This rFDD algorithm is a non-parametric Frequency Domain method, originally developed and implemented within MATLAB.

Then, Chapter 4 summarized the synthetic analyses performed with the rFDD algorithm, under strong ground motion structural response signals and at heavy damping conditions. Linear frame structures were adopted, for all the analyses. Starting from a reference three-storey frame, a realistic ten-storey frame was then adopted, towards approaching even more realistic cases. That by considering base-excitation instances from a selected earthquake dataset of ten seismic signals. These earthquake recordings have been chosen also among ones that were expected to possibly lead to considerable identification troubles, due to their intrinsic characteristic signal features and non-stationary. Furthermore, an additional inspection with the FEMA P695 earthquake database was explored by the rFDD processing, by adopting all the 22×2 seismic recordings, on three different shear-type frames (namely, a two-, a three- and a six-storey frame), for a total of 132 analysed cases.

Further analyses with the rFDD algorithm have been reported in Chapter 5, where a five-storey shear-type frame with underlying Sway-Rocking Soil-Structure Interaction was considered. After the explanation of the adopted model, the focus moved onto the analysed cases, where the selected earthquake dataset of ten seismic signals was adopted as base excitation for the five-storey building, and five different underlying soil conditions have been modelled. In this case, the purpose was that of detecting both flexible- and fixed-base modal parameters with the rFDD algorithm and with some preliminary arrangements attached to it.

In Chapter 6, a Data-Driven Stochastic Subspace Identification (SSI-DATA) implementation has been introduced and explained in detail in all its computational steps, as specifically arranged here to work with earthquake-induced structural response signals and heavy damping conditions. This is a parametric Data-Driven Time Domain method, again developed and implemented within MATLAB. Then, synthetic analyses with the same reference three-storey frame and realistic ten-storey frame adopted for rFDD were proposed, with comparisons between the outcomes from the two methods.

In Chapter 7, the third developed output-only algorithm has been presented, namely the innovative Full Dynamic Compound Inverse Method (FDCIM). Starting from its theoretical background, both for General and Rayleigh damping, the focus went to its main computational steps, all addressed in large detail. This is a parametric deterministic

two-stage iterative algorithm in the Time Domain, originally developed and implemented within MATLAB. Synthetic analyses with the same reference three-storey frame and realistic ten-storey frame adopted for the rFDD and SSI-DATA techniques have been proposed and made the subject of consistent comparisons. Further, such FDCIM is able to extract also element-level structural features, Rayleigh damping parameters and input ground motion excitation; the two synthetic frames were adopted towards an inspection of these features, too.

Finally, Chapter 8 proposed a comparison between the results achievable from the adoption of the three OMA techniques with real earthquake-induced structural response signals, coming from a real instrumented six-storey RC building in California with data taken from a seismic database (CESMD). This in order to explore possible real Earthquake Engineering applications of the present output-only methods.

Thus, both synthetic and real earthquake-induced structural response signals have been adopted and consistently analysed in the present work, by using the three implemented OMA methods. As concerning the synthetic analyses, for all the adopted cases, the estimates turned out strongly consistent with the target values, in particular for the natural frequency identification. Also the other modal parameters were estimated with quite limited errors, and this holds true for the heavy-damped cases as well, especially for the ten-storey frame. Just the SSI-DATA method revealed some problems with the damping estimation, and this may be the target of future investigations. Thus, the achieved outcomes have shown that the present rFDD, SSI-DATA and FDCIM OMA methodologies turned out rather robust in terms of global modal identification capability, within the considered seismic engineering range, by allowing for objective and readable estimates of all the modal parameters.

Good results from synthetic seismic response signals have been also corroborated and validated by consistent outcomes from real seismic response recordings, especially for the rFDD and SSI-DATA techniques. The rFDD algorithm, a main subject of the present work, looks the riper modal identification tool among the adopted methods, within the present implementation. SSI-DATA may need to be further enhanced and refined, especially for the modal damping ratio estimates, while FDCIM needs to release the present fully-deterministic framework, towards introducing a stochastic framework that may be able to reconstruct the missing channels, i.e. the unmonitored floors, of the buildings under analysis. That in order to getting even closer to the real structural behaviour of the buildings themselves. As a specific identification outcome, within the considered and analysed cases, rFDD looks overall superior to SSI-DATA, both with synthetic and real structural recordings. Concerning synthetic data only,

FDCIM comes out as the better method among all investigated ones, by allowing also for element-level structural parameters and input estimation, though it still suffers from some intrinsic modelization limitations when dealing with real earthquake-induced structural response signals on a specific structure.

Thus, these three OMA methodologies, within the present enhanced implementations, may be effectively used, either separately or all together, for the stated challenging identification purposes within the seismic engineering range. The achieved results help in the understanding of the behaviour of the adopted OMA algorithms, by varying the earthquake excitations and by taking as fixed the remaining structural parameters.

In the following, specific outcomes, results and issues on the formulation and application of the present three OMA approaches developed in the thesis are summarized below in itemized form, for each considered output-only identification method.

Refined Frequency Domain Decomposition (rFDD):

- The devised time-frequency signal analysis (Section 3.2.1) drives the selection of the correct frequency range that shall be adopted in the subsequent computational steps, as well as for the set-up of the parameters of the procedure. Time-frequency Gabor Wavelet Transforms and a specific data filtering applied before identification are adopted in the rFDD procedure.

- The processing of the auto- and cross-correlation matrix (Section 3.2.2) acts as a sort of "regularization process", by helping in removing possible troubles and noises related to the use of non-stationary seismic data. This procedure results into clearer and well-defined SVs.

- The integrated approach for the PSD matrix computation (Section 3.2.3), combining both Weiner-Khinchin and Welch's methods, leads to fundamental support in the case of strong ground motion input and simultaneous heavy damping, especially when real earthquake-induced response signals are taken into account as input channels. This directly reflects into a better detection of the modal peaks and of all the modal identification outcomes.

- The estimation of the modal damping ratios takes advantage of the iterative optimization algorithm, which is able to detect the damping decay associated to each SDoF spectral bell, i.e. to each mode of vibration, with more efficacy. This procedure allows for better

modal damping ratio estimates, also with heavy structural damping, in terms of identification challenge (Section 3.3.2).

- The strategy for the enhancement of the modal parameter estimates via coupled Chebyshev Type II filters (Section 3.3.3) takes particular benefit when the adopted earthquakes exhibit stronger non-stationary and "borderline features" for the rFDD approach. The procedure aims at isolating each single modal contribution, i.e. each SDoF spectral bell, from the remaining spectra, and then on the SVs after the SVD computation. This results into even better modal parameter estimates, especially as concerning the modal damping ratios.

- The estimation of the modal parameters has been performed by operating on different SVs (and on their composition), leading to well-defined spectral bells, without the need of so-called Blind Source Separation methods (Section 3.4.1).

- The enhancement of the frequency resolution (Section 3.4.2) appears to be a fundamental step towards achieving reliable modal parameter estimates, especially with low frequency sampling acquisitions and/or very short durations.

- The combined use of different Modal Assurance Criterion (MAC) indexes (Section 3.4.3), i.e. MAC, Auto-MAC and Auto-MPC, helps for modal identification and validation, especially when dealing with seismic input and heavy damping and when no target parameters are available.

- The effectiveness of the rFDD technique has been definitely proven, by adopting the complete Far-Field set from the FEMA P695 seismic database (44 earthquake records), with simultaneous heavy damping conditions (Section 4.3). Modal damping ratios ranged from $\zeta_i = 2\%$ to $\zeta_i = 5\%$, and then until values of $\zeta_i = 10\%$, for the last analyses, which focussed on the earthquake excitation instances that have lead to the most demanding rFDD identification conditions.

- The synthetic analysis reported in Chapter 5 demonstrates that the present rFDD approach can deal also with Soil-Structure Interaction effects. Soil-Structure modal parameters, in terms of fixed- and flexible-base estimates, have been effectively identified within the adopted output-only conditions.

Data-Driven Stochastic Subspace Identification (SSI-DATA):

- The specific filtering applied before the identification procedure helps in reaching better stabilization diagrams, while the decimation of the signals does not allow for the improvement of the achievable estimates.

- The LQ factorization and implementation outlined in Section 6.1.2 demonstrate to work very well also with rather short seismic structural response signals and heavy damping, in terms of identification challenge.

- The adoption of the Canonical Variate Analysis (CVA) weighting (Sections 6.1.1 and 6.1.3) turns out to be the most stable and performing option towards achieving reliable estimates at seismic response input and heavy damping, since it returns also clear and well-defined stabilization diagrams.

- The specifically developed stabilization diagrams originate from a sort of "fusion" of rFDD and SSI-DATA information. These diagrams combine classical stabilization graphs (from SSI-DATA) with the simultaneous use of SV curves, which are computed from the SVD of the direct output spectral matrix, through a routine of the rFDD algorithm (Section 6.1.3). The so-developed original procedure provides a reliable tool to support the individuation of the stable SSI poles within the stabilization diagrams, which most of times are very difficult to be read, specifically once earthquake-induced structural response signals are adopted.

- Within the stabilization diagrams, tolerance levels for the stable poles need to be revised for this specific field. Specifically, they are set to $\Delta f_k = |f_k - f_{k+1}|/f_k < 0.01$, $\Delta\zeta_k = |\zeta_k - \zeta_{k+1}|/\zeta_k < 0.075$ and $\Delta\mathrm{MAC}_k = 1 - \mathrm{MAC}(\boldsymbol{\phi}_k, \boldsymbol{\phi}_{k+1}) < 0.02$ for frequencies, modal damping ratios and MACs, respectively, being k the current system order.

- The selection of the correct system order, towards modal dynamic characterization, results to be a critical issue with seismic response signals, due to their intrinsic short duration. Then, the Block Hankel matrix shall be set with the maximum number of columns ($j = N - 2i + 1$) and with a limited number of block rows (variable in the range $30 \leq i \leq 80$), in order to make it possible for the adoption of higher system orders ($n = m \cdot i$, as a function of number of response channels m and number of block rows i), required for a better readability of the stabilization diagrams.

- The combined use of different Modal Assurance Criterion (MAC) indexes, as seen with the rFDD algorithm (Section 3.4.3), results to be necessary also with SSI-DATA, towards effective modal identification and validation.

Full Dynamic Compound Inverse Method (FDCIM):

- The theoretical framework of the new FDCIM technique has been innovatively developed and presented in Sections 7.1 and 7.2, starting from the underlying mathematical model and the basic governing equations (Section 7.1.1), by aiming at a complete and exhaustive description of the identification method.
- The proposed FDCIM technique works in a completely-deterministic way, it is fully developed in State-Space form and does not require continuous- to discrete-time transformations. Further, it does not depend on computational initialization conditions or on the state estimation.
- The developed FDCIM approach releases strong assumptions of earlier known element-level techniques, especially for the required knowledge of the mass matrix, which is considered here as unknown and thus to be identified. That towards the simultaneous identification of modal parameters, input ground motion excitation and mass, damping and stiffness matrices at the element-level, through an innovative two-stage iterative algorithm (Section 7.1.2). The first stage provides an estimation of the stiffness and damping realizations, while the second stage renders an estimation of the mass realizations and of the input ground motion excitation.
- A Statistical Average technique, a modification process and a parameter projection strategy have been developed within the iterative FDCIM algorithm (Sections 7.1.2 and 7.2.2) and adopted to provide correct constraints and to achieve stronger and faster convergence on the identification estimates.
- The element-level identification procedure (Section 7.1.3), by starting from the estimated realizations of state and output matrices or, equivalently, of mass, damping and stiffness matrices, is able to restore the real amount of each mass, damping and stiffness element by knowing (or estimating) Fixing Factor δ, i.e. a single multiplying scalar parameter allowing to bring the realizations to true element-level estimations.
- The FDCIM technique is able to work not only with the specific form of viscous damping conceived in Section 7.1.1, but also with wider

General or Rayleigh damping behaviours (Section 7.2.1), by adopting specific modifications on the original formulation. To deal with these more general types of damping, the parameter projection strategy has been totally rescheduled (Section 7.2.2).

- The estimation of Rayleigh damping coefficients α and β is possible through an innovative, specifically-developed procedure, working with the solution of a pre-determined set of linear systems and of an average technique (Section 7.2.3), bypassing the difficult problem of non-linear identification, known but basically unsolved in the previous literature.

The on-going research on the three OMA methods may range over different perspectives. For all the considered OMA methods, the first issue may concern the adoption of artificial earthquake excitations, instead of real recorded ones, in order to make it possible for a complete control (and variability) of the seismic excitations acting then as shaking input on the considered structural systems. Then, also the adoption of nonlinear structural models and the consideration of damage scenarios, in that context, may be the target of future investigations.

As concerning rFDD, further research may include the study of alternative methods for the Power Spectral Density calculation and the Singular Value Decomposition, in order to possibly deal with even better handling of non-stationary earthquake-induced structural response signals.

On the SSI-DATA implementation, further studies and refinements on the present methodology would be necessary to improve the performance of the algorithm, especially concerning the challenging modal damping ratio estimates. One possible way may be that of creating an iterative SSI-DATA algorithm, which may be able to recalibrate the estimates at each step, by getting closer and closer to the target values. Then, for the FDCIM technique, further on-going research may concern first some attempts with even more complex embedded structural modelizations.

Then, the possible integration or support by FDCIM to other common output-only methods working with State-Space parametric Time Domain frameworks may be addressed, jointly with additional theoretical investigations towards the transposition of the method into a wider stochastic framework. That in order to deal also with monitoring conditions where not all the DoFs are recorded, by getting even closer to real earthquake-induced structural response signals, where additional work shall be performed in order to improve even more the performance of the new FDCIM technique.

List of Figures

3.1 Auto-PSD of some of the adopted structural input excitations with related linear interpolation. 25

3.2 Accelerogram, Auto-PSD and Gabor Wavelet Transform of Tabas earthquake signal, WE component. 27

3.3 Instantaneous ACF of Tabas earthquake signal, WE component. 27

3.4 Accelerogram, Auto-PSD with linear regression, residuals and GWT of El Centro earthquake (1940). 31

3.5 SVD obtained by the rFDD algorithm (a) without ($\mathbf{R}_{yy}(\tau)$) and (b) with ($\mathbf{R}_{yy}^{\mathrm{detr}}(\tau)$) processing of the correlation matrix, ten-storey frame, L'Aquila earthquake, NS component. 32

3.6 SVD obtained from integrated computation of the PSD matrix: (a) Corr Approach; (b) Welch Approach; response to Encino earthquake (2014), NS component. 34

3.7 Display of the peak-picking technique on the first singular value and of the spectral bell identification of the first mode; six-storey frame, L'Aquila earthquake. 37

3.8 Selected time window of the normalized IDFT and linear regression technique for the estimate of the modal damping ratio; first mode, six-storey frame, L'Aquila earthquake. 38

3.9 ACF curve fitting for the 1st mode of vibration of a two-, three- and six-storey frame, Kocaeli b) (12082), Superstition Hills b) (12122) and Chi-Chi a) (12141) earthquakes, NS component. . 42

3.10 Magnitude and phase response of the adopted Chebyshev Type II bandpass filter for the enhancement of the II mode SDoF spectral bell, two-storey frame. 43

3.11 Chebyshev Type II bandpass filtering on the I and II mode on the 1st-storey responses and FFT of the responses, Chi-Chi a) (12141) earthquake, NS component, two-storey frame. 45

3.12 SVD obtained from the Chebyshev Type II bandpass filtering on the first and second mode, Chi-Chi a) (12141) earthquake, NS component, two-storey frame. 45
3.13 SVD obtained from basic rFDD and rFDD+filter for: (a) two-storey frame, Chi-Chi a) (12141) earthquake, NS component; (b) three-storey frame, Superstition Hills b) (12122) earthquake, NS component. 46
3.14 Display of the SVD and of the fictitious SV related to the fourth vibration mode, six-storey frame, L'Aquila earthquake. 47
3.15 MAC, Auto-MAC and Auto-MPC for the estimated mode shapes; six-storey frame, L'Aquila earthquake ($\zeta_k = 1\%$). . . . 50

4.1 Deviations of estimated f_i and ζ_i, and MAC indexes, three-storey frame, synthetic response signals, rFDD algorithm, complete considered earthquake dataset. 55
4.2 Dispersion diagrams for the deviations of estimated f_i and ζ_i, and for the MAC indexes, three-storey frame, synthetic response signals, rFDD algorithm, complete considered earthquake dataset. 56
4.3 Boxplot diagrams for estimated f_i, ζ_i and MAC indexes, three-storey frame, synthetic response signals, rFDD algorithm, complete considered earthquake dataset. 57
4.4 Deviations of estimated f_i and ζ_i, and MAC indexes, ten-storey frame, synthetic response signals, rFDD algorithm, complete considered earthquake dataset. 58
4.5 Dispersion diagrams for the deviations of estimated f_i and ζ_i, and for the MAC indexes, ten-storey frame, synthetic response signals, rFDD algorithm, complete considered earthquake dataset. 59
4.6 Boxplot diagrams for estimated f_i, ζ_i and MAC indexes, ten-storey frame, synthetic response signals, rFDD algorithm, complete considered earthquake dataset. 59
4.7 Deviations of estimated f_i and ζ_i, and MAC indexes, two-storey frame, $\zeta_i = 5\%$, Far-Field FEMA P695 database, NS and WE components. 64
4.8 Deviations of estimated f_i and ζ_i, and MAC indexes, three-storey frame, $\zeta_i = 3\%$, Far-Field FEMA P695 database, NS and WE components. 65
4.9 Deviations of estimated f_i and ζ_i, and MAC indexes, six-storey frame, $\zeta_i = 2\%$, Far-Field FEMA P695 database, NS and WE components. 67

4.10 Histograms and truncated Gaussian fit of f_i and ζ_i deviations and of MAC indexes for three sample cases, two-, three- and six-storey frames, Far-Field FEMA P695 database, NS and WE components. 68

4.11 Dispersion diagrams for the deviations of estimated f_i and ζ_i, and for the MAC indexes, two-storey frame, $\zeta_i = 5\%$, Far-Field FEMA P695 database, NS component, WE component, NS and WE components. 69

4.12 Dispersion diagrams for the deviations of estimated f_i and ζ_i, and for the MAC indexes, three-storey frame, $\zeta_i = 3\%$, Far-Field FEMA P695 database, NS component, WE component, NS and WE components. 70

4.13 Dispersion diagrams for the deviations of estimated f_i and ζ_i, and for the MAC indexes, six-storey frame, $\zeta_i = 2\%$, Far-Field FEMA P695 database, NS component, WE component. 71

4.14 Dispersion diagrams for the deviations of estimated f_i and ζ_i, and for the MAC indexes, six-storey frame, $\zeta_i = 2\%$, Far-Field FEMA P695 database, NS and WE components. 72

4.15 Deviations of estimated f_i and ζ_i, and MAC indexes, six-storey frame, $\zeta_i = 10\%$, indicated selected six-earthquakes from the FEMA P695 dataset, NS and WE components. 74

4.16 Boxplot diagrams for estimated f_i, ζ_i and MAC indexes, six-storey frame, $\zeta_i = 10\%$, selected six earthquakes from the FEMA P695 dataset, NS, WE and all (both NS and WE) components. 75

5.1 Adopted linear Sway-Rocking Soil-Structure Interaction model of a multi-storey shear-type frame. 78

5.2 Acceleration, Auto-PSD and GWT of the structural response to Tabas earthquake, Rayleigh damping (ζ_{R}). First-storey response of fixed-base and very-soft soil cases and horizontal sway and system rocking of the very-soft soil case. 82

5.3 Acceleration, velocity and displacement structural responses to Loma Prieta earthquake, Soil-Structure Interaction flexible-base cases (at different soil type), Mass-proportional damping (ζ_{M}). First-storey responses, top-storey responses, horizontal sway responses, system rocking responses. 83

5.4 Targeted mode shapes of the five-storey SR frame at variable soil properties. 86

5.5 Deviations of rFDD estimated f_i and ζ_i for the flexible-base models, and MAC calculated between rFDD estimated and target flexible-base mode shapes, L'Aquila earthquake, Mass-proportional (ζ_M) and Rayleigh damping (ζ_R). 87
5.6 Deviations of estimated f_i and ζ_i, and MAC indexes for the flexible-base models, complete earthquake dataset, Mass-proportional damping (ζ_M). 89
5.7 Deviations of estimated f_i and ζ_i, and MAC indexes for the flexible-base models, complete earthquake dataset, Rayleigh damping (ζ_R). 90
5.8 Estimated mode shapes for the soft soil case, complete earthquake dataset, Mass-proportional (ζ_M) and Rayleigh damping (ζ_R). 91
5.9 Fourier amplitude spectra of top-storey and foundation-sway accelerations and their Ratio |R| for the very-soft soil and for the fixed-base cases, El Centro earthquake (EC), ζ_M and ζ_R dampings. 93
5.10 Deviations of rFDD-OMAX estimated flexible-base and fixed-base natural frequencies with respect to the targets computed for the fixed-base model. 96

6.1 SVD and peak-picking of the modes of vibration by rFDD and Global Stabilization Diagram with 1st rFDD SV by SSI-DATA, three-storey frame, synthetic response signals, earthquake of Maule (CH). 109
6.2 SVD and peak-picking of the modes of vibration by rFDD and Global Stabilization Diagram with 1st rFDD SV by SSI-DATA, San Bruno six-storey office building, real response signals, earthquake of Loma Prieta (LP), NS component. 110
6.3 Deviations of estimated f_i and ζ_i, and MAC indexes, three-storey frame, synthetic response signals, SSI-DATA algorithm, complete considered earthquake dataset. 112
6.4 Dispersion diagrams for the deviations of estimated f_i and ζ_i, and for the MAC indexes, three-storey frame, synthetic response signals, SSI-DATA algorithm, complete considered earthquake dataset. 113
6.5 Boxplot diagrams for estimated f_i and ζ_i, and MAC indexes, three-storey frame, synthetic response signals, SSI-DATA algorithm, complete considered earthquake dataset. 113
6.6 Deviations of estimated f_i and ζ_i, and MAC indexes, ten-storey frame, synthetic response signals, SSI-DATA algorithm, complete considered earthquake dataset. 115

6.7 Dispersion diagrams for the deviations of estimated f_i and ζ_i, and for the MAC indexes, ten-storey frame, synthetic response signals, SSI-DATA algorithm, complete considered earthquake dataset. 116

6.8 Boxplot diagrams for estimated f_i, ζ_i and MAC indexes, ten-storey frame, synthetic response signals, SSI-DATA algorithm, complete considered earthquake dataset. 116

7.1 Lumped mass structural model of the adopted shear-type frame subjected to ground motion base excitation $\ddot{\mathbf{u}}_g$. 120

7.2 Deviations of estimated f_i and ζ_i, and MAC indexes, three-storey frame, synthetic response signals, FDCIM algorithm, Rayleigh damping, complete considered earthquake dataset. . 138

7.3 Dispersion diagrams for the deviations of estimated f_i and ζ_i, and for the MAC indexes, three-storey frame, synthetic response signals, FDCIM algorithm, Rayleigh damping, complete considered earthquake dataset. 139

7.4 Boxplot diagrams for estimated f_i, ζ_i and MAC indexes, three-storey frame, synthetic response signals, FDCIM algorithm, Rayleigh damping, complete considered earthquake dataset. . 140

7.5 Deviations of identified mass m_i, damping c_i and stiffness k_i parameters, three-storey frame, synthetic response signals, FDCIM algorithm, Rayleigh damping, complete considered earthquake dataset. 141

7.6 Deviations of identified α and β Rayleigh damping coefficients and estimated input ground motion excitation in terms of PGA and RMS, three-storey frame, synthetic response signals, FDCIM algorithm, Rayleigh damping, complete considered earthquake dataset. 141

7.7 Dispersion diagrams for the deviations of identified mass m_i, damping c_i and stiffness k_i parameters, three-storey frame, synthetic response signals, FDCIM algorithm, Rayleigh damping, complete considered earthquake dataset. 142

7.8 Boxplot diagrams for identified mass m_i, damping c_i and stiffness k_i parameters, three-storey frame, synthetic response signals, FDCIM algorithm, Rayleigh damping, complete considered earthquake dataset. 142

7.9 Deviations of estimated f_i and ζ_i, and MAC indexes, ten-storey frame, synthetic response signals, FDCIM algorithm, Rayleigh damping, complete considered earthquake dataset. . 144

7.10 Dispersion diagrams for the deviations of estimated f_i and ζ_i, and for the MAC indexes, ten-storey frame, synthetic response signals, FDCIM algorithm, Rayleigh damping, complete considered earthquake dataset. 144
7.11 Boxplot diagrams for estimated f_i, ζ_i and MAC indexes, ten-storey frame, synthetic response signals, FDCIM algorithm, Rayleigh damping, complete considered earthquake dataset. . 145
7.12 Deviations of identified mass m_i, damping c_i and stiffness k_i parameters, ten-storey frame, synthetic response signals, FDCIM algorithm, Rayleigh damping, complete considered earthquake dataset. 146
7.13 Deviations of identified α and β Rayleigh damping coefficients and estimated input ground motion excitation in terms of PGA and RMS, ten-storey frame, synthetic response signals, FDCIM algorithm, Rayleigh damping, complete considered earthquake dataset. 146
7.14 Dispersion diagrams for the deviations of identified mass m_i, damping c_i and stiffness k_i parameters, ten-storey frame, synthetic response signals, FDCIM algorithm, Rayleigh damping, complete considered earthquake dataset. 147
7.15 Boxplot diagrams for identified mass m_i, damping c_i and stiffness k_i parameters, ten-storey frame, synthetic response signals, FDCIM algorithm, Rayleigh damping, complete considered earthquake dataset. 147

8.1 External view of the San Bruno six-storey office building, California, and three-dimensional sensor layout. 150
8.2 MAC indexes for the estimated mode shapes, computed between rFDD vs. SSI-DATA, rFDD vs. FDCIM and SSI vs. FDCIM eigenvector estimates, San Bruno six-storey office building, real response signals, earthquake of Loma Prieta (LP), NS and WE components. 154
8.3 Natural frequency and modal damping ratio barplots for rFDD, SSI-DATA and FDCIM, San Bruno six-storey office building, real response signals, earthquake of Loma Prieta (LP), NS and WE components. 155

List of Tables

4.1 Main features of the adopted set of ten selected earthquake base excitations. 52
4.2 Properties of the analysed reference three-storey frame. . . . 53
4.3 Properties of the analysed realistic ten-storey frame. 53
4.4 Main characteristics of the 22 Far-Field set of earthquakes, FEMA P695. Subsets (1/2) and (2/2) refer to the graphs later reported in Section 4.3.2. 61
4.5 Structural properties of the adopted two-, three- and six-storey shear-type frames. 62
4.6 Modal properties of the adopted two-, three- and six-storey shear-type frames (adopted also in [92]). 63
4.7 Processing parameters for the adopted seismic response signals and considered frame structures. 63

5.1 Characteristic mechanical parameters of the soil-foundation SR system for the four adopted soil types. 82
5.2 Targeted natural frequencies of the five-storey SR frame at variable soil properties. 85
5.3 Targeted modal damping ratios of the five-storey SR frame at variable soil properties, Mass-proportional damping (ζ_{M}). 85
5.4 Targeted modal damping ratios of the five-storey SR frame at variable soil properties, Rayleigh damping (ζ_{R}). 85

8.1 Main local characteristics and properties of the Loma Prieta earthquake. 151
8.2 Identified f_i, ζ_i and related deviations, computed among rFDD, SSI-DATA and FDCIM estimates, San Bruno six-storey office building, real response signals, earthquake of Loma Prieta (LP), NS component. 153

8.3 Identified f_i, ζ_i and related deviations, computed among rFDD, SSI-DATA and FDCIM estimates, San Bruno six-storey office building, real response signals, earthquake of Loma Prieta (LP), WE component. 153
8.4 FDCIM identified mass m_i, damping c_i and stiffness k_i parameters, Rayleigh damping coefficients α and β, PGA and RMS three-storey frame, real response signals, earthquake of Loma Prieta (LP), NS and WE components. 156

Bibliography

[1] Allemang R. (2003), The Modal Assurance Criterion - Twenty years of use and abuse. *Sound and Vibration Magazine*, 37(8):14–23.

[2] Arici Y., Mosalam K.M. (2000), System identification and modeling of bridge systems for assessing current design procedures. In *Proceedings of the Seminar on Utilization of Strong-Motion Data (SMIP2000)*, 14 September 2000, Sacramento, California, Volume 1, pages 77–95.

[3] Arslan M.E., Durmus A. (2013), Modal testing and finite element model calibration of in-filled reinforce concrete frames. *Journal of Vibration and Control*, 20(13):1946–1959.

[4] Au S.K., Zhang F.L. (2016), Fundamental two-stage formulation for Bayesian system identification. Part I: General theory. *Mechanical Systems and Signal Processing*, 66-67:31–42.

[5] Balendra T., Tan Y.P., Lee S.L. (1981), Frequency independent stiffness and damping coefficients for structure-foundation systems. *International Journal of Mechanical Sciences*, 23(9):531–546.

[6] Beck J. (1982), System identification applied to strong motion records from structures. *Earthquake Ground Motion and its Effects on Structures*, Vol. ASME Publications AMD-53, New York, Datt S.K. (Ed.), pages 109–134.

[7] Beck J., Jennings P. (1980), Structural identification using linear models and earthquake recordings. *Earthquake Engineering and Stuctural Dynamics*, 8(2):145–160.

[8] Behmanesh I., Moaveni B., Lombaert G., Papadimitriou C. (2015), Hierarchical Bayesian model updating for structural identification. *Mechanical Systems and Signal Processing*, 64-65:360–376.

[9] Bendat J., Piersol A. (1986), *Random Data, Analysis and Measurements Procedures*. John Wiley & Sons, New York.

[10] Benedetti D., Gentile C. (1994), Identification of modal quantities from two earthquake responses. *Earthquake Engineering and Stuctural Dynamics*, 23(4):447–462.

[11] Boashash B. (2003), *Time Frequency Signal Analysis and Processing - A Comprehensive Reference*. Elsevier, Sidney, Australia.

[12] Brewick P., Smyth A. (2013), An investigation of the effects of traffic induced local dynamics on global damping estimates using operational modal analysis. *Mechanical Systems and Signal Processing*, 41(2):433–453.

[13] Brincker R. (2010). Ideas and Concepts of OMA - Lectures 1-6, CISM Course 2010, 24-28 May 2010, Udine, Italy.

[14] Brincker R., Ventura C., Andersen P. (2001), Damping estimation by frequency domain decomposition. In *Proceedings of the 19th International Modal Analysis Conference (IMAC-XIX)*, 5-8 February 2001, Kissimmee, Florida, Volume 1, pages 698–703.

[15] Brincker R., Zhang L. (2009), Frequency domain decomposition revisited. In *Proceedings of the 3rd International Operational Modal Analysis Conference (IOMAC'09)*, 4-6 May 2009, Portonovo (Ancona), Italy, Volume 1, pages 615–626.

[16] Brincker R., Zhang L., Andersen P. (2000), Output-only modal analysis by frequency domain decomposition. In *Proceedings of the 25th International Conference on Noise and Vibration Engineering (ISMA25)*, 13-15 September 2000, Leuven, Belgium, Volume 1, pages 717–724.

[17] Brincker R., Zhang L., Andersen P. (2001), Modal identification of output-only systems using frequency domain decomposition. *Smart Materials and Structures*, 10(3):441–445.

[18] Cara F., Juan J., Alarcon E., Reynders E., De Roeck G. (2013), Modal contribution and state space order selection in operational modal analysis. *Mechanical Systems and Signal Processing*, 38(2):276–298.

[19] Castelli S., Rota L. (2015), *Applicazione di algoritmo refined Frequency Domain Decomposition volta all'identificazione dinamica*

modale mediante input sismico. B.Sc. Thesis in Building Engineering, Advisor E. Rizzi, Co-advisor F. Pioldi, Università degli Studi di Bergamo, Scuola di Ingegneria, 188 pages, March 2015.

[20] Celebi M. (1996), Comparison of damping in buildings under low-amplitude and strong motions. *Journal of Wind Engineering and Industrial Aerodynamics*, 59(2):309–323.

[21] Celebi M., Phan L.T., Marshall R.D. (1993), Dynamic characteristics of five tall buildings during strong and low-amplitude motions. *The Structural Design of Tall Buildings*, 2(1):1–15.

[22] CESMD Database. (2016), *Center for Engineering Strong Motion Data (CESMD), a cooperative database effort from U.S. Geological Survey (USGS), California Geological Survey (CGS) and Advanced National Seismic System (ANSS)*. Available at: `http://www.strongmotioncenter.org`, accessed at August 2016.

[23] Chen J., Li J. (2004), Simultaneous identification of structural parameters and input time history from output-only measurements. *Computational Mechanics*, 33(5):365–374.

[24] Chen J., Li J., Xu Y.L. (2002), Simultaneous estimation of structural parameter and earthquake excitation from measured structural response. In *Proceedings of the International Conference on Advances and New Challenges in Earthquake Engineering Research (ICANCEER 2002)*, 15-20 August 2002, Hong Kong, China, Volume 3, pages 537–544.

[25] Cho H.N., Paik S.W. (2000), Time domain system identification technique with unknown input and limited observation. In *Proceedings of the 8th ASCE Specialty Conference on Probabilistic Mechanics and Structural Reliability (PMC2000)*, 24-26 July 2000, Notre Dame, Indiana, United States, Volume 3, pages 1–6.

[26] Choi J.S., Lee J.S., Yun C.B. (2004), Identification of the soil-structure interaction system using earthquake response data. *Journal of Engineering Mechanics*, 130(7):753–761.

[27] Chopra A.K. (2012), *Dynamics of Structures: Theory and Applications to Earthquake Engineering, 4th Edition*. Prentice Hall, Englewood Cliffs, New Jersey.

[28] Chopra A.K., Gutierrez J.A. (1974), Earthquake response analysis of multistory buildings including foundation interaction. *Earthquake Engineering and Structural Dynamics*, 3(1):65–77.

[29] Comon P., Jutten C. (2010), *Handbook of Blind Source Separation: Independent Component Analysis and Applications*. Academic Press, Elsevier, Waltham, Massachusetts.

[30] Concha A., Icaza L.A., Garrido R. (2016), Simultaneous parameters and state estimation of shear buildings. *Mechanical Systems and Signal Processing*, 70:788–810.

[31] Datta T.K. (2010), *Seismic Analysis of Structures*. John Wiley & Sons, New York.

[32] Ding Y., Zhao B.L., Wu B. (2014), Structural system identification with extended Kalman filter and orthogonal decomposition of excitation. *Mathematical Problems in Engineering*, 2014(Article ID 987694):10 pages, doi: 10.1155/2014/987694.

[33] Doebling S.W., Farrar C.R. (1999), The state of the art in structural identification of constructed facilities. *Earthquake Ground Motion and its Effects on Structures - Report by the ASCE Committe on Structural Identification of Constructed Facilities*, Datt S.K. (Ed.), Los Alamos National Laboratory, New Mexico.

[34] Durbin J., Koopman S. (2001), *Time Series Analysis by State Space Methods*. Oxford University Press, Oxford, England.

[35] El-Borgi S., Neifar M., Cherif F., Choura S., Smaoui H. (2008), Modal identification, model updating and nonlinear analysis of a reinforced concrete bridge. *Journal of Vibration and Control*, 14(4):511–530.

[36] Ewins D. (2000), *Modal Testing: Theory, Practice and Applications - Second Edition*. Research Studies Press LTD, Baldock, Hertfordshire, England.

[37] Federal Emergency Management Agency. (2009), Quantification of Building Seismic Performance Factors. *Report FEMA P695*, Washington DC, USA, 421 pages.

[38] Ferrari R., Froio D., Chatzi E., Gentile C., Pioldi F., Rizzi E. (2015), Experimental and numerical investigation for the structural characterization of a historic RC arch bridge. In *Proceedings of the 5th ECCOMAS Thematic Conference on Computational Methods in Structural Dynamics and Earthquake Engineering (COMPDYN 2015)*, 25-27 May 2015, Crete Island, Greece, Volume 1, pages 2337–2353.

[39] Ferrari R., Pioldi F., Rizzi E., Gentile C., Chatzi E., Klis R., Serantoni E., Wieser A. (2015), Heterogeneous sensor fusion for reducing

uncertainty in Structural Health Monitoring. In *Proceedings of the 1st ECCOMAS Thematic Conference on Uncertainty Quantification in Computational Sciences and Engineering (UNCECOMP 2015)*, 25-27 May 2015, Crete Island, Greece, Volume 1, pages 511–528.

[40] Ferrari R., Pioldi F., Rizzi E., Gentile C., Chatzi E., Klis R., Serantoni E., Wieser A. (2016), Fusion of Wireless and Non-Contact Technologies for the Dynamic Testing of a Historic RC Bridge. *Measurement Science and Technology*, 27(2):124014, 15 pages, doi: 10.1088/0957-0233/27/12/124014.

[41] Fladung W., Brown D. (1993), Multiple reference impact testing. In *Proceedings of the SPIE - Internaational Society for Optical Engineering*, 19-22 February 1993, Los Angeles, California, Volume 1, pages 1221–1229.

[42] Gade S., Moller N., Herlufsen H., Konstantin-Hansen H. (2003), Frequency domain techniques for Operational Modal Analysis. In *Proceedings of the 21st International Modal Analysis Conference (IMAC-XXI)*, 3-6 February 2003, Kissimmee, Florida, Volume 1, pages 17–26.

[43] Ghahari S., Abazarsa F., Ghannad M., Taciroglu E. (2013), Response-only modal identification of structures using strong motion data. *Earthquake Engineering and Structural Dynamics*, 42(11):1221–1242.

[44] Ghahari S., Ghannad M., Taciroglu E. (2013), Blind identification of soil–structure systems. *Soil Dynamics and Earthquake Engineering*, 45:56–69.

[45] Golub G.H., Van Loan C.F. (1983), *Matrix Computations*. Johns Hopkins University Press, Baltimore, USA.

[46] Gomez H., Ulusoy H., Feng M. (2013), Variation of modal parameters of a highway bridge extracted from six earthquake records. *Earthquake Engineering and Structural Dynamics*, 42(4):565–579.

[47] Gouache T., Morlier J., Michon G., Coulange B. (2013), Operational Modal Analysis with non stationary inputs. In *Proceedings of the 5th International Modal Analysis Conference (IOMAC'13)*, 13-15 May 2013, Guimaraes, Portugal, Volume 1, pages 1527–1534.

[48] Guillaume P., De Troyer T., Devriendt C., De Sitter G. (2007), OMAX: Operational Modal Analysis in presence of eXogenous inputs. In *Proceedings of the 25th International Modal Analysis Con-*

ference (IMAC-XXV), 19-22 February 2007, Orlando, Florida, Volume 2, pages 1018–1028.

[49] Haldar A., Ling X., Wang D. (1997), Nondestructive identification of existing structures with unknown input and limited observations. In *Proceedings of the 7th International Conference on Structural Safety and Reliability (ICCOSAR 97)*, 24-28 November 1997, Kyoto, Japan, Volume 1, pages 363–370.

[50] Hart G., Yao J. (1977), System identification in structural dynamics. *Journal of Engineering Mechanics ASCE*, 103(6):1089–1104.

[51] Hegde G., Sinha R. (2008), Parameter identification of torsionally coupled shear buildings from earthquake response records. *Earthquake Engineering and Structural Dynamics*, 37(11):1313–1331.

[52] Heredia-Zavoni E., Montes-Iturrizaga R., Esteva L. (1999), Optimal instrumentation of structures on flexible base for system identification. *Earthquake Engineering and Structural Dynamics*, 28(12):1471–1482.

[53] Hoshiya M., Saito E. (1984), Structural identification by extended Kalman filter. *Journal of Engineering Mechanics ASCE*, 110(12):1757–1770.

[54] Hoshiya M., Sutoh A. (1995), Identification of input and parameters of a MDOF system. In *Building for the 21st Century: Proceedings of the 5th East Asia-Pacific Conference on Structural Engineering and Construction (EASEC-5)*, 25-27 July 1995, Griffith, Australia, Volume 3, pages 1309–1314.

[55] Housner G.W. (1947), Characteristics of strong-motion earthquakes. *Bulletin of the Seismological Society of America*, 37(1):19–31.

[56] Huang C., Lin H. (2001), Modal identification of structures from ambient vibration, free vibration, and seismic response data via a subspace approach. *Earthquake Engineering and Structural Dynamics*, 30(12):1857–1878.

[57] Jiménez R., Icaza L.A. (2007), A real-time estimation scheme for buildings with intelligent dissipation devices. *Mechanical Systems and Signal processing*, 21(6):2427–2440.

[58] Johnson N.L., Kotz S., Balakrishnan N. (1994), *Continuous Univariate Distributions - Volume 1, 2nd edition.* John Wiley & Sons, New York.

[59] Kausel E. (2010), Early history of soil–structure interaction. *Soil Dynamics and Earthquake Engineering*, 30(9):822–832.

[60] Kramer S.L. (1996), *Geotechnical Earthquake Engineering*. Prentice Hall, Upper Saddle River, New Jersey.

[61] Kun Z., Law S., Zhongdong D. (2009), Condition assessment of structures under unknown support excitation. *Earthquake Engineering and Engineering Vibration*, 8(1):103–114.

[62] Lawson C.L., Hanson R.J. (1974), *Solving Least Squares Problems*. Prentice Hall, Englewood Cliffs, New Jersey.

[63] Lei Y., Liu C., Liu L.J. (2014), Identification of multistory shear buildings under unknown earthquake excitation using partial output measurements: numerical and experimental studies. *Structural Control and Health Monitoring*, 21(5):774–783.

[64] Leurs W., Deblauwe F., Lembregts F. (1993), Modal parameter estimation based on Complex Mode Indicator Functions. In *Proceedings of the 11th International Modal Analysis Conference (IMAC-XI)*, 1-4 February 1993, Kissimmee, Florida, Volume 1, pages 1035–1041.

[65] Li J., Chen J. (1997), Inversion of ground motion with unknown structural parameters (in Chinese). *Earthquake Engineering and Engineering Vibration*, 17(3):27–35.

[66] Li J., Chen J. (2000), Structural parameters identification with unknown input. In *Proceedings of the 8th International Conference on Computing in Civil and Building Engineering (ICCCBE-VIII)*, 14-16 August 2000, Stanford, California, Volume 1, pages 287–293.

[67] Li J., Chen J. (2003), A statistical average algorithm for the dynamic compound inverse problem. *Computational Mechanics*, 30(2):88–95.

[68] Lin C., Hong L., Ueng Y., Wu K., Wang C. (2005), Parametric identification of asymmetric buildings from earthquake response records. *Smart Materials and Structures*, 14(4):850–861.

[69] Ling X., Haldar A. (2004), Element level system identification with unknown input with Rayleigh damping. *Journal of Engineering Mechanics ASCE*, 130(8):877–885.

[70] Liu M.Y., Chiang W.L., Hwang J.H., Chu C.R. (2008), Wind-induced vibration of high-rise building with tuned mass damper including soil–structure interaction. *Journal of Wind Engineering and Industrial Aerodynamics*, 96(6):1092–1102.

[71] Lourens E., Papadimitriou C., Gillijns S., Reynders E., De Roeck G., Lombaert G. (2012), Joint input-response estimation for structural systems based on reduced-order models and vibration data from a limited number of sensors. *Mechanical Systems and Signal Processing*, 29:310–327.

[72] Luco J.E., Trifunac M.D., Long H.L. (1988), Isolation of soil-structure interaction effects by full-scale forced vibration tests. *Earthquake Engineering and Structural Dynamics*, 16(1):1–21.

[73] Magalhães F., Cunha A., Caetano E., Brincker R. (2010), Damping estimation using free decays and ambient vibration tests. *Mechanical Systems and Signal Processing*, 24(5):1274–1290.

[74] Mahmoudabadi M., Ghafory-Ashtiany M., Hosseini M. (2007), Identification of modal parameters of non-classically damped linear structures under multi-component earthquake loading. *Earthquake Engineering and Structural Dynamics*, 36(6):765–782.

[75] Maia N.M.M., Silva J.M.M. (1997), *Theoretical and Experimental Modal Analysis*. Research Studies Press LTD, Taunton, England.

[76] Marshall R.D., Phan L.T., Celebi M. (1992), Measurement of structural response characteristics of full-scale buildings: comparison of results from strong-motion and ambient vibration records. *Report No. NISTIR 4884*, US Department of Commerce, National Institute of Standards and Technology, 74 pages.

[77] Michel C., Guéguen P., Bard P.Y. (2008), Dynamic parameters of structures extracted from ambient vibration measurements: An aid for the seismic vulnerability assessment of existing buildings in moderate seismic hazard regions. *Soil Dynamics and Earthquake Engineering*, 28(8):593–604.

[78] Michel C., Guéguen P., El Arem S., Mazars J., Panagiotis K. (2010), Full-scale dynamic response of an RC building under weak seismic motions using earthquake recordings, ambient vibrations and modelling. *Earthquake Engineering and Structural Dynamics*, 39(4):419–441.

[79] Oppenheim A.V., Shafer R.W., Buck J.R. (1999), *Discrete-Time Signal Processing*. Prentice Hall, Upper Saddle River, New Jersey.

[80] Ott N., Meder H.G. (1972), The Kalman filter as a prediction error filter. *Geophysical Prospecting*, 20(3):549–560.

[81] Pais A., Kausel E. (1988), Approximate formulas for dynamic stiffnesses of rigid foundations. *Soil Dynamics and Earthquake Engineering*, 7(4):213–227.

[82] Pansieri S. (2016), *Time domain output-only modal dynamic Stochastic Subspace Identification algorithm for seismic applications.* M.Sc. Thesis in Building Engineering, Advisor E. Rizzi, co-Advisor F. Pioldi, Università di Bergamo, Scuola di Ingegneria, 203 pages, March 2016.

[83] Peeters B. (2000), *System Identification and Damage Detection in Civil Engineering.* Ph.D. Thesis, Katholieke Universiteit Leuven, Departement Burgerlijke Bouwkunde, Leuven, Belgium, 238 pages.

[84] Peeters B., De Roeck G. (1999), Reference-based stochastic subspace identification for output-only modal analysis. *Mechanical Systems and Signal Processing*, 13(6):855–878.

[85] Peeters B., De Roeck G. (2001), Stochastic system identification for operational modal analysis: a review. *Journal of Dynamic Systems, Measurement, and Control*, 123(4):659–667.

[86] Perry M.J., Koh C.G. (2008), Output-only structural identification in time domain: Numerical and experimental studies. *Earthquake Engineering and Structural Dynamics*, 37(4):517–533.

[87] Perry M.J., Koh C.G., Choo Y.S. (2006), Modified genetic algorithm strategy for structural identification. *Computers and Structures*, 84(8):529–540.

[88] Pioldi F. (2012), *Sulla stima dello smorzamento modale mediante algoritmo Frequency Domain Decomposition.* B.Sc. Thesis in Building Engineering, Advisor E. Rizzi, Università di Bergamo, Dipartimento di Ingegneria, 169 pages, February 2012.

[89] Pioldi F. (2013), *Sulla formulazione di algoritmi ottimizzati di identificazione dinamica modale e loro applicazione in ambito sismico.* M.Sc. Thesis in Building Engineering, Advisor E. Rizzi, Università di Bergamo, Dipartimento di Ingegneria, 359 pages, December 2013.

[90] Pioldi F., Ferrari R., Rizzi E. (2014), A refined FDD algorithm for Operational Modal Analysis of buildings under earthquake loading. In *Proceedings of the 26th International Conference on Noise and Vibration Engineering (ISMA2014)*, 15-17 September 2014, Leuven, Belgium, Volume 1, pages 3353–3368.

[91] Pioldi F., Ferrari R., Rizzi E. (2015), Earthquake structural modal estimates of multi-storey frames by a refined FDD algorithm. *Journal of Vibration and Control*, doi: 10.1177/1077546315608557, available on line.

[92] Pioldi F., Ferrari R., Rizzi E. (2015), Output-only modal dynamic identification of frames by a refined FDD algorithm at seismic input and high damping. *Mechanical Systems and Signal Processing*, 68-69:265–291, doi: 10.1016/j.ymssp.2015.07.004.

[93] Pioldi F., Ferrari R., Rizzi E. (2016), Seismic FDD modal identification and monitoring of building properties from real strong-motion structural response signals. *Structural Control and Health Monitoring*, in press.

[94] Pioldi F., Pansieri S., Rizzi E. (2016), On the processing of earthquake-induced structural response signals by suitable Operational Modal Analysis identification techniques. In *Proceedings of the 27th International Conference on Noise and Vibration Engineering (ISMA2016)*, 19-21 September 2016, Leuven, Belgium, Volume 1, pages 2873–2883.

[95] Pioldi F., Rizzi E. (2015), On modal identification of structures from earthquake response signals by a refined Frequency Domain Decomposition approach. In *Proceedings of the 22nd Conference of the Associazione Italiana di Meccanica Teorica e Applicata (AIMETA 2015)*, 14-17 September 2015, Genova, Italy, Volume 1, pages 307–316.

[96] Pioldi F., Rizzi E. (2016), A Full Dynamic Compound Inverse Method for output-only element-level system identification and input estimation from earthquake response signals. *Computational Mechanics*, 58:307–327, doi: 10.1007/s00466-016-1292-0.

[97] Pioldi F., Rizzi E. (2016), A refined Frequency Domain Decomposition tool for structural modal monitoring in earthquake engineering. *Earthquake Engineering and Engineering Vibration*, in press.

[98] Pioldi F., Rizzi E. (2016), Earthquake-induced structural response output-only identification by two different Operational Modal Analysis techniques. *Submitted for publication.*

[99] Pioldi F., Rizzi E. (2016), Full Dynamic Compound Inverse Method: Extension to General and Rayleigh damping. *Computational Mechanics*, in press, doi: 10.1007/s00466-016-1347-2.

[100] Pioldi F., Rizzi E. (2016), Refined Frequency Domain Decomposition modal dynamic identification from earthquake-induced structural responses. *Submitted for publication.*

[101] Pioldi F., Salvi J., Rizzi E. (2015), FDD modal identification from earthquake response data with evaluation of Soil-Structure Interaction effects. In *Proceedings of the 11th International Conference on Engineering Vibration (ICoEV 2015)*, 7-10 September 2015, Ljubljana, Slovenia, Volume 1, pages 412–421.

[102] Pioldi F., Salvi J., Rizzi E. (2016), Refined FDD modal dynamic identification from earthquake responses with Soil-Structure Interaction. *International Journal of Mechanical Sciences*, in press, doi: 10.1016/j.ijmecsci.2016.10.032, available on line.

[103] Pridham B., Wilson J. (2004), Identification of base-excited structures using output-only parameter estimation. *Earthquake Engineering and Structural Dynamics*, 33(1):133–155.

[104] Pridham B., Wilson J. (2012), System identification methods for (Operational) Modal Analysis: review and comparison. *Archives of Computational Methods in Engineering*, 19(1):51–124.

[105] Priestley M.B. (1981), *Spectral Analysis and Time Series.* Academic Press, Elsevier, Waltham, Massachusetts.

[106] Rainieri C., Fabbrocino G. (2014), *Operational Modal Analysis of Civil Engineering Structures. An Introduction and Guide for Applications.* Springer, Berlin.

[107] Renzi S., Madiai C., Vannucchi G. (2013), A simplified empirical method for assessing seismic soil-structure interaction effects on ordinary shear-type buildings. *Soil Dynamics and Earthquake Engineering*, 55:100–107.

[108] Safak E. (1995), Detection and identification of soil–structure interaction in buildings from vibration recordings. *Journal of Structural Engineering*, 121(5):899–906.

[109] Salvi J., Pioldi F., Rizzi E. (2015), Effectiveness of seismic-tuned passive Tuned Mass Dampers accounting for Soil-Structure Interaction. In *Proceedings of the 11th International Conference on Engineering Vibration (ICoEV 2015)*, 7-10 September 2015, Ljubljana, Slovenia, Volume 1, pages 641–650.

[110] Salvi J., Pioldi F., Rizzi E. (2016), Optimum Tuned Mass Dampers under seismic Soil-Structure Interaction. *Submitted for publication.*

[111] Salvi J., Rizzi E. (2015), Optimum tuning of Tuned Mass Dampers for frame structures under earthquake excitations. *Structural Control and Health Monitoring*, 22(4):707–725.

[112] Sevim B., Atamturktur S., Altunisik A.C., Bayraktar A. (2016), Ambient vibration testing and seismic behavior of historical arch bridges under near and far fault ground motions. *Bulletin of Earthquake Engineering*, 14(1):241–259.

[113] Singh J.P., Agarwal P., Kumar A., Thakkar S.K. (2014), Identification of modal parameters of a multistoried RC building using ambient vibration and strong vibration records of Bhuj eartquake, 2001. *Journal of Earthquake Engineering*, 18(3):444–457.

[114] Smyth A., Pei J., Masri S. (2003), System identification of the Vincent Thomas Bridge using earthquakes records. *Earthquake Engineering and Structural Dynamics*, 32(3):339–367.

[115] Stewart J.P., Fenves G. (1998), System identification for evaluating soil–structure interaction effects in buildings from strong motion recordings. *Earthquake Engineering and Structural Dynamics*, 27(8):869–885.

[116] The MathWorks Inc. (2016), *MATLAB - The Language of Technical Computing: User's Guide (R2015a)*. Available at: `http://uk.mathworks.com/products/matlab/`, accessed at August 2016.

[117] Todorovska M.I. (2009), Soil–structure identification of Millikan Library North–South response during four earthquakes (1970–2002): what caused the observed wandering of the system frequencies? *Bulletin of the Seismological Society of America*, 99(2A):626–635.

[118] Toki K., Sato T., Kiyono J. (1989), Identification of structural parameters and input ground motion from response time histories. *Proceedings of the Japan Society of Civil Engineers - Structural and Earthquake Engineering N.410/I12*, 6(2):413–421.

[119] Trifunac M.D., Ivanovic S.S., Todorovska M.I. (2001), Apparent periods of a building. I: Fourier analysis. *Journal of Structural Engineering*, 127(5):517–526.

[120] Valerio J. (1992), Spectral analysis of earthquake accelerations as realizations of a non-stationary stochastic process. In *Proceedings of the 10th World Conference on Earthquake Engineering (10WCEE)*, 19-24 July 1992, Madrid, Spain, Volume 2, pages 901–907.

[121] van Overschee P., De Moor B. (1996), *Subspace Identification for Linear Systems - Theory, Implementation, Applications*. Kluwer Academic Publishers, London.

[122] Ventura C.E., Brincker R., Andersen P. (2005), Dynamic properties of the Painter Street Overpass at different levels of vibration. In *Proceedings of the 6th International Conference on Structural Dynamics (EURODYN2005)*, 4-7 September 2005, Paris, France, Volume 1, pages 167–172.

[123] Villaverde R., Koyama L.A. (1993), Damped resonant appendages to increase inherent damping in buildings. *Earthquake Engineering and Structural Dynamics*, 22(6):491–507.

[124] Wang D., Haldar A. (1994), Element-level system identification with unknown input. *Journal of Engineering Mechanics ASCE*, 120(1):159–176.

[125] Wang T., Zhang L., Tamura Y. (2005), An operational modal analysis method in frequency and spatial domain. *Earthquake Engineering and Engineering Vibration*, 4(2):295–300.

[126] Welch P.D. (1967), The use of Fast Fourier Transform for the estimation of Power Spectra: a method based on time averaging over short, modified periodograms. *IEEE Transactions on Audio and Electroacoustics*, 15(2):70–73.

[127] Wolf J.P. (1985), *Dynamic Soil–Structure Interaction*. Prentice Hall, Englewood Cliffs, New Jersey.

[128] Wolf J.P. (1997), Spring-dashpot-mass models for foundation vibrations. *Earthquake Engineering and Structural Dynamics*, 26(9):931–949.

[129] Zhang F.L., Au S.K. (2016), Fundamental two-stage formulation for Bayesian system identification. Part II: Application to ambient vibration data. *Mechanical Systems and Signal Processing*, 66-67:43–61.

[130] Zhang L., Tamura Y. (2003), Damping estimation of engineering structures with ambient response measurements. In *Proceedings of the 21st International Modal Analysis Conference (IMAC-XXI)*, 3-6 February 2003, Kissimmee, Florida, Volume 1, pages 226–233.

[131] Zhang L., Wang T., Tamura Y. (2010), A frequency-spatial domain decomposition (FSDD) technique for operational modal analysis. *Mechanical Systems and Signal Processing*, 24(5):1227–1239.

[132] Zhao X., Xu Y.L., Chen J. (2006), Hybrid identification method for multi-story buildings with unknown ground motion: theory. *Journal of Sound and Vibration*, 291(1):215–239.

[133] Zu F., Mak C.M. (2011), Estimation of best mounting positions for vibratory equipment in buildings. *Journal of Vibration and Control*, 17(2):301–310.